The Radio Science Bulletin

ISSN 1024-4530

INTERNATIONAL
UNION OF
RADIO SCIENCE

UNION
RADIO-SCIENTIFIQUE
INTERNATIONALE

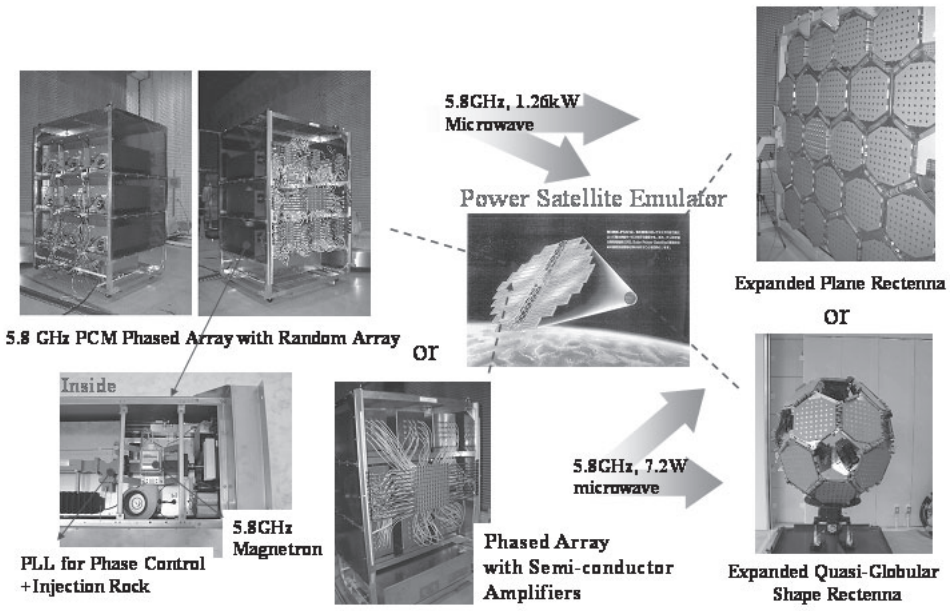

No 310
September 2004

Publié avec l'aide financière de l'ICSU
URSI, c/o Ghent University (INTEC)
St.-Pietersnieuwstraat 41, B-9000 Gent (Belgium)

Contents

Front cover: The SPORTS-5.8, a concept for the Space Solar Power System (SPSS) based on phase-controlled magnetrons: see "Phase Controlled Magnetron Development for SPORTS: Space Power Radio Transmission System."

For information, please contact :
The URSI Secretariat
c/o Ghent University (INTEC)
Sint-Pietersnieuwstraat 41, B-9000 Gent, Belgium
Tel.: (32) 9-264 33 20, Fax: (32) 9-264 42 88
E-mail: ursi@intec.rug.ac.be
http://www.ursi.org

Editorial

It's General Assembly Time!

No, the XXVIIIth General Assembly of URSI won't be held until October 23-29, 2005, in New Delhi, India. However, it *is* time to start submitting your papers: the abstracts must be submitted by **February 1, 2005**, via the Web site: **http://www.ursiga2005.org**. You should submit your abstract(s) and start making plans to attend the General Assembly now. New Delhi –indeed, India – is a wonderful, fascinating place, and you will love the hospitality of our Indian hosts. A call for papers appears in this issue, but you will also need to consult the Web site for complete information on how to submit papers.

Also, the application form for URSI Young Scientists appears in this issue. *The deadline for submission has been extended to* **January 15, 2005**. If you are a radio scientist who will be less than 35 years old on September 1, 2005, please submit a paper to the General Assembly and apply for the Young Scientists program. If you know someone who fits this criterion, please encourage them to apply. URSI Young Scientists will receive free registration and financial support for board and lodging at the General Assembly. They will have unique opportunities to interact with other Young Scientists from around the world, and with all of the radio scientists who attend the General Assembly. Limited funds will also be available as a contribution to the travel costs of Young Scientists from developing countries. Please participate, and encourage the participation of others, in the URSI Young Scientist program. It is our future.

This Issue

This issue of the *Radio Science Bulletin* is late. Although the causes were largely beyond anyone's control, the delay was mine. I'm sorry. However, I think you'll agree that the issue was well worth waiting for.

We have four contributions from the *Reviews of Radio Science* in this issue. Phil Wilkinson deserves much praise for his excellent efforts in coordinating the *Reviews*.

We also have the first part of a two-part Special Section on Space Solar Power Systems (SSPS). These papers were invited by the organizing committee of the 2003 Japan-United States Joint Workshop on Space Solar Power Systems (JUSPS'03), held July 3-4, 2003, at Kyoto University, Japan, from among those presented at the workshop. Very special thanks go to the co-Chairs of the workshop, Hiroshi Matsumoto and Tatsuo Itoh, and to the members of the organizing committee: Kozo Hashimoto, Shigeo Kawasaki, Tomohiko Mitani, Tamotsu Nishino, Naoki Shinohara, and Haruo Tanaka, for providing us with these very interesting papers. As indicated, this is the first of two parts for this special session: the second part will appear in the December issue.

Special thanks, too, to John Volakis, for coordinating the reviews of our papers.

In cellular telephony, the basic method employed to permit multiple mobile users to simultaneously use the same cell is of huge importance. How many users can be supported simultaneously in one cell – and with what quality of service – has a fundamental impact on the cost of the system per user, and thus on the basic profitability of the cellular-service provider. In their *Review of Radio Science* paper from Commission C, Hermann Rohling and Dirk Galda describe orthogonal frequency-division multiplexing (OFDM). This is a multiple-access transmission system that has been used in some applications, but has not yet been used significantly in cellular communication systems. It operates by dividing the available bandwidth into narrowband orthogonal sub-channels. It is the orthogonality of the sub-channels that permits multiple use of the same cell. Indeed, such a system can even permit adjacent cells to operate on the same frequency, leading to the potentially very significant advantages associated with a single-frequency network for a cellular system. However, there are always tradeoffs among system capability and flexibility, and added system requirements and complexity. This *Review* does an admirable job of exploring and explaining these factors. Andy Molisch is the Associate Editor for Commission C, and his efforts in bringing us this review are greatly appreciated.

Surface-based remote sensing of the troposphere plays a critical role in many areas of atmospheric physics, weather forecasting, communications, and other science and engineering. In their Commission F *Review of Radio Science* paper, Ed Westwater, Susanne Crewell, and Christian Mätzler provide us with an excellent overview of microwave and millimeter-wave radiometric techniques for such remote sensing. They begin by providing a very understandable explanation of microwave absorption and emission in the atmosphere and clouds, and go on to explain the key models involved that relate the quantities of interest to the quantities

that can be directly measured. They then provide a review of the basic methods of making such measurements, and of calibrating the measurements. This is followed by an extensive, critical survey and comparison of the various available radiometric systems. They then survey the various tropospheric meterological variables that can be measured, and how the various types of equipment can be used to make such measurements. They take a specific look at climate applications, and conclude with an assessment of the outlook for such radiometric remote sensing. Martti Hallikainen's efforts in bringing this *Review* on behalf of Commission F are greatly appreciated.

Ray tracing is one of the oldest methods of understanding and predicting electromagnetic propagation and, in particular, propagation in the ionosphere. It is still in wide use today. Ray tracing in the ionosphere is the topic of the Commission G *Review of Radio Science* paper by J. A. Bennett, P. L. Dyson, and R. J. Norman. The authors begin with a simple but elegant derivation of the basic equations of rays as an approximate solution to Maxwell's equations. The derivation is readily understandable and remains focused on the physics, while at the same time developing the minimum necessary mathematics to support the rest of the paper. How field intensity can be determined from rays, and the concept of the additional phase shift that occurs when propagation is accompanied by rotation of polarization, are explained. Quantities associated with the variation of rays, including the Doppler shift and absorption, are introduced. The review then takes a critical look at historical methods of ray tracing, followed by overviews of numerical and analytical methods for ray tracing. A very interesting and valuable survey of recent progress in ray tracing is given, including several examples of recent applications. Thanks go to the efforts of Paul Cannon, Associate Editor for Commission G, for bringing this review to us.

There are some fundamental physical limitations involved in the exploration of space beyond Earth's moon. These are clearly and concisely established in the Commission H *Review* by Edgar Bering, Franklin Chang-Díaz, and Jared Squire. They explain that exploration of our solar system will require an engine in which an external source of energy is used to accelerate the propellant: the spacecraft can't carry enough of its own fuel. Furthermore, the propellant must either be kept out of contact with nozzle walls, or must use a non-thermal method of acceleration. They show that these constraints lead directly to the conclusion that some type of electric propulsion system will be used. This leads to a discussion of the fundamental physical principles involved in electric propulsion, followed by a more detailed description of the operation of a several specific RF propulsion systems. The result is a fascinating look at the probable future of space propulsion for exploring our solar system: a future in which radio science will play an important part. Richard Horne is the Associate Editor for Commission H who was responsible for bringing us this most interesting *Review*.

The first Special Section on Space Solar Power Systems (SSPS), in this issue, contains five invited papers. It begins with the paper by S. Sasaki and the USEF SSPS Study Team, which provides a very nice overview of the motivation and concept for SSPS. The authors then introduce the requirements for SSPS. They go on to describe an experiment to demonstrate a number of the key technologies necessary for SSPS.

In several SSPS concepts, solar energy is collected, converted to RF energy at microwave frequencies, and transmitted to the ground. The spacecraft antenna used for transmitting the energy to the ground is a key component of such a system. Shiegeo Kawasaki describes one approach to the design and construction of this antenna. The approach is based on multiple layers in which amplifiers are integrated with the antenna elements into modules. The modules are then assembled to create an antenna array. The results of experiments on demonstration versions of such array elements and on small arrays using these elements are presented.

Another approach to the SSPS spacecraft antenna is presented in the paper by Takashi Hikage, Kousuke Munakata, Toshio Nojima, Manabu Oniya, and Kiyohiko Itoh. They describe a novel cavity-backed slot antenna, in which the usual conducting sidewalls of the cavity are replaced by metal posts. They also present new methods of exciting the antenna element. The design has interesting potential benefits from the standpoints of both mechanical construction and heat dissipation.

Instead of using solid-state amplifiers in an active antenna array to beam the microwave energy to the Earth, Naoki Shinohara, Hiroshi Matsumoto, and Kozo Hashimoto present a system based on an array of phase-controlled magnetrons. Magnetrons have very high efficiencies, and high power output. By using common, commercially available tubes, the cost can be very low. Several technologies had to be developed for such a system, including a phase-controlled magnetron and a low-loss beam-control system. The results of experiments demonstrating these technologies are presented. It appears that the novel method used for phase-controlling the magnetron may well be useful in other applications.

Carbon nanotubes and MEMS (micro-electromechanical systems) are two technologies that hold substantial potential for many applications. Vijay Varadan, Jining Xie, K. J. Vinoy, and Hargsoon Yoon describe several ways these can be used to augment an SSPS. In particular, they show how the electron-transport properties of carbon nanotubes might be used to produce solar panels with enhanced efficiencies. They also examine the use of coiled carbon nanotubes to produce several high-performance large-scale-integration components. They then describe a method of producing RF phase shifters by using barium strontium titanate thin films that are fabricated with micromachining techniques. In addition to the SSPS

applications, this paper provides a very nice, readily understood introduction to the physics and fabrication of carbon nanotubes.

In his Radio-Frequency Radiation Safety and Health column, Jim Lin takes a critical look at recent experimental work on the effects of cell-phone radiation on the blood-brain barrier in rats. Although there is evidence that a significant effect may have been observed, replication of the experiments is needed. This makes for interesting reading from two standpoints: the information regarding potential cell-phone radiation effects, and what is to be learned about replication and verification of experimental results.

The Swedish radio station SAQ has been added to the UNESCO World Heritage List. It is a fascinating bit of history, and URSI played a part. Be sure to read Carl Henrik Walde's report. There is a new Commission G Working Group on Ionospheric Research to Support Radio Systems. A description and an invitation to become involved appears in this issue. Congratulations to the German URSI Member Committee on its fiftieth anniversary! A brief report appears in this issue.

It's *Still* General Assembly Time!

I'll close with the same thought with which I began this column: go submit a paper to the General Assembly. Go convince a young scientist to apply for the Young Scientists program. As is usual with good things, you'll get a very positive return from your efforts – and you'll get to interact with some interesting colleagues, experience a fascinating part of the world, and make a difference in radio science.

New Delhi General Assembly

23 - 29 October 2005

YOUNG SCIENTISTS PROGRAMME

Deadline applications YS has been changed !!!

Please note that the closing date for YS applications to reach the secretariat was shifted from 15 November **to 15 January 2005**!!!

In early June the list of selected YS will appear on the URSI website.
Each YS applicant will receive a letter by mail with the message whether or not he or she receives a YS award.

Please check the Latest News section on the URSI homepage :

http://www.ursi.org/

and the site of the GA05:

http://www.ursiga2005.org/

Call for Papers

XXVIIIth General Assembly of
International Union of Radio Science (URSI)
New Delhi, India
23-29 October, 2005

The International Union of Radio Science, URSI (Union Radio-Scientifique Internationale), is one of 27 Scientific Unions that adhere to the International Council for Science (ICSU). One of the main objects of URSI is to stimulate and to coordinate, on an international basis, studies in the fields of radio, telecommunications, and electronic sciences (http://www.ursi.org). The General Assembly of URSI is held at intervals of three years. The main objective of the Assembly is to review current trends in research, presents new results, and make plans for future research work for specific projects, especially where it seems desirable to arrange for cooperation on an international scale. The next General Assembly of URSI will be held in New Delhi, India, in 2005. Radio scientists from all countries are encouraged to participate.

Topics

The topics of the General Assembly are reflected in the 10 Scientific Commissions of URSI (a schedule of planned sessions is available on the Web site):

- A. *Electromagnetic Metrology*; Chair: Dr. Quirino Balzano (qbalzano@eng.umd.edu)
- B. *Fields & Waves*; Chair: Prof. Makoto Ando (mando@antenna.ee.titech.ac.jp)
- C. *Radio-Communication Systems & Signal Processing*;
  Chair: Prof. Masami Akaike (akaike@ee.kagu.tus.ac.jp)
- D. *Electronics & Photonics*; Chair: Prof. Peter Russer (russer@ei.tum.de)
- E. *Electromagnetic Noise & Interference*;
  Chair: Prof. Pierre Degauque (Pierre.Degauque@univ-lille1.fr)
- F. *Wave Propagation & Remote Sensing*;
  Chair: Prof. Martti T. Hallikainen (martti.hallikainen@avasun.hut.fi)
- G. *Ionospheric Radio & Propagation*; Chair: Prof. Christian Hanuise (hanuise@cnrs-orleans.fr)
- H. *Waves in Plasmas*; Chair: Prof. Umran S. Inan (inan@nova.stanford.edu)
- J. *Radio Astronomy*; Chair: Prof. Makoto Inoue (inoue@nro.nao.ac.jp)
- K: *Electromagnetics in Biology & Medicine*; Chair: Dr. Bernard Veyret (b.veyret@enscpb.fr)

Submissions

Abstracts can be submitted only through the Web site: **http://www.ursiga2005.org**.
Deadlines: Submission of abstract: **February 1, 2005**; Submission of full paper: **June 15, 2005**.
Support for **Young Scientists** is available: the deadline is **November 15, 2004**. See the Web site for details.

Contacts

Conference Secretariat: URSI GA 2005 Secretariat, National Physical Laboratory, Dr. K. S. Krishnan Road, New Delhi 110 012 INDIA; Tel: +91 11 2584 1506; Fax: +91 11 2572 6952; +91 11 2584 1506;
E-mail: ursiga2005@mail.nplindia.ernet.in

Further Information

For information regarding venue, registration, fees, accommodations, and schedule please see the Web site:

http://www.ursiga2005.org

UNION RADIO-SCIENTIFIQUE INTERNATIONALE

INTERNATIONAL UNION OF RADIO SCIENCE

URSI AWARDS FOR YOUNG SCIENTISTS

CONDITIONS

A limited number of awards are available to assist young scientists from both developed and developing countries to attend the General Assembly of URSI.

To qualify for an award the applicant :

1. must be less than 35 years old on September 1 of the year of the URSI General Assembly;

2. should have a paper, of which he or she is the principal author, submitted and accepted for oral or poster presentation at a regular session of the General Assembly;

Applicants should also be interested in promoting contacts between developed and developing countries.

All successful applicants are expected to participate fully in the scientific activities of the General Assembly. They will receive free registration, and financial support for board and lodging at the General Assembly. A basic accommodation is provided by the assembly organizers that permits the Young Scientists from around the world to collaborate and interact. Young scientists may arrange alternative accommodation, but such arrangements are entirely at their own expense. Limited funds will also be available as a contribution to the travel costs of young scientists from developing countries.

*Apply before **15 January 2005** to the URSI Secretariat (address below). Please submit **THREE COPIES** of each of the following: (1) a completed application form, (2) a CV and list of publications, (3) an abstract of proposed paper.*

*Applications will be assessed by the URSI Young Scientist Committee taking account of the national ranking of the application and the technical evaluation of the abstract by the relevant URSI Commission. Awards will be announced on the URSI web-site in **June 2005.***

The URSI Secretariat
c/o Ghent University / INTEC
Sint-Pietersnieuwstraat 41
B-9000 GENT
BELGIUM
fax : (32) 9-264.42.88
e-mail : ursi@intec.rug.ac.be

For more information about URSI, the General Assembly and the activities of URSI Commissions, please look at the URSI web site at: http://www.ursi.org

APPLICATION FOR A YOUNG SCIENTISTS AWARD

I wish to apply for an award to attend the XXVIIIth General Assembly of the International Union of Radio Science in New Delhi, India, 23-29 October 2005.

Name : Prof./Dr./Mr./Mrs./Ms. .....

Sex : male / female Family Name First Name Middle Initials

Date of birth (day / month / year) : .... / .... / .... Nationality : .....

Studying/Employed at : .....

Institution .....

Department .....

Mailing address : Please send all correspondence to my ☐ business / ☐ home address, i.e.

Street .....

City and postal code .....

Province/State ..... Country .....

Fax ..... E-mail .....

Academic qualifications, with date(s) obtained : .....

.....

Title of abstract submitted : .....

.....

Type of session preferred: ☐ in an oral session ☐ in a poster session

The subject of the paper is relevant to URSI Commission …….session (leave blank if uncertain).

Date : ..... Signed .....

For applicants from developing countries only :

I estimate the cheapest return fare to the URSI meeting is EURO .....

For graduate students only - Supervisor's endorsement :

I support the application for an award to enable this young scientist to attend the forthcoming General Assembly of URSI for the following reasons : .....

.....

.....

.....

Supervisor's Name and Title : .....

Address : .....

Date : ..... Signed : .....

Conceptual Study of SSPS Demonstration Experiment

S. Sasaki, K. Tanaka,
S. Kawasaki, N. Shinohara
K. Higuchi, N. Okuizumi,
K. Senda, K. Ishimura &
theUSEF SSPS Study Team

Abstract

An SSPS (Space Solar Power System) study team was organized under the USEF/METI (Institute for Unmanned Space Experiment Free Flyer/Ministry of Economy, Trade, and Industry) committee on SSPS technologies for practical use. The study team, composed of researchers from universities and national laboratories, has made a conceptual study of a demonstration experiment, planned for the near future, to verify the essential technologies for SSPS. The basic plan is to place a satellite in low Earth orbit to demonstrate microwave power transmission to the ground. The satellite has a 16 m × 17.6 m plate consisting of 400 power-generation/transmission modules and an end mass, which are connected with a truss and tether wires. The attitude is stabilized by the gravity-gradient force so that the transmitting antennas in the lower panel are always directed toward the ground. The experiment will be able to demonstrate microwave power transmission of more than 100 kW from orbit to the ground target. The study team has also led the development and testing of the microwave circuits for phase control and power amplification, which are critical for the demonstration experiment.

1. Introduction

The idea for the Space Solar Power System was first proposed by P. Glaser in 1968 [1], as a sustainable energy source for mankind in the future. Solar energy is converted into electricity and fed to microwave generators in orbit. The microwave antenna transmits the microwave power beam to a receiving antenna on the ground. The microwave energy is reconverted to electricity, and then transferred to commercial power utilities. One of the key technologies for the SSPS is the microwave power transmission, which was demonstrated by W.C. Brown in 1964 [2]. The most significant benefit of this idea is the potential for a large-scale clean energy system that can be substituted for existing nonrenewable energy sources.

An extensive feasibility study of the SSPS concept was conducted by NASA and the U Department of Energy in the 1970s [3]. In this study, an SSPS with an output power of 5 GW was designed and assessed as a reference model for the aspects of technology, economy, and environmental acceptability. Since then, various types of SSPS have been studied in Japan, the United States, and Europe [4-8]. However, no further steps toward its demonstration in orbit have been taken so far, because the concept of the demonstration experiment has not been well defined in the past studies.

The USEF (Institute for Unmanned Space Experiment Free Flyer) SSPS study team, organized in June, 2001, has developed the concept of a practical/commercial SSPS to be realized around the 2030s, and has also made a conceptual design of the SSPS demonstration model for the near term [9]. The study team employed a design policy for the creation of a new concept for a practical SSPS. Since the practical SSPS is composed of a huge number of electrical parts, such as the solar-cell arrays and the microwave

S. Sasaki, K. Tanaka, K. Higuchi, and N. Okuizumi are with the Institute of Space and Astronautical Science (ISAS)/ Japan Aerospace Exploration Agency (JAXA), 3-1-1 Yoshinodai, Sagamihara, Kanagawa 229-8510, Japan; Tel: 81-42-759-8330; Fax: 81-42-759-8464; E-mail: sasaki@newslan.isas.jaxa.jp.
S. Kawasaki is with Tokai University
M. Shinohara is with Kyoto University.
K. Senda is with Kanazawa University
K. Ishimura is with Hokkaido University.

This invited paper is part of the Special Section on Space Solar Power Systems. An oral version was originally presented at the 2003 Japan-US Joint Workshop on Space Solar Power System (JUSPS'03), July 3-4, 2003, Kyoto University, Uji, Kyoto, Japan.

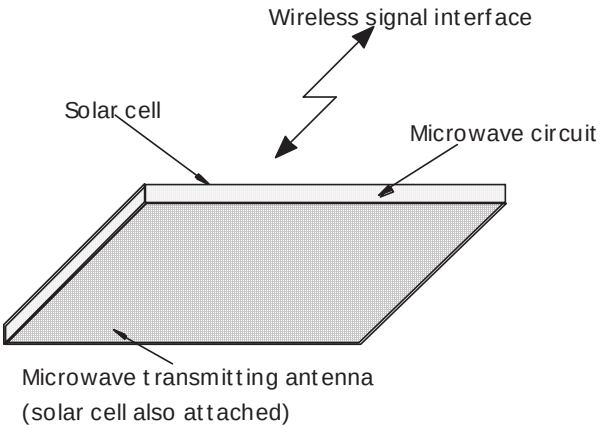

Figure 1. The concept of the power-generation/ transmission module.

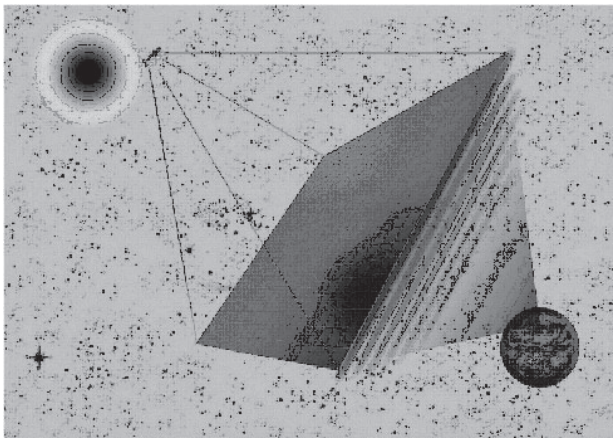

Figure 2. The concept of a practical SSPS.

circuits, the design needs to be based on COTS (commercial off-the-shelf) products. If the design is based on special products created only for the SSPS, the system cannot be economically realized. The commercial off-the-shelf products, procured under commercial competition, usually have high performance at a reasonable price.

In order for the structure and mechanism to be simple and robust, an active attitude control and a movable mechanism are not considered in the baseline configuration. This philosophy is quite different from other SSPS concepts proposed so far.

The power system is composed of individual power-generation/transmission modules. In each power module, the power generated by the solar cells is converted into microwave power. There is no power interface between the power modules. This modularized system is safe and robust, as compared with a bus power system, in which the electric power from all the solar-cell arrays is collected by the power bus and distributed to the microwave transmitting system. Figure 1 shows the concept of the power module, which has the function of power generation and transmission. The power module has thin-film solar cells on the upper/lower plane, and a microwave transmitting antenna on the lower plane, including batteries, microwave circuits, and their controller between the two planes. It is easy to attach elements to and detach them from the main structure for construction and maintenance. The modular structure has advantages in fabrication (mass production), testing, integration, and maintenance. Contrary to a dispersed configuration for the electric power, information is concentrated for efficient control and monitoring of the total system, using a wireless LAN (local-area network) system.

Based on the policy described above, a new concept of the practical SSPS, illustrated in Figure 2, has been developed. The system has a large panel, suspended by multi-tether wires and connected to a bus system, which is stabilized by the gravity-gradient force. The panel consists of many of the power modules. The solar cells are attached to both the upper and lower planes of the power module, while the antennas for the microwave power transmission are installed in the lower plane. The microwave antennas are always directed toward the ground without any active attitude control. The power generated by the panel varies with local time as the sun's angle changes. The average power amounts to 64% of the maximum power.

A demonstration experiment in the near term has been investigated, targeting the practical SSPS in the future. The

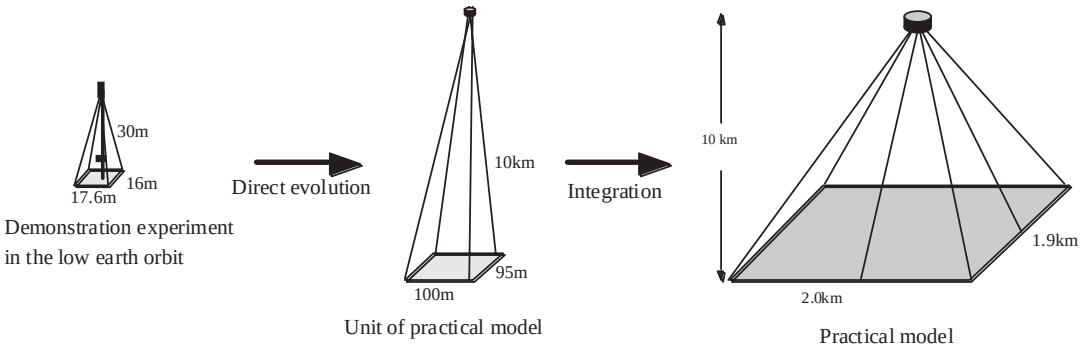

Figure 3. The evolutionary relationship from the demonstration experiment to a practical SSPS.

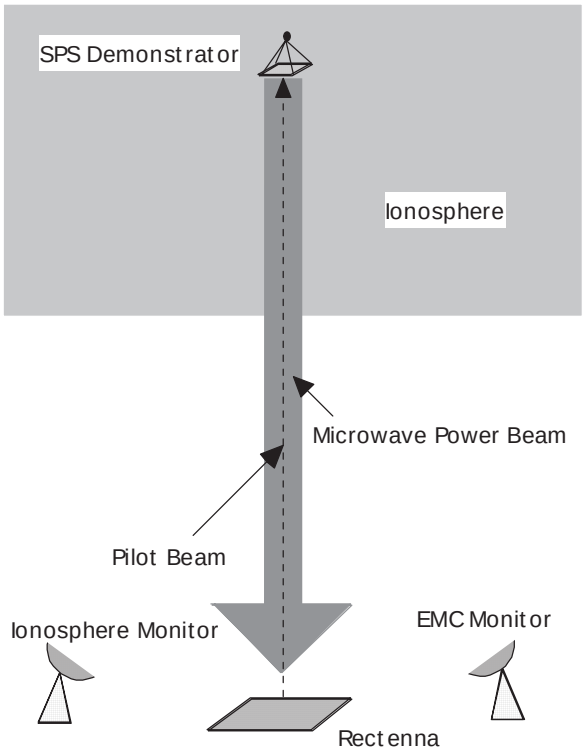

Figure 4. An outline of the demonstration experiment.

evolutionary relationship from the demonstration experiment to the practical SSPS is shown in Figure 3. The demonstration experiment will be conducted using a part of the practical SSPS. The basic concept of the power-generation/transmission module and gravity-gradient stabilization by the tether system will be verified in the demonstration experiment.

Figure 4 shows the outline of the demonstration experiment. The most important objective towards a practical SSPS, at this stage, is demonstration of the power transmission from the orbit to the ground. The main objectives of the experiment are: demonstration of the microwave beam-control precisely to the rectenna on the ground from the large-panel antenna in orbit, evaluation of the over-all power efficiency as an energy system, demonstration of electromagnetic compatibility with the existing communications infrastructure, and study of the operational procedures of the SSPS.

2. System Descriptions

The H2A rocket, an advanced type, is being considered for the launch vehicle for the demonstration experiment. The sub-recurrent orbit, at an altitude of 370 km, was selected as a compromise between the requirements of the microwave power density and the orbit-maintenance operation. From the perspective of the experimental objectives, the microwave power density in the ionosphere needs to be comparable to that of a practical SSPS, and the power density on the ground needs to be large enough to operate the rectifiers of the rectenna. With a decrease in altitude, the power densities in the ionosphere and on the ground increase, but more fuel is required to keep the altitude against the air-drag force. Figure 5 illustrates the configuration of the experimental system. The attitude of the system is stabilized by the gravity-gradient force of the H2A's second stage, used as an end mass, and the power-generation/transmission panel, which are connected by a truss and four tether wires. The panel consists of 88 foldable sub-panels. Each sub-panel is 0.8 m × 4 m wide and 0.1 m thick. 80 sub-panels are used for the power transmission, while the other eight are blank panels, to stabilize the yaw motion. The sub-panel for the power transmission contains five power-generation/ transmission modules of dimensions 0.8 m × 0.8 m. There is no electrical-wire interface between the power modules. The cylindrical bus system is installed on the truss at the center of gravity. The bus system has a control and data-management system, and a propulsion system to keep the orbit. A hydrazine thruster system or an electric propulsion system are being considered for the propulsion. Since the large panel interrupts direct communication between the bus system and the ground station, a communication-relay system needs to be installed in part of the panel.

Two kinds of construction are being considered for the microwave power-transmission system. One is the combination of a PCM (phase-controlled magnetron) and integrated antennas with phase-shifting capability composed of semiconductors. In this configuration, the microwave power of the phase-controlled magnetron, typically more than 1 kW, is divided among the 625 antenna elements in each power module. Another system is the combination of a phase-controlled magnetron in the bus system and the active integrated antennas (AIA) in each power module. In

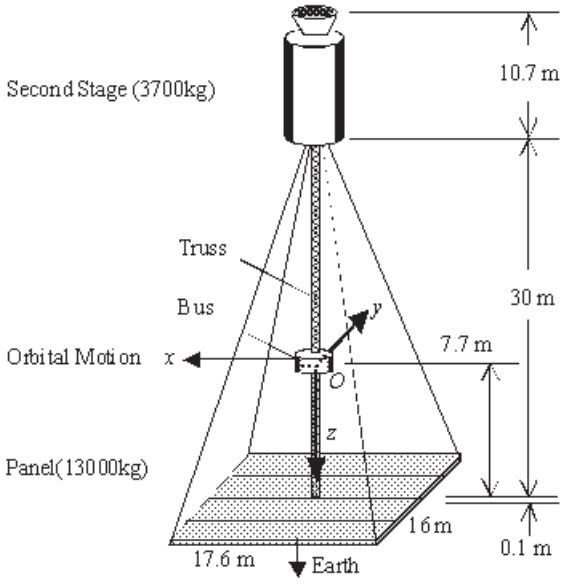

Figure 5. The configuration of the demonstration experiment.

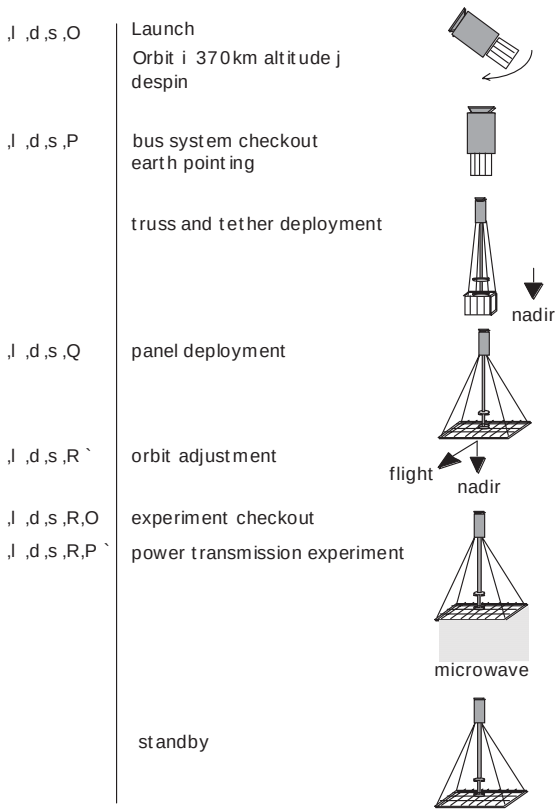

Figure 6. The sequence of the mission's operation.

this configuration, the microwave source signal is radiated from the bus system and is amplified by the 625 sets of active integrated antennas up to a total power of more than 1 kW in the power module. The selection between the two configurations depends on the efficiency of the power amplification of the semiconductors in the active integrated antennas. The latter configuration will be adopted if the active integrated antenna power efficiency exceeds 42%.

The microwave circuit is designed to control the direction of the beam within ±10° from the normal line of the sub-panel. If we install 50-150 WH batteries in each power-generation/transmission unit, the total microwave power injected from the demonstrator can be 140-420 kW for a short time period, typically 10-20 seconds. This level of microwave-power injection will generate a power density above 100 watt/m^2 for more than 10 km in the ionosphere. The power density on the ground is calculated to be 0.1-0.3 watt/m^2. It is necessary to use a parabola to concentrate the microwave power to be rectified by the existing diodes. If we have a rectenna area of 500 m in diameter, the output power from the rectenna will be more than 10 kW.

The analysis of the microwave beam pattern transmitted from the panel indicates that the misalignment and the gap between the sub-panels need to be less than 5° and 10 mm, respectively, from the standpoints of the allowable beam divergence and avoidance of unnecessary radiation. The analysis of the dynamic motion of the system in orbit has been conducted to find the orbital and structural conditions necessary to satisfy the requirements of the microwave beaming. The results of the computer simulation have shown that the pitch (pendulum) motion should be within 3.5° for an orbit eccentricity of less than 0.01, which is within the capability of the beam control. Based on the linear elastic analysis, the characteristic frequency of the

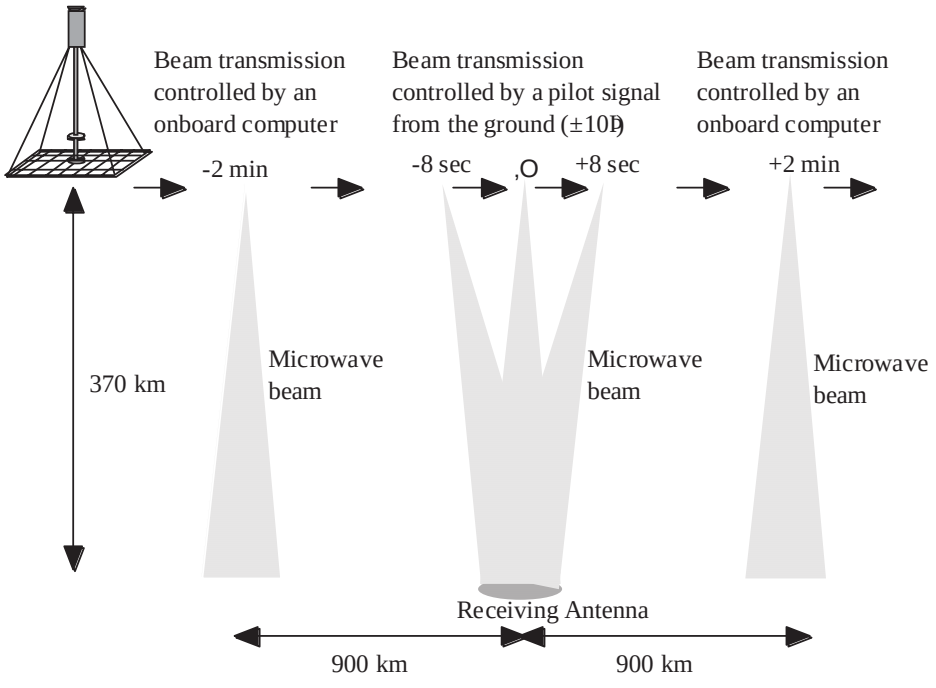

Figure 7. The experimental sequence.

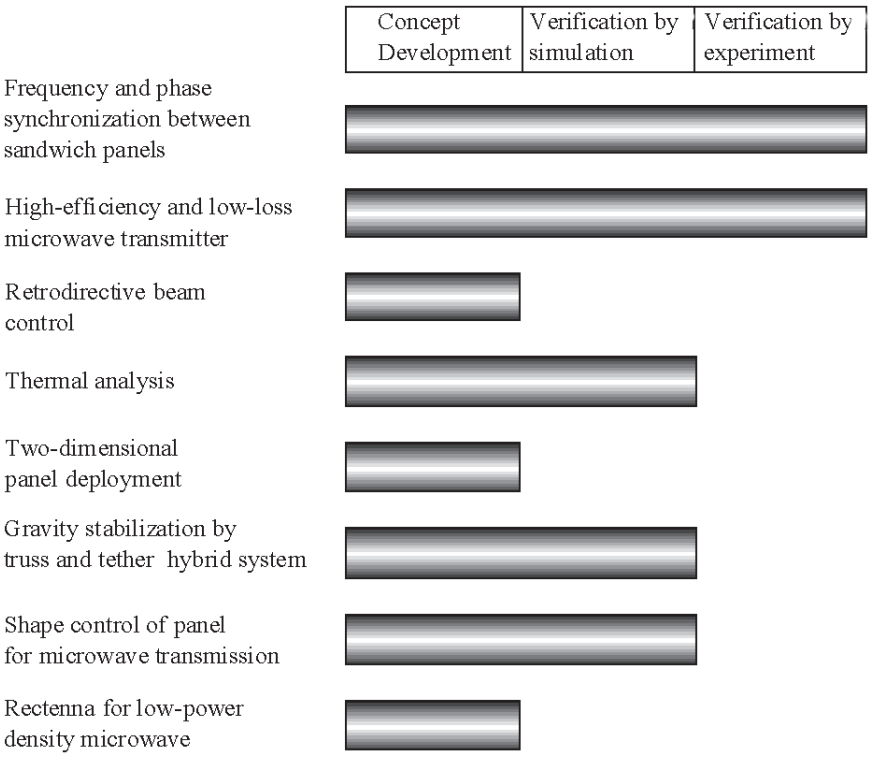

Figure 8. The status of the research subjects.

oscillation of the panel will be less than 10 Hz for a realistic range of the stiffness values of the panel, truss, and wire. Since the feedback frequency for the beam control is expected to be more than 100 Hz, the direction of the beam can be well controlled, regardless of the dynamic motion of the panel. In the current design, the sub-panels are latched to each other in two dimensions, to avoid any gaps between the sub-panels. However, the dynamic analysis has shown that even if the sub-panels are not latched in one direction, the gaps between the non-latched sub-panels will still be less than 10 mm, which is allowable for the microwave beaming.

A thermal analysis was conducted for the power module, composed of the phase-controlled magnetron, batteries, integrated antennas, and the other electric parts. The analysis results showed that the temperature will be maximum at the phase-controlled magnetron, but that it can be kept below 100° C for intermittent operation if a thermal capacitor is combined with the phase-controlled magnetron.

The orbit analysis showed that 500 kg of fuel will be required for the two-year mission, if we use the hydrazine thruster system. The dominant force on the system is the air-drag force on the H2A's second stage, used as an end mass. An electric propulsion system would be more beneficial, considering the amount of fuel and attitude disturbances during the operation, but additional solar-array paddles, extended from the bus system, would be required to supply electric power to an electric propulsion system.

3. Flight Operations

The mission-operation sequence is shown in Figure 6. After separation from the H2A rocket at an altitude of 370 km, the experimental system is automatically controlled into an Earth-pointing attitude. The bus system and folded sub-panels are first deployed from the H2A's second stage by extending the truss and tether wires. Then, the folded sub-panels are deployed from the bus system by another truss. Finally, the folded sub-panels are extended to the 16 m × 17.6 m panel. The microwave-transmission experiment will be started approximately one month after the launch, when the possibility of electric discharge in the high-voltage system has been completely excluded. During this month, evacuation of the fuel from the H2A's second stage, checkout of the experimental system, and orbit adjustment to the sub-recurrent orbit (47 revolutions per three days) will be conducted.

The experimental sequence is shown in Figure 7. For the first two minutes, the microwave beam, at 10% of full power, is transmitted to the ground. The onboard computer controls the beam direction without a pilot signal from the ground. When the experimental system passes over the rectenna site, the microwave beam is transmitted to the rectenna at full power for 16 seconds, guided by the pilot signal from the rectenna site. The beam direction is changed over ±10° from the normal to the panel to target the rectenna. After full-power operation, the same experiment as the initial phase at 10% of full power is performed for two minutes.

4. Associated Technologies

There are several engineering challenges in the development of the experimental system for the demonstration. They are associated with the microwave-power transmitter and the panel-deployment mechanism. New technologies are required to synchronize the frequency and phase of the microwave source in each power module for retro-directive control of the microwave transmission from all the power modules. A wireless synchronization system using two 5.8 GHz oscillators has been developed for laboratory testing, and satisfactory results have been obtained. Semiconductor amplifiers with phase shifters at 5.8 GHz have been also developed and tested to evaluate the maximum power efficiency for the use of an active integrated antenna [10]. For the panel-deployment mechanism, a new concept, using a shape-memory alloy, has been investigated as a robust and lightweight actuator [11]. A unique idea of using a sheet magnet has been studied as the latch mechanism. Model panels, equipped with the actuator and latch mechanism, will be fabricated for testing in the near future.

A new technology is also required to get dc power from the low-power-density microwaves (0.1-0.3 mW/cm^2). One idea is to use a parabola to concentrate the microwave power. Three types of parabola – cylindrical, rectangular, and square – have been designed and evaluated from the standpoints of power efficiency and manufacturing cost.

Figure 8 summarizes the critical technologies required for the demonstration experiment, and the current status of the research for each subject performed by the study team.

5. Summary

A demonstration experiment directed towards a practical Space Solar-Power System (SSPS) has been investigated. The power-generation/transmission module, the wireless interface between the modules, stabilization by the gravity-gradient force using a tether and truss, and a rectenna combined with a parabola are the major characteristic features. The study has shown that a power transmission from space to ground of more than 100 kW is feasible, using the H2A rocket. Further study is required, especially for retro-directive beam control, two-dimensional panel deployment, and the rectenna for low-power-density microwaves.

This study has been conducted by the members of the USEF study team: K. Asakura (Hitotsubashi University), N. Abe (AIST), K. Higuchi (ISAS), Y. Fujino (CRL), Y. Inatani (ISAS), K. Ishimura (Hokkaido University), S. Kawasaki (Tokai University), S. Nakasuka (University of Tokyo), H. Ogawa (ISAS), S. Sasaki (ISAS), K. Senda (Kanazawa University), M. Shinohara (Kyoto University), and K. Tanaka (ISAS).

6. References

1. P. E. Glaser, "Power from the Sun: Its Future," *Science*, **162**, 1968, pp. 867-886.

2. W. C. Brown, "The History of Power Transmission by Radio Waves," *IEEE Transactions on Microwave Theory and Techniques*, **MTT-32**, 9, 1984, pp. 1230-1242.

3. DOE/NASA, "Program Assessment Report Statement of Finding – Satellite Power Systems, Concept Development and Evaluation Program," DOE/ER-0085, 1980.

4. M. Nagatomo and K. Itoh, "An Evolutionary Satellite Power System for International Demonstration in Developing Nations," *Space Power*, **12**, 1993, pp. 23-36.

5. MRI Report, "Study of Solar Power Satellite," NEDO Contract, March 1994, (in Japanese).

6. J. C. Mankins, "A Fresh Look at Space Solar Power: New Architectures, Concepts and Technologies," *Acta Astronautica*, **41**, 1997, pp. 347-359.

7. W. Seboldt and M. Klimke, "European Sail Tower SPS Concept," *Acta Astronautica*, **48**, 5-12, 2001, pp. 785-792.

8. C. Carrington and H. Feingold, "Space Solar Power Concepts: Demonstrations to Pilot Plants," IAC-02-R.P.12, 2002.

9. T. Kobayashi, M. Ohmura, and S. Sasaki, "Space Solar Power System (SSPS) Study for Realization of the Terrestrial Power Utilities," 53rd International Astronautical Congress, Houston, October 2002.

10. T. Kimura, K. Yamamoto, T. Nakada, K. Kito, and USEF SSPS Study Team, "High Efficient Active Integrated Antenna," 23rd ISAS Space Energy Symposium, March 2004.

11. K. Higuchi, K. Tanaka, S. Sasaki, N. Okuizumi, S. Nogami, and H. Morita, "Deployment Mechanisms of Thick Panels with SMA Actuators," 23rd ISAS Space Energy Symposium, March 2004.

A Unit Plate of a Thin, Multilayered Active Integrated Antenna for a Space Solar Power System

S. Kawasaki

Abstract

In this paper, the prospects for the use of microwave technology to realize the Space Solar Power System are surveyed, and a demonstration of prototypes of the active integrated antenna technique are given. Experimental results from our test fabrication of thin and multilayered active integrated antenna arrays are shown to prove its effectiveness. One example of a unit plate configuration is identified for constructing the huge space antenna system. In addition, development items for the Space Solar Power System, focused on the active integrated antenna technique, are considered.

1. Introduction

Recently, interest in the Space Solar Power System (SSPS) has been growing, due to the necessity for clean energy utilizing solar power for reduction of CO_2. This project has been proposed and developed as one of the concrete initiatives for microwave wireless power transmission [1]. This system has a couple of unique points. One of them is that this is an enormous system, including construction of a tremendous space station and a huge antenna array. Furthermore, from the microwave point of view, attention has been paid to the delivery of power with a pure carrier frequency, as a third utilization of microwave technology, following its use in the communication system and in the sensor system.

These days, two Japanese government research and technical organizations (NASDA and USEF) have proposed their own SSPS models [2]. In both cases, a large plate model, characterized by a layered configuration in a sandwich or "hamburger" fashion, was proposed for the effective combination of DC power generation, microwave circuits and radiation, and their control. Starting from these models, many researchers and engineers in this field have discussed ways to realize this enormous system. Through this discussion, microwave engineers have recognized the importance of the rapid development of the "spacetenna" (the transmitting antenna in the SSPS system).

Points associated with this development involve the realization of a light, thin, and multifunctional antenna and transmitter system, to provide high, clean, and low-cost power by way of precise beam control and high-efficiency power generation. One of the technologies being considered for meeting these requirements is the use of the active integrated antenna (AIA) technique, because it is light-weight and has multiple functions [3].

In this paper, the requirements for the microwave technology for the SSPS are introduced. Then, a design method and the experimental results for a multilayered active integrated antenna, and a unit-plate configuration for the active integrated antenna array, are demonstrated. Future development items are also discussed in the text.

2. Microwave Technology in SSPS

The requested properties for the SSPS at the system level are the ability to supply high-power energy, highly accurate beam control for safety, and a hazard-avoidance system leading to public acceptance. Furthermore, the SSPS requires a huge antenna system that is light and compact, for low launch cost and low payload. In addition, it should have long-lifetime subsystems, with low running costs and good maintenance [4, 5].

Shigeo Kawasaki is with Tokai University, Department of Electric and Electronic Engineering, 1117 Kita-Kaname, Hiratsuka, Kanagawa 259-1292 Japan;
Tel: +81-463-58-1121; Fax: +81-463-59-4014; E-mail: kawasaki@keyaki.cc.u-tokai.ac.jp.

This invited paper is part of the Special Section on Space Solar Power Systems. An oral version was originally presented at the 2003 Japan-US Joint Workshop on Space Solar Power System (JUSPS'03), July 3-4, 2003, Kyoto University, Uji, Kyoto, Japan.

Performance	Technologies
Microwave power generation, amplification and power combining	An electronic tube Semiconductor devices Spatial power combining techniques A circuit design tool with a wide dynamic range
Light and compact configuration	Microwave integrated circuits An electromagnetic simulator Active integrated antenna techniques with multi-layered structure
Synchronization of power generation for the huge array antenna	A data communication technology under high power circumstance
Beam synthesis	An aperture antenna or a planar antenna Taper and density distribution
Precise beam control	A closed loop by a pilot signal from the Earth and high-power transmission A retro-directive array and a hazard detection system

Table 1. Applicable microwave technologies in the spacetenna

These system requirements can be broken into those relating to the microwave devices, and to the circuit and antenna technologies. Significant performance to be attained in microwave-circuit technology includes high power generation with a light and compact configuration, and high dc-RF/RF-dc conversion efficiency. Furthermore, beam synthesis and highly accurate beam control in the huge array antenna, consisting of many sub-arrays operated independently, should be accomplished. From the commercial viewpoint, low cost, using mass-production and good maintenance by robots, should be taken into account. In addition, the influence of microwave illumination on animals and plants should be carefully investigated to insure public acceptance. The concrete applicable microwave technologies are listed in Table 1. Using these candidates, a feasible SSPS system can be proposed.

A conceptual design, based on preliminary experiments using a feasible microwave subsystem for the SSPS, has already been started by the author's research group, utilizing the spatial power-combining technique [3]. A block diagram of the power-transmission system applicable to the SSPS is shown in Figure 1. In this example, a high-power electronic tube is adopted as the original

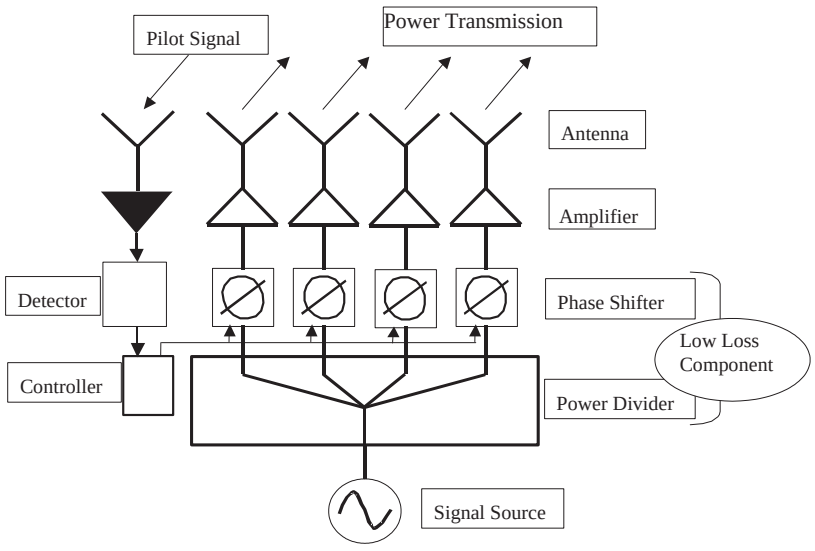

Figure 1. The block diagram of the feasible power-transmission system.

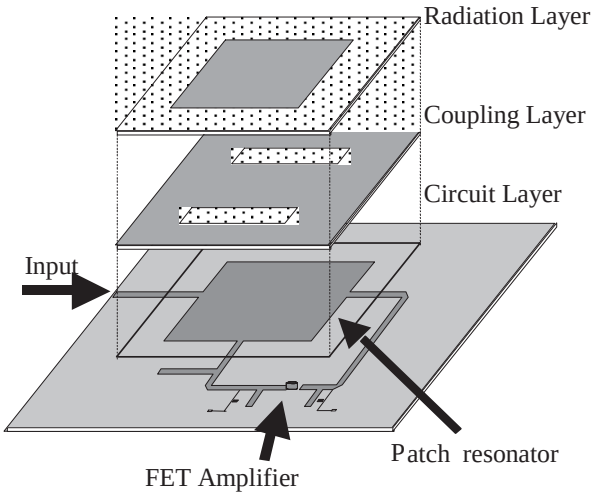

Figure 2a. The configuration of the multi-layered active integrated antenna.

frequency source [6]. This signal is divided and delivered through many passive components with low insertion losses to avoid the heat problems created by such losses. The divided signal is input to a phase-control-and- amplification block, consisting of a phase shifter and a solid-state amplifier [7, 8]. Finally, this power is radiated from a small, thin antenna, using a spatial power-combining technique. When the pilot signal is received, the request from the Earth is returned via a retro-directive function, which operates by creation of the conjugated phase. For instance, in an analog circuit system, this mechanism can be achieved by a harmonic mixer through the operation of the subtraction of the phases between the pilot signal and its second harmonic [9].

3. Use of Active Integrated Antenna Technique and a Unit Plate Subsystem

In order to realize the system considered here, the details of the microwave technology should be addressed. Regarding the microwave devices and circuits, the specifications for these subsystems must include high power, high efficiency, low spurious emissions, and low harmonics [10, 11]. In addition, the subsystem has to operate stably with heat proofing in the RF devices and the solar battery, and should be low in cost through mass production. There are many options for satisfying these requirements, such as GaAs, InP, GaN, and SiGe semiconductor materials, and HBT or FET devices. Furthermore, an F-class amplifier and a phase shifter with low insertion loss are applicable at the circuit level. However, tradeoffs between performance and cost should be taken into account.

The antenna system should have characteristics such as being small, having a light and thin configuration, and being compact with multiple functions. An active integrated antenna with plated and planar-type antennas was chosen as a solution for the integrated antenna system [12-15]. Although the active integrated antenna technique is the most promising candidate, when the components including the planar antenna are integrated into one substrate a penalty involving an increase in the area is usually paid. In order to avoid increasing the area for the circuit and the antenna, an active integrated antenna with a multilayered structure is preferable [3]. In this configuration, it is possible to allocate one layer to each function, such as a circuit layer and a radiation layer. The coupling between the circuit layer and the antenna layer for a thin and light active integrated antenna is accomplished electromagnetically, through an aperture. This concept of a multilayered active integrated antenna array, proposed by the author, is given in Figure 2a, which shows the case of a three-layered array [16].

As shown in Figure 2b, the signal flow occurs as follows. The input signal from an external source travels through the width direction of the patch resonator in the circuit layer. This works as a simple filter. Then, the filtered signal is amplified through the FET, and the amplified signal is returned to excite the patch resonator in the length direction. Due to polarization switching, good low-crosstalk performance can be maintained. The patch antenna in the top layer is excited by the two slot apertures embedded in the common ground for the upper patch radiator, as well as for the bottom patch resonator, in the circuit layer. The main transmission lines were designed to have a characteristic impedance of 50 Ω, using microstrip line as well as stripline.

It is possible to add other functions to the configuration shown in Figure 2a. The functions of the circuit layer can be extended by adding a phase shifter, a mixer, a multiplier, and so on. For instance, using an active integrated antenna with a phase shifter and a high-power amplifier, the beam

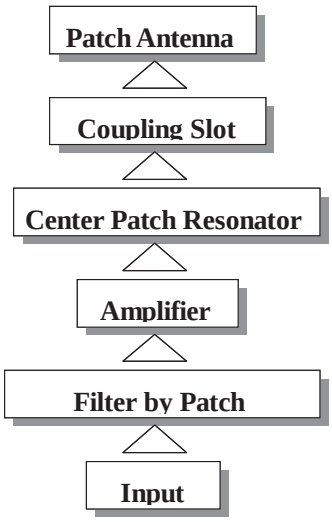

Figure 2b. The signal flow of the multi-layered active integrated antenna.

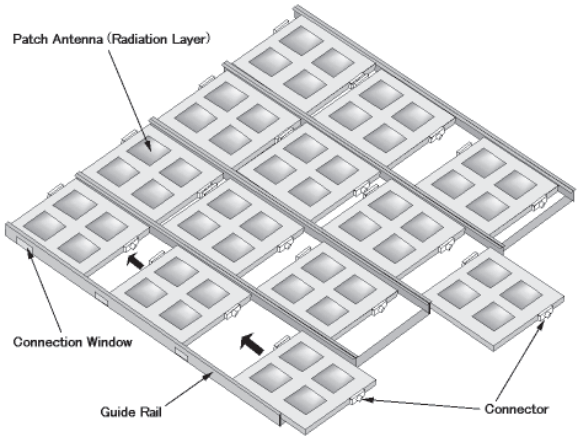

Figure 3. The combination of the unit plates.

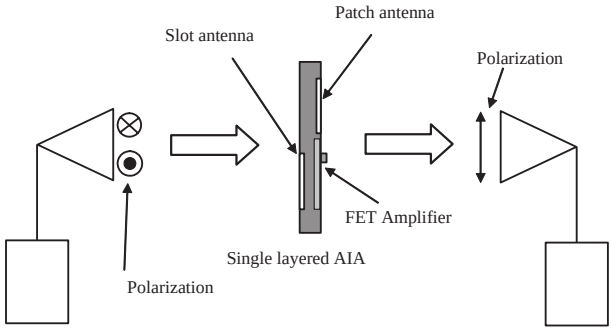

Figure 4a. The experimental setup for the two-element integrated spatial amplifier antenna with a slot and a patch

control for the retro-directive function can be attained by adjusting the phase shifter in accordance with the request from the pilot signal.

In order to establish the huge two-dimensional array in space, the active integrated antenna idea discussed above has to be extended. For this purpose, the subsystem had best be made in a unit-plate configuration, consisting of appropriate numbers of elements of the multilayered active integrated antenna [16]. This unit plate has to be small in weight and volume. As a result, the actual huge array antenna can be built from units with suitable size and weight, that is to say, sub-arrays, and can be launched by a rocket. Furthermore, the concept of the unit plate combination has good features from the viewpoints of actual manufacturing and maintenance.

When the huge array is constructed, many unit plates are combined, as shown in Figure 3. Each unit plate is positioned by a guide frame, and combined electrically and mechanically through a connector. It is possible that a robot can operate along the frame for both construction and maintenance.

4. Test Fabrication and Experimental Results

In order to obtain the fundamental data, multilayered active integrated amplifier antennas were fabricated by the author's research group. As an example of the single (mono) layered active integrated antenna, an integrated spatial-amplifier antenna, consisting of a slot and a patch, is shown with the experimental setup in Figures 4a and 4b. In this case, both faces of one substrate were utilized so that the receiving slot was embedded in the ground plane on the back side, and the transmitting patch antenna with the FET amplifier was embedded on the top side.

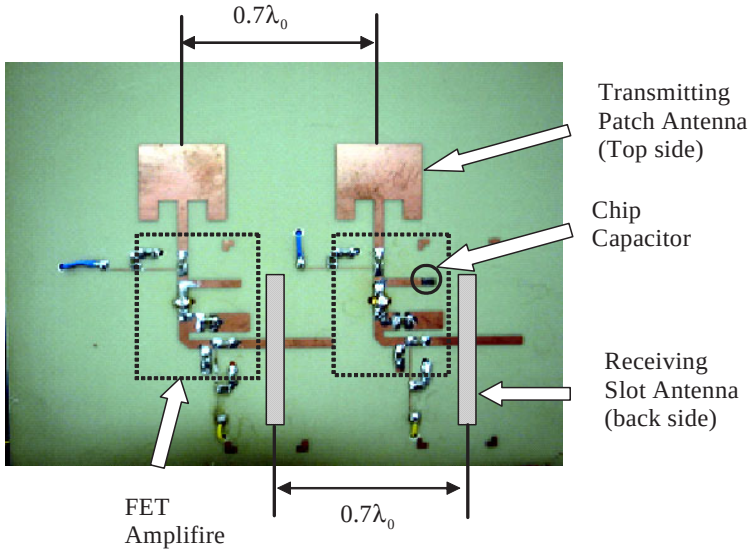

Figure 4b. The fabricated single-layered active integrated antenna for the two-element integrated spatial amplifier antenna with a slot and a patch.

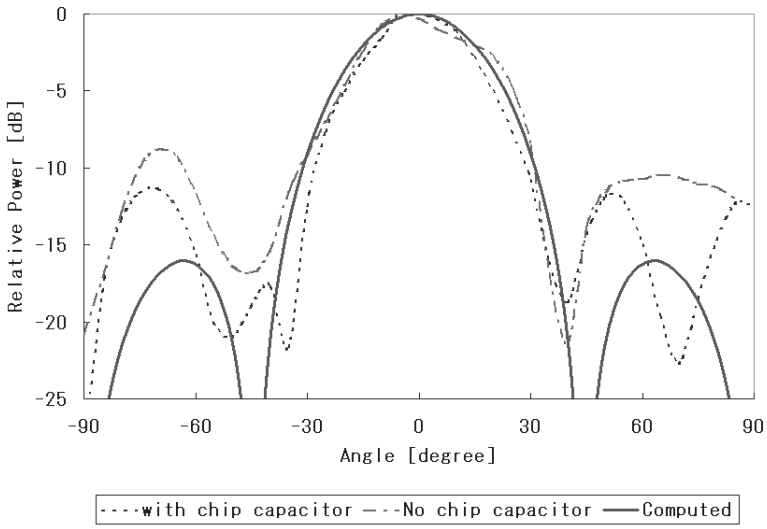

Figure 4c. A comparison of the antenna patterns for the single-layered active integrated antenna.

The spatial amplification takes place as follows. As shown in Figure 4a, the electromagnetic wave radiating from the signal source is captured at the receiving slot antenna in the spatial amplifier. The slot antenna is coupled electromagnetically through a transition with the microstrip line leading to the input of the FET amplifier. Then, the wave captured through the slot turns into the input signal to the FET amplifier on the top side. The amplified wave travels to the transmitting patch antenna, and is finally radiated into space. Hence, there is no external source connecting to the circuit-and-antenna substrate. As explained above, this integrated spatial amplifier antenna is made in a sheet (mono-layer) fashion. To cope with the requirement that the antenna be light and thin, this configuration can be adopted in the unit plate and reinforced mechanically.

The operating frequency was 5.8 GHz, under conditions on the FET amplifier with Ids = 20 mA and Vds = 3.55 V, total. A comparison between the measured antenna pattern with two different bias voltages and the calculated pattern is given in Figure 4c. The agreement between the measured antenna pattern, without tuning, and the calculated pattern is good. A beam-steering angle of 5° was obtained by tuning the gate-bias voltage of the FET amplifier in each active integrated antenna element.

In order to improve the antenna's gain, a two-(double-) layered active integrated antenna, designed at 5.8 GHz, was also demonstrated. The simple multi-layered configuration of the single element and a photograph of the two-layered active integrated antenna as fabricated are shown in Figures 5a and 5b. The bottom layer consisted of the amplifier circuit and the patch antenna, and the unfed patch antenna on the top layer covered the circuit layer, to increase the gain. The measured antenna patterns are also indicated in Figures 5c and 5d. Although the measured antenna pattern in the E plane was distorted by the radiation from the FET amplifier, the fundamental data of the two-layered active integrated antenna were obtained. In the state

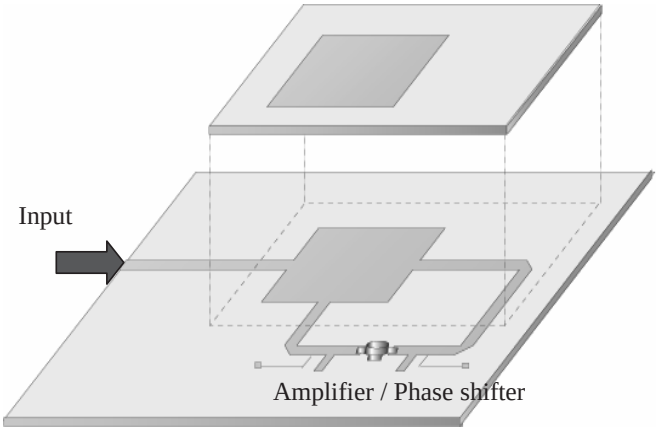

Figure 5a. The structure of the two-layered active integrated antenna

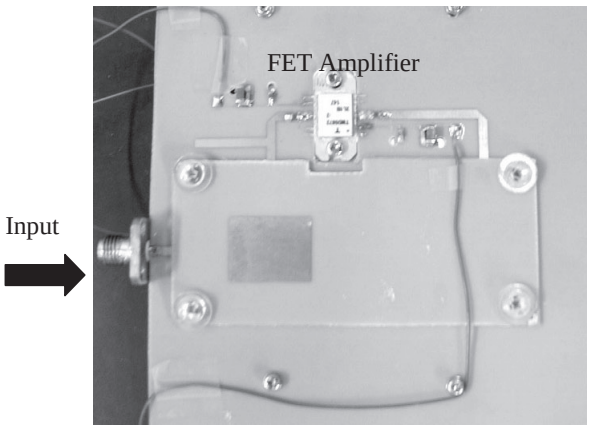

Figure 5b. The fabricated two-layered active integrated antenna.

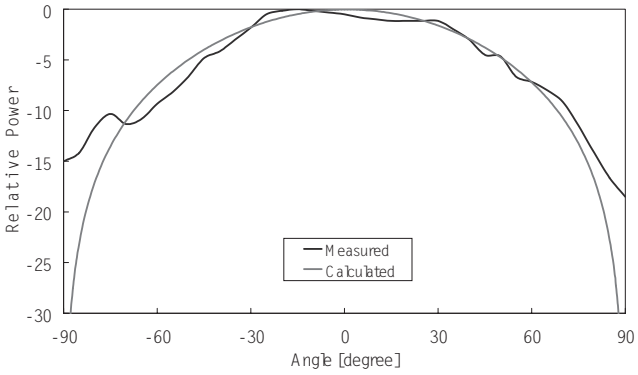

Figure 5c. A comparison of the H-plane antenna patterns comparison for the two-layered active integrated antenna

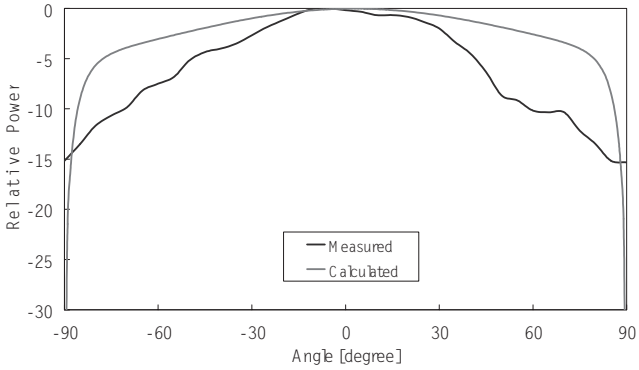

Figure 5d. A comparison of the E-plane antenna patterns comparison for the two-layered active integrated antenna

of the art, this two-layered configuration is very promising from the viewpoints of design flexibility, alignment accuracy, and cost effectiveness for both the fabrication process and for material. Furthermore, the three-layered active integrated antenna shown in Figure 2 was fabricated by adding the coupling layer between the circuit layer and the radiation layer. Inserting this coupling layer plays the role of reducing unexpected radiation from the circuit layer and providing good isolation between the top and the bottom layers. However, their is a penalty of a cost increase due to inserting the additional substrate that must be paid.

An example of a 2 × 2 unit plate array was made by combining four elements. The configuration and the fabricated array are indicated in Figure 6, along with the antenna patterns. This array operated at 2.45 GHz. The relatively narrow pattern in the E plane was believed to result from the unexpected radiation from the edge of the upper antenna substrate. The fundamental operating performance was confirmed through the experimental results.

In order to realize the concept introduced in the previous section, as a preliminary demonstration using the fabricated unit plate, the 2 × 2 unit plate arrays were combined into a 4 × 4 array as shown in Figure 7. This unit plate array also operated at 2.45 GHz. As introduced before, each unit plate was supported by the guide frame, and the adjacent unit plates were connected electrically and mechanically through the connectors. It is believed that the fundamental data for extending to the huge number of unit plates were obtained through the good performance resulting from this unit plate array.

5. Requested Development

The demonstration presented in the previous section basically proves the effectiveness of the active integrated antenna technique for the SSPS. However, there remain several development items for the technologies of the components, as well as for those of the antenna and the control system.

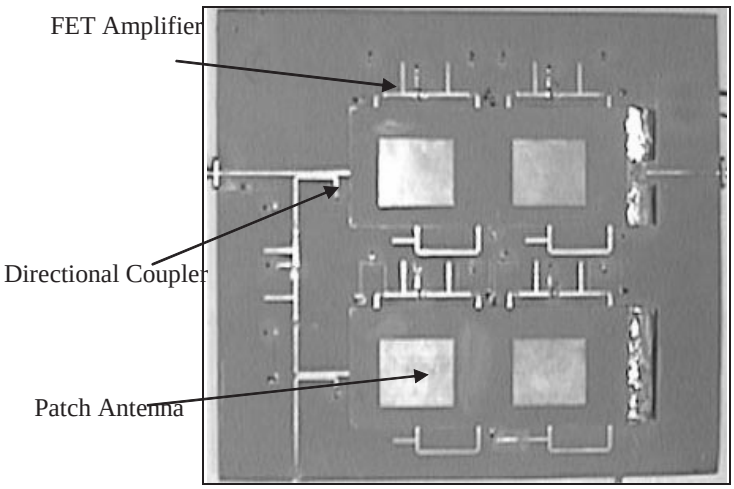

Figure 6a. The unit plate fabricated with the 2 × 2 active integrated antenna amplifier array

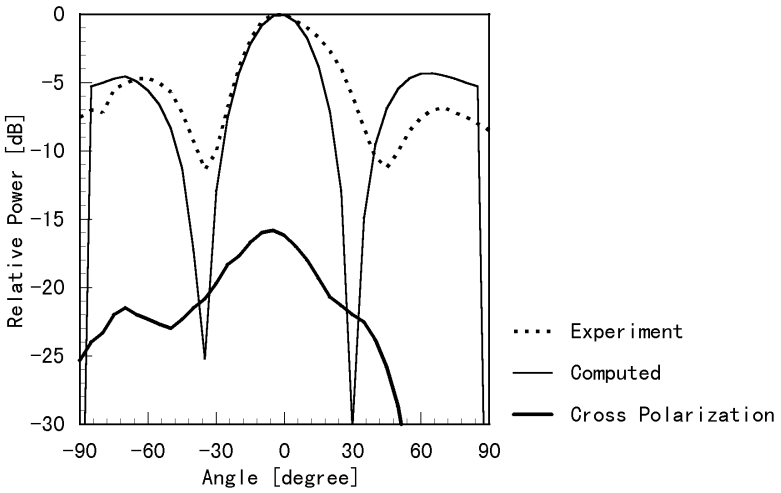

Figure 6b. The H-plane antenna patterns from the unit plate fabricated with the 2 × 2 active integrated antenna amplifier array.

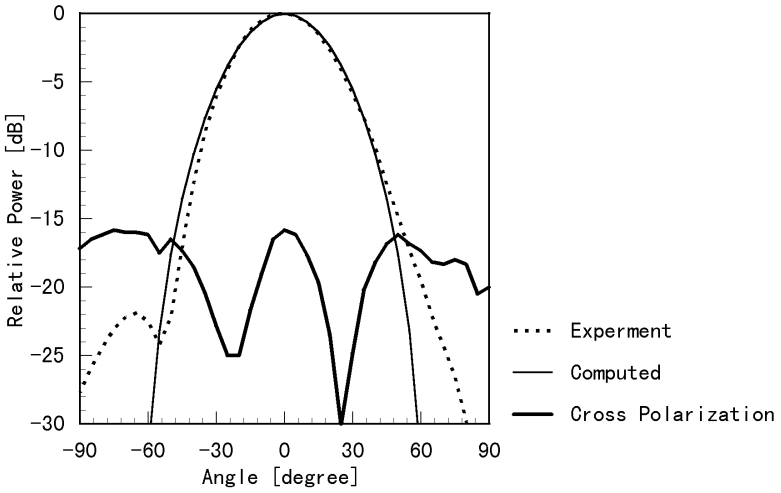

Figure 6c. The E-plane antenna patterns from the unit plate fabricated with the 2 × 2 active integrated antenna amplifier array.

A microwave circuit designer desires to have a good design tool or a simulator with a dynamic range of more than 100 dB. This is because large values of the spurious and harmonic powers are predicted, due to the gigantic transmission power. Therefore, this tool is needed to investigate and eliminate undesired nonlinear effects from active devices and integrated circuits over the very wide dynamic range. The device and circuit engineers must try to develop high-power and high-efficiency devices and circuits with new semiconductor materials, and low-insertion-loss passive components, for instance, a phase shifter using high-power-handling MEMS.

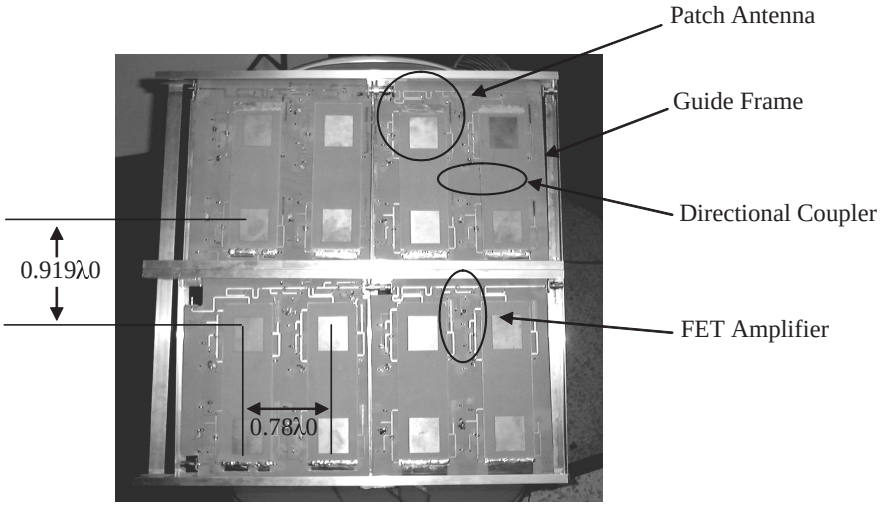

Figure 7. The 2 × 2 unit plate array with 16 elements.

A low-sidelobe-profile and low-leakage antenna should be studied. Electromagnetic bandgap technology may be applicable for the reduction of interference due to the surface wave in the antenna substrate. In addition, the avoidance of unstable operation due to heat should be taken into account. Some of the solutions for a highly stable operating system may be found in the development of wide-bandgap semiconductor devices and circuit technology. Regarding precise beam control, the establishment of a closed loop with the pilot signal and power transmission is necessary. A first, simple algorithm, including information from the retro-directive function and hazard detection, should be developed.

6. Conclusions

The prospects for applications of microwave technology in the SSPS were introduced in this paper. In this overview, the requirements and possible solutions using the active integrated antenna technique, including a multi-layered structure and the unit plate configuration, were explained. Variations of the active integrated antennas and the unit plate were demonstrated, and their effectiveness in the SSPS was also confirmed. Furthermore, the items that must be solved for the multi-layered active integrated antenna, as well as for the control system for the huge array antenna in the SSPS, were indicated.

7. Acknowledgement

The author would like to thank to Profs. H. Matsumoto and N. Shinohara of Kyoto University, N. Nagatomo, S. Sasaki, and T. Takano of ISAS, and T. Itoh of UCLA for encouragement and helpful discussion.

8. References

1. S. Kawasaki, "A Patch-Plate Array Type of Active Integrated Array Antenna for SPS2000," *ISAS Bulletin*, **43**, March 2001, pp. 47-55.

2. H. Matsumoto, "Research on Solar Power Satellites and Microwave Power Transmission in Japan," *IEEE Microwave Magazine*, **3**, 4, December 2002, pp. 36-45.

3. S. Kawasaki, Y. Kido, and T. Takano, "Laminated Active Integrated Amplifier Antenna Arrays for a Space Solar Power Satellite," *IEEE Transactions on Microwave Theory and Techniques*, **MTT-47**, September 1999, pp. 1901-1909.
4. B. Strassner and K. Chang, "5.8 GHz Circular Polarized Rectifying Antenna for Microwave Power Transmission," 2001 IEEE MTT-S International Microwave Symposium Digest, **3**, Phoenix AZ, June 2001, pp. 1859-1862.

5. T. Hikage, T. Nojima, M. Omiya, and K. Itoh, "Development of Cavity-Backed Slot Antenna for Spacetenna of Space Solar Power Satellite at the Frequency of 5.8 GHz," *APMC2002*, November 2002, pp. 799-802.

6. N. Shinohara, H. Matsumoto, and K. Hashimoto, "Solar Power Station/Satellite (SPS) with Phase Controlled Magnetrons," *APMC2002*, November 2002, pp. 795-798.

7. C. Ortiz, T. Ivanov, and A. Mortazawi, "A CPW-Fed Microstrip Patch Quasi-Optical Amplifier Array," *IEEE Transactions on Microwave Theory and Techniques*, **MTT-48**, February 2000, pp. 276-280.

8. S. Kawasaki, T. Oishi, N. Shinohara, K. Hashimoto, and H. Matsumoto, "Beam Steering in Active Integrated Antenna for Microwave Wireless Power Transmission," 2002 URSI General Assembly, The Netherlands, August 2002.

9. R. Miyamoto and T. Itoh, "Retrodirective Arrays for Wireless Communications," *IEEE Microwave Magazine*, **3**, 1, March 2002, pp. 71-79.

10. H. Minamide, M. Kohno, N. Yoshita, K. Yajima, K. Mori, T. Ogata, and T. Sonoda, "70% High Efficient C-Band 27W Hetero-Structure FET for Space Application," 2002 IEEE MTT-S International Microwave Symposium Digest, **3**, Seattle WA, July 2002, pp. 621-623.

11. J. Ozaki, K. Arai, M. Miyauchi, S. Watanabe, and S. Kamihashi, "C-Band GaAs MMIC Limiting Power Amplifier with Small Insertion Phase Variation.," 1991 IEEE MTT-S International Microwave Symposium Digest, **1**, 1991 pp. 331-334.

12. J. Mink, "Quasi-Optical Power Combining of Solid-State Millimeter-Wave Sources," *IEEE Transactions on Microwave Theory and Techniques*, **MTT-34**, 2, February 1986, pp. 273-279.

13. J. Bae, Y. Aburakawa, H. Kondo, T. Tanaka, and K. Mizuno. "Millimeter and Submillimeter Wave Quasi-Optical Oscillator with Gunn Diodes." *IEEE Transactions on Microwave Theory and Techniques*, **MTT-41**, October 1993, pp. 1851-1855.

14. Z. B. Popovic, R. M. Weikle, II, M. Kim, and D. B. Rutledge. "A 100-MESFET Planar Grid Oscillator." *IEEE Transactions on Microwave Theory and Techniques*, **MTT-39**, February 1991, pp. 193-200.

15. S. Kawasaki and T. Itoh, "Quasi-Optical Planar Arrays with FET's and Slots," *IEEE Transactions on Microwave Theory and Techniques*, **MTT-41**, 10, October 1993, pp. 1838-1844.

16. S. Kawasaki, Y. Kido, H. Hayakawa, K. Iwasaki, and H. Urabe, "Laminated Active Integrated Antenna Arrays Composed of Functional Layers for Microwave Wireless Power Transmission in Space," International Symposium on Antennas and Propagation 2000, Fukuoka, Japan, August 2000, pp. 705-708.

Cavity-Backed Slot Antennas and Arrays with Simple Geometry Adapted to Microwave Energy Transmission

T. Hikage
K. Munakata
T. Nojima
M. Omiya
K. Itoh

Abstract

We give simple design rules for antenna elements and large-scale array antennas for an energy-transmission antenna system for the solar power satellite. Finite-Difference Time-Domain (FDTD) techniques are employed to evaluate the impedance characteristics of a single element and of elements in the antenna array, as well as to estimate values of mutual coupling. The large-scale array antenna under consideration consists of numerous cavity-backed slot antenna elements, operating at a frequency of 2.45 GHz. The cavity-backed slot antenna is superior to other types of antenna elements in mechanical strength and heat dissipation. The conventional antenna structure is a rectangular conductive cavity with a slot. Hence, it is difficult to fabricate an antenna array, due to the conductive sidewall assembly and its electrically perfect connection with the upper and bottom conductive plates. Instead of using conductive sidewalls in the cavity, we propose a new type of slot-antenna element, consisting of parallel conductive plates separated by metal posts, and excited by a shorted probe or an inverted-F element. Such a new configuration makes it easy to fabricate low-profile antenna elements, as well as array antennas.

1. Introduction

The Solar Power Satellite (SPS) [1] has been proposed as a sustainable and reusable energy source for mankind in the future. In the SPS system, the solar power is converted into electricity by solar cells, and fed to microwave generators on the satellite. The microwave antenna ("spacetenna") transmits the microwave power to a rectifying antenna (rectenna) on the ground. The most significant benefit of the SPS is the potential for large-scale clean energy systems to substitute the existing non-renewable energy sources. In Japan, the SPS2000 task team of the ISAS Solar Power Satellite Working Group was involved in research on developing a solar power satellite system referred to as SPS2000 [2]. In the study, the cavity-backed slot antenna was proposed as an element of the spacetenna. It has superior characteristics of mechanical strength and heat dissipation, compared with other elements such as dipole antennas and microstrip-patch antennas. The geometry of a dipole antenna is much simpler, but it needs a reflector set a quarter wavelength apart from it, and a post to fix the space between the dipole and the reflector. Therefore, a dipole antenna with a reflector tends to be tall and structurally weak. On the other hand, a cavity-backed slot antenna makes can have a lower profile with a stronger antenna array structure. Similarly, a microstrip patch antenna is low profile and light in weight, but it needs a special heat sink to decrease the temperature, because it is covered with dielectric materials that heat up due to energy transmission losses. In spite of high temperatures, the cavity-backed slot antenna, which consists of metallic pieces, radiates heat by itself and prevents degradation of its characteristics. As a result, it is concluded that the cavity-backed slot antenna is superior as an element of a spacetenna, compared to a dipole antenna or a microstrip-patch antenna, from the points of view of mechanical strength and heat dissipation.

The conventional structure of a cavity-backed slot antenna is a rectangular conductive cavity with a slot. It is difficult to produce an array antenna composed of these

Takashi Hikage, Kosuke Munakata, and Toshio Nojima are with the Graduate School of Engineering, Hokkaido University, Kita 13, Nishi 8, Kita-ku, Sapporo 060-8628, Japan; Tel: +81-11-706-6526; Fax: +81-11-706-7144; E-mail: hikage@ice.eng.hokudai.ac.jp, munakata@ice.eng.hokudai.ac.jp, nojima@ice.eng.hokudai.ac.jp.
Manabu Omiya is with the Information Initiative Center, Hokkaido University, Kita 11, Nishi 5, Kita-ku, Sapporo 060-0811, Japan; Tel: +81-11-706-2946; Fax: +81-11-706-2936; E-mail: omiya@iic.hokudai.ac.jp.
Kiyohiko Itoh is with Tomakomai National College of Technology, 433 Nishikioka, Tomakomai 059-1275, Japan; Tel: +81-144-67-0734; Fax: +81-144-67-8366; E-mail: itoh@office.tomakomai-ct.ac.jp.

This invited paper is part of the Special Section on Space Solar Power Systems. An oral version was originally presented at the 2003 Japan-US Joint Workshop on Space Solar Power System (JUSPS'03), July 3-4, 2003, Kyoto University, Uji, Kyoto, Japan.

elements, due to the sidewall assembly and its electrically perfect connection with the upper and bottom conductive plates. Replacing the conductive sidewalls with metal posts, we propose a new type of slot-antenna element consisting of parallel conductive plates separated by metal posts. Such a new configuration makes it easy to produce low-profile antenna elements as well as array antennas. Moreover, we discuss a design method for the antenna elements, and prove the effectiveness of the method by evaluating the input characteristics and mutual coupling for the case of a large-scale array antenna.

The authors have proposed several types of conventional cavity-backed slot antennas with a cavity height of one-tenth of the wavelength in our previous study [3]. These meet the requirements of the spacetenna. One of them was a cavity-backed slot antenna fed by a shorted probe, and the other was fed by an inverted-F element. Moreover, we have shown useful relationships between antenna parameters and antenna characteristics in designing elements. Impedance matching at the frequency of 2.45 GHz was obtained by using an appropriate probe location, slot length, and slot width. The effectiveness of the method was experimentally confirmed.

This paper discusses a design method for post-wall antenna elements, realizing sufficient impedance matching at the frequency of 2.45 GHz. The relationships between post intervals and input characteristics are clarified for several cases with different total numbers of posts. The design parameters are applied to the antenna array, and the numerical evaluations of mutual coupling are carried out for small-scale and large-scale antenna arrays, in order to prove the effectiveness of the derived antenna geometry and the antenna parameters. For this purpose, we employed the Finite-Difference Time-domain (FDTD) technique to design and analyze antennas [4, 5].

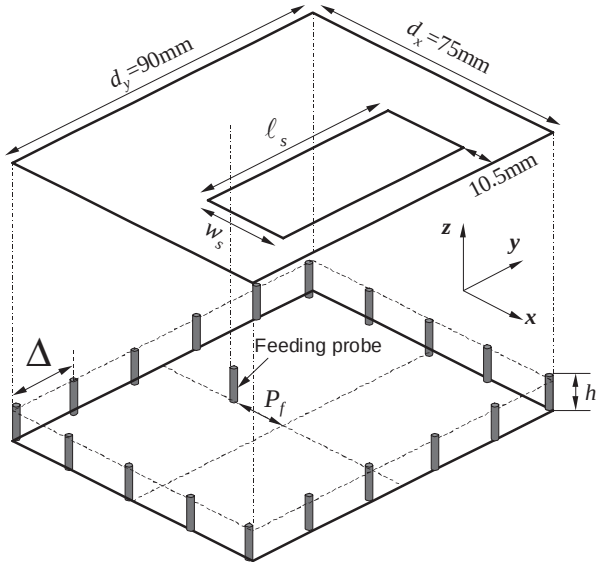

Figure 1. The geometry of the antenna element.

This paper is divided into three sections after this introduction. Section 2 describes the geometry of a slot antenna fed by the shorted probe, and the method for designing it to obtain good impedance matching of a single antenna element at a frequency of 2.45 GHz. By using the proposed method, we show antenna parameters realizing good impedance matching. We calculate input characteristics of the element, as well as mutual coupling, for nine-element and twenty-five-element square array antennas. The effectiveness of the design method is verified by measurements. Section 3 describes the design results of the antenna element excited by an inverted-F element. This type of antenna element requires fewer posts than the previous elements. Finally, a brief summary of this paper is provided in the last section.

2. Antenna Geometry and Design Method

Figure 1 shows the geometry and the dimensions of the antenna element investigated by authors as an element of the SPS2000 spacetenna [3]. The spacetenna is a large-scale phased-array antenna of 132 m by 132 m, composed of about 2.5 million elements. The polarization is linear, and the bandwidth is not specified, since a sinusoidal wave at a frequency of 2.45 GHz is used to transmit the microwave energy. The dimensions of the element, d_x and d_y, are 75 mm (0.612λ) and 90 mm (0.735λ) respectively, where λ denotes the wavelength of 122.4 mm, and the antenna height is h. To be suitable for mass production, a simple geometry for a feed located at the bottom plane of the cavity should be adopted. One of feeds that meets these requirements and that is appropriate for a low-profile geometry is a shorted probe, terminated on the plane of the slot. P_f denotes the probe location, measured from the center of the bottom plane. ℓ_s and w_s denote the slot length and width, respectively. The two conductive plates in the element are separated by metal posts of 1.04 mm diameter, with spacing intervals of Δ.

We used the FDTD technique to analyze the antenna characteristics [6]. The problem space, including the antenna, was quantized by Yee cells (cubical cells) in order to develop the FDTD formulation for the model of an antenna element [7]. We used 1.5 mm cubical cells. On the outer boundary, the FDTD algorithm employed the PML absorbing boundary condition [8] to simulate the field-sampling space extending to infinitely by suppressing reflections off of the outer boundary. The excitation for a wire-fed antenna geometry was performed using a coaxial-line feed model with a characteristic impedance of 50 Ω [5].

Here, we used the design method of low-profile antenna elements proposed in [9]. The antenna parameters taken into account were the probe location, P_f, the slot length, ℓ_s, and the slot width, w_s. The slot location was set to 10.5 mm from the edge of the cavity [9]. The general procedures for realizing the impedance matching can be

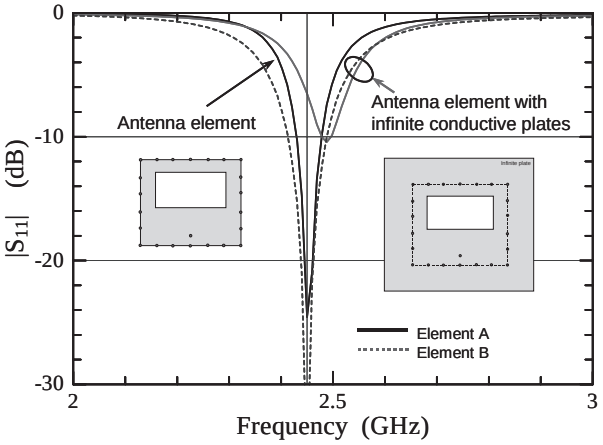

Figure 2. The input characteristics of the elements

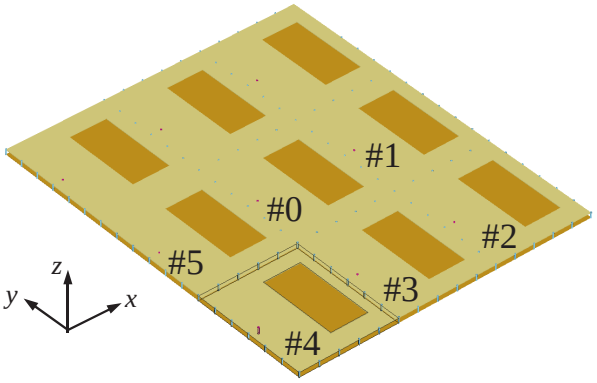

Figure 3. The geometry of the nine-element array antenna.

summarized as follows:

1. The probe location was shifted away from the element's center to the opposite side of the slot, so that the curve of the frequency characteristics passes through the center of the Smith chart.
2 The slot width was expanded to make the resonant frequency correspond to 2.45 GHz.

Figure 2 shows the input characteristics of the antenna elements. In the figure, we assumed that the antenna height, h, was 3 mm; the slot length, ℓ_s, was 60 mm; the spacing between posts, Δ, was 15 mm; and the total number of posts was 22. The antenna element depicted in Figure 1 gave a return loss of 22 dB at a frequency of 2.45 GHz for $w_s = 29.4$ mm and $P_f = 33.0$ mm (Element A). Here, it is appropriate that the top and the bottom planes were equivalently infinite, since the spacetenna is a large-scale array antenna. Assuming the two infinite planes in Element A, the resonant frequency was shifted to 2.5 GHz, and the return loss was decreased by about 10 dB at the frequency of 2.5 GHz. Hence, we again adopted the same design method for the antenna element with the infinite planes. We then obtained the frequency characteristic denoted by the dashed line in Figure 2 for $w_s = 27.5$ mm and $P_f = 30.0$ mm (Element B). This shows that a good impedance matching was obtained, such that the return loss was more than 30 dB at a frequency of 2.45 GHz. Because of the propagation of electromagnetic fields into the region of the parallel plates through the post walls, Element B should be adopted for the element with sidewalls consisting of posts. On the other hand, the narrower post intervals prevented electromagnetic fields from leaking into the parallel-plate regions with an increase of the total number of posts.

Next, we studied the mutual coupling in the array antenna [10]. Figure 3 shows the geometry of a nine-element array antenna under consideration, where the index #0 was assigned to a centrally sited element. Finite conductive plates were assumed in the FDTD analysis and experiments. Moreover, a magnetic wall was employed at the symmetry plane to carry out a cost-effective computation.

Figure 4 shows the input characteristics and mutual coupling for the nine-element array antenna when element #0 was excited and the other elements were terminated by

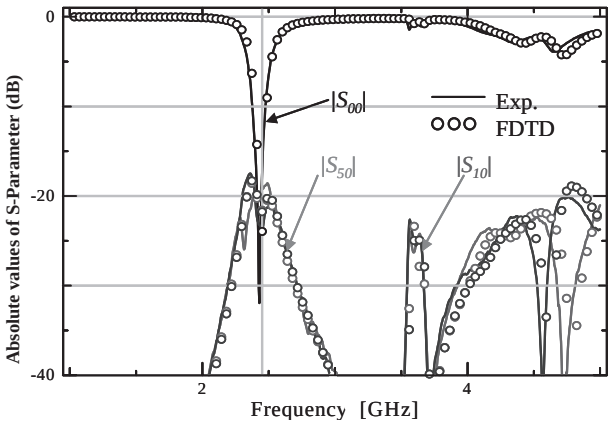

Figure 4a. Evaluations of $|S_{00}|$, $|S_{10}|$, and $|S_{50}|$ mutual coupling in the nine-element array antenna when element #0 is excited.

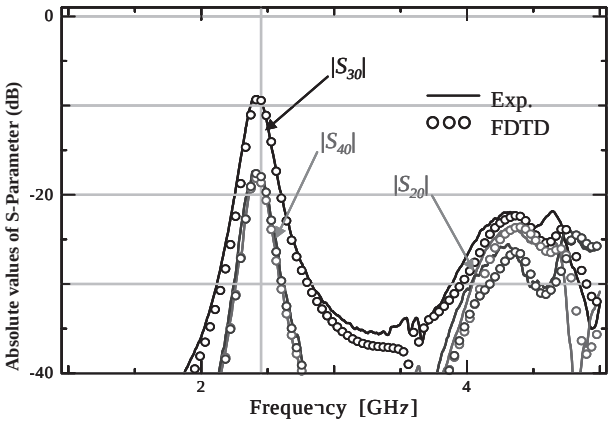

Figure 4b. Evaluations of $|S_{20}|$, $|S_{30}|$, and $|S_{40}|$ mutual coupling in the nine-element array antenna when element #0 is excited.

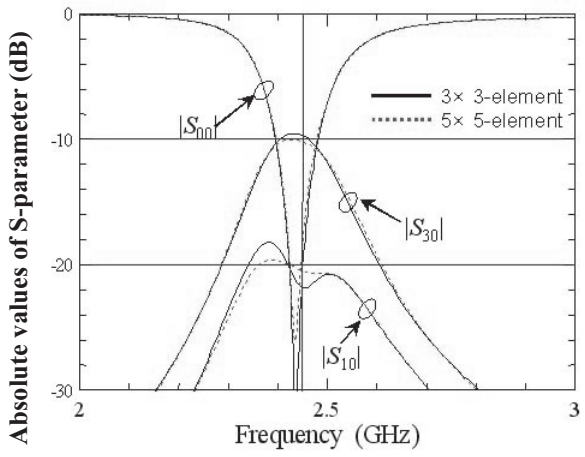

Figure 5. A comparison of the mutual coupling in the nine-element and twenty-five element square array antennas

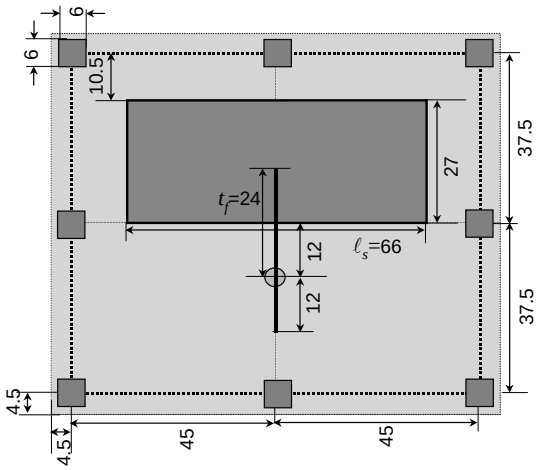

Figure 6b. A top view of the antenna element with an inverted-F element feed and thick posts

matching loads. Each antenna element had the same structure as Element B. The experimental data are the solid curves, and the FDTD calculations are the circles. It is found from the figures that the computed results agreed well with the experimental results. The computed $|S_{00}|$ was -24 dB at 2.45 GHz, and sufficient impedance matching was still obtained for the antenna array. On the other hand, the maximum value of the mutual coupling $|S_{30}|$ was about -9 dB at a frequency of 2.45 GHz. As a result, it was concluded that Element B, designed under the assumption of infinite conductive plates, is also effective for the array antenna.

Figure 5 shows the numerical results of the input characteristic, $|S_{00}|$, and mutual couplings, $|S_{30}|$ and $|S_{10}|$, for the nine-element and the twenty-five-element square array antennas with infinite conductive plates. It is clear from the figure that the computed results were almost the same for both array antennas. Here it was also assured that the design method and Element B are effective for the case of a large-scale array antenna, such as the spacetenna.

3. Antennas Fed by an Inverted-F Element

We discuss another type of antenna element, excited by an inverted-F element. Figure 6 depicts the antenna geometry, composed of two metal plates, an inverted-F element, and eight pillars with a square cross section of 6 mm x 6 mm and a height of 12 mm. The antenna dimensions were the same as for the previous case. The eight metal posts were placed at the four corners of the element and at the center of the four edges. It was assured, by using the FDTD computation, that the minimum number of posts was eight. Compared with the previous element, fed by a shorted probe, this type of antenna element had a distinct advantage. Namely, we can fabricate both parts of the slot and feed individually, since the feed is set on the bottom plate and is not connected with the upper plate. If we use metal pipes as the posts, we can realize an easy way to configure the element, since the two metal plates separated by posts are fixed with screws. As a result, the element,

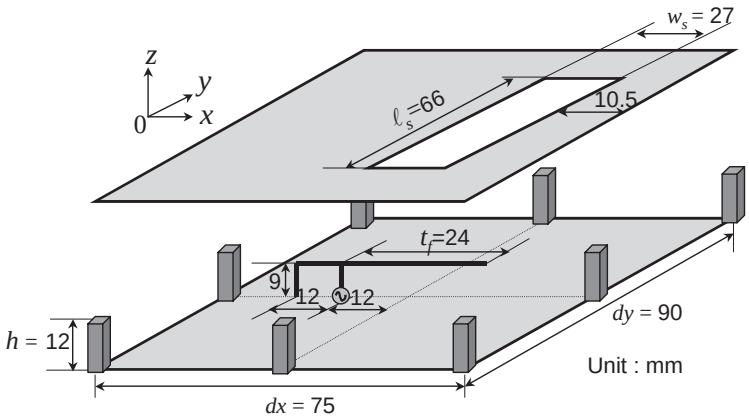

Figure 6a. The geometry of the antenna element with an inverted-F element feed and thick posts

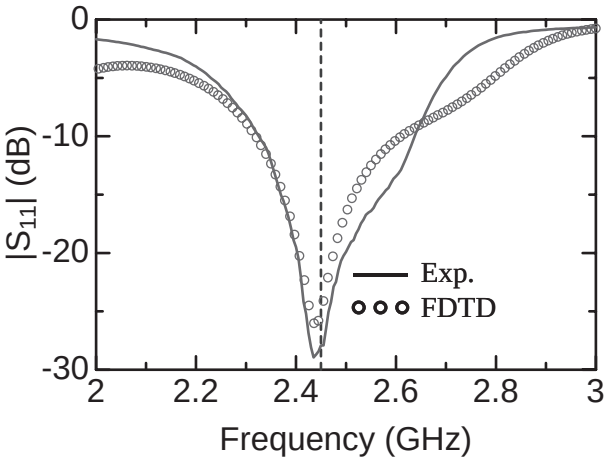

Figure 7. The input characteristics of the antenna element, for $\ell_s = 66$ mm, $w_s = 27$ mm, and $t_f = 24$ mm

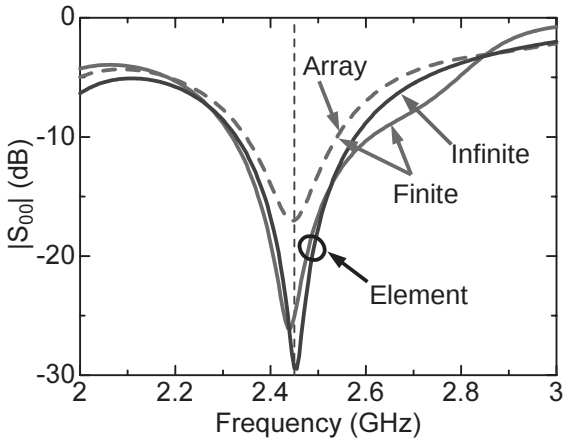

Figure 8. The computed input characteristics of three types of antenna element.

except the feed, can be assembled without soldered connections. The thick posts are expected to be useful in reducing the total number of posts in the element, and in decreasing the amount of mutual coupling in the antenna array. For the reasons stated above, it is desirable to use thick posts instead of thin wires.

We adopted a design method based on adjusting the slot length, ℓ_s, the slot width, w_s, and the wire length of the inverted-F element, t_f. Their various combinations accomplished the impedance matching at the frequency of 2.45 GHz. One combination was $\ell_s = 66$ mm, $w_s = 27$ mm, and $t_f = 24$ mm for the antenna geometry shown in Figure 6.

Figure 7 shows the computed input characteristic of the antenna element compared to the measurement. The experimental data are the solid curves, and the circles are an FDTD calculation. It was found that both results agreed with each other. We verified the effectiveness of the design results by the experiments and calculations.

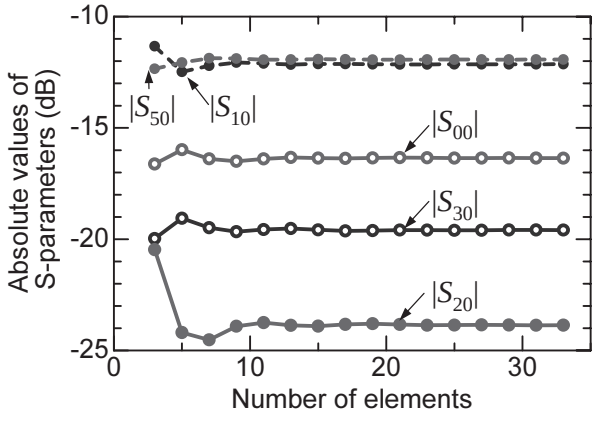

Figure 9. The relationships among the number of elements and the values of return loss and mutual coupling

Figure 8 shows the computed input characteristics of a single antenna element with finite or infinite metal plates and the antenna element placed in the middle of the nine-element antenna array. The solid curves denote the frequency characteristics of the single element, and the dashed curve denotes the frequency characteristics of an element in the array antenna. The resonant frequencies were about 2.45 GHz for all, except that the return loss was decreased to 17 dB for the antenna array. It was expected that the level of mutual coupling between antenna elements was high. However, the return loss obtained was a sufficient value for microwave energy transmission.

Figure 9 shows the relationships among the number of elements in the antenna arrays and the values of return loss and mutual coupling, where the square- shaped array antennas shown in Figure 10 were assumed to be composed of 3 x 3 to 33 x 33 elements. The horizontal axis denotes the number of elements in *x* or *y* coordinates. The element with the index of #0 was excited and placed at the center of the antenna array, and the other elements were terminated by the load. It was found from Figure 9 that $|S_{00}|$ was −16.4 dB, and the mutual couplings, $|S_{10}|$ and $|S_{50}|$, were about −12 dB. These values did not depend upon the number of elements when the number of elements was more than nine. The possibility of improving the input characteristics was examined for several antenna parameters. We found that the antenna parameters derived above were almost the optimum values.

4. Conclusion

The paper proposed a new type of slot antenna, consisting of two conductive plates separated by thin wires or thick pillars. The antenna configuration makes it easy to fabricate antenna elements and array antennas.

First, we showed an effective design method for an antenna element with a height of 3 mm, excited by a shorted probe. We derived two designs for the elements, A and B,

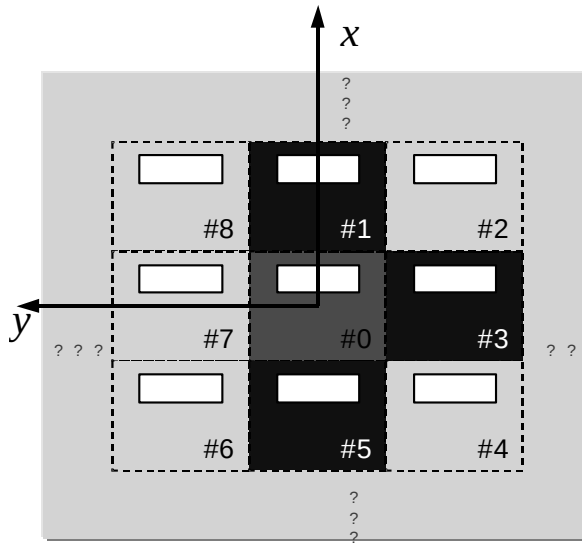

Figure 10. The geometry of the square-shaped array antenna.

with finite and infinite conductive plates, respectively. We obtained impedance matching for both at a frequency of 2.45 GHz. It was found that Element B was effective for the array antenna design, and that the level of mutual coupling between the excited element and its adjacent elements in the H-plane direction was high. Additional calculations for the nine-element and the twenty-five-element array antennas showed that the values of return loss and mutual coupling were almost the same for both array geometries. So, the evaluation of mutual coupling for the nine-element array antenna gave us a good perspective of that for the large-scale array antenna.

Second, we discussed another type of antenna element, excited by an inverted-F element. The elements were composed of two metal plates, separated by eight square pillars, 12 mm high. If we use metal pipes as the pillars, we can realize an easy way for configuring the element, since the two metal plates are fixed with screws. Furthermore, the antenna configuration has such advantages as the feed being set on the bottom metal plate and not being connected with the upper plate. This type of element can be configured with fewer posts than the previous element.

Further research on this subject is needed to elucidate the difference in heat dissipation from using the metal-post design compared to a solid-cavity-wall design.

5. Acknowledgements

This work was supported by Grant-in-Aid for Scientific Research (C) (2) 12650357 from Japan Society for the Promotion of Science (JSPS). Numerical analyses were performed using the resources provided by the High Performance Computing System at the Information Initiative Center, Hokkaido University.

6. References

1. P. E. Glaser, F. P. Davidson, and K. I. Csigi (eds.), *Solar Power Satellite – The Emerging Energy Option*, New York, Ellis Horwood, 1993.

2. SPS2000 Task Team for Solar Power Satellite (SPS) Working Group, *English Summary of SPS2000 Project Concept – A Strawman SPS System (Preliminary Edition)*, Sagamihara, Inst. Space Astronautical Science, 1993.

3. T. Hikage, N. Ohno, M. Omiya, and K. Itoh, "Proposal of Cavity-Backed Slot Antennas for the Microwave Energy Transmission," *IEICE Transactions (B-II)*, **J81-B-II**, 3, March 1998, pp. 218-225.

4. M. Omiya, T. Hikage, N. Ohno, K. Horiguchi, and K. Itoh, "Design of Cavity-Backed Slot Antennas Using the Finite-Difference Time-Domain Technique," *IEEE Transactions on Antennas and Propagation*, **AP-46**, 12, December 1998, pp. 1853-1858.

5. T. Hikage, M. Omiya, and K. Itoh, "Considerations on Performance Evaluation of Cavity-Backed Slot Antenna Using the FDTD Technique," *IEEE Transactions on Antennas and Propagation*, **AP-49**, 12, Dec. 2001, pp. 1712-1717.

6. A. Taflove, *Computational Electromagnetics*, Norwood, MA, Artech House, 1995.

7. K. S. Yee, "Numerical Solution of Initial Boundary Value of Problems Involving Maxwell's Equations in Isotropic Media," *IEEE Transactions on Antennas and Propagation*, **AP-14**, 5, May 1996, pp. 302-307.

8. J. P. Berenger, "A Perfectly Matched Layer for the Absorption of Electromagnetic Waves," *J. Computational Physics*, **114**, 1994, pp. 185-200.

9. M. Omiya, T. Hikage, and K. Murakami, "FDTD Analysis and Design of Cavity-Backed Slot Antennas for Microwave Energy Transmission," The 18th Annual Review of Progress in Applied Computational Electromagnetics, **S3-1**, March 2002, pp. 125-132.

10. T. Hikage, M. Omiya, and K. Itoh, "FDTD Analysis of Mutual Coupling of Cavity-Backed Slot Antenna Array," *IEICE Trans. Electronics*, **E81-C**, 12, December 1998, pp. 1838-1844.

Phase-Controlled Magnetron Development for SPORTS: Space Power Radio Transmission System

N. Shinohara
H. Matsumoto
K. Hashimoto

Abstract

Since the first proposal of a Space Solar Power Station (SPS) in 1968, many different types of SPS have been proposed. Some of them are designed with microwave power transmission (MPT) technology based on a microwave power transmitter with microwave tubes. The microwave tubes, such as klystrons or magnetrons, have high efficiency ($> 70\%$) and high power output (over 1 kW). We show a new concept for a microwave transmitter with phase-controlled magnetrons (PCM), for satisfying both requirements of high efficiency and beam control. We also propose a new phased-array system with the phase-controlled magnetrons for the SPS.

We use the injection-locking technique and phase-locked-loop (PLL) feedback by controlling an anode current for the phase-controlled magnetron. We can stabilize and control the frequency and phase of the microwave emission of the phase-controlled magnetron. However, we have a power loss after the phase-controlled magnetron for SPS use, because the output power from one antenna is designed to be less than 1 W in a recent SPS design, and we have to insert a power divider and phase shifters after the phase-controlled magnetron. In order to decrease the power loss after the phase-controlled magnetron, we have recently proposed some new concepts, and have developed a phase-controlled magnetron array called SPORTS (Space POwer Radio Transmission System) in FY2000 and FY2001 at Kyoto University.

1. Introduction

Microwave power transmission (MPT) technology is one of the most important technologies in the Space Solar Power System (SPS). The dc-RF-dc conversion efficiency, the accuracy of the microwave beam control, and the cost of the microwave power transmission system are especially important. We believe that a magnetron is well-suited for the microwave power transmission system of the SPS [1], especially a small experimental SPS, because its dc-RF conversion efficiency is high ($> 70\%$) and it is very inexpensive ($< \$5$). Weight is also important for a space system, because it strongly affects cost. The weight-power ratio (g/W) of the magnetron system, which includes the dc-dc converter and heat radiation, is smaller than that for a semiconductor amplifier system, because the output power of the magnetron is high (> 1 kW). Of cause, the magnetron does have some unsuitable characteristics for microwave power transmission including a communication system. It has been difficult to control the frequency and the phase of the microwave output of the magnetron, because it is just a microwave oscillator.

One result of our study is to show that the output microwave spectrum of a magnetron depends on the stability of the dc power source and the filament current [2]. If we use a stabilized dc power source for the magnetron and turn off the filament current after stable oscillation occurs, the spectrum, including low frequencies and high frequencies, is quiet and pure, and it is adequate for use in a microwave power transmission system (Figure 1). The main frequency, the high frequency, and the low frequency were measured by a spectrum analyzer with a spiral antenna, a horn antenna, and a current probe, respectively. The harmonics did not show great improvement between turning on the filament current and turning it off. This is because the harmonics of the magnetron are caused by distortion of the fundamental, and the distortion is independent of the effect of the filament current. However, almost all spurious emissions are suppressed except some spiky noise. The cause of the other spurious signals is complex; however, we consider that it is enough to suppress interference. However, there remains the problem of the frequency shift caused by heating of the magnetron; still, the spurious emissions are suppressed.

Naoki Shinohara, Hiroshi Matsumoto, and Kozo Hashimoto are with the Research Institute of Sustainable Humanosphere, Kyoto University, Uji, Kyoto 611-0011, Japan; Tel: +81-774-38-3818; Fax: +81-774-31-8463; E-mail: shino@rish.kyoto-u.ac.jp

This invited paper is part of the Special Section on Space Solar Power Systems. An oral version was originally presented at the 2003 Japan-US Joint Workshop on Space Solar Power System (JUSPS'03), July 3-4, 2003, Kyoto University, Uji, Kyoto, Japan.

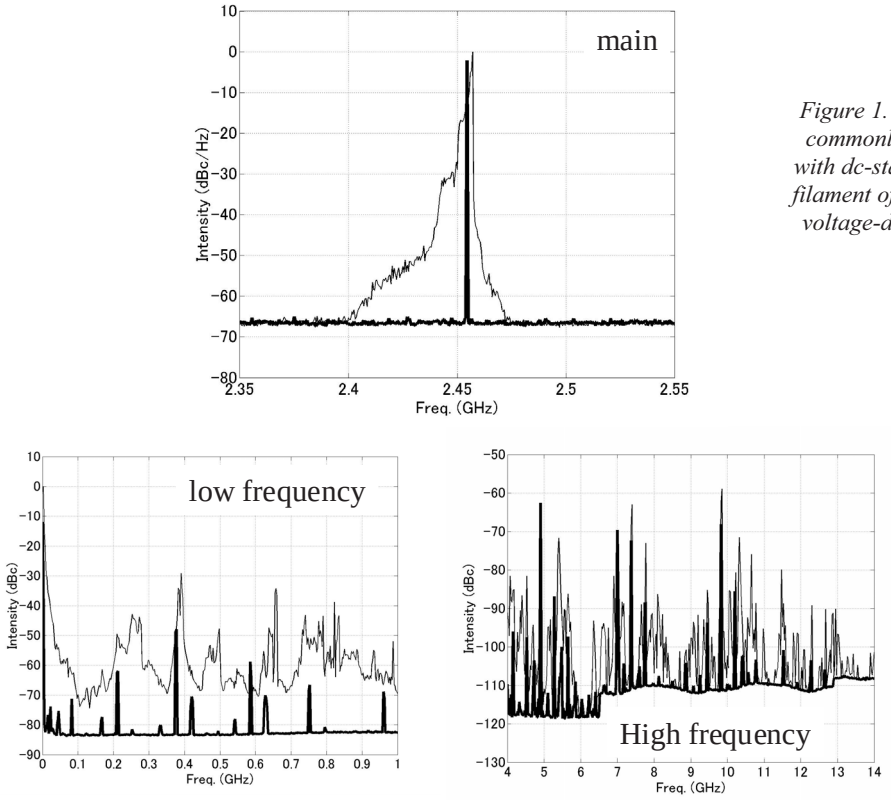

Figure 1. The output spectrum of a commonly used magnetron (bold: with dc-stabilized power supply and filament off; normal: with half-wave voltage-doubler power supply and filament on)

Therefore, in order to stabilize the magnetron frequency and to control its phase, we have developed a phase-controlled magnetron (PCM) with injection locking and phase-locked-loop (PLL) feedback obtained by controlling the anode current of the magnetron (Figure 2) [1]. We use a commonly used, inexpensive magnetron for the phase-controlled magnetron. The phase of the magnetron can be tuned in several different ways. One is to change the magnetic field by using an external coil [3]. Another is to change the anode current flow. We have chosen the anode current control, because the range of frequency control and phase control is wider with anode current control than is

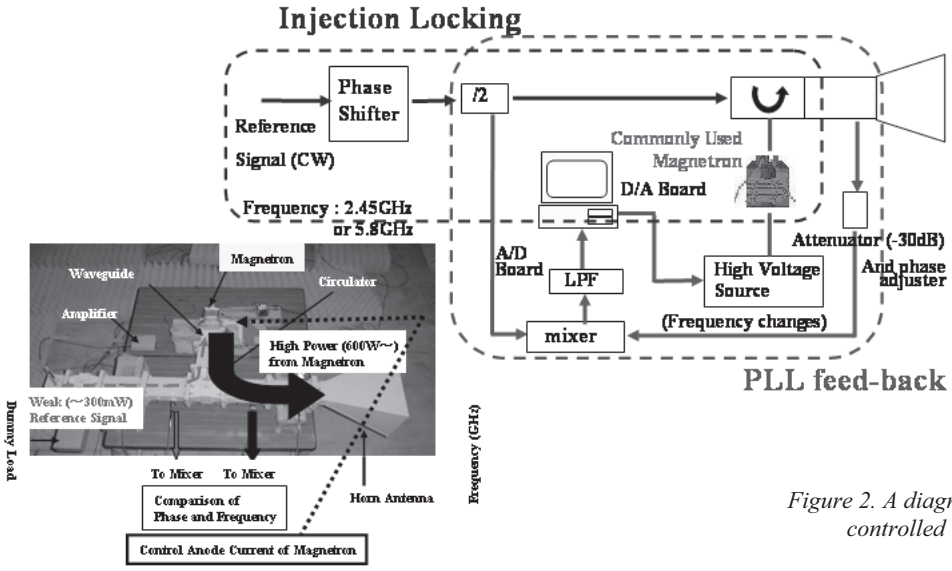

Figure 2. A diagram of the phase-controlled magnetron

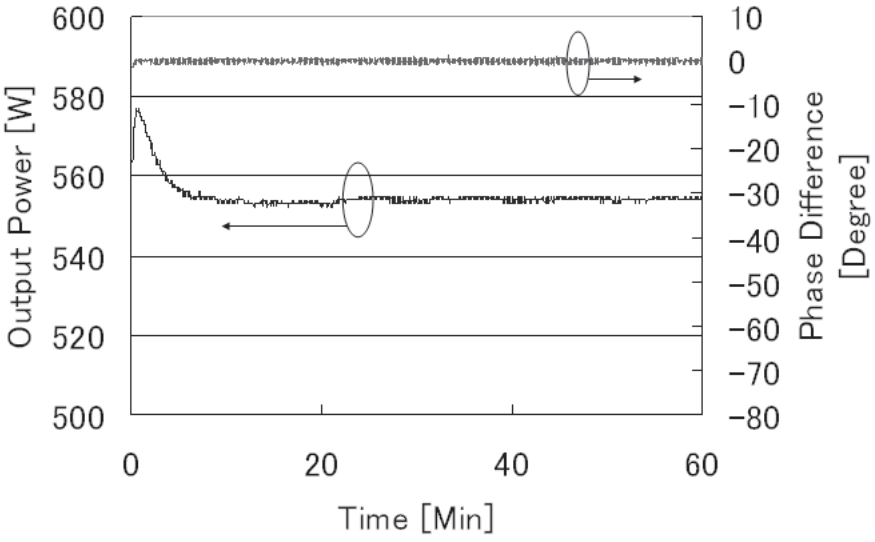

Figure 3. The time dependence of the phase and power of a phase-controlled magnetron.

possible with control of the magnetic field. Figure 3 indicates the time dependence of the phase and the power output of the phase-controlled magnetron. After an initial time delay, the output power and the phase of the phase-controlled magnetron's output are stabilized. We have carried out a phased-array experiment with the phase-controlled magnetrons, and we successfully controlled the beam direction with the phase-controlled magnetrons [4].

Based on the phase-controlled-magnetron technique, we have developed some microwave power transmission systems for equipment at Kyoto University. One is a 2.45 GHz system called SPORTS-2.45 (Space POwer Radio Transmission System for 2.45 GHz), and the other is a 5.8 GHz system called SPORTS-5.8 (Space POwer Radio Transmission System for 5.8 GHz). The phase-controlled magnetron has characteristics of high efficiency, high power, high voltage, and small weight-power ratio. However, for some SPS applications, the high-output-power advantage of the phase-controlled magnetron is weakened, because the output power from one antenna is designed to be less than one watt in a recent SPS design [5]. Therefore, we have to put a power divider and phase shifters before the antenna, in order to control the beam direction electrically and to suppress grating lobes. Commonly used power dividers and phase shifters have a large power loss. However, the SPS must have a low-loss microwave power transmission system because of cooling problems in dissipating generated heat, and cost considerations. The SPORTS system has therefore been developed with means for decreasing the power loss after the phase-controlled magnetron, in order to realize a beam-control system.

There is no law regarding the use of the frequency for microwave power transmission. Only the ISM (Industrial, Scientific, and Medical) band is now open for microwave power transmission. We would like to use microwaves for power transmission from space to the ground because of (system and propagation) efficiency and cost. 2.45 GHz and 5.8 GHz belong to the ISM band, and these are microwaves. Therefore, we have chosen the frequencies of 2.45 GHz and 5.8 GHz. If other microwave frequencies become available for microwave power transmission, we will use the new frequencies.

2. SPORTS-2.45

SPORTS-2.45 is composed of four subsystems (Figure 4): a phase-controlled magnetron phased array as a microwave transmitter subsystem, a microwave receiver (rectenna array), solar panels for dc supply, and a near-field scanner for measurement. SPORTS-2.45 was designed and developed at Kyoto University as a test bed for a space microwave power transmission experiment in FY2000.

The solar panels provide 8.4 kW of dc power to the microwave transmitter subsystem, composed of a phased array with twelve phase-controlled magnetrons. The design specifies 200 V dc, as would be suitable in space use. For the phase-controlled magnetron of the SPORTS-2.45, we used a cooker-type magnetron, 2M234, made by Matsushita Co. Typical characteristics of the 2M234 are as follows: the frequency (matched load) is 2.455 GHz; the peak anode voltage is 3.85 kV; the average output power (matched load) is 550 W. We always turn off the filament current during power transmission after stable oscillation occurs. We achieved a frequency stability of better than 10^{-8}, relative to the frequency stability of an input reference signal. The transmitted microwave power and frequency were 4 kW and 2.45 GHz, respectively. One reference signal was divided and injected into each phase-controlled magnetron through a phase shifter. This was the first phase-controlled magnetron array in the world.

The SPORTS-2.45 system has two different types of antenna arrays. One is a twelve-horn antenna array, with low power loss but with a limited narrow-beam scanning capability. The gain of each horn antenna is 17.73 dB. The other antenna is a 96-dipole antenna array with reflector and

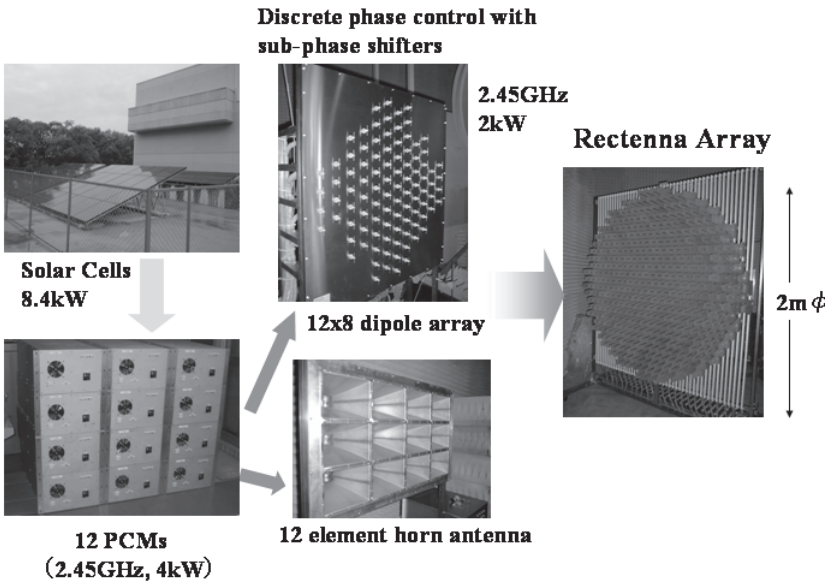

Figure 4. The SPORTS-2.45 system.

sub-phase shifters. The sub-phase shifter can control the phase of a microwave signal with only the options of –60°, 0°, +60°. It is a 96-antenna array with twelve eight-way power dividers and 96 sub-phase shifters, with which the microwave beam can be scanned into a much wider range of directions. We have shown that we can keep high beam-collection efficiency when we control a beam to a two-times-larger direction with the sub-phase shifters in the SPS system [1].

For target detection, we use a retro-directive system with a CW pilot signal of 400 MHz in the SPORTS-2.45. We use three receiving antennas for the pilot signal, and we calculate the direction of a target with a computer. We put the receiving antennas in triangular locations, and the element spacing of the receiving antennas is 1.3 m (1.7λ). We can easily change the frequency of the pilot signal by hardware and software changes because we calculate the direction of the target with a computer. We succeeded in detecting the target under conditions of power transmission with the phase-controlled magnetrons.

The rectenna array is composed of four types of rectennas, which are placed accordingly for optimum microwave input power, yielding the highest RF-dc conversion efficiency [6] in the presence of a spatially-varying gradient power density of the microwave beam. All rectennas in an array cannot be of highest RF-dc conversion efficiency because the RF-dc conversion efficiency of the rectenna has an input-power dependence. We use a Yagi-Uda antenna and a power divider for the rectenna. The maximum RF-dc conversion efficiency of each rectenna was 77.7%, 75.7%, 73.0%, and 68.6% with 1 W, 2.1 W, 4.1 W, and 6.7 W of input microwave power, respectively

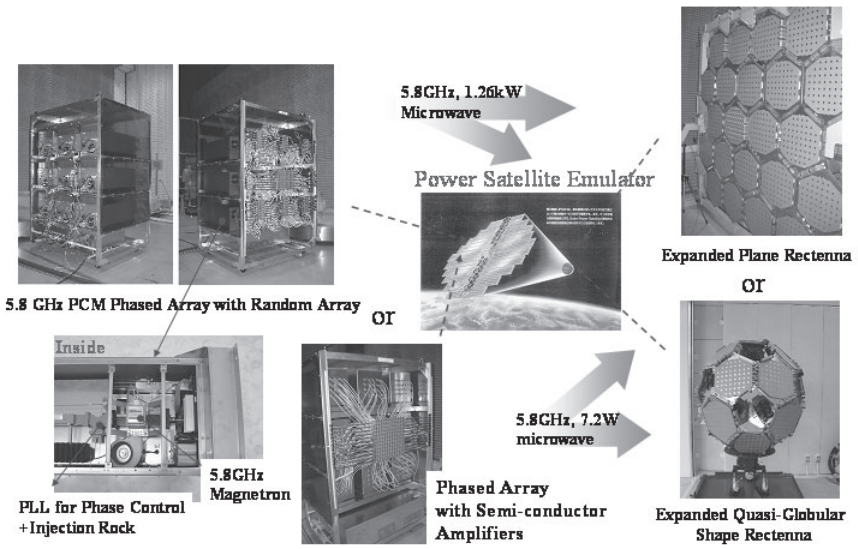

Figure 5. The SPORTS-5.8 system

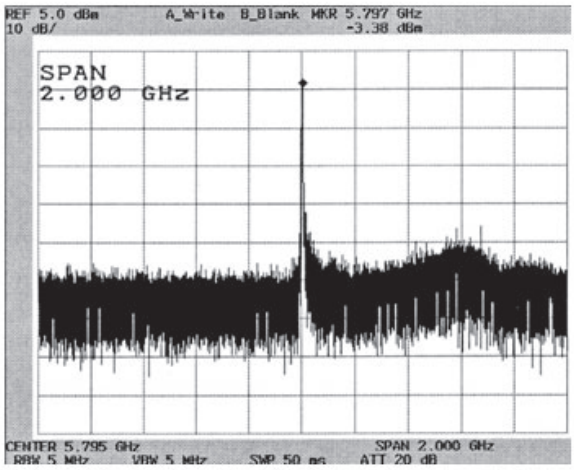

Figure 6a. The output spectrum of the 5.8 GHz magnetron of SPORTS-5.8 (the span is 2 GHz)

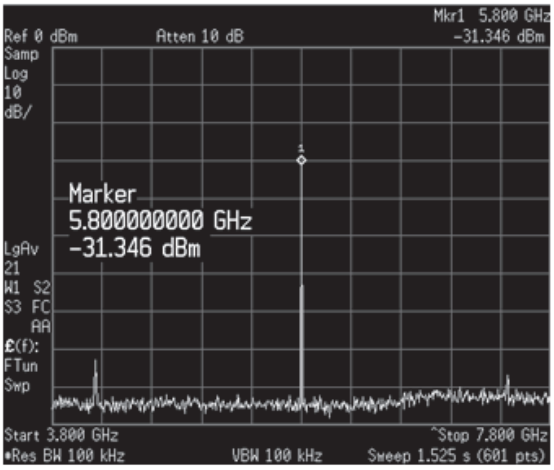

Figure 6b. The output spectrum of the semiconductor amplifier of SPORTS-5.8 (the span is 4 GHz).

[7]. There are 2,692 rectenna elements, and the diameter of the rectenna array is approximately 2 m.

3. SPORTS-5.8

In FY2001, we also developed SPORTS-5.8, with 5.8 GHz magnetrons for the phase-controlled magnetron (Figure 5). SPORTS-5.8 is composed of several transmitting subsystems and rectenna arrays. The main microwave transmitting system is composed of nine phase-controlled magnetrons, based on a newly developed magnetron with a frequency of 5.8 GHz. Typical performance values of the 5.8 GHz magnetron, developed by Matsushita Co., are as follows: the frequency (matched load) is 5.800 GHz; the peak anode voltage is 4.0 kV; the average output power (matched load) is 300 W. We always turn off the filament current during power transmission after stable oscillation occurs. Four-stage eight-way power dividers were developed to distribute the microwave power from one phase-controlled magnetron to 32 microstrip-antenna elements. The transmitted microwave power from the 288 antennas was over 1.26 kW. In the main transmitter system, we adopted a random array, in order to decrease the level of grating lobes and to decrease power loss after the phase-controlled magnetron. The power loss after the phase-controlled magnetron was below −1.5 dB.

For target detection, we use a retro-directive system with a pilot signal of 4.8 GHz that is modulated with a spread spectrum [8]. We use four receiving antennas for a pilot signal, and we calculate the direction of a target with a computer. This does not respond to fake or wrong signals, because direct-sequence spread-spectrum is used for the signals. It is expected to be more reliable in the presence of noise and power transmission. The pilot signal can be modulated, e.g., for sending information on power reception and authentication. This is a useful technique, even for a single receiving site. It has been confirmed that the new direction-finding system for multiple spread-spectrum pilot signals works well. Figure 7 shows the result of direction finding with a modulated spread-spectrum pilot signal in the SPORTS-5.8 system [9]. The distance between Tx and Rx was approximately 4 m. We used two receiving antennas for the pilot signal, which were put in the horizontal plane with a spacing of 0.5λ. The error in the direction finding

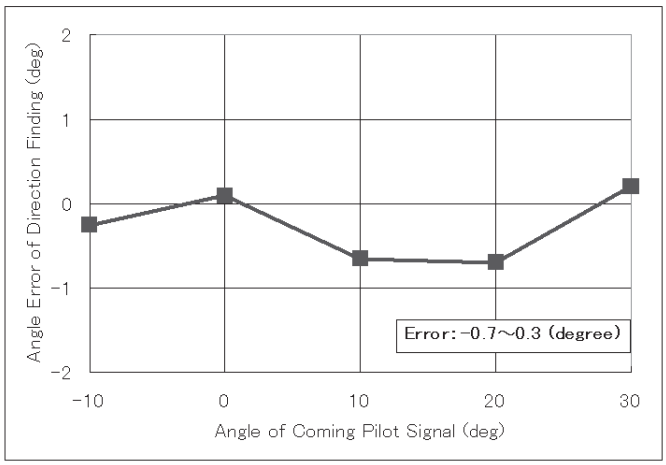

Figure 7. The result of direction finding with a modulated spread-spectrum pilot signal [9].

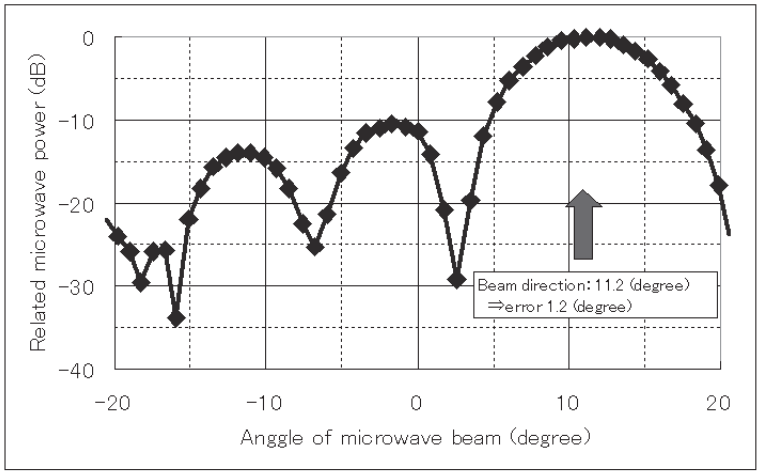

Figure 8. The result of beam forming with the retro-directive system [10].

was below 0.7°. This is sufficient for the final SPS system because we use a large number of the direction-finding systems in the SPS, and the direction-finding error is expected to be much smaller in total.

We have another, alternative microwave power transmission system in the SPORT-5.8. It is called a "beam-forming subsystem," with one semiconductor amplifier, power dividers, 144 four-bit phase shifters, and 144 (12 × 12) microstrip antennas. The performance characteristics of the semiconductor amplifier are as follows: the frequency is 5.77 GHz; the frequency stability is better than 1.4 ppm; the saturation output microwave power is 26.9 W; and the saturation gain is 8.5 dB. The total microwave power emitted from the antenna array through the power dividers and phase shifters is over 7 W. Figure 8 shows the result of beam forming with the retro-directive system with a distance of 4 m. The element spacing of the transmitting antenna was 0.7λ. The error of direction finding and beam forming was below 1.2°. We can use the same retro-directive system both for the beam-forming subsystem and for the transmitting subsystem. We can carry out experiments concerning beam forming with the subsystem.

We show spectral data for the 5.8 GHz magnetron and the semiconductor amplifier of the SPORTS-5.8 system in Figure 6. Unfortunately, the parameters of the measurements were different between Figure 1 and Figure 6, and we can not exactly compare these data. However, there is no interference from these transmitting systems with the retro-directive system, and we experimentally succeeded in detecting the target with the retro-directive system with a 4.8 GHz pilot signal.

We have two types of rectenna array in the SPORTS-5.8. We emulate a small experimental satellite with rectennas, and both rectenna arrays can be stored in a small shape and expanded. The same rectenna element is used for both arrays, and only the shape of the arrays is different. One is a plane rectenna array, and the other is a quasi-globe-shaped rectenna array. The maximum RF-dc efficiency of the rectenna element is over 71.8% with 100 mW of 5.8 GHz microwave input power and with a 200-ohm load.

4. SPORTS-5.8 options

The SPORTS-2.45 and SPORTS-5.8 systems were developed with the concept of "high efficiency beam control." In order to decrease the loss after a phase-controlled magnetron array with high efficiency, we use a sub-phase-shifter system for SPORTS-2.45, and a random array for SPORTS-5.8. Besides these experiments, we have developed two different types of microwave transmitters with a

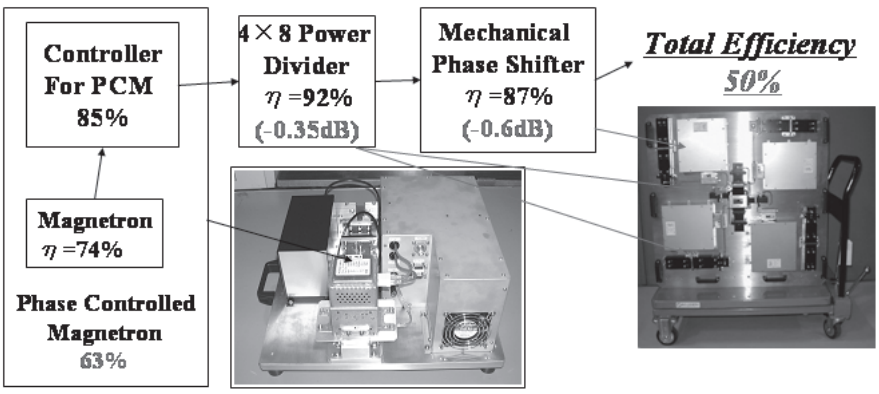

Figure 9. A diagram showing the efficiency of the SPORTS-5.8 option system.

frequency of 5.8 GHz. One uses three parabolic antennas, which form a one-dimensional phased array of parabolic antennas. We can decrease the loss after the phase-controlled magnetron because we do not need phase shifters after the phase-controlled magnetron in the parabolic phased array.

The other is a revised phase-controlled magnetron without the injection-locking technique and with a low-loss phase-shifter system. This is a circulator-less phase-controlled magnetron. The size of the circulator-less phase-controlled magnetron module is 400 mm × 400 mm × 150 mm. Its weight is below 13 kg, which includes the magnetron, dc/dc converter, waveguide, PLL control unit, and structure. The weight of the magnetron is only 0.6 kg, and the output microwave power is approximately 300 W. The weight/power ratio is below 43 g/W. The frequency stability of the SPORTS-5.8 option is approximately 10^{-5}; however, we can improve the frequency stability with an improvement in the performance of the PLL. For a low-loss phase shifter, we adopted a mechanical (moving dielectric substance) system, and its loss is −0.6 dB with analog phase shift. An efficiency diagram is shown in Figure 9. We have achieved 50% total efficiency of the microwave transmitter with beam control. The mechanical phase shifter, however, still has many problems: for instance, moving speed and lifetime.

We tried to decrease the size and weight of the SPORTS-5.8 option; however, we did not try to decrease the size and weight of both SPORTS systems. Generally speaking, the 5.8 GHz system is smaller than the 2.45 GHz system in microwave power transmission.

5. Conclusion

The SPS must have a low-loss microwave power transmission system with beam control because of the cooling limitation problem and cost considerations. Generally, the SPS has been designed with a microwave transmitting system with a phased array of over 80% efficiency. However, present microwave technology does not permit such a high-efficiency phased array. Our group focused on the magnetron as the microwave transmitter for microwave power transmission because of its cost, efficiency, and weight. We have developed the phase-controlled magnetron and its phased arrays, called SPORTS.

The SPORTS systems have been developed with concepts to decrease the power loss after the phase-controlled magnetron, in order to realize a low-loss beam-control system. The concepts are the "sub-phase shifter," "random array," "parabolic phased array," and "mechanical phase shifter." The SPORTS systems also include a retro-directive system for target detection, a beam-forming subsystem with a semiconductor amplifier, and receiving rectenna arrays. The SPORTS systems have achieved totally high efficiency with beam control; however, we are still trying to increase the efficiency and stability of the phase-controlled magnetron, and trying to decrease power loss after the phase-controlled magnetron with the SPORTS systems.

The eventual goal is a practical SPS. We work towards a microwave power transmission system with higher efficiency and lighter weight at Kyoto University.

6. Acknowledgements

The authors gratefully appreciate the participation of E&C Engineering K.K., Mitsubishi Heavy Industries, Ltd., Mitsubishi Electric Co., and IHI aerospace Co., Ltd., in the co-development of the SPORTS systems. This work is partly supported by the 21st COE program "Establishment of COE on Sustainable Energy System" at Kyoto University.

7. References

1. N. Shinohara, H. Matsumoto, and K. Hashimoto, "Solar Power Station/Satellite (SPS) with Phase Controlled Magnetrons," *IEICE Trans. Electron.*, **E86-C**, 8, 2003, pp. 1550-1555.

2. T. Mitani, N. Shinohara, H. Matsumoto, and K. Hashimoto, "Experimental Study on Oscillation Characteristics of Magnetron after Turning Off Filament Current," *Electronics and Communications in Japan, Part II : Electronics*, **E86**, 5, 2003, pp. 1-9.

3. W. C. Brown, "The SPS Transmitter Designed around the Magnetron Directional Amplifier," *Space Power*, **7**, 1, 1988, pp. 37-49.

4. N. Shinohara, J. Fujiwara, and H. Matsumoto, "Development of Active Phased Array with Phase-Controlled Magnetrons," *Proceedings of ISAP2000*, **2**, 2000, pp. 713-716.

5. M. Mori, H. Nagayama, T. Hanyu, and H. Matsumoto, "Summary of Studies on Space Solar Power System of NASDA" (in Japanese), *Proceedings of 4th SPS Symposium*, 2001, pp. 121-125.

6. T. Miura, N. Shinohara, and H. Matsumoto, "Experimental Study of Rectenna Connection for Microwave Power Transmission," *Electronics and Communications in Japan, Part 2*, **84**, 2, 2001, pp. 27-36.

7. T. Miura, K. Hirayama, N. Shinohara, and H. Matsumoto, "Study of a High Power Rectenna for Microwave Power Transmission" (in Japanese), *IEICE Trans. B*, **J83-B**, 4, 2000, pp. 525-533.

8. K. Hashimoto, K. Tsutsumi, N. Shinohara, and H. Matsumoto, "Beam Control System with Spread Spectrum Pilot Signals for Solar Power Satellite," *Proceedings of the URSI General Assembly*, 2002, p. 1284 (H Special P.7).

9. K. Morishita, O. Hasegawa, K. Iizuka, T. Kimura, H. Makimura, H. Matsumoto, K. Hashimoto, and N. Shinohara, "Technology and Applications of Microwave Energy Transmission" (in Japanese), *Mitsubishi Juko Giho*, **40**, 6, 2003, pp. 340-343.

Nano- and Micro-Devices for Performance Improvement of Space Solar Power System

V. K. Varadan
J. Xie
K. J. Vinoy
H. Yoon

Abstract

Since the development of a space solar power (SSP) system involves energy conversion at different stages, the key factor in improving the viability of the overall system is to enhance the efficiency of its building blocks. In this paper, we address the development of highly efficient components and devices, based on carbon nanotubes and RF MEMS (micro-electromechanical systems), which will enable the safe deployment and distribution of power generated using the SSP-based scheme. Carbon nanotubes show distinctive properties – such as the electron ballistic transport property and a high current-density capacity – that may not be available in any existing semiconductor materials. One of the developments in carbon-nanotube-based solar panels is to utilize the property of fast charge transfer to improve the energy-conversion efficiency.

Microwave transmission of power from an SSP to Earth requires precisely controlled highly directive antennas. This antenna system should ensure that the power is directed towards the receptor station. In this paper, an antenna system with a reconfigurable beam-steering reflector using micro-machined barium-strontium-titanate thin-film based phase shifters is also investigated.

1. Introduction

Increasing fears over the exhaustion of fossil fuels has brought the attention of the scientific community towards research into alternative energy resources. The most promising among these is solar energy. Several new approaches to improve the efficiency and efficacy of photovoltaic units are being vigorously pursued. However, these systems depend entirely on the availability of the primary source of energy: the sun. Thus, power generation and distribution may be affected at night and when the area is clouded. In contrast, if the primary energy-conversion system is located in space – sufficiently far from Earth, where the sun is available almost continuously – electrical power can be generated constantly. Space solar power (SSP) satellite-based power-generation systems assume significance in this context. Energy from these satellites is beamed to receiver locations – stationary or moving, ground-based or aerospace – by wireless power transmission (WPT) [1]. In addition, the power can be dynamically allocated between several such receiver stations, depending on the demand: providing an additional flexibility in scarce energy management, especially in the context of fluctuating energy needs due to the unpredictable nature of population expansion.

In SSP-based power generation, the objective is to deploy as many as 60 satellites at a high-elevation orbit such as the geosynchronous Earth orbit [2]. These satellites are the generating stations, consisting of extremely large arrays of photovoltaic cells (which convert solar energy into electrical energy), microwave power generators, large transmitter antennas (which launch the energy), and the necessary intelligent control systems. The components involved in such a satellite are described in Figure 1. A rectifying-antenna-(rectenna-) based system on the Earth converts the beamed microwave power into dc/ac for distribution through a utility grid.

Based on data available in the current literature, typical power-conversion efficiencies of various components on this power generation system are as follows:

1. Crystalline Si- (the best thus far) based solar cells have approximately 25% efficiency, when measured under an AM 1.5 spectrum (1000 Wm^{-2}) at 25° C [3, 4]. Up to 56% has been claimed elsewhere [5]; however, this number is not credible. Spectrolab recently reported 36.9% terrestrial concentrator cell efficiency [6].

Vijay K Varadan, Jining Xie, K. J. Vinoy, and Hargsoon Yoon are with the Center for the Engineering of Electronic and Acoustic Materials and Devices, The Pennsylvania State University, University Park, PA 16803, USA; Tel: +1 (814) 863-4210; Fax: +1 (814) 865-3052; E-mail: vjvesm@engr.psu.edu.

This invited paper is part of the Special Section on Space Solar Power Systems. An oral version was originally presented at the 2003 Japan-US Joint Workshop on Space Solar Power System (JUSPS'03), July 3-4, 2003, Kyoto University, Uji, Kyoto, Japan.

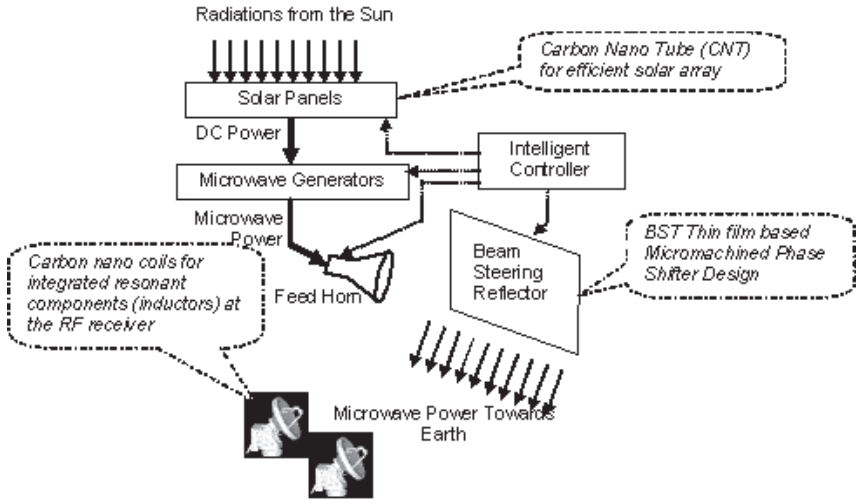

Figure 1. The component systems of a space solar power system (SSPS). Systems having a potential for significant improvement based on our approach are mentioned in bold.

2. State-of-the-art pulsed magnetrons for microwave power generation have efficiencies below 54% [7]. Continuous-power magnetrons can have efficiencies above 80%.
3. The aperture efficiency of reflector antennas developed for space-communication applications is typically below 75% [8]. This figure may vary if other antenna configurations, such as phased-array antennas and reflectarrays, are used.
4. The power-conversion efficiency at the rectenna developed by NASA was reported to be about 50% to 60% [9, 10]. A higher conversion efficiency of 82% has also been reported for a 5.8 GHz rectenna [11].

It is clear that three areas that need immediate attention to improve the overall efficiency are the conversion of solar energy to electrical energy, and its conversion and re-radiation to microwave power. In the present work, we address the development of highly efficient components and devices that will enhance safe deployment and distribution of power generated using the SSP-based scheme by (a) designing carbon-nanotube-based solar cells to make solar-to-electrical energy conversion more efficient; (b) replacing phased-array antennas with a beam-steering reflector incorporating tunable barium strontium titanate (BST) thin films; and (c) designing and developing new components with coiled carbon nanotubes in the rectennas, facilitating fabrication by LSI (large-scale integration) techniques. The next three sections in this paper are devoted to separately addressing these approaches. Our perspectives on the future of SSP technology based on these studies are presented in the last section.

2. Synthesis and Characterization of Carbon Nanotubes for Improved Solar Panels

At present, most solar cells available in the market are either "first-generation" devices. based on crystalline silicon wafers. or "second-generation" devices. based on amorphous or polysilicon compound semiconductors. A key parameter for a solar cell is its energy-conversion efficiency, defined as the ratio of output electrical power to incident optical power. This determines the area, and hence the cost, for a given power rating. However, the bandgap energy and charge mobility that are the intrinsic properties of semiconductor materials have slowed further progress towards high-efficiency photovoltaic cells. This efficiency for the first- and second-generation technology is quite modest (less than 30%), which leads to the possibility of a "third-generation" of solar photovoltaic cell.

Carbon nanotubes show distinctive properties – such as the electron ballistic transport property and high-current density capacity – that may not be available from any existing semiconductor materials. Their potential use in solar photovoltaic cell applications has recently been explored [12]. To improve the photovoltaic-conversion efficiency, a device with an active layer containing a mixture of donor and acceptor materials can be fabricated. The discovery of photo-induced electron transfer with sub-picosecond transfer rates in a composite of donor and acceptor has provided a molecular approach to high-efficiency photovoltaic conversion. Efficient charge separation and collection can be achieved in such a device. A carrier-collection efficiency of ~80% electrons/photon was reported [13]. Conjugated polymers and carbon nanotubes can be used as electron donors and acceptors, respectively. Because of their different electro-negativity and electron affinity, the separation of photo-generated species is favorable at the interface between polymer and nanotubes. The ultrafast photo-induced electron transportation and collection, with quantum efficiencies approaching unity (in sub-picosecond times) in nanotubes, are other possible reasons leading to highly efficient photovoltaic conversion. Compared with the pristine polymer diodes, the short-circuit current was increased by two orders of magnitude [14].

The carbon nanotube, as a novel member of the carbon family, has become an active research topic since its discovery in 1991. Basically, carbon nanotubes can be imagined as rolled-up cylinders of graphene sheets of sp^2-bonded carbon atoms, with cylinder diameters of less than

100 nm. The length of individual carbon nanotubes can vary from a few nanometers to several microns. Caps are always observed at both ends of these cylinders, which could be hemispheres of different fullerenes, such as C_{60}. Theoretical calculations show that carbon nanotubes have extraordinary mechanical, thermal, and electrical properties, due to their unique carbon structure as well as the nano-size scale.

The successful development of a solar cell involving carbon nanotubes requires several research steps. These include the development of a viable synthesis method for large-scale fabrication of high-purity carbon nanotubes, extensive characterization of the product by electron microscopy, ascertaining their electronic and optical properties, their incorporation into a solar photovoltaic cell, and the characterization of these solar cells. Several of these steps have already been accomplished, as described below.

2.1 Synthesis of Carbon Nanotubes

There are three major methods for producing carbon nanotubes with different properties (size, single- or multi-walled, helicity, etc.). Arc-discharge and laser-vaporization methods have been actively pursued in the past ten years. Both methods involve the condensation of carbon atoms generated from evaporation of solid carbon sources. The temperatures for both methods are close to the melting temperature of graphite, which is 3000-4000° C. Recently, chemical vapor deposition (CVD) has also been used as a method for preparing carbon nanotubes. In this method, hydrocarbons decompose at 500-1000° C, and carbon atoms form nanotube structure on catalysts. The chemical vapor deposition method is believed to be the most promising method for large-scale synthesis of high-quality carbon nanotubes with better-controlled morphology.

A set up for microwave catalytic chemical vapor deposition (CCVD), developed to synthesize high-purity carbon nanotubes, is shown in Figure 2. This system can be used to prepare carbon nanotubes, carbon nanocoils, coiled carbon nanotubes, and microcoiled carbon fibers [14-16]. It consists of a microwave magnetron, a circulator, a four-stub tuner, a waveguide, a cavity, an optical pyrometer, and a flow-controller system. The reaction temperature is measured and controlled by the optical pyrometer. Compared with the conventional thermal filament chemical vapor deposition method, this method has much faster heating, and results in high purity of the raw nanotube sample.

The experimental procedure for synthesizing carbon nanotubes with this method starts with dispersing a known amount of fine catalyst powder on the SiC substrate. The substrate is then loaded into the center of the cavity. The microwave magnetron heats the substrate to the reaction temperature (~700° C). During initial heating, argon gas (flow rate = 190 sccm) is used for purging the reaction chamber. Acetylene gas is used as the source of carbon atoms, which are deposited on the substrate. After the reaction is completed (~ 30 min) and the reactor is cooled to room temperature, the product is removed from the substrate.

The electronic and mechanical properties, quantity, and purity of the product are affected by the chemical composition and preparation method of the catalyst, the reaction temperature, and the flow rate of the gases. The resulting carbon materials are analyzed by electron microscopy.

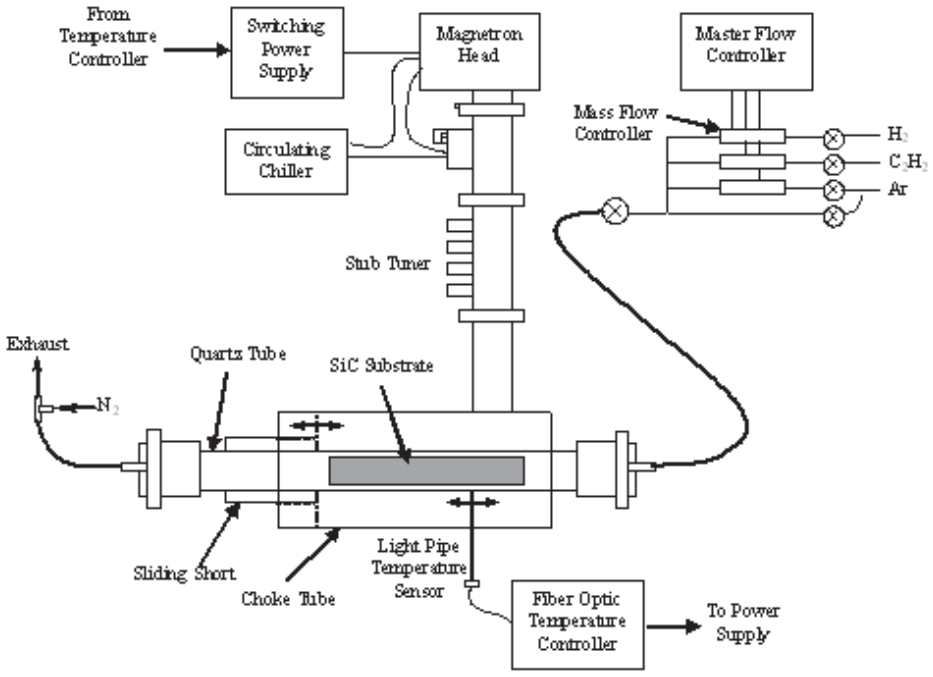

Figure 2. A schematic diagram of a microwave chemical vapor deposition system for synthesizing carbon nanotubes.

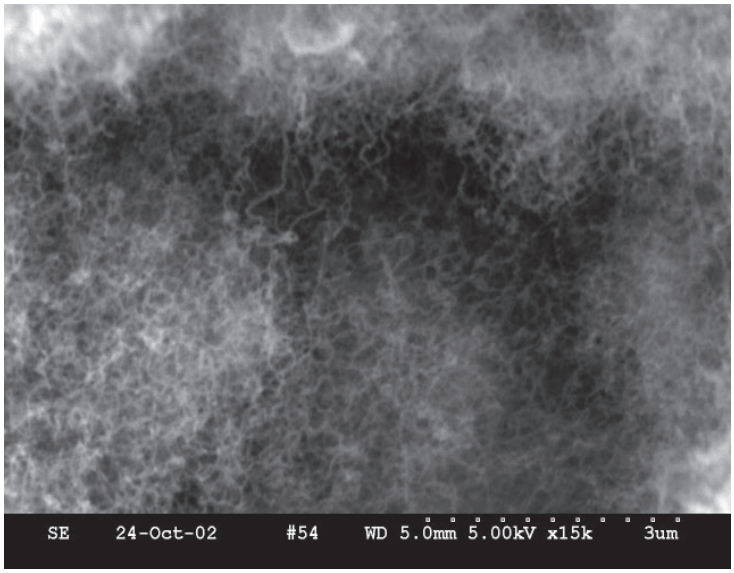

Figure 3. A scanning electron microscope (SEM) micrograph of a nanotube sample.

2.2 Characterization of Carbon Nanotubes

Various techniques are used to characterize carbon nanotubes. A Hitachi 3000N scanning electron microscope (SEM) was used to investigate the morphology of the materials. A scanning electron-microscopy micrograph, as shown in Figure 3, shows raw nanotubes obtained by the microwave chemical vapor deposition method.

A Philips 420T transmission electron microscope (TEM), equipped with an X-ray energy-dispersive spectrometer (XEDS), was used to study the nanostructure of carbon nanotubes. Sample preparation of carbon nanotubes for transmission electron microscope observation was done by ultrasonic vibration of a small number of nanotubes in acetone for about 20 minutes, and then dispersion of a drop of the suspension on a 300-mesh copper grid (from Electron Microscopy Sciences). Figure 4 is the transmission electron microscopy image, which confirmed the hollow structure of carbon nanotubes.

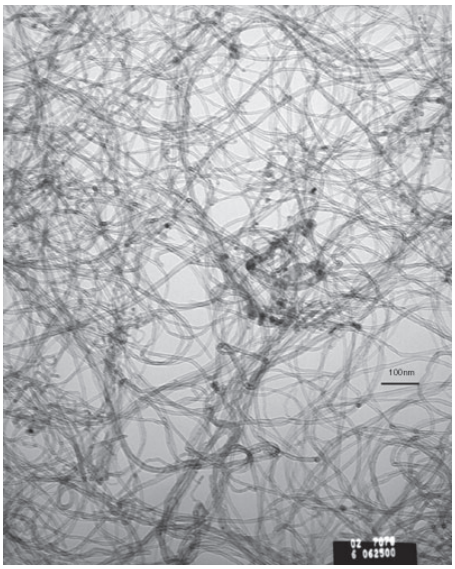

Figure 4. A transmission electron microscope (TEM) image of a nanotube sample.

2.3 Electronic Properties

The hexagonal orientation of the carbon with respect to the tubule axis could be different for different carbon nanotubes. The electronic properties of carbon nanotubes can be explained in terms of screw axes and chirality of atomic arrangement. Carbon nanotubes exhibit different properties depending on their diameters and chiralities. Wildöer and coworkers used scanning tunneling microscopy (STM) to measure the conductivities of an individual carbon nanotube, and found that the conductivity of an individual nanotube depends on the chiral angle and diameter [17]. It was reported that the bandgap energy for nanotubes is

$$E_{gap} = \frac{2\gamma_0 a_{c-c}}{d}, \qquad (1)$$

where γ_0 is the C-C tight-binding overlap energy, a_{c-c} is the nearest-neighbor C-C distance (0.142 nm), and d is the diameter. Therefore, only nanotubes with small diameters (~1-2 nm) have semiconducting properties.

In addition, carbon nanotubes show distinctive properties, such as the electron ballistic transport property and a high current density capacity that may not be available from any existing semiconductor materials (or any other material). It has been demonstrated that the propagation of electrons in the metallic nanotube is largely free from scattering over distances of thousands of atoms [18]. Due to this ballistic transport, no energy is dissipated in the conductor. Carbon nanotubes can withstand remarkable

current densities, exceeding 10^9 A/cm^2, in part due to their strong carbon-carbon bonding [19]. These advantages make carbon nanotubes a promising candidate for solar photovoltaic-cell applications.

2.4 Carbon-Nanotube-Based Photovoltaic Cell

One method to improve the photovoltaic conversion efficiency is to use a mixture of donor and acceptor materials in a device so that charge separation and collection can be done more efficiently. A mixture of carbon nanotube/conjugated polymer can be used for this purpose. Because of the difference in their electro-negativity and electron affinity, a greater separation of photo-generated species is possible at the interface between the polymer and nanotubes. In addition, the ballistic transport within nanotubes will further improve the efficiency of photovoltaic conversion.

It has been reported that single-walled carbon nanotube/conjugated polymer (poly (3-octylthiophene)) photovoltaic devices have better performance than the pristine polymer diodes [12]. The main reason for this increase is expected to be photo-induced electron transfer at the polymer/nanotube interface. Single-walled nanotubes (SWNT) act as electron acceptors and help to transfer electrons by providing percolation paths. This study also indicated that a higher open-circuit voltage (V_{oc}) of 0.75 V is possible in such devices [20]. The energy-conversion efficiency, η, is related to V_{oc} by

$$\eta = \frac{FI_{sc}V_{oc}}{P_{in}} . \qquad (2)$$

P_{in} is the incident light power, I_{sc} is the short-circuit current, and F is the fill factor. The fill factor is a figure of merit indicating how much of the available power can be extracted form the solar cell:

$$F = \frac{I_{max}V_{max}}{I_{sc}V_{oc}} , \qquad (3)$$

where V_{max} and I_{max} are the voltage and current at the maximum power point in the *I-V* characteristics of the device. The device fabricated was reported to have an external power conversion efficiency of 0.06% [18]. However, in these studies carbon nanotubes were randomly blended with a semiconducting conjugated polymer, where a bi-continuous network was formed. In order to further improve the efficiency, aligned carbon nanotubes embedded in the conjugated polymer can be envisioned as a promising approach.

The schematic diagram of a solar cell incorporating aligned carbon nanotubes is shown in Figure 5. A semiconductor layer (e.g., Si) and an aligned nanotube film are combined together in this solar cell. This could be fabricated by chemical vapor deposition of aligned nanotubes on the Si substrate. When photons impinge on the top surface of the aligned nanotube film through a transparent ITO (indium tin oxide) film, electron-hole pairs are photogenerated in the conjugated polymer. These free electrons undergo a ballistic motion through the nanotube surface along the nanotube axes under a built-in electric potential. Compared with randomly blended nanotube/polymer material, electron transportation and collection are expected to be faster because of the directional confinement of electron transportation in aligned nanotubes. These electrons, arriving at the interface between the aligned nanotubes and the semiconductor film, are captured by the Schottky barrier structure. Only those electrons with energy

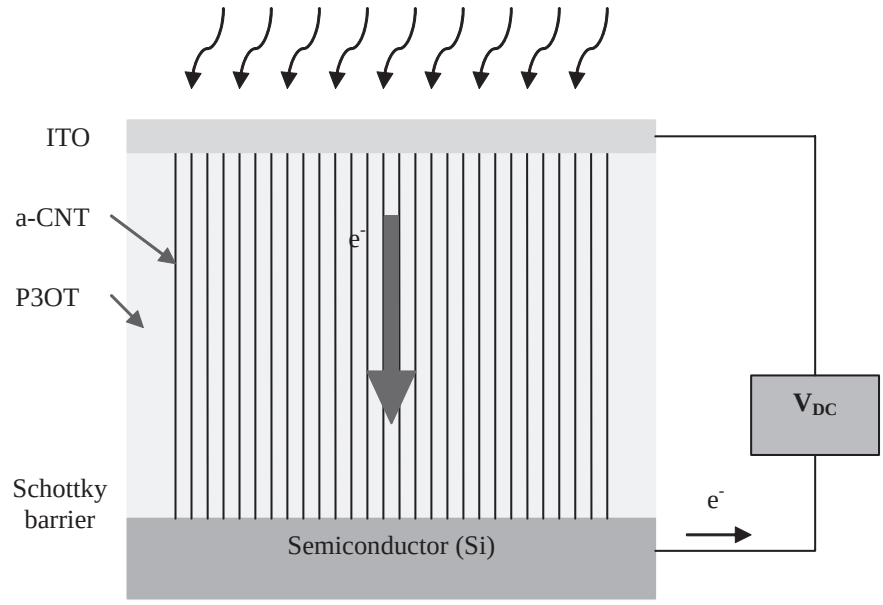

Figure 5. A schematic diagram of a carbon-nanotube-based photovoltaic cell

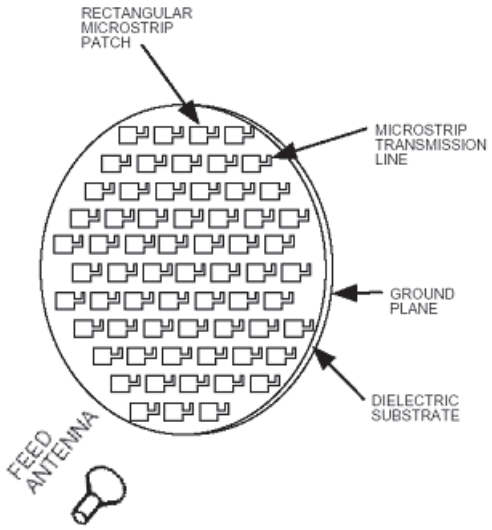

Figure 6. A planar reflectarray antenna with microstrip patch elements [21]

high enough to overcome the Schottky barrier will contribute to the photo-induced current. A bias voltage applied on the Schottky diode could adjust the height of the Schottky barrier, and hence control the photo-induced current.

The carbon-nanotubes photovoltaic solar cells can be built into ultra-thin-film structures that are flexible and conformable. The high energy-conversion efficiency could significantly decrease the area of the solar cell. Fabrication of such a device is presently ongoing.

3. Development of a Steerable Reflectarray Antenna for Wireless Power Transmission

Wireless power transmission (WPT) from SSP uses microwaves for transmitting energy. Due to operational safety requirements and for conserving energy, these transmission systems must be capable of directing their beam of energy towards a predefined set of receiver stations, be it on Earth or on another aerospace platform. Additionally, there may be a requirement to switch or steer these beams among a set of such receptor units to meet the diurnal variation in demand, requiring the use of reconfigurable beam antennas. One of the possibilities is to use a phased-array antenna as the transmitter.

A phased-array antenna often has a large number of elements that are individually fed using an extensive feed network. The antenna elements are generally arranged as a planar array. To incorporate beam-steering capability, the feed line for each antenna element has a phase shifter, which is often based on ferrite, pin diode, or GaAs MMIC technology. To realize large gain, a very many antenna elements and as many phase shifters are required. Accurate control of phase in all elements is necessary for the proper operation of a phased-array antenna.

An alternative approach is to use a steerable reflectarray antenna [21-24]. This eliminates the use of the large number of phase shifters and other components required in the feed network of the radiating antenna. Instead, the phase shifters used here are attached to elements in the reflecting surface. The primary radiator antenna can have a common single feed, or a set of feeds with or without a switching mechanism for the first level of beam control. The reflector in this configuration consists of a passive array of patch elements that are individually terminated with phase shifters. The antenna system may be visualized as one in which the effectively continuous surface of a reflector antenna is replaced with an array of passive elements. The reflecting elements are often arranged in the form of a two-dimensional array. These elements are made identically, so as to have a unique resonance characteristic for the antenna.

Inflatable reflectarray antennas have already been developed by NASA for space applications. Various microstrip-patch elements can form the reflectarray. Proper impedance matching of these elements is an important

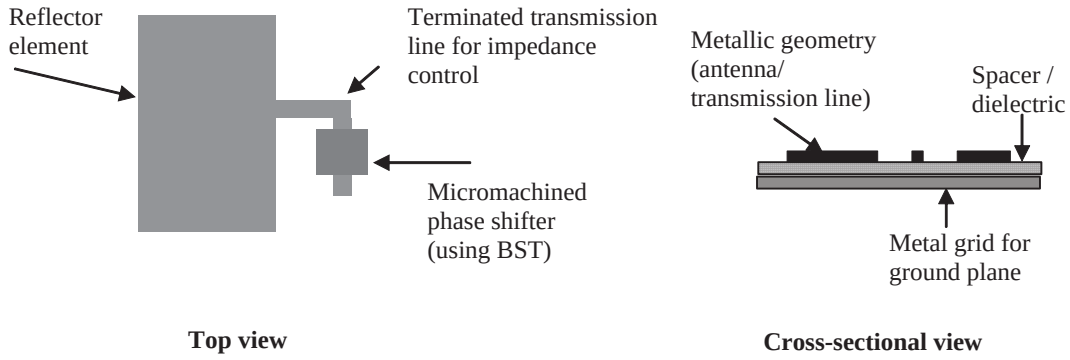

Figure 7. The elements in a planar reflectarray antenna.

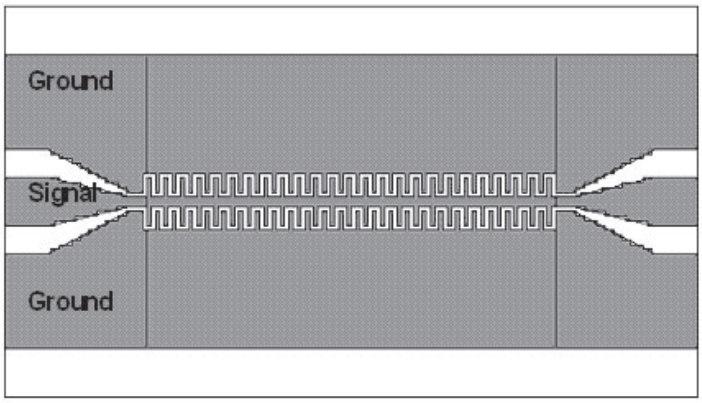

Figure 8a. A top view of a bilateral interdigital phase shifter

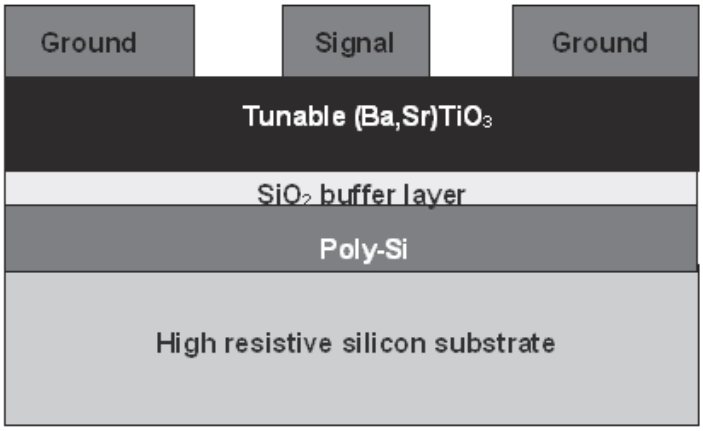

Figure 8b. A cross section of a bilateral interdigital phase shifter.

design step [21, 22]. The schematic of such an antenna is shown in Figure 6. There is a small feed line attached to each of these elements for impedance matching and phase control (Figure 7). The surface-impedance profile can be tailored by properly designing the elements and their terminations. In the following section, we describe the development of micromachined phase shifters for controlling the terminating reactances of these patches.

3.1 Phase Shifter Design

It has been established that the $Ba_xSr_{1-x}TiO_3$ series ferroelectric materials are well suited for the microwave phase shifters [25, 26]. These are nonlinear dielectric materials, where the application of a bias electric field can significantly alter the dielectric constant of the material. This property is known as the dielectric tunability. The dielectric tunability of these materials can be above 50%, depending on the stoichiometric composition and the applied bias field. This class of materials has the additional advantage that a wide range of dielectric values can be obtained by suitably choosing their composition [27].

Highly tunable barium strontium titanate thin films with low losses and low voltage requirements have recently been investigated for the development of phase shifters using various configurations of microstrip line and coplanar waveguide. The development of this technology has been primarily driven by the thrust towards the relatively new area of RF-MEMS devices [28].

The design of a coplanar waveguide (CPW) type of phase shifter is described here, due to its ease of integration with high-frequency circuits and low manufacturing cost. The use of a coplanar waveguide configuration enables a low operating voltage, without being affected by process limitations such as film stress and thickness [29]. The layout and cross-sectional view of a BI-CPW (bilateral interdigital coplanar waveguide) phase shifter are shown in Figure 8. Interdigital fingers on both sides of the signal line give a higher filling factor and effective dielectric constant than a regular coplanar waveguide structure.

Poly-Si, which acts as electrodes under the dielectric, can cause high electric fields in barium strontium titanate when a biasing voltage is applied to the stacked metal-dielectric-polysilicon structure. Undoped poly-Si behaves as a conducting electrode at low frequencies, and as a dielectric layer at high frequencies, due to the relaxation characteristics of its trapping sites. The capacitance of bilateral interdigital coplanar waveguide on two dielectric layers can be calculated by the conformal mapping method [30, 31]. It can then be used to obtain a closed-form analytical expression for the effective dielectric constant and characteristic impedance.

3.2 Fabrication

High resistivity ($> 5000\,\Omega$-cm) n-type silicon was used as the low-loss substrate. Fabrication was started with SC1 and SC2 cleaning, to remove surface contamination and native oxide. Amorphous silicon, 1μm, was deposited by a LPCVD process and annealed at 950° C. Oxidation was carried out to grow a thin oxide of 400 nm, which suppressed formation of an interfacial silicide layer by Ti and Si diffusion during the high-temperature process [32].

After oxidation, $BaSrTiO_3$ films were directly deposited by reactive RF sputtering. During the process, the samples were preheated for one hour in the sputtering chamber. To get a well-aligned barium strontium titanate thin film, the temperature, gas mixture, and sample distance were optimized. A polycrystalline barium strontium titanate film of 3500 Å could be deposited in 10 mTorr pressure, 10% oxygen gas, and 120 W RF power at 700° C. After RF sputtering, the films were post-annealed at 700° C in excess oxygen gas for one hour, and cooled down in the sputtering chamber. To avoid damage to the barium strontium titanate surface during the etching process, metal patterning was done by a liftoff process.

The phase shift obtained in a coplanar structure is related mainly to the dielectric tunability, permittivity, and film thickness of barium strontium titanate. Although the interfacial layer has little effect on these, the interfacial reaction has to be suppressed to avoid possible dielectric loss and leakage behavior. A thin SiO2 layer, thermally grown by dry oxidation, was chosen as a diffusion barrier.

3.3 Measurements and Discussion of Results

The preliminary characterization of the thin films was done by X-ray diffraction (XRD) and scanning electron microscopy (SEM). The electrical characteristics of the barium strontium titanate film was conveniently characterized by capacitance characterization of a MIM (metal-insulator-metal) configuration, using an impedance analyzer at low frequencies. The dielectric permittivity showed 30% tunability at 25 V.

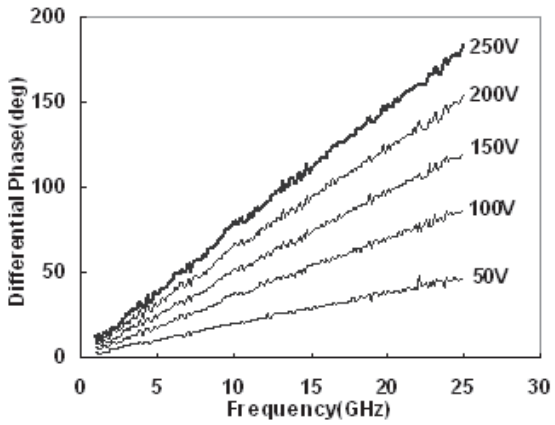

Figure 9. The differential phase shift of a bilateral interdigital coplanar waveguide (BI-CPW) phase shifter.

Phase shifters were characterized using a HP8510C network analyzer and Cascade microprobe station. A biasing network was connected between the network analyzer and input. Transmission and reflection loss measurements were made over a frequency range from 1 GHz to 26 GHz at room temperature. A dc bias voltage up to 250 V was applied between ground and the signal line of the coplanar waveguide. An on-wafer calibration standard was used for SOLT calibration. Since the primary capacitance contribution was due to the fringing field between two planar electrodes, the operating voltage of the present coplanar waveguide phase shifter was rather high.

The differential phase shift (with respect to the insertion phase at zero bias) increased continuously with applied voltage, as shown in Figure 9. The present prototype showed

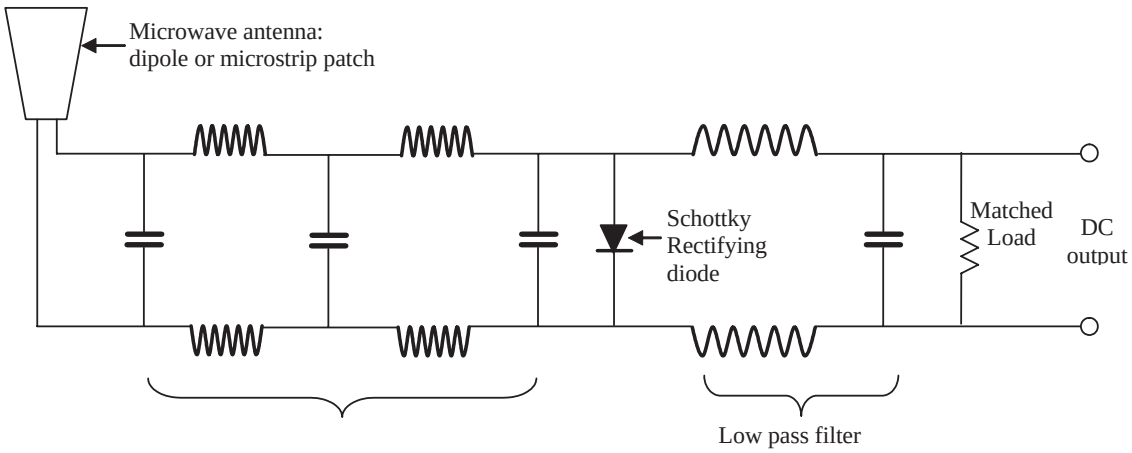

Figure 10. Electronic circuits associated with each rectenna element

a variation up to 180° at 25 GHz for 250 V. As the high operational voltage was attributed to the voltage drop by the barrier SiO_2 layer on polysilicon, this could be reduced if the oxide thickness was optimized. It may be noted that in the reflectarray configuration, it is the reflection phase that is more significant than the transmission in the device.

Furthermore, the currently proposed frequency of operation of a wireless power transmission (WPT) system is much lower. The present device shows a phase shift of about 45° at 5.85 GHz for a device area of 8 mm2. Hence, a further optimization of the design is required to obtain satisfactory performance for wireless power transmission systems. However, the results presented here indicate that micromachined RF phase shifters have a great potential for realizing such steerable reflectarray antennas for wireless power transmission using microwaves.

The proposed design of barium strontium titanate phase shifters has approximately 0.8 dB insertion loss at 5.8 GHz. The dc current leakage is of the order of 100 pA for operation up to 100 V. These values are comparable with GaAs MMIC phase shifters, which are currently used for phased-array antennas. Barium strontium titanate phase shifters have cost advantages over GaAs MMIC phase shifters for reflectarray applications.

The unavailability of heat dissipation by convection in space poses a serious problem of increasing device temperature. Achieving low insertion loss and small current-leakage levels in barium strontium titanate phase shifters by improving the design is still being investigated to meet the specification of power loss and heat generation issues required for the SSP system operation. In addition to such modifications, high-temperature superconducting materials for electrodes [33] are also being considered to reduce heat generation.

4. LSI Components for Rectenna System

While a steerable reflector antenna offers a possibility as the transmitting antenna for wireless power transmission (WPT), rectennas, consisting of rectifier circuits and antennas, can operate as the receiving stations that convert microwave energy into dc. The word "rectenna" was first used by Brown in the 1960s [34] for such a system, which consists of an antenna, an input filter, and a rectifying circuit (a balanced bridge or a single diode) with an output filter and a matched resistive load (Figure 10) [35]. Typically, dipoles or microstrip-patch antennas are used for the antenna for the rectenna. The dc outputs from individual rectenna elements are combined electrically to supply sufficient power.

In addition to 2.45 GHz, the next higher Industrial, Scientific, and Medical (ISM) band, centered at 5.8 GHz, has also been investigated for wireless power transmission, to decrease the aperture sizes without sacrificing component efficiency. This frequency is advantageous for wireless power transmission due to smaller component sizes and a greater transmission range, compared to 2.45 GHz [36]. The first C-band rectenna was demonstrated in 1992, with an overall efficiency of 70% [37].

While the total power handling capability in a typical SSP system is in the GW range, individual rectenna elements collect power in miniscule amounts. It may be recalled that a prohibitively large number of such elements is required at a station. In order to reduce the production cost of such numerous, identical components, their fabrication by large-scale integration (LSI) has been suggested [38]. While the technologies for semiconductor components, such as diodes, are well established, several approaches for fabricating

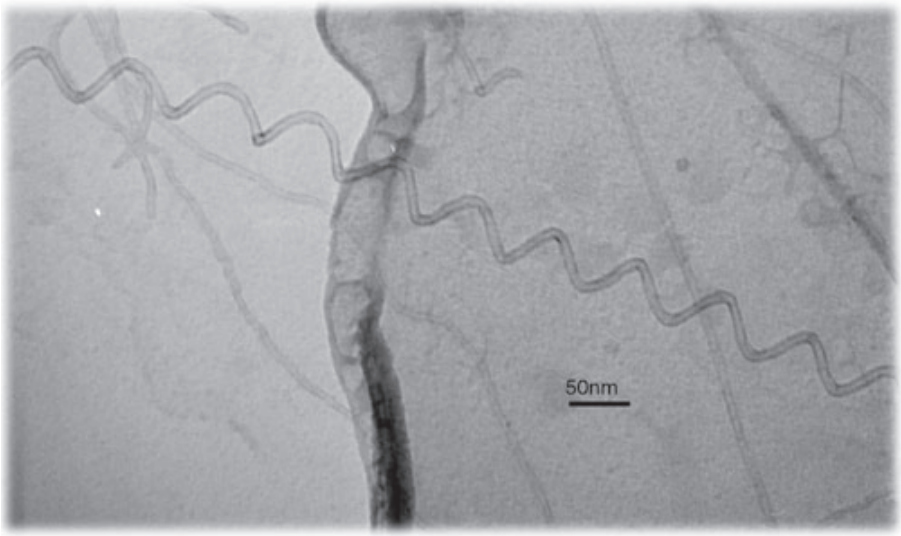

Figure 11. A transmission electron microscope (TEM) image of a nanocoil.

passive components, such as inductors, are being pursued. MEMS and micromachining offer one such possibility [28]. However, conventional inductive components are inherently three-dimensional in nature, and the implementation of these components in a planar shape is quite challenging using MEMS. Also, the inductors thus fabricated generally have a limited quality factor. An alternate approach is to use coiled carbon nanotubes, due to their small size, light weight, and low power consumption.

Fabricated coiled carbon nanotubes have physical parameters (tube diameter ~10-20 nm, coil diameter ~40-50 nm, coil pitch ~60-100 nm) small enough for LSI. In such a device, the coiled nanotube will act as inductive elements. It may be recalled that the electrical conductivity of such nanotubes can be tailored by changing process conditions. The synthesis of these coiled carbon nanotubes is quite similar to the process described in Section 2.1. Reaction conditions are appropriately modified to increase the yield of this type of nanotubes. An image of such a coiled nanotube, obtained by a transmission electron microscope, is shown in Figure 11.

The fabrication of passive components, such as resistors, capacitors, and inductors, often limits the overall size of any electric circuit. Typically, IC-compatible micromachining techniques are employed for the fabrication of such components. The use of coiled carbon nanotubes is an alternative approach for the integration of such components. Due to the micro-scale sizes, their RF characteristics can only be evaluated after fabricating an entire device and, hence, this has not yet been done. However, it is expected that the diameter and pitch of these coiled nanotubes can be tailored by optimizing the reaction conditions to obtain high-performance components at the operational frequencies of wireless power transmission.

5. Summary

This paper introduced three possibilities for improving the overall efficiency of space solar power (SSP) systems. The first was to utilize the distinctive properties of carbon nanotubes to improve the efficiencies of solar panels. Composites of aligned carbon nanotubes with conjugate polymers on a semiconducting substrate can utilize several novel features of carbon nanotubes. We expect that the device will have improved efficiency due to the exceptional electron ballistic transport properties in nanotubes. Coiled carbon may also be used to realize large-scale-integration (LSI) components, such as inductors, for resonant circuits in the receiver stations that convert microwave power to dc.

We have proposed the use of steerable reflectarray antennas as a means of dynamic allocation of wireless power transmission, providing additional flexibility in energy management. These antennas may use RF phase shifters as their termination to control the impedance of the reflecting surface. Such phase shifters, using barium strontium titanate thin films, are fabricated by micromachining techniques. Fabrication modifications for improving the phase of the transmission/reflection (reactance) of these devices were also suggested.

6. Acknowledgements

The authors gratefully acknowledge invigorating discussions and useful suggestions by Dr. Sang K. Choi at the NASA Langley research Center.

7. References

1. F. R. Shapiro, "Utilities in the sky?: Comparison of Space-Based and Terrestrial Solar Power Systems," *Refocus*, **2002**, 11-12, 2002, pp. 54-57.

2. J. C. Mankins, "A Fresh Look at Space Solar Power: New Architectures, Concepts and Technologies," 48th Congress of the International Astronautical Federation, Turin, Italy, October 6-10, 1997, paper IAF-97-R.2.03.

3. M. A. Green, K. Emery, D. L. King, S. Igari, and W. Warta, "Solar Cell Efficiency Tables (Version 21)," *Progress in Photovoltaics: Research and Applications*, **11**, 1, January 2003, pp. 39-45.

4. J. Zhao, A. Wang, M. Green, and F. Ferrazza, "Novel 19.8% Efficient Honeycomb Textured Multicrystalline and 24.4% Monocrystalline Silicon Solar Cell," *Appl. Phys. Letters*, **73**, 1998, pp. 1991-1993.

5. "A Constellation of Orbital Power:", http://www.spacedaily.com/news/ssp-01b.html, http://www.spacedaily.com/news/solarcell-03c.html

6. R. W. Lemke, T. C. Genoni, and T. A. Spencer, "Effects that Limit Efficiency in Relativistic Magnetrons," *IEEE Transactions on Plasma Science*, **28**, June 2000, pp. 887-897.

7. J. Huang, "The Development of Inflatable Array Antennas," *IEEE Antennas and Propagation Magazine*, **43**, 4, August 2001, pp. 44-50.

8. L. W. Epp, A. R. Khan, H. K. Smith, and R. P. Smith, "A Compact Dual-Polarized 8.51 GHz Rectenna FR High Voltage (50V) Actuator Applications," *IEEE Transactions on Microwave Theory and Techniques*, **MTT-48**, 2000, pp. 111-120.

9. J. O. McSpadden and J. C. Mankins, "Space Solar Power Programs and Microwave Wireless Power Transmission Technology," *IEEE Microwave Magazine*, **3**, 4, December 2002, pp. 44-57.

10. J. O. McSpadden, L. Fan, and K. Chang, "Design and Experiments of a High-Conversion-Efficiency 5.8-GHz Rectenna," *IEEE Transactions on Microwave Theory and Techniques*, **MTT-46**, 12, 1, December 1998, pp. 2053-2060.

11. E. Kymakis and G. A. J. Amaratunga, "Single-Wall Carbon Nanotube/Conjugated Polymer Photovoltaic Devices," *Applied Physics Letters*, **80**, 1, 2002, pp. 112-114.

12. G. Yu and A. J. Heeger, "Charge Separation and Photovoltaic Conversion in Polymer Composites with Internal Donor/Acceptor Heterojunctions," *J. Appl. Phys.*, **178**, 1995, pp. 4510-4515.

13. V. K. Varadan, R. D. Hollinger, V. V. Varadan, J. Xie, and P. K. Sharma, "Development and Characterization of Micro-Coil Carbon Fibers by a Microwave CVD System," *Smart Materials and Structures*, **9**, 2000, pp. 413-420.

14. V. K. Varadan and J. Xie, "Large-Scale Synthesis of Multi-Walled Carbon Nanotubes by Microwave CVD," *Smart Materials and Structures*, 11, 2002, pp. 610-616.

15. V. K. Varadan and J. Xie, "Synthesis of Carbon Nanocoils by Microwave CVD," *Smart Materials and Structures*, **11**, 2002, pp. 728-734.

16. J. W. G. Wildöer, L. C. Venema, A. G. Rinzler, R. E. Smalley, and C. Dekker, "Electronic Structure of Atomically Resolved Carbon Nanotubes," *Nature*, **391**, 1998, pp. 59-62.

17. C. T. White and T. N. Todorov, "Nanotubes Go Ballistic," *Nature*, **411**, 2001, pp. 649-650.

18. P. G. Collins, M. S. Arnold, and P. Avouris, "Engineering Carbon Nanotubes and Nanotube Circuits Using Electrical Breakdown," *Science*, **292**, 2001, pp. 706-709.

19. E. Kymakis, I. Alexandrou, and G. A. J. Amaratunga, "High Open-Circuit Voltage Photovoltaic Devices from Carbon-Nanotube-Polymer Composites," *J. Applied Physics*, **93**, 2003, pp. 1764-1768.

20. J. Huang, "Analysis of a Microstrip Reflectarray Antenna for Microspacecraft Applications," NASA TDA Report 42-120, February 15, 1995., (http://tmo.jpl.nasa.gov/tmo/progress_report/42-120/120H.pdf)

21. D. G. Berry, R. G. Malech, and W. A. Kennedy, "The Reflectarray Antenna," *IEEE Transactions on Antennas and Propagation*, **AP-11**, November 1963, pp. 645-651.

22. http://ctd.grc.nasa.gov/5640/Tutorials.html

23. D. Sievenpiper, J. Schaffner, R. Loo, G. Tangonan, S. Ontiveros, and R. Harold, "A Tunable Impedance Surface Performing as a Reconfigurable Beam Steering Reflector," *IEEE Transactions on Antennas and Propagation*, **AP-50**, 2002, pp. 384-390.

24. V. K. Varadan, F. Selmi, and V. V. Varadan, "Voltage Tunable Dielectric Ceramics Which Exhibit Low Dielectric Constants and Applications Thereof to Antenna Structures," US Patent No. 5,557,286, 1996.

25. V. K. Varadan, D. K. Ghodgaonkar, V. V. Varadan, J. F. Kelly, and O. Gilkerdas, "Ceramic Phase Shifters for Electronically Steerable Antenna Systems," *Microwave J.*, **35**, 1992, pp. 116-127.

26. S. B. Herneti, F. A. Selmi, V.V. Varadan, and V. K. Varadan, "Effect of Various Dopants on the Dielectric Properties of Barium Strontium Titanate," *Materials Lett.*, **15**, 1993, pp. 317-324.

27. V. K. Varadan, K. J. Vinoy, and K. A. Jose, *RF MEMS and Their Applications*, London, John Wiley, 2002.

28. H.-T. Lue, T.-Y. Tseng, and Q.-W. Huang, "A Method to Characterize the Dielectric and Interficial Properties of Metal-Insulator-Semiconductor Structures by Microwave Measurement," *J. Appl. Phys.*, **91**, 2002, pp. 5275-5282.

29. S. S. Gevorgian and T. Martinsson, "CAD Models for Multilayered Substrate Interdigital Capacitors," *IEEE Transactions on Microwave Theory and Techniques*, **MTT-44**, June 1996, pp. 896-904.

30. H. Yoon, K. J. Vinoy, and V. K. Varadan, "Design and Development of Micromachined Bilateral Interdigital Coplanar Waveguide RF Phase Shifter Compatible with LDMOS Voltage Controller on Silicon," *Smart Mater. Struct.*, **12**, 2003, pp. 769-775.

31. Y. Gao, A. H. Mueller, E. A. Irene, O. Auciello, and A. Krauss, "In Situ Study of Interface Reactions of Ion Beam Sputter Deposited $(Ba_{0.5}Sr_{0.5})TiO_3$ Films on Si, SiO_2, and Ir" *J. Vac. Sci. Technol.*, **A17**, 4, 1999, pp. 1880-1886.

32. F. W. Van Keuls, R. R. Romanofsky, D. Y. Bohman, M. D. Winters, F. A. Miranda, C. H. Mueller, R. E. Treece, T. V. Rivkin, and D. Galt, "(YBa2Cu3O7-2d,Au)/SrTiO3/LaAlO3 Thin Film Conductor/ Ferroelectric Coupled Microstripline Phase Shifters for Phased Array Applications" *Appl. Phys. Lett.*, **71**, 1997, pp. 3075-3077.

33. W. C. Brown, "The History of Power Transmission by Radio Waves," *IEEE Transactions on Microwave Theory and Techniques*, **MTT-32**, 1984, pp. 1230-1242.

34. S. H. Choi, K. D. Song, G. C. Glen, and C. Woodall, "Rectenna Performances for Smart Membrane Actuators," *Proceedings of the SPIE Conference on Smart Electronics & MEMS*, March 18-21, 2002, *SPIE Proceedings*, **4700**, pp. 213-221.

35. J. O. McSpadden, L. Fan, and K. Chang; "Design and Experiments of a High-Conversion-Efficiency 5.8-GHz Rectenna," *IEEE Transactions on Microwave Theory and Techniques*, **MTT-46**, 1998, pp. 2053-2060.

36. S. S. Bharj, R. Camisa, S. Grober, F. Wozniak, and E. Pendleton, "High Efficiency C-Band 1000 Element Rectenna Array for Microwave Powered Applications," *IEEE MTT-S Int. Microwave Symp. Dig.*, Albuquerque, NM, June 1992, pp. 301-303.

37. S. H. Choi, private communication.

OFDM Transmission Technique: A Strong Candidate for Next-Generation Mobile Communications

H. Rohling
D. Galda

Abstract

The orthogonal frequency-division multiplexing (OFDM) transmission technique is used for some broadcast applications (DVB-T, DAB, DRM) and for wireless local loop (WLL) standards (HIPERLAN/2, IEEE 802.11a). However, OFDM has not been used so far in cellular communication networks. The system flexibility and the use of subcarrier-specific adaptive modulation schemes in frequency-selective radio channels are some advantages that make the OFDM transmission technique a strong and technically attractive candidate for the next generation of mobile communications. The general idea of OFDM is to split the total bandwidth into many narrowband sub-channels that are equidistantly distributed on the frequency axis. The sub-channel spectra overlap each other, but the subcarriers are orthogonal and can therefore be separated in the receiver.

OFDM can efficiently deal with the interference effects of multipath propagation situations in broadband radio channels. Consequently, the OFDM receiver can also deal with superimposed signals that have been transmitted by several distinct and adjacent base stations (BSs) in a cellular environment. This is the basis for setting up a cellular single-frequency network (SFN), in which all adjacent base stations operate simultaneously in the same frequency band, which leads to a reuse factor of one.

The objective of this paper is to describe an OFDM-based system concept, and to discuss all technical details for establishing a cellular single-frequency network, which requires synchronization in time and frequency with sufficient accuracy. In the cellular environment, a flexible frequency-division multiple-access scheme, based on OFDM-FDMA, is developed, and radio-resource management (RRM) employing dynamic channel allocation (DCA) techniques is used. A purely decentralized and self-organized synchronization technique, based on specific test signals, and radio-resource management techniques, based on co-channel interference (CCI) measurements, are developed.

1. Introduction

In the evolution of mobile communication systems, a periodicity of approximately 10 years can be observed between consecutive system generations. Research work for the current second generation of mobile communication systems (GSM) started in Europe in the early 1980s, and the system was ready for market in 1990. At that time, the first research activities had already been started for the third generation of mobile communication systems (UMTS, IMT-2000), and the transition from the current second-generation (GSM) to the new third-generation (3G) systems will be observed this year. Compared to today's GSM networks, these new UMTS systems will provide higher data rates, typically in the range of 64 to 384 kbps, while the peak data rate for low mobility or indoor applications will be 2 Mbps.

The current pace that can be observed in the mobile communications market already shows that the 3G systems will not be the ultimate system solution. Consequently, general requirements for a 4G system have to be considered, which will mainly be derived from the types of service a user will require in the future. Generally, it is expected that data services – instead of pure voice services – will play a predominant role, in particular due to a demand for mobile IP (Internet protocol) applications. Variable and especially high data rates (20 Mbps and more) will be requested, which should also be available at high mobility in general, or high vehicle speeds in particular (see Figure 1). Moreover, data services that are asymmetrical between the up- and downlink are assumed, and should be supported by 4G systems in such a scenario where the downlink carries most of the traffic and needs the higher data rate compared with the uplink.

Hermann Rohling and Dirk Galda are with the Department of Telecommunications, Technical University Hamburg-Harburg, Eißendorfer Straße 40, 21073 Hamburg, Germany; E-mail: rohling@tu-harburg.de; http://www.et2.tu-harburg.de.

This is one of the invited *Reviews of Radio Science*, from Commission C.

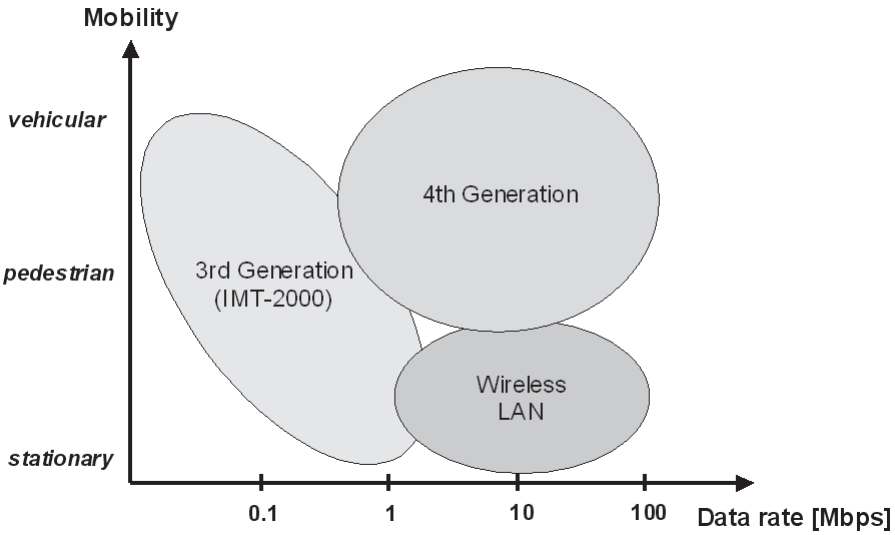

Figure 1. General Requirements for 4th generation mobile communication systems.

To fulfill all these detailed system requirements, the orthogonal frequency-division multiplexing (OFDM) transmission technique, applied in a wideband radio channel, is a strong candidate for an air interface in future 4G systems, due to its flexibility and adaptability in the technical system design. From the above considerations, it already becomes apparent that a radio transmission system for 4G must provide great flexibility and adaptability at different levels, ranging from the highest layer (the requirements of the application) to the lowest layer (the transmission medium, the physical layer, i.e., the radio channel) in the ISO-OSI [International Standards Organization open systems interconnection] stack. Today, the OFDM transmission technique is in a completely matured stage for application to wideband communication systems integrated into a cellular mobile communications environment.

2. Radio Channel Behavior

The mobile communication system design is always dominated by the radio channel's behavior [1, 2]. In typical radio channels, multipath propagation occurs due to the reflections of the transmitted signal at several objects and obstacles. The various propagation paths are technically characterized by different delays and individual Doppler frequencies, which lead to a frequency-selective and time-variant behavior of the radio channel. This is described by the time-variant radio-channel transfer function, $H(f,t)$, as shown in Figure 2.

Future mobile communication systems require extremely large data rates. If conventional single-carrier

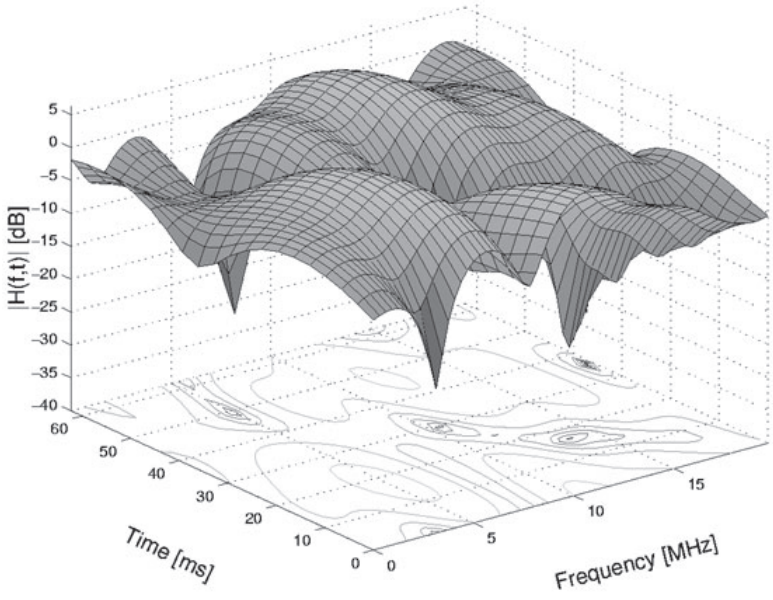

Figure 2. The frequency-selective and time-varying transfer function of the mobile radio channel.

(SC) modulation schemes are applied in a multipath propagation situation, strong inter-symbol interference (ISI) is caused in wideband applications. This situation has to be taken into consideration in the development phase for a new radio transmission system and for a new 4G air interface. The measures that have to be taken depend on the data rate to be transmitted or, equivalently, on the system bandwidth that must be processed by the air interface. The computational complexity for the necessary equalizer techniques increases for a given radio channel with increasing bandwidth and can be very large, especially in wideband systems.

For high-data-rate applications, the symbol duration in a classical single-carrier transmission system is extremely small compared to the typical values of maximum delay in the radio channels considered. In this case, strong inter-symbol interference will occur in each receiver due to the multipath propagation situation. Therefore, an equalization procedure, which needs high computational complexity in a wideband system, must be integrated into each receiver. These general assumptions about the frequency-selective and time-variant radio-channel behavior strongly motivate an alternative transmission technique with less computational complexity but high performance figures for the 4G system.

3. Advantages of the OFDM Transmission Technique

If a high data rate is transmitted over a frequency-selective radio channel with a large maximum multipath propagation delay compared to the symbol duration, an alternative to the classical single-carrier approach is given by the OFDM transmission technique. The general idea of the OFDM transmission technique is to split the total available bandwidth, B, into many narrowband sub-channels at equidistant frequencies. The sub-channel spectra overlap each other, but the sub-carrier signals are orthogonal. The single high-rate-data stream is divided into many low-rate data streams in the several sub-channels, which are transmitted in parallel. Each sub-channel is modulated individually, and will be transmitted simultaneously in a superimposed form.

An OFDM transmitted signal therefore consists of N adjacent and orthogonal sub-carriers, spaced by the frequency distance. All sub-carrier signals are mutually orthogonal within the large symbol duration, of length T_S, if the sub-carrier distance and the symbol duration are chosen such that $T_S = 1/\Delta f$. The kth unmodulated sub-carrier signal is described analytically by an exponential function with carrier frequency $k\Delta f$, $\tilde{g}_k(t), k = 0,\ldots,N-1$.

$$\tilde{g}_k(t) = \begin{cases} e^{j2\pi k\Delta f t} & \forall t \in [0, T_S] \\ 0 & \forall t \notin [0, T_S] \end{cases}. \qquad (1)$$

Since the system bandwidth, B, is subdivided into N narrowband sub-channels, the OFDM symbol duration, T_S, is N times as large as in the case of an alternative single-carrier transmission system covering the same bandwidth, B. Typically, for a given system bandwidth, the number of sub-carriers is chosen in a way that the symbol duration, T_S, is sufficiently large compared to the maximum multipath delay of the radio channel. On the other hand, in a time-variant radio channel, the Doppler spread imposes restrictions on the subcarrier spacing, Δf. In order to keep the resulting inter-carrier interference (ICI) at a tolerable level, Δf must be large enough compared to the maximum Doppler frequency, $f_{D,max}$. In [7], the appropriate range for choosing T_S in practical systems is given as

$$4\tau_{max} \le T_S \le 0.03 \frac{1}{f_{D,max}}. \qquad (2)$$

The duration of the sub-carrier signal $\tilde{g}_k(t)$ is additionally extended by a cyclic prefix (the so-called guard interval) of length T_G, in order to completely avoid inter-symbol interference completely, which could occur in multipath channels in the transition interval between two adjacent OFDM symbols [16]:

$$g_k(t) = \begin{cases} e^{j2\pi k\Delta f t} & \forall t \in [-T_G, T_S] \\ 0 & \forall t \notin [-T_G, T_S] \end{cases}. \qquad (3)$$

The guard interval is directly removed in the receiver after the time-synchronization procedure. From this point of view, the guard interval is a pure system overhead, and the total OFDM symbol duration is therefore $T = T_S + T_G$. It is an important advantage of the OFDM transmission technique that inter-symbol interference can be avoided completely, or can at least be considerably reduced by a proper choice of OFDM system parameters.

The orthogonality of all sub-carriers is completely preserved in the receiver, even in frequency-selective radio channels. The reason for this system behavior is given by the radio-channel model, which is based on linear time-invariant (LTI) system theory if only a short time interval of a few OFDM symbol lengths is considered. All complex exponential signals (e.g., all sub-carrier signals) are eigenfunctions of each linear time-invariant system, which means that only the signal amplitude and phase will be changed if a sub-carrier signal is transmitted in the radio channel. The sub-carrier frequency is not affected at all by the radio channel. Therefore, the radio channel changes the amplitudes and phases of all received sub-carrier signals individually, but all sub-carrier signals are still mutually orthogonal. Due to this property, the received signal can be split directly into the different sub-carrier components, and each sub-carrier signal can be individually demodulated in the receiver.

In the transmitter, each sub-carrier signal is modulated independently with the complex modulation symbol Sn,k, where the subscript n refers to the time interval, and k refers to the number of the sub-carrier signal in the OFDM symbol considered. Thus, within the symbol duration, T, the continuous-time signal of the nth OFDM symbol is formed by a superposition of all N simultaneously modulated sub-carrier signals:

$$s_n(t) = \frac{1}{\sqrt{N}} \sum_{k=0}^{N-1} S_{n,k} g_k (t - nT) . \qquad (4)$$

The total continuous-time transmitted signal, consisting of all OFDM symbols sequentially transmitted on the time axis, is described analytically by the following equation:

$$s(t) = \frac{1}{\sqrt{N}} \sum_{n=0}^{\infty} \sum_{k=0}^{N-1} S_{n,k} g_k (t - nT) . \qquad (5)$$

The analytical transmitted signal description shows that a rectangular pulse shaping is applied for each sub-carrier signal and each OFDM symbol. But due to the rectangular pulse shaping, the spectra of all the considered sub-carrier signals are sinc functions, equidistantly located on the frequency axis, e.g., for the kth sub-carrier signal, the spectrum is described in the following equation:

$$G_k(f) = T \sin c\left[\pi T (f - k\Delta f)\right],$$

where

$$\sin c(x) = \frac{\sin(x)}{x} . \qquad (6)$$

The spectra of the considered sub-carriers overlap on the frequency axis, but the sub-carrier signals are still mutually orthogonal, which means that the transmitted modulation symbols, $S_{n,k}$, can be recovered by a simple correlation technique in each receiver if the radio channel is assumed to be ideal:

$$\langle g_k, g_l \rangle = \int_0^{T_S} g_k(t) \overline{g_l(t)} dt = T_S \delta_{k,l} , \qquad 7)$$

$$S_{n,k} = \frac{\sqrt{N}}{T_S} \left\langle s_n(t), \overline{g_k(t - nT)} \right\rangle ,$$

where $\overline{g_k(t)}$ is the conjugate complex version of the sub-carrier signal, $g_k(t)$.

In practical applications, the OFDM transmitted signal, $s_n(t)$, is generated in a first step as a discrete-time signal in the digital-signal-processing part of the transmitter. Using the sampling theorem while considering the OFDM transmitted signal inside the bandwidth $B = N\Delta f$, the transmitted signal must be sampled with the sampling interval $\Delta t = 1/B = 1/N\Delta f$. The individual samples of the transmitted signal are denoted by $s_{n,i}$, $i = 0,1,\ldots,N-1$, and can be calculated as follows:

$$s_{n,i} = \frac{1}{\sqrt{N}} \sum_{k=0}^{N-1} S_{n,k} e^{j2\pi ik/N} . \qquad (8)$$

The above equation exactly describes the inverse discrete Fourier transform (IDFT), applied to the complex-valued modulation symbols, $S_{n,k}$, of all sub-carrier signals inside a single OFDM symbol. This Fourier transformation is typically implemented in real systems as an IFFT (inverse fast Fourier transform) to further reduce computational complexity.

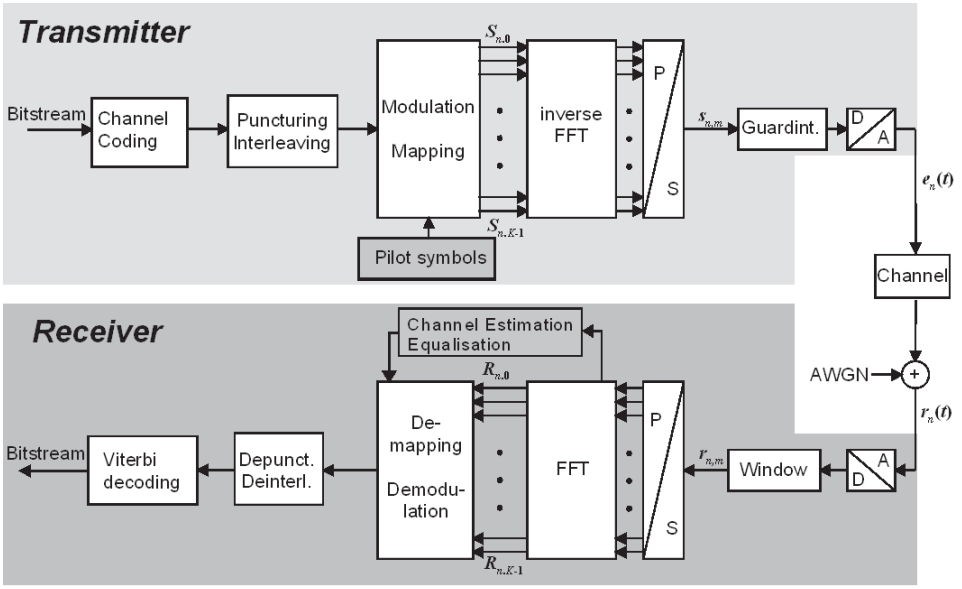

Figure 3. The OFDM system structure in a block diagram.

The individually modulated and superimposed signals are transmitted in a parallel way over many narrowband sub-channels. Thus, in each sub-channel the symbol duration is quite large, and can be chosen much larger compared to the maximum multipath delay of the radio channel. In this case, each sub-channel has the property of being frequency nonselective. Figure 3 shows the general OFDM system structure in a block diagram.

The basic principles of the OFDM transmission technique have already been described in several publications such as [1, 4]. In the very early and classical multi-carrier system considerations such as [5, 6], narrowband signals were generated independently, assigned to various frequency bands, transmitted, and separated by analog filters at the receiver. The new and modern aspect of the OFDM transmission technique is that the various sub-carrier signals are generated digitally and jointly by an inverse FFT in the receiver, and that their spectra overlap. As a result, generating the transmitted signal is simplified, and the bandwidth efficiency of the system is significantly improved.

It is assumed in this paper that the coherence time, T_C, is much larger compared to a single OFDM symbol duration, T, in a realistic time-varying radio channel. Therefore, the received continuous-time signal, $r_n(t)$, can be separated into the orthogonal sub-carrier signals even in frequency selective fading situations by applying a simple correlation technique:

$$R_{n,k} = \frac{\sqrt{N}}{T_S}\left\langle r_n(t), \overline{g_k(t-nT)}\right\rangle . \qquad (9)$$

Equivalently, the correlation process at the receiver side can be applied to the discrete-time received signal at the output of an A/D converter, and can be implemented as a discrete Fourier transform (DFT) or an FFT, respectively. This leads to the following equation:

$$R_{n,k} = \frac{1}{\sqrt{N}}\sum_{i=0}^{N-1} r_{n,i}e^{-j2\pi ik/N} . \qquad (10)$$

In this case, $r_{n,i}$ describes the ith sample of the received continuous-time baseband signal $r_n(t)$, and $R_{n,k}$ is the received complex-valued symbol at the FFT output of the kth sub-carrier. The correlation process can be implemented very efficiently using the FFT/IFFT algorithm.

If the OFDM symbol duration, T, is chosen much smaller than the coherence time, T_C, of the radio channel, then the time-varying transfer function of the radio channel, $H(f,t)$, can be considered constant within the time duration, T, of each modulation symbol, $S_{n,k}$, for all sub-carrier signals. In this case, the effect of the radio channel in multipath propagation situations can be described analytically by only a single multiplication of each sub-carrier signal, $g_k(t)$, with the complex transfer factor $H_{n,k} = H(k\Delta f, nT)$. As a result, the received complex-valued symbol $R_{n,k}$ at the FFT output can be described analytically as follows:

$$R_{n,k} = H_{n,k}S_{n,k} + N_{n,k}, \qquad (11)$$

where $N_{n,k}$ describes an additive noise component for each specific sub-carrier generated in the radio channel. This equation shows the most important advantage of applying the OFDM transmission technique in practical applications. The above equation describes the complete signal-transfer situation of the OFDM block diagram including the IFFT, the guard interval, D/A conversion, up- and down-conversion in the RF part, the frequency-selective radio channel, the A/D conversion and FFT process in the receiver, neglecting the non-ideal behavior of system components.

It should be pointed out that especially the frequency synchronization at the receiver must be very precise in order to avoid inter-carrier interference. In a single frequency network formed by multiple base stations, this also implies that the base stations must be precisely synchronized. Algorithms for time and frequency synchronization in OFDM systems are described in [8, 9], for example.

The trade-off between single-carrier and OFDM transmission techniques is depicted qualitatively in Figure 4 against the background of computational complexity only with respect to the considered data rate and radio-channel behavior. The OFDM transmission technique is especially of interest for radio channels with a maximum propagation delay that is much larger than the single-carrier symbol duration. This is almost always true for broadband data-transmission systems.

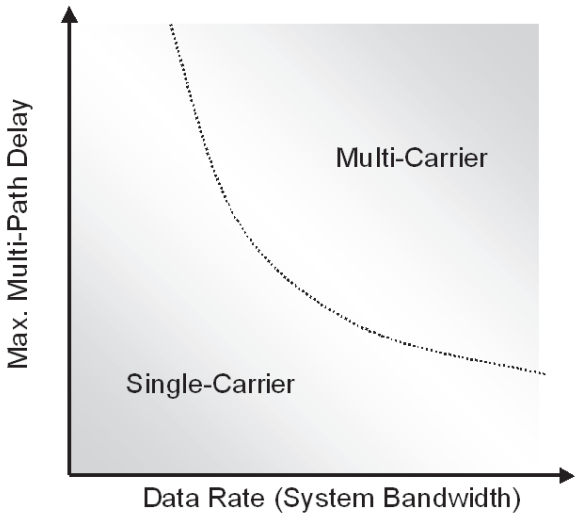

Figure 4. OFDM vs. single carrier transmission technique regarding the resulting computational complexity.

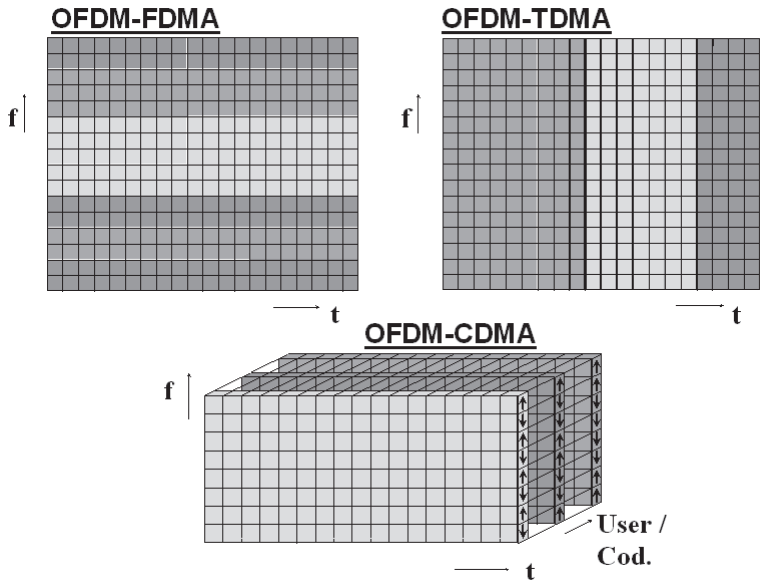

Figure 5. The OFDM transmission technique and some multiple-access schemes.

Besides the complexity aspects, another advantage of the OFDM techniques lies in their high degree of flexibility. Division of the available bandwidth into many frequency-nonselective subbands gives additional advantages for the OFDM transmission technique. It allows a subcarrier-specific adaptation of transmission parameters, such as modulation scheme (PHY modi) and transmitter power in accordance with the observed and measured radio-channel status. In a multi-user environment, the OFDM structure additionally offers an increased flexibility for resource-allocation procedures compared to single-carrier systems [17].

4. OFDM Transmission Technique Combined with Multiple-Access Schemes

Very high degrees of flexibility and adaptability are required for a 4G air interface. The combination between multiple-access schemes and the OFDM transmission technique is an important factor in this respect. In principle, multiple-access schemes for the OFDM transmission technique can be categorized according to OFDM-FDMA (OFDM frequency-division multiple access), OFDM-TDMA (OFDM time-division multiple access), and OFDM-CDMA (OFDM code-division multiple access) [10, 11]. Clearly, hybrid schemes can be applied that are based on a combination of the above techniques. The principles of these basic multiple-access schemes are summarized in Figure 5, where the time-frequency plane is depicted, and the user-specific resource allocation is distinguished by different colors.

These access schemes provide a great variety of possibilities for flexible user-specific resource allocation. In the following, one example for OFDM-FDMA (OFDM frequency-division multiple access) is briefly sketched (cf. [12]). In the case where the magnitude of the channel transfer function is known, the sub-carrier selection for an OFDM-FDMA scheme can be processed in the base station individually for each user. The system performance can be improved by allocating a subset of all sub-carriers with the highest SNR (signal-to-noise ratio) to each user. This allocation technique, based on the knowledge of the channel transfer function, shows a large performance advantage and a gain in quality of service (QoS). Nearly the same flexibility in resource allocation is possible in OFDM-CDMA systems. But in this case, the code orthogonality is destroyed by the frequency-selective radio channel, resulting in multiple-access interferences (MAI), which reduce the performance.

5. OFDM-Based Cellular Single-Frequency Network (SFN)

In current cellular radio networks, each base station assigns resources independently and exclusively to its users. To be able the use of a TDMA or FDMA multiple-access scheme in a cellular environment, offline radio-resource planning is required to avoid co-channel interference situations between adjacent cells. As a consequence, only a small fraction of the available resource determined by the spatial reuse is assigned to each cell, which can dynamically be accessed by its users. However, due to this fixed resource distribution among adjacent cells, a dynamic and flexible shift of resources between cells is technically difficult. Such a conventional cellular network with fixed frequency planning is shown in Figure 6 for a time-division duplex (TDD) system, as an example.

The limitations of fixed resource allocation can be overcome by introducing the OFDM transmission technique in such a cellular environment. Since the OFDM transmission technique is robust in multipath propagation situations, a single-frequency network (SFN) can be established. All

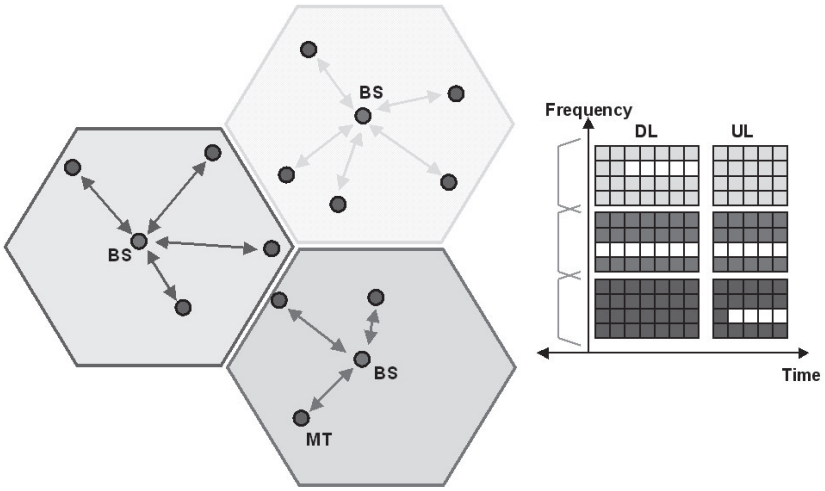

Figure 6. A conventional cellular network with fixed resource allocation.

base stations and mobile terminals are synchronized in this case, and the signals from adjacent base stations will be received with a mutual relative delay no longer than the guard interval. Under these single-frequency network conditions, each base station can use all available resources simultaneously. With this technique at hand – which has been intensively studied, e.g., for DVB-T broadcast systems – it is possible to add an additional "macro" diversity to a cellular environment by transmitting the same signal from synchronized base stations.

However, a single-frequency network applied in a cellular mobile communications environment does not require transmitting the same information on the same resources as in a broadcast application. It can also be used to implement a dynamic resource allocation scheme by assigning different sub-carriers of an OFDM-FDMA multiple-access scheme to users in adjacent cells. Since the OFDM sub-carriers remain orthogonal in an single-frequency network, no multiple-access interference between users will occur, even in adjacent.

In this case, all resources can be accessed by the mobile terminal inside a cellular network. A single-frequency network can be used to provide the needed flexibility inside a cellular environment for allocating system resources in those cells where this bandwidth is needed. If the flexibility of a single-frequency network is used, the system capacity can be greatly increased, especially for non-uniformly distributed users inside a cellular environment, or for hot-spot situations. The single-frequency network concept is shown in Figure 7 for an OFDM-FDMA and time-division duplex system as an example. In this case, the resource management could be based on co-channel interference (CCI) measurements.

6. Autonomous Cell Synchronization

The dynamic sharing of all available resources between adjacent cells requires tight time and frequency synchronization of all base stations and all mobile terminals inside the cellular environment. All mobile terminals are synchronized to a single base station using a specific test signal, which is transmitted in a downlink preamble. It is assumed in this paper that the required network synchronization is achieved without any assistance of a

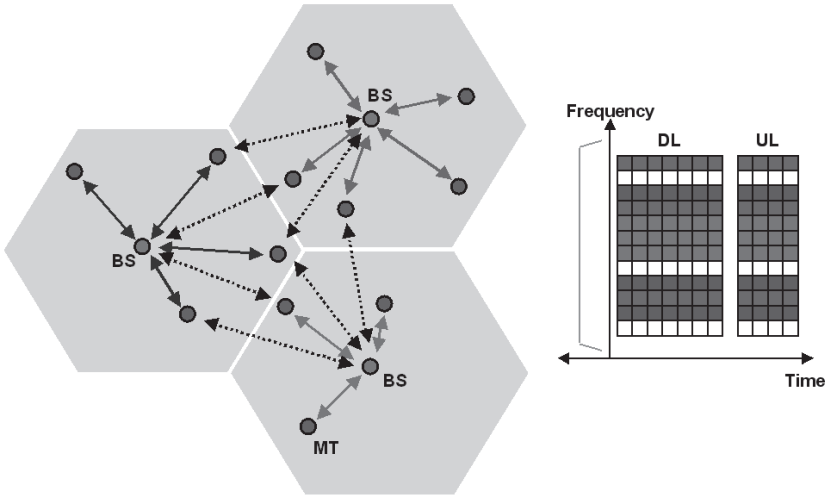

Figure 7. Flexible radio resource management by making all resources available to all cells in an single-frequency network OFDM-based cellular environment.

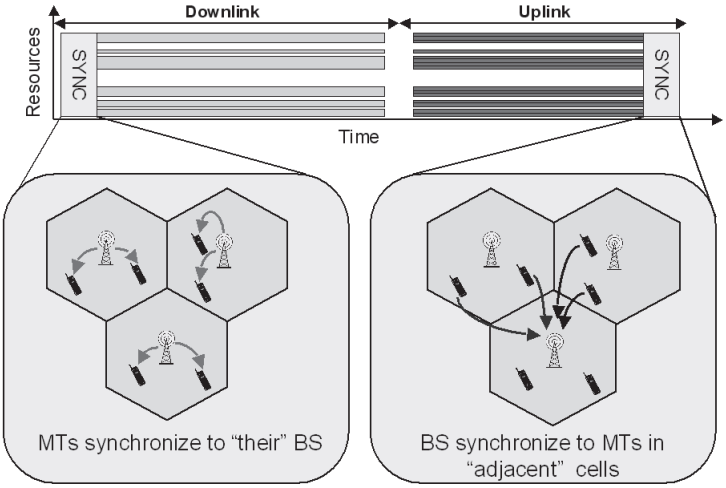

Figure 8. The test signal structure that is used for the synchronization of mobile terminals to a single base station during downlink, and of a base station to its adjacent cells during the uplink phase.

central controller, but in a totally decentralized and self-organized way. Furthermore, a time-division duplex system is assumed. Synchronization between adjacent base stations can be achieved not in a direct way, but indirectly, if all mobile terminals inside a single cell transmit a specific test signal at the end of each frame in an uplink postamble. These different test signals, transmitted from all mobile terminals in adjacent cells, will be received in all base stations inside a local environment. Each base station can process this information to synchronize clock and carrier simultaneously to establish a synchronized network.

Test signals will therefore be used in the down- and uplinks to synchronize all base stations in a local environment and all mobile terminals inside a single cell: see Figure 8. The test signal itself is designed to allow an almost interference-free time- and frequency-offset estimation.

To generate the test-signal structure, each base station selects a single pair of two adjacent sub-carriers for each frame inside the preamble, as is shown in Figure 9. The sub-carriers inside the test signal are chosen randomly and independently by each base station from a set of allowed sub-carrier pairs placed equidistantly in the frequency band, and separated by a guard band of unused sub-carriers to reduce interference in a non-synchronized situation. During the downlink preamble, each base station transmits the specific test signal on the individually selected pair of sub-carriers.

In the uplink, all mobile terminals inside a single cell transmit a test signal that is identical to the one they have received in the preamble at the beginning of the data frame. Each base station receives these test signals in a superimposed form from all mobile terminals inside the cell on the same sub-carrier pair. Test signals from mobile terminals in adjacent cells will be observed by the base station on distinct pairs of sub-carriers, and can therefore be distinguished and processed separately.

Each base station randomly selects the sub-carrier pair for the test signal in the preamble of each data frame. Therefore, data collisions between test signals of adjacent base stations will only rarely occur, but do not influence the synchronization process at all. All received test signals are evaluated in the frequency domain. as shown in Figure 10. The signal processing and test-signal evaluation are identical in the downlink and uplink. To avoid inter-symbol interference and inter-carrier interference during the fine synchronization procedure, the test signals are designed to be phase continuous for the duration of N_P consecutive OFDM symbols, as shown in Figure 10.

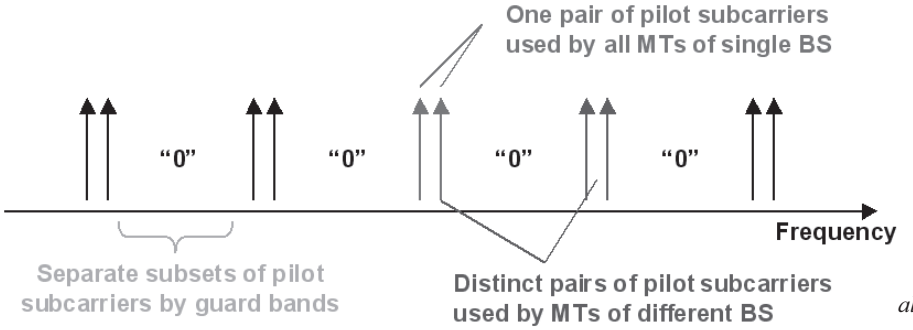

Figure 9. Subcarrier allocation of the test signal.

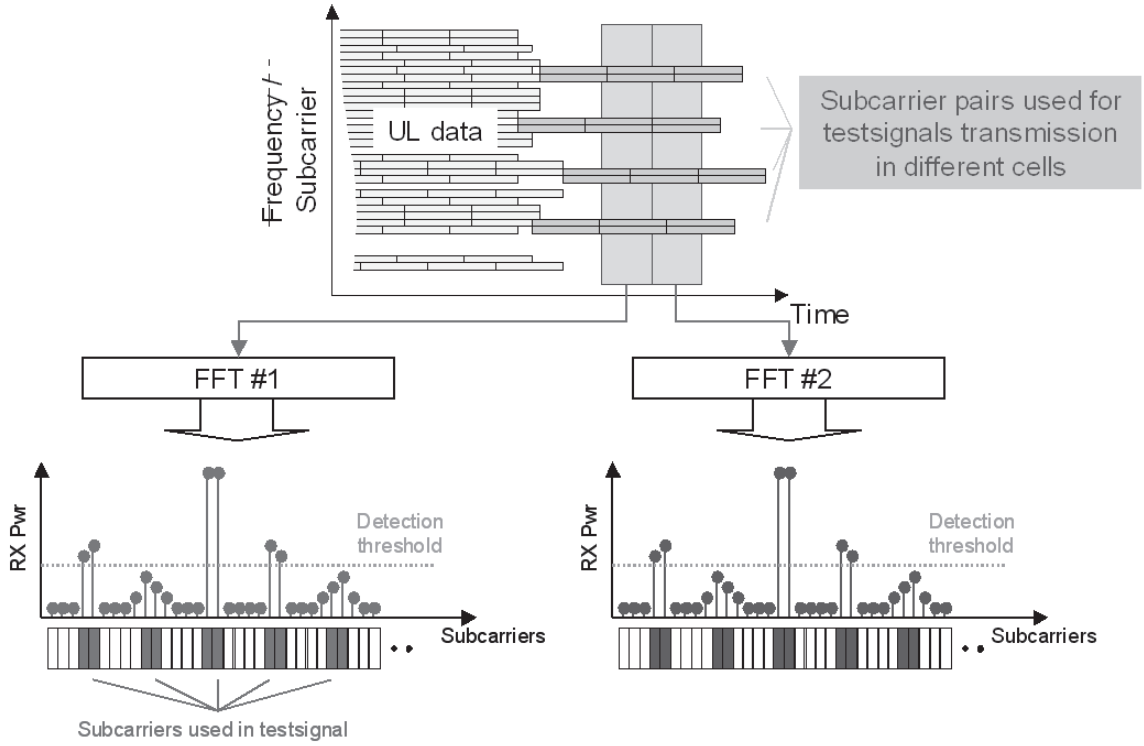

Figure 10. The time interval free of inter-symbol interference and inter-carrier interference between different test signals is used for the estimation of fine time and frequency offsets

In the downlink case and in the mobile-terminal synchronization phase, a single FFT output signal already contains the time-offset information between the base station and the mobile terminal in a certain phase rotation between the two adjacent sub-carriers considered. The carrier-frequency offset between the base station and mobile terminal is given by the phase rotation between the FFT output signals of the same sub-carrier.

Using this synchronization technique, which is based on phase-difference measurements, in each base station and mobile terminal, the time- and frequency-offset estimates are obtained simultaneously for each possible received sub-carrier pair. But only those measurements that exceed a certain amplitude threshold will be used for the subsequent adjustment of the base-station time and frequency offsets. After the time and frequency synchronization process, a cellular single-frequency network has been established.

7. Self-Organized Resource Management

One important design aspect for a 4G system is the capability to efficiently serve the time-varying data rate demands of all mobile terminals, incorporating high traffic peaks at isolated base stations. Therefore, dynamic channel allocation (DCA) is considered to be an important feature for future networks. Centralized resource-management schemes, in which a central unit has complete knowledge about the resource allocation in all cells, have been investigated with respect to OFDM systems in [14, 15], for example.

In the following, however, it is assumed that each base station decides, in the radio-resource-management (RRM) procedure and in the sub-carrier-allocation process in a self-organizing (SO) way, without any cooperation or communication between adjacent cells, and without a central management unit. Therefore, the proposed system concept is termed SO-DCA.

The assumed OFDM-FDMA and time-division duplex scheme shown in Figure 7 is only one possible way of arranging the resource management. The SO-DCA concept can be applied for any orthogonal multiple-access scheme with a TDMA and/or FDMA component. A MAC (media-access control) frame consists of one downlink (DL) and one uplink (UL) period, and has a total duration of $T_F = T_{UL} + T_{DL}$.

This paper introduces a suitable dynamic channel allocation algorithm that strongly benefits from the tight synchronization between all base stations and mobile terminals inside the cellular environment. The radio resource management process is mainly based on continuous co-channel interference measurements in each frame. Based on the available co-channel interference measurements (see Figure 11), each base station decides independently of other base stations which resources will be covered for a new mobile terminal.

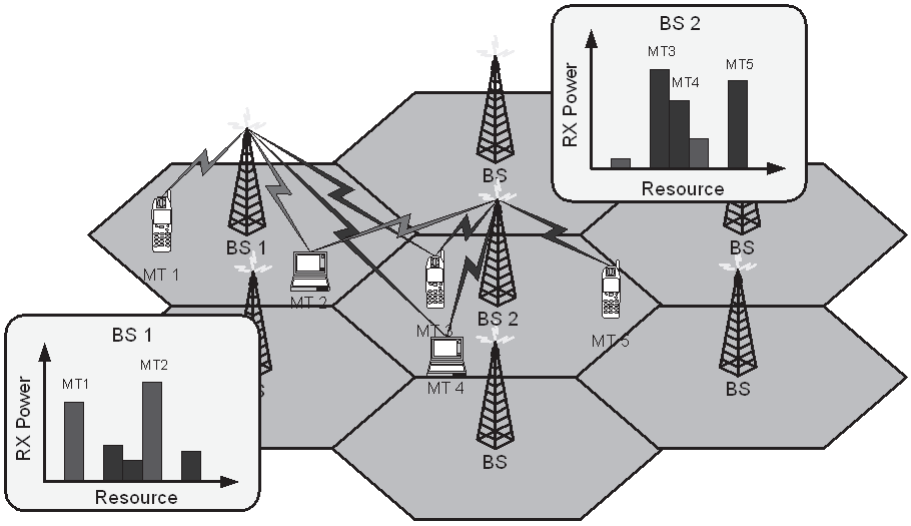

Figure 11. Each base station determines the resource allocation process by measuring the signal power on all sub-carriers inside the available bandwidth.

In order to increase the system throughput, a link adaptation (LA) procedure is further introduced. Each base station makes decisions about the modulation scheme and channel code rate (PHY mode) that can be used currently on the individual link. The choice of the applied PHY mode selection signal-to-noise rate (SNR) thresholds is derived from the radio channel measurement. The main task for the dynamic channel allocation algorithm is to assign a sufficient number of sub-carrier resources to a specific user (mobile terminal) to satisfy the current quality-of-service (QoS) demand. The sub-carrier selection process in the dynamic channel allocation procedure is important for allocating those sub-carriers that are less attenuated by the radio channel. This selection process is mainly based on co-channel interference measurements in the mobile terminal and base station. The resource-allocation process is summarized in Figure 12.

8. Technical Example for a 4G Air Interface

Taking all of these important results from the previous sections into consideration, a system design example is considered in this section. OFDM system parameters for a 4G air interface are considered, and three different multiple-access schemes inside a single cell are compared quantitatively. A bandwidth of 20 MHz in the 5.5 GHz domain is assumed. The assumed multi-path radio channel has a maximum delay of $\tau_{max} = 5\mu s$ (the coherence bandwidth is therefore $B_c = 200$ kHz). Table 1 shows an example for the system parameters of a 4G air interface.

Three different multiple-access concepts have been analyzed and compared for the system considered. The first proposal is based on a pure OFDM-TDMA structure, while

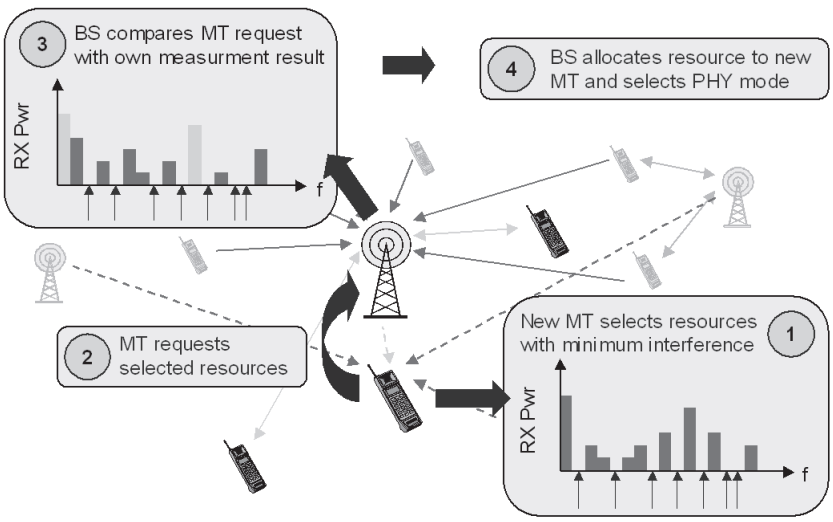

Figure 12. Resource allocation and PHY Mode selection based on interference measurements at the mobile terminal and the base station.

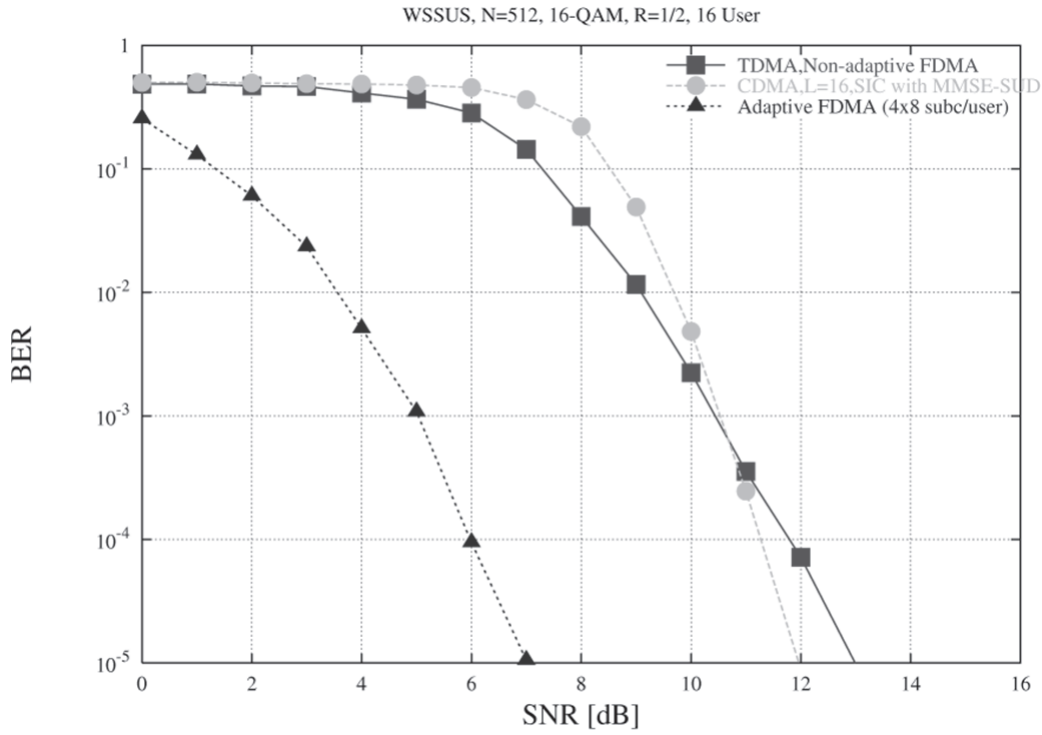

Figure 13. Bit error rate (BER) results for a coded OFDM system employing different multiple-access techniques.

the second proposal considers an OFDM-FDMA technique with an adaptive sub-carrier selection scheme, as described in Section 4. The third proposal is based on OFDM-CDMA where the user data are spread over a subset of sub-carriers. In this case, multiple-access interference occurs, and an interference-cancellation technique implemented in each mobile terminal is useful.

To compare the different multiple-access schemes, Figure 13 shows the bit error rate for an OFDM system with the system parameters shown in Table 1. A single cell situation has been considered in this case, with perfect time and carrier synchronization. As can be seen from this figure, the best performance can be achieved by an OFDM-FDMA system that exploits the frequency-selective fading of the mobile radio channel by always allocating the best-available sub-carrier to each user. Note that a channel-adaptive FDMA scheme requires a good prediction of the channel transfer function, which has been considered to be perfect in this comparison. If a non-adaptive FDMA technique was used (i.e., fixed or random allocation of sub-carriers), the performance would be comparable to the OFDM-TDMA curve.

In the case of an OFDM-TDMA system, the frequency selectivity of the radio channel can be exploited by the Viterbi decoder, in conjunction with bit interleaving. A pure coded OFDM-CDMA system, which utilizes an

Parameter	**Value**
FFT length	$N_C = 512$
Guard interval length	$N_G = N_C/8 = 64$
Modulation technique	16-QAM
Code rate	$R = 1/2$, $m = 6$
FDMA	Best available sub-carrier is selected.
TDMA	
CDMA spreading matrix	Walsh-Hadamard ($L = 16$)
CDMA detection technique	SUD with MMSE, MUD with soft interference cancellation plus MMSE

Table 1. The proposed OFDM system parameters.

orthogonal spreading matrix with minimum-mean-square-error (MMSE) equalization and single-user detection (SUD) to exploit the diversity of the channel, suffers from multiple-access interference due to loss of code orthogonality in frequency-selective fading. A performance improvement can be achieved for an OFDM-CDMA scheme applying multi-user detection (MUD) techniques. By successively removing inter-code/user interference using a multi-user detection procedure, a gain of approximately 2 dB can be achieved. However, an OFDM-FDMA system still outperforms an optimized OFDM-CDMA system. Additionally, the OFDM-CDMA technique has a much higher computational complexity in the multi-user detection scheme.

9. Summary

Some aspects for future mobile communication networks have been considered in this paper. The OFDM transmission technique itself has a large potential, due to its robust behavior in wideband frequency-selective and time-varying radio channels. Combination with multiple-access schemes showed good performance under realistic channel assumptions. Future cellular networks require high flexibility for data sources with different and time-varying data rates in multi-path propagation environments. Therefore, a cellular single-frequency network has been proposed, and the completely decentralized time and carrier synchronization aspects have been discussed. Finally, self-organized radio resource management has been proposed to establish a totally decentralized organization inside each base station. All these different techniques and technical concepts can be combined in a way to establish a future powerful and flexible mobile communications network for the fourth generation.

10. References

1. P. A. Bello, "Characterization of Randomly Time-Variant Linear Channels," *IEEE Transactions on Communications*, December 1964.

2. M. Pätzold, *Mobile Fading Channels*, New York, Wiley, 2002.

3. J. Bingham, "Multicarrier Modulation for Data Transmission: An Idea Whose Time Has Come," *IEEE Communications Magazine*, May 1990.

4. S. B. Weinstein and P. M. Ebert, "Data Transmission by Frequency-Division Multiplexing Using the Discrete Fourier Transform," *IEEE Transactions on Communication Technology*, **COM-19**, 5, October 1971, pp. 628-634.

5. R. W. Chang, "Synthesis of Band-Limited Orthogonal Signals for Multichannel Data Transmission, *Bell System Technical Journal*, **45**, December 1966, pp. 1775-1796.

6. B. R. Saltzberg, "Performance of an Efficient Parallel Data Transmission System," *IEEE Transactions on Communications*, December 1967.

7. M. Aldinger, "Multicarrier COFDM Scheme in High Bit Rate Radio Local Area Networks," *Proceedings of Wireless Computer Networks*, Den Haag, Netherlands, 1994.

8. F. Classen and H. Meyr, "Frequency Synchronization Algorithms for OFDM Systems Suitable for Communication over Frequency Selective Fading Channels," *Proceedings of the IEEE Vehicular Technology Conference 94*, 1994, pp. 1655-1659.

9. M. Mizoguchi et al., "A Fast Burst Synchronization Scheme for OFDM," *Proc ICUPC 98*, **2**, pp. 125-129.

10. H. Rohling and R. Grünheid, "Performance Comparison of Different Multiple Access Schemes for the Downlink of an OFDM Communication System," *Proceedings of the IEEE Vehicular Technology Conference 1997*.

11. S. Kaiser, "Multi-Carrier CDMA Mobile Radio Systems – Analysis and Optimization of Detection, Decoding, and Channel Estimation," *Fortschritt-Berichte VDI*, **10**, 531, VDI-Verlag, Düsseldorf, Germany, 1998.

12. Dirk Galda, Hermann Rohling, Elena Costa, Harald Haas, and Egon Schulz, "A Low Complexity Transmitter Structure for the OFDM-FDMA Uplink," *Proceedings of the IEEE Vehicular Technology Conference 2002 Spring*, Birmingham, Alabama, USA, May 2002.

13. J. Zander and S. L. Kim, *Radio Resource Management for Wireless Networks*, Norwood, MA, Artech House, 2001.

14. M. Wahlqvist et al., "Capacity Comparison of an OFDM Based Multiple Access System Using Different Dynamic Resource Allocation," *Proceedings of the IEEE Vehicular Technology Conference 1997*, May 1997, pp. 1664-1668.

15. W. Wang et al., "Impact of Multiuser Diversity and Channel Variability on Adaptive OFDM," *Proceedings of the IEEE Vehicular Technology Conference 2003 Fall*, Orlando, FL, October 2003.

16. A. Peled and A. Ruiz, "Frequency Domain Data Transmission Using Reduced Computational Complexity Algorithms," *Proc. IEEE ICASSP*, Denver, CO, 1980, pp. 964-967.

17. L. Hanzo et al., *OFDM and MC-CDMA for Broadband Multi-User Communications, WLANs and Broadcasting*, New York, Wiley, 2003.

A Review of Surface-Based Microwave and Millimeter-Wave Radiometric Remote Sensing of the Troposphere

E.R. Westwater
S. Crewell
C. Mätzler

Abstract

Surface-based radiometric sensing of tropospheric parameters has a long history of providing useful measurements of temperature, water vapor, and cloud liquid. In this review, a general overview of physical fundamentals, measurement techniques, and retrieval methodology is given. Several contemporary instruments are then discussed and representative results are presented. Recent and promising developments include multi-frequency radiometers, scanning observations of clouds, and combined active-passive remote sensing. The primary applications of these new technologies are weather forecasting and climate, communications, geodesy and long-baseline interferometry, satellite data validation, air-sea interaction, and fundamental molecular physics.

1. Introduction

Surface-based radiometric measurements of atmospheric thermal emission have proven useful in a variety of meteorological applications, including meteorological observations and forecasting, communications, geodesy and long-baseline interferometry, satellite validation, climate, air-sea interaction, and fundamental molecular physics. One reason for the utility of these measurements is that with careful design, radiometers can be operated in a long-term unattended mode in nearly all weather conditions [1, 2, 3]. The measurements also enable the continued development of absorption and radiative transfer models in both clear [4, 5] and cloudy [6] atmospheres. This development has been greatly aided by long-term, carefully calibrated radiometer measurements, supplemented by frequent radiosonde releases using active sensors for cloud identification [7, 8]. Last but not least is the development of retrieval and data assimilation algorithms [9, 10], with which radiometer data can be combined with external data sources, such as forecasts or soundings from active sensors. In this overview of surface-based radiometers, we confine our attention to radiometric soundings of water vapor, temperature, and clouds in the troposphere.

2. Microwave Absorption and Emission

The principal sources of atmospheric emission and absorption are water vapor, oxygen, and cloud liquid. In the frequency region from 20 GHz to 200 GHz, water-vapor absorption arises from the weak absorption line at 22.235 GHz and the much stronger line at 183.31 GHz. In addition, the so-called continuum absorption of water vapor arises from the far wing contributions from higher-frequency resonances that extend into the infrared region. In the frequency band from 50 GHz to 70 GHz and the region about 118 GHz, oxygen absorbs due to a series of magnetic dipole transitions centered around 60 GHz and the isolated line at 118.75 GHz. Because of pressure broadening, the oxygen absorption extends outside of the immediate frequency region of the resonant lines. There are also resonances by ozone that are important for stratospheric sounding [11]. In addition to gaseous absorption, scattering,

Ed R. Westwater is with the Cooperative Institute for Research in Environmental Sciences, University of Colorado/NOAA Environmental Technology Laboratory, 325 Broadway MS R/E/ET1, Boulder, CO, 80305 USA; Tel: +1 (303) 497-6527; Fax: +1 (303) 497-3577; E-mail: Ed.R.Westwater@noaa.gov; http://www.etl.noaa.gov/~ewestwater
Susanne Crewell is with the Meteorologisches InstitutUniversitaet Muenchen, Theresienstr. 37 80333 Muenchen, Germany;
Tel: +49 (0) 89/2180-4210; Fax: +49 (0) 89/2805508; E-mail: crewell@meteo.physik.uni-muenchen.de; http://www.meteo.physik.uni-muenchen.de/.
Christian Mätzler is with the Institute of Applied Physics, University of Bern, Sidlerstr. 5, CH-3012 Bern, Switzerland; Tel: +41 31 631 45 89; Fax: +41 31 631 37 65; E-mail: matzler@iap.unibe.ch; http://www.iapmw.unibe.ch.

Editors Note: This is one of the invited *Reviews of Radio Science*, from Commission F.

absorption, and emission also originate from hydrometeors in the atmosphere. Our focus in this article is on non-precipitating clouds, for which emission and absorption are of primary importance.

2.1 Gaseous Absorption Models

Detailed calculations of absorption by water vapor and oxygen were first published by J. H. Van Vleck. The quantum mechanical basis of these calculations, including the Van Vleck-Weisskopf line shape, together with laboratory measurements, have led to increasingly accurate calculations of gaseous absorption. Both these historical and recent developments are discussed in [12]. Currently, there are three absorption models that are widely used in the propagation and remote-sensing communities. Starting with laboratory measurements that were made in the late 1960s and continuing for several years, H. Liebe developed and distributed the computer code of his Microwave Propagation Model (MPM). One version of the model [13] is still extensively used, and many subsequent models are compared with this one. Liebe later made changes to both water-vapor and oxygen models, especially to parameters describing the 22.235 GHz H_2O line and the so-called water-vapor continuum [14]. More recently, Rosenkranz [5a, 5b] developed an improved absorption model that also is extensively used in the microwave propagation community. However, there are many issues in the determination of parameters that enter into water-vapor-absorption modeling, and a clear discussion of several of these issues is given in [5]. Relevant to the discussion is the choice of parameters to calculate the pressure-broadened line width, which, in the case of water vapor, arises from the collisions of H_2O with other H_2O molecules (self broadening), or from collisions of H_2O molecules with those of dry air (foreign broadening). In fact, Rosenkranz [5a, 5b] based his model on using Liebe and Layton's [13] values for the foreign-broadened component, and those from Liebe et al. [14] for the self-broadened component. Another model that is used extensively in the US climate research community is the Line by Line Radiative Transfer Model (LBLRTM), by S. Clough and his colleagues[7]. One feature of the Clough model is that it has been compared extensively with simultaneous radiation and radiosonde observations near 20 GHz and 30 GHz.

2.2 Cloud Absorption Models

For spherical particles, the classical method of calculating scattering and absorption coefficients is through the Lorenz-Mie Equations [15, 16, 17]; for sufficiently small particles, the Rayleigh approximation can be used. The particle contribution is calculated for a given wavelength and single particle; the total coefficients are then obtained by integration over the size distribution of particles. An important physical property for the calculations is the complex dielectric constant of the particle. This dielectric constant of liquid water is described by the dielectric relaxation spectra of Debye [18]. The strong temperature dependence of the relaxation frequency is linked to the temperature-dependent viscosity of liquid water; therefore, the cloud-absorption coefficient also shows significant temperature sensitivity. The dielectric constant can be well measured in the laboratory above 0°C, and a variety of measurements have been made from 5 GHz to 500 GHz [6]. However, for super-cooled water – below 0°C – the situation is less certain, and, for example, models of [6, 19, 20] differ by 20% to 30% in this region [21]. This is relevant for cloud remote sensing, because measurements of super-cooled liquid are important for detection of aircraft icing [22]. When calculating absorption for non-precipitating clouds, we assume Rayleigh absorption, for which the liquid absorption depends only on the total liquid amount and does not depend on the drop-size distribution, and scattering is negligible. The Rayleigh approximation is valid when the scattering parameter $\beta = \left|n\left(2\pi r/\lambda\right)\right| \ll 1$ [16]. Here, r is the particle radius, λ is the free-space wavelength, and n is the complex refractive index. For rain and other situations for which the β is greater than roughly 0.1, the full Mie equations, combined with a modeled (or measured) size distribution, must be used.

Due to the non-spherical shape of ice hydrometeors, the situation is more complicated when scattering plays a role. Although this situation is beyond the scope of this article, at millimeter wavelengths the particle size of cirrus clouds can be of the order of 100 to 200 microns, and scattering may be important near transmission windows. On the other hand, the dielectric properties of ice [23, 24] are very different from those of liquid water. The dielectric losses of ice have a minimum near 1 GHz, and ice is an almost perfectly loss-free medium over a large frequency range. Therefore, microwave emission of pure ice particles can be neglected in most cloud situations. Special situations occur when ice particles start to melt. A very thin skin of liquid water can be sufficient to cause significant absorption, and thus emission. Usually, these conditions apply to precipitating clouds, or in the so-called radar "bright band."

2.3 Calculations of Absorption Spectra

For standard conditions at sea level, we calculated the water vapor (H_2O), oxygen (O_2), and total clear ($H_2O + O_2$) contributions to the absorption coefficient. In addition, we calculated the liquid absorption coefficient for $\rho_L = 0.1\ \mathrm{gm}^{-3}$ at $T = 293$ K and 273 K. From the results shown in Figure 1, we note the strong oxygen absorption regions near 60 GHz and 118 GHz due to oxygen, and the large absorption near 183 GHz. For a given location and altitude, the oxygen absorption is relatively constant, with variations of 10% to 20%, while both the 22.235 GHz and the 183.31 GHz absorptions can vary by a factor of 10 to 20. Note also the strong temperature dependence of cloud absorption, and the reversal of this dependence at around 150 GHz.

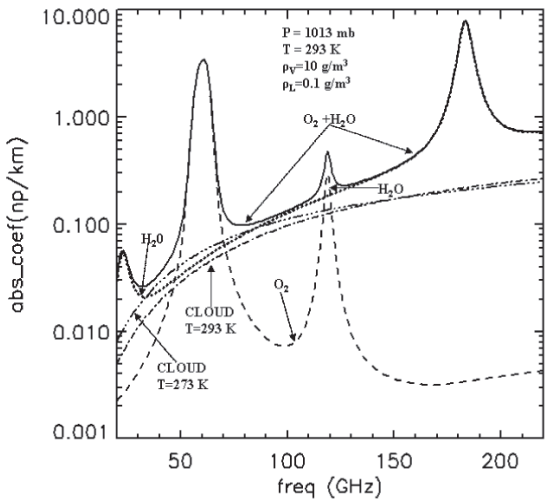

Figure 1. Microwave absorption spectra from 20 GHz to 220 GHz. The absorption models used were Liebe 89 [4] for clear absorption, and Liebe et al. 1991 [6] for cloud liquid. In this figure, P is pressure, T is temperature, ρ_V is absolute humidity, and ρ_L is cloud liquid density.

2.4 Microwave Thermal Emission

Neglecting scattering, we relate our primary observable, brightness temperature, T_b, to the atmospheric state by the radiative transfer equation (RTE) [25]:

$$B_\nu(T_b) = B_\nu(T_c)\exp(-\tau)$$

$$+\int_0^\infty B_\nu\left[T(s)\right]\alpha(s)\exp\left[-\int_0^s \alpha(s')\,ds'\right]ds\,, \quad \text{(1a)}$$

where s is the path length in km, $T(s)$ is the temperature (K) at the point s, and T_c is the cosmic background brightness temperature of 2.75 K. τ = opacity = total optical depth along the path s:

$$\tau = \int_0^\infty \alpha(s)\,ds\,, \quad \text{(1b)}$$

where $a(s)$ is the absorption coefficient (nepers/km) at the point s, and $B_\nu(T)$ is the Planck function at frequency ν and temperature T:

$$B_\nu(T) = \frac{2h\nu^3}{c^2}\frac{1}{\exp(h\nu/kT)}\,. \quad \text{(1c)}$$

h is Planck's constant, and k is Boltzman's constant.

Scattering, although neglected here, may arise from liquid, ice, or melting liquid, depending on the size distribution of the particles. For simplicity of notation, we have suppressed the frequency dependence of τ and α in Equation (1). This equation and its Rayleigh-Jeans approximation are discussed in [25], and its more general form, including scattering, is discussed in [26]. For our purposes, we note the dependence on the temperature profile $T(s)$ and the implicit dependence on pressure, water vapor, and cloud liquid through $\alpha(s)$. For a plane-parallel atmosphere, the path length, s, and the height, h, are related by $s\sin(\theta) = h$, where θ is the elevation angle. Information on meteorological variables is obtained from measurements of T_b as a function of ν and/or θ. Equation (1) is used (a) in forward model studies in which the relevant meteorological variables are measured by radiosonde in situ soundings [27, 28, 29]; (b) in inverse problems and parameter-retrieval applications, in which meteorological information is inferred from measurements of T_b; and (c) in system modeling studies for determining the effects of instrument noise on retrievals and optimum measurement ordinates, such as ν and θ. Calculations of T_b for a warm (surface temperature T_s = 293 K) atmosphere are shown in Figure 2. We note the transmission windows near 30-50 GHz, 70-100 GHz, and 130-150 GHz. Radiometer measurements near these windows are used primarily for remote sensing of clouds and water vapor. The strong absorption features near 60 GHz and 118 GHz are used for temperature sensing. Finally, the strong absorption region near 183 GHz can be used to study very low amounts of water vapor [30].

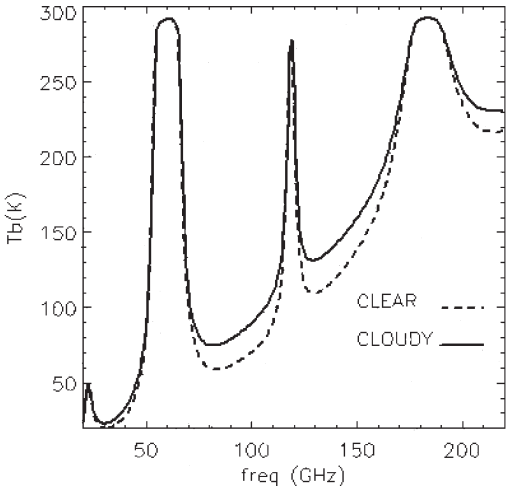

Figure 2. Calculated brightness temperatures (K) from 20 GHz to 220 GHz for clear and cloudy conditions. The clear calculations were based on a standard atmosphere with the surface values (S) of P_S = 1013 mb, T_S = 293 K, ρ_S = 10 gm^{-3}, and IWV = 2.34 cm. The cloudy atmosphere contained 1 mm of integrated cloud liquid with a cloud layer of liquid density of 0.1 gm-*3* between 1 and 2 km. The absorption models used are given in Figure 1.

3. Observation Techniques

Measuring downwelling thermal emission by microwave and millimeter-wavelength radiometers from a surface-based platform is now routinely performed on an operational basis [2, 3]. In addition, surface-based

radiometers are frequently deployed in campaigns specifically designed to study water vapor [29], clouds [31], and temperature [32, 33, 34]. In some deployments – specifically designed to measure water vapor and clouds in combination with other zenith-looking sensors – zenith observations are of primary interest. In others, particularly those used to measure boundary-layer temperature profiles, elevation-scanning radiometers are frequently used. More recently, radiometers scanning in both azimuth and elevation are also used to observe clouds [35].

The fundamentals of microwave radiometers are clearly discussed in [25, 36, 37]. Radiometers used to observe the atmosphere are comprised of a highly directional antenna and a sensitive receiver, followed by a detector unit and a data-acquisition system: a total system that requires calibration. In this section, we briefly discuss general techniques common to ground-based systems, and then give examples of contemporary radiometers.

3.1 Antennas

An antenna measures the antenna temperature, T_A, which is the integration over 4π steradians of the product of the angular distribution of brightness temperature and the power pattern of the antenna Usually, the antennas have symmetric beam patterns, with typical widths from 1° to 6°. Because most remote-sensing systems perform scanning in a vertical plane, low sidelobes are required to minimize contamination from ground emission. In addition, because surface-based antennas are deployed in rain and snow, protection from and reduction or elimination of environmental effects is of primary concern.

Perhaps the simplest antenna used to observe the atmosphere is a horn, either scalar or corrugated, that has a suitable beam pattern. If a multi-frequency and equal-beamwidth system is desired, the dimensions of the horns can be scaled appropriately. For some systems, the entire electronics package is rotated with the antenna. A more common system is to direct the antenna beam from the primary antenna onto a flat reflecting mirror that is scanned. In this configuration, only the flat reflector is moved. An example of this type of system is shown in Figure 3 [38]. Another common method is to use a lens antenna, which, again, views a flat reflector. More sophisticated scanning designs are also possible, such as the use of sub-reflectors, reflectors, and mirrors [35]. Frequently, the electronics package and the antenna are enclosed within a radome to protect the system from the environment.

During precipitation events, radiometer antennas/radomes usually get wet. One approach to reducing the effects of rain on a flat reflector was described by [39]. The reflector, when rotated rapidly, would quickly remove precipitation, although the reflector surface would accumulate a thin film of liquid. After a rain event, the reflector would dry within one to five minutes, and uncontaminated measurements could then be obtained. However, the measurements taken during rain were still contaminated. Hydrophobic coatings can reduce the amount of water drops on the radome surface [40], but this reduction is never complete. Blowers are useful to avoid the formation of dew on the microwave window, in particular when combined with heated air. Blowers are less effective for evaporation of raindrops, which was shown in the microwave radiometer inter-comparison campaign (MICAM) [41]. The time required to dry the radome after the rain event varied from a few minutes to several hours, depending on the radiometer design. For strong precipitation events, only the French DRAKKAR radiometer [41], which combines a small radiometer aperture with a strong blower system, needed less than an hour to dry. For larger systems, a shutter system controlled by a precipitation detector proved to be useful, as was done with the 22-channel radiometer MICCY (see Section 4.6), operated by the University of Bonn/Germany. One efficient way to allow measurements during precipitation is the observation at non-zenith elevation angles using a shelter protecting the instrument.

Another concern is the loss from dielectric lens antennas. Lenses for remote sensing are usually constructed from low-loss material (loss tangent less than ~ 10^{-3}). A lossy antenna attenuates an incoming signal and adds noise due to its own physical temperature. If the loss factor and the

Figure 3. The ASMUWARA in operation in Bern. The openings of the four horns appear as grey disks at the left of the rotatable mirror, while the IR radiometer looks through the white cylinder below the largest horn.

lens temperature are known, the unwanted signal can be corrected from the measured brightness temperature. The effect can be calibrated out by external targets or tipping curves (see Section 3.3.2), and a limitation is imposed by the time spent between valid calibration observations.

3.2 Receivers

A variety of receiver designs are also common in surface-based radiometry, and several involve Dicke modulation-type radiometers, in which the input to the receiver is alternatively switched between the scene (sky) and an internal calibration load [37]. In the original ETL design [1], the receiver was based on the Hach [42] design, in which the signal was sequentially switched between the scene and two internal blackbody targets (hot = 145° C and reference = 45° C). These targets were simply waveguide terminations kept at strictly controlled and measured temperatures. In the Radiometrics Corporation design (http://www.radiometrics.com), a signal generated by a noise diode is alternatively turned off and on and added to the signal from the scene at each angle, including the target. The Russian-designed scanning radiometers for boundary-layer temperature measurement [32, 33, 34] are total-power radiometers, but have been modified to include the signal from a noise generator. Both the NOAA/ETL Dual Channel radiometer (see Section 4.1) and the NOAA/ETL Ground-based Scanning Radiometer (see Section 4.9) receivers use either conventional Dicke or Hach switches that alternate between an internal reference load(s) and the scene. Finally, all of the above receivers are of double-sideband design, in which the signal from a stable local oscillator is mixed with the incoming radio-frequency signal emanating from the scene; the intermediate-frequency (IF) signal is then amplified and detected. With IF bandwidths usually around 500 MHz to 1 GHz, one-second radiometric sensitivities of 0.1 K are common. Also noteworthy is a specially constructed high-stability radiometer [43]. Based on typical analysis (see Section 3.3.3), this unit gave rms errors of less than 0.05 K over time periods of a month, and stabilities of better than 0.01 K over time scales of 1000 s to 10000 s. Another possibility is to use direct detection at the radio frequency of interest, thus eliminating the mixer and local oscillator. As improvements are made in radio-frequency amplifiers, increasing use of direct detection is expected. The use of Dicke or Hach switching overcomes the effect of receiver-gain variations, but can reduce the sensitivity of the receiver. As improvements are made in temperature and other environmental controls, total-power radiometers may become more common. Both MICCY (see Section 4.6) and RPG-HATPRO (see Section 4.7) illustrate some of these more recent developments.

3.3 Calibration

To derive quantitative information from radiometric measurements, accurate calibration is required, with accuracies of 0.5 K to 1.0 K. Most radiometric receivers have one or two internal noise sources that provide some measure of calibration. However, waveguide losses, lack of complete knowledge of radiometric parameters, and a host of other causes usually dictate that some external calibration method also be employed. We assume that the radiometer uses a square-law detector, in which the output voltage is proportional to the input power: i.e., voltage is proportional to the antenna temperature. We will briefly describe three commonly used calibration techniques.

3.3.1 External Blackbody Reference Targets

A seemingly straightforward calibration method is to view two external blackbody targets that are kept at two widely separated temperatures [37]. If T_1 and T_2 are the two target temperatures, with respective output voltages of v_2 and $v1$, then

$$\left(T_A\right)_S = T_1 + \frac{T_2 - T_1}{v_2 - v_1}\left(v_S - v_1\right), \qquad (2)$$

where $\left(T_A\right)_S$ is the antenna temperature of the scene and v_S is the corresponding voltage.

Preferably, the target temperatures bracket the range of antenna temperatures emitted from the scene. Also, it is important to construct targets with high emissivity such that reflections from external sources are negligible, and to have the targets sufficiently large that at least one and one-half to two projected antenna diameters are captured by the target system. Targets are frequently constructed with a surface having high thermal conductivity, covered with a thin layer of very absorbent material. Many times, a corrugated pyramidal surface, with wavelength-dependent spacing and depth ratios, is constructed to reduce reflections and hence to increase emissivity. The target is frequently embedded in a thermal insulator that is transparent to incoming radiation. Finally, when a target is placed in a thermal environment in which the environmental temperature differs greatly from the desired target temperature, measurements of target temperatures at several locations within the target are essential. The target calibration methods are most useful when the atmospheric brightness temperatures are within the range of easily achieved target temperatures: e.g., near the center of the 60 GHz O_2 absorption, or near the 183.31 GHz water-vapor line.

3.3.2 The Tipping-Curve Calibration Method

In the transmission windows from 20 GHz to 45 GHz or from 70 GHz to 150 GHz, clear-sky T_b values can be in the 10 K to 50 K range, and operational deployment of targets with temperatures that are in this range is difficult.

In this low transmission case, the so-called tipping-curve calibration method (tipcal) can give a high degree of accuracy [2, 44], and has been commonly used throughout the microwave community. In this method, brightness temperatures are measured as a function of elevation angle, θ, and are then converted to opacity, $\tau(\theta)$, using the mean radiating temperature approximation [45].

For each angle, an angularly-dependent mean radiating temperature, $T_{mr}(\theta)$, is used to derive the optical depth, $\tau(\theta)$, from

$$\tau(\theta) = \ln\left\{\frac{B_\nu\left[T_{mr}(\theta)\right] - B_\nu(T_c)}{B_\nu\left[T_{mr}(\theta)\right] - B_\nu\left[T_b(\theta)\right]}\right\}. \qquad (3)$$

If the system is in calibration, then the plot of $\tau(\theta)$ as a function of (normalized) air mass, m $(= \csc(\theta))$, will pass through the origin; conversely, if $\tau(m) = \tau(1)m + b$ does not pass through the origin, then a single parameter in the radiometer equation is adjusted until it does. Note that when the calibration is achieved, then the slope of the line is equal to the zenith opacity. Several of the factors affecting the accuracy of tipcals were analyzed in [44], and their major results are summarized below:

A. The effect of the refractive-index profile on system calibration is negligible, and the fact that the Earth's curvature has a relatively large effect that can be conveniently corrected to less than 0.05 K for air mass ≤ 4.
B. Pointing errors could have a serious impact on the performance of the tipcal if only one-sided scans are used. Experience and simulations strongly suggest that antenna scans used for calibration should be taken in pairs, at symmetric elevation angles.
C. A correction must be made when converting the antenna temperature $T_a(\theta)$ to $T_b(\theta)$. A correction based on half-power beamwidths was given in [44].
D. The quantity T_{mr} plays a role in mapping brightness temperature, T_b, to opacity, τ. Using a T_{mr} that is a function of elevation angle and is estimated by surface meteorological measurements is an effective way of reducing errors in T_{mr}. The prediction could also be improved significantly by using remote sensor observations [82].
E. The system random noise affects system precision, but with both the ETL and the ARM systems (rms noise ~ 0.1 K), the calibration uncertainties are about 0.1 K - 0.4 K. Reference [44] also found that the use of T_b at larger air masses suffers less than the use of T_b at smaller air masses due to a larger signal-to-noise ratio at lower elevation angles. The impact of the system noise can usually be reduced by temporal averaging.
F. Errors caused by uncertainty in the offset term of the radiometer equation will not cause serious calibration problems if the offset uncertainty is less than 1 K. See [44] for two common types of radiometer equations.
G. Errors caused by non-stratified atmospheric conditions are the most serious limitation for tipcal, and can occur due to clouds and horizontal variations in the water-vapor field. Various criteria based on symmetric scans are available to determine the quality of a tipcal [2, 44].

In summary, the tipcal method, when applicable, can give absolute accuracies of 0.3 K to 0.5 K rms.

3.3.3 Brightness Temperature Calculations to Calibrate

For a highly stable radiometer, such as the NOAA/ETL prototype [1] that was operated at a radiosonde launch facility, radiosonde data that are taken during clear-sky conditions can be used with a forward radiative transfer model, Equation (1), to calculate T_b values. If the T_b values are taken over a variety of elevation angles, or over a range of meteorological conditions, the measured data can be used as calibration points. This method implicitly assumes the correctness of the forward model and also of the radiosondes. The technique is most applicable near highly absorbing spectral regions, such as in the 60 GHz oxygen region, for which the calculated T_b values are insensitive to the choice of forward model. When applied to all channels of a multi-frequency radiometer that derives meteorological information, it also ensures internal consistency between radiometric data and the forward model used in retrievals.

4. Examples of Radiometric Systems

In this section, we discuss several types of contemporary ground-based radiometers. Since some of these are commercially available, we, of course, do not endorse any particular instrument.

4.1 NOAA/ETL Dual-Channel Radiometer

NOAA/ETL designed, constructed, and currently operates several dual-frequency radiometers at (20.6 GHz or 23.87 GHz, 31.65 GHz) that are used for measuring integrated water vapor (IWV) and liquid water path (LWP) [1]. For each of the radiometers, the electronics and the antenna and feed, are all housed in a benign environment, such as a seatainer. In this environment, the radiometer is free from precipitation, and the internal temperature of the seatainer is controlled to about 5°. The antenna is an offset paraboloid with a hybrid-mode feed, which results in high-quality radiation patterns that minimize the effect of extraneous sources of noise; the antenna aperture is devoid of blockage, and the beam is steerable in a vertical plane. The antenna has the same beamwidths at both frequencies (the full width at half power – FWHP – is either 2.5° or 4.0°), thus minimizing differential beam-filling during non-homogeneous cloud conditions. Some ETL systems have rapidly rotating reflectors to reduce the effects of rain [39]. The radiometer is triple switched in the Hach [42] mode; this results in continuous internal calibration and high stability. External calibration is accomplished on roughly a weekly basis using the tipcal method.

4.2 Radiometrics Corporation Microwave Radiometer (MWR)

Radiometrics Corporation has designed, constructed, and sold several dual-frequency (23.8 GHz and 31.4 GHz) MWRs for measuring integrated water vapor and liquid water path [2]. Each radiometer is easily portable, and all electronics, antenna, and calibration targets are enclosed in a radome. The antenna is a corrugated horn with a dielectric lens that views a stepping mirror, for scanning the atmosphere, and a blackbody target. The FWHP beamwidths of the system are 5.9° at 23.8 GHz and 4.5° at 31.4 GHz. The gain of the system is determined by viewing the target with and without noise injected by a noise diode. Calibration of the system consists of determining the effective noise-diode temperature, T_{ND} , and is done by the tipcal method. When tipcal can't be done, T_{ND} is estimated by a procedure described in [2]. The MWR is equipped with a heated blower and a moisture detector to minimize the effects of rain and dew.

4.3 Tropospheric Water Vapor Radiometer (TROWARA)

A first-generation radiometer system for continuous measurements of integrated water vapor and of liquid water path was operated at the Institute of Applied Physics (IAP) at the University of Bern. The instrument, called TROWARA, was designed and built at the IAP. It operated at 21 GHz and 31 GHz [46] with internal calibration, supplemented by hourly tipping curves [44, 47]. The limitation to two channels required an estimate of the effective tropospheric temperature [48]. TROWARA has provided a large data set over the years. Inter-comparisons of measured integrated water vapor with other remote-sensing methods and with nearby radiosonde data showed reasonable agreement, but at the same time, these revealed systematic differences on the order of 1 kg/m^2 [49, 50, 51]. A special test was the participation of TROWARA in the Cloud-Liquid Water Network (CLIWA-NET) [31]. Due to the failure of the 21 GHz channel during the first campaign, a method was developed to retrieve the required information by combining the 31 GHz radiation with Global Positioning System (GPS) data [38]. The instrumental degradation initiated a renovation and system reanalysis, leading to a new calibration model and the relocation from outdoor to indoor operation, viewing the sky through a Styrofoam window for enhanced stability [53]. In this way, TROWARA is able to observe downwelling brightness temperatures at an elevation angle of 40° under all weather conditions, including rain, since November, 2002. The data will form part of a database for climate research to be established within the project called "Studies in atmospheric radiative transfer and water-vapor effects," and is sponsored by the Swiss NCCR Climate Program (http://www.nccr-climate.unibe.ch/).

4.4 Meteorological Temperature Profiler MTP5

Kipp & Zonen BV is now marketing a radiometer that was originally designed and deployed by the Russian firm ATTEX [32, 34]. This radiometer is designed to measure temperature profiles in the boundary layer from 0 m to 600 m AGL. The radiometer is a single-channel (61 GHz) solid-state Dicke-type superheterodyne receiver that is electronically chopped at 1 KHz between the sky and a reference noise source. The antenna is a scalar horn with a FWHP beam width of 6°, and scans by viewing a flat reflector at each of 11 scanning angles. Because of the 2 GHz bandwidth and a low receiver noise temperature of 600 K, a high sensitivity of 0.04 K is achieved. Calibration of the receiver is achieved by 0.1° C temperature control and a switched internal noise generator. A one-point absolute calibration is achieved either by viewing an external target, or by knowing the emission temperature in the horizontal direction. A variation of this radiometer, developed at NOAA/ETL, scans continuously in a 360° vertical plane, and, in addition to temperature profiles, can also be used to measure air-sea temperature difference [54].

4.5 Radiometrics Corporation Microwave Profiler

Radiometrics Corporation has developed a multi-frequency microwave radiometer that is based on a highly stable, tunable, synthesized local oscillator in the receiver. This design overcomes errors caused by receiver frequency drift, while allowing observation of a large number of frequencies across wide tuning ranges. The total power receiver has a highly stable noise diode that is used as a gain reference. The radiometer observes atmospheric brightness temperatures in five frequency bands from 22 GHz to 30 GHz, and in seven bands from 51 GHz to 59 GHz [3, 55, 90]. It also measures zenith infrared temperature, surface temperature, humidity, and pressure. The radiometer has automated elevation- and azimuth-scanning capability, and the observation interval can be as short as several seconds. The instrument is relatively portable, with a volume of 0.12 m^3 and a weight of 32 kg.

4.6 Microwave Radiometer for Cloud Cartography (MICCY)

MICCY is a 22-channel radiometer operated by the University of Bonn [35]. It is capable of high temporal (0.1 s) and spatial (< 1°) resolution. The radiometer has 10 channels on the high-frequency side of the 22.235 GHz water-vapor line, 10 channels on the low-frequency side of the 60 GHz O_2 absorption ban, and two channels at 90 GHz. Both H and V polarization are measured at each frequency of operation. MICCY is a single-sideband total-power

radiometer that is based on a heterodyne receiver filter-bank design (parallel detection of all frequency channels). A Dicke modulation scheme is not foreseen for the system, since the thermal stability of the receivers is less than 20 mK, which implies that the instrument is capable of maintaining its radiometric accuracy for several minutes without recalibration. Both targets and inserted noise from highly stable diodes are used in calibration. With FWHP beam widths of about 0.9°, the radiometer is capable of full 360° scanning in azimuth and a zenith scan of 0° to 90°. The entire system can be scanned in azimuth and elevation for mapping of clouds. The latter is performed by a planar mirror that reflects the incoming radiation into a fixed 1 m Cassegrain system. The system comprises a quasi-optical multiplexer for three frequency bands. Internal ambient and cold blackbodies are used for absolute calibration, while internal noise calibration standards are used in between absolute calibrations. The entire system is mounted on a transportable trailer, and all parts are enclosed in a radome.

4.7 Radiometer Physics GmbH-Humidity and Temperature Profiler (RPG-HATPRO)

Because the implementation of an operational network of microwave radiometers is presently hampered by the cost and complexity of the available instruments, it was a major objective of the European CLIWA-NET project [31] to develop a network-suitable low-cost microwave radiometer. At first, the radiometer was only intended for the measurement of liquid water path, the key variable within CLIWA-NET. However, the design studies showed that a full profiling system, capable of simultaneous observation of liquid water path as well as temperature and humidity profiles, could be achieved for slightly higher costs. This radiometer – RPG-HATPRO – has been built by the German company Radiometer Physics GmbH (http://www.radiometer-physics.de/html/RPG_home.html). It fulfills the requirements defined within CLIWA-NET. For example, the maintenance interval is two months, the outside temperature range is from –30° C to +45° C, and the following features are available: rain detection and protection by a shutter system; GPS clock; measurements of environmental temperature, pressure, and humidity; possible Internet connection; and portability. The radiometer avoids lossy components, such as lenses, in the optical section. Instead, an off-axis paraboloid is used for both beam imaging and elevation scanning.

The RPG-HATPRO comprises total-power radiometers utilizing direct-detection receivers at all frequencies (14 channels up to 60 GHz). This approach avoids any problems that might arise from mixers or local oscillators (standing waves, frequency drifts, insufficient isolation, sideband suppression, higher system complexity, and cost). Thus, the stability and accuracy of the system are drastically improved. Furthermore, possible IF interference – caused, for example, by communication systems – is eliminated. The receivers of each frequency band are designed as filter banks in order to acquire each frequency channel in parallel. In addition, the flexibility to adjust each channel bandwidth individually allows for optimizing temperature profiling for both boundary layer and full troposphere.

4.8 All-Sky Multi-Wavelength Radiometer (ASMUWARA)

The ASMUWARA is a radiometer system designed for remote sensing of tropospheric water vapor, cloud liquid water, and temperature profiles [38]. It was designed and built at the IAP. The instrument consists of nine microwave channels in the frequency range from 18 GHz to 151 GHz; a broadband thermal infrared radiometer (wavelength band: 8 μm to 14 μm); meteorological sensors, including a rain detector; and an optional camera. The radiometers are housed in a temperature-controlled cylinder, with all beams aligned in a horizontal direction pointing to a rotating mirror that scans the sky and two calibration loads. The entire instrument can be rotated around its vertical axis. The beams perform a Rosetta-like pattern to map the sky hemisphere within 20 minutes. All channels

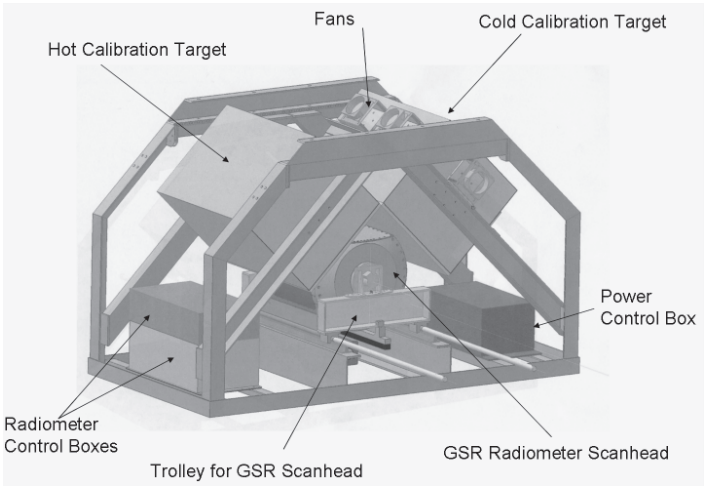

Figure 4. A schematic diagram of the GSR calibration and scanner system. The GSR scan head periodically moves out of the framework for atmospheric viewing on a trolley system, and shares time observing the atmosphere and the two thermally controlled blackbody reference targets.

have the same view and a common full beamwidth of 9°, formed by corrugated horns. The beamwidth is a compromise between angular resolution and sky coverage within the time scale of atmospheric variations. All horns are vertically polarized. The mirror reflection rotates the polarization during the scan from vertical, at the horizon, to horizontal, at nadir and zenith. A special challenge was the broad bandwidth required for the common instrument optics, ranging from 18 GHz to the thermal infrared. The solution was to construct a sufficiently large, flat aluminum mirror that allowed parallel beams for each spectral range, and to avoid any sort of radome. In this way, the instrument works well in periods without precipitation. A planned extension to all-weather operability will include a movable roof with a limited sky view during periods of rain. Figure 3 shows the weather-exposed parts of ASMURARA in operation on the roof at IAP. In principle, ASMUWARA is similar to other radiometer systems recently developed for the troposphere [3, 35. 90]. The main difference is the availability of and the concentration on the hemispheric imaging mode for all channels, including the infrared.

To avoid problems of internal calibration, two external calibration loads with good thermal properties were designed. In addition, tipcals are used for channels with low optical thickness. Whereas one load is kept as close as possible to the outside air temperature, the other load is warmer by about 10° C. Because of its favorable dielectric and thermal properties [56], beech wood was selected as the emitting material. A zigzag surface profile was selected to enhance the emissivity to at least 0.995 at all channels and at the relevant linear polarization. The temperatures of the loads are homogenized by internal ventilation, by a Styrofoam cover, and by monitoring with five thermocouples each.

4.9 NOAA/ETL Ground-Based Scanning Radiometer (GSR)

NOAA/ETL designed and constructed a multi-frequency scanning radiometer operating from 50 GHz to 380 GHz. The radiometers are installed into a scanning drum or scan head (see Figure 4). The GSR uses a sub-millimeter scan head with 11 channels in the 50-56 GHz region, a dual-polarization measurement at 89 GHz, seven channels around the 183.31 GHz water-vapor absorption line, a dual-polarized channel at 340 GHz, and three channels near 380.2 GHz. It also has a 10.6 μm infrared radiometer within the same scan head. All of the radiometers use lens antennas and view two external reference targets during the calibration cycle. In addition, the design of each of the radiometers includes two internal reference points for more-frequent calibration. The GSR instrument is a modification of a similar instrument that operated at the North Slope of Alaska/Adjacent Arctic Ocean site in 1999 [91]. A substantial improvement in radiometer calibration for ground observation in the Arctic environment has been achieved. Based on experience from the 1999 experiment, a new set of thermally stable calibration targets with high emission coefficients were also designed, constructed, and deployed. The primary use of the instrument is to measure temperature, water vapor, and clouds at cold ($-20°\,\mathrm{C}$ to $-55°\,\mathrm{C}$) and dry (PWV $< 5\,\mathrm{mm}$) conditions. A schematic of the GSR is shown in Figure 4. The beamwidths of the GSR channels are 1.8°, and can be averaged to give beamwidths that are consistent with the MWR (4.5° to 5.5°). The GSR was deployed in the NSA/AAO Arctic Winter Radiometric Experiment that was conducted in Barrow, Alaska, USA, during March-April, 2004 [92].

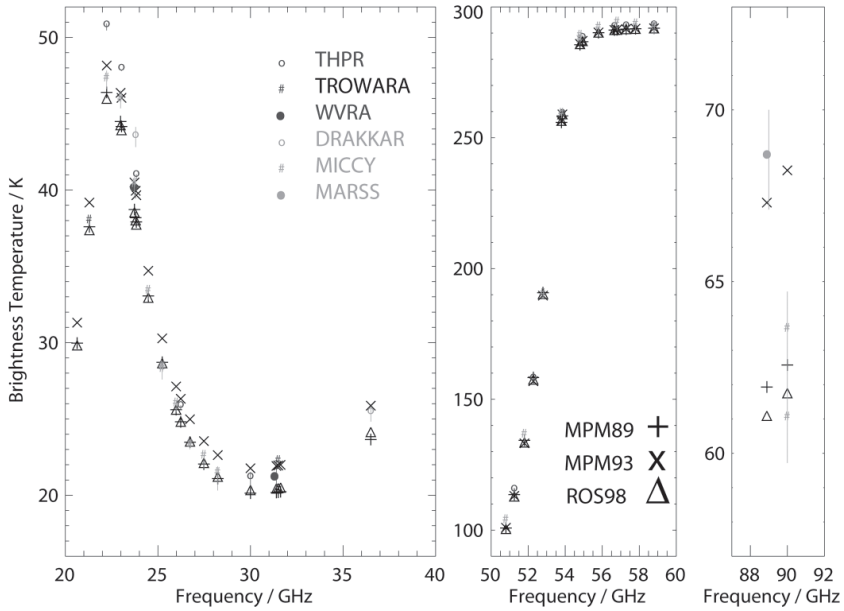

Figure 5. Simulated and measured brightness temperatures for a radio sounding on August, 2001, 11 UTC at Cabauw, the Netherlands. The radiometer measurements were averaged over 10 minutes past launch, and thin lines connect the maximum and minimum values within this interval. Simulations were performed using the gas absorption models MPM89 [4,13], MPM93 [14], and ROS98 [5].

4.10 Microwave Inter-Comparison Campaign

The Microwave Inter-Comparison Campaign (MICAM), during the first two weeks of August, 2001, comprised a unique comparison of eight microwave radiometers of different designs. It was performed at the central facility of the Dutch Weather Service (KNMI) in Cabauw, The Netherlands, where simultaneous measurements with cloud radar, ceilometer, radiosonde soundings, and many other instruments were performed. Most radiometers were already involved in the BALTEX Cloud Liquid Water Network, CLIWA-NET [31], at different locations within Europe. Thus, MICAM was intended to demonstrate that the measurements of the different radiometers were sufficiently comparable to be used to evaluate numerical weather prediction and climate models.

The radiometers were operated in Cabauw with a maximum separation distance of 30 m. In total, measurements at 47 different frequencies were performed. The observed brightness temperatures were compared with results from forward calculations based on high-quality radiosondes (RS-90). Meaningful comparisons can only be performed during cloud-free conditions, because it is not possible to model the liquid water content from radiosondes. Figure 5 shows one example for August 2, 2001. The spectral characteristics along the 22 GHz line and the 60 GHz oxygen complex are depicted well by the radiometers. Obviously, the 23.8 GHz channel of the DRAKKAR radiometer [31] overestimated the brightness temperature measured by three other radiometers (THPR [31], WVRA [31], MICCY [35]) at similar frequencies. A calibration problem has been identified by the responsible group (the French National Center for Scientific Research-CNRS), and a correction scheme has to be developed. The largest discrepancies between measurements occurred at 90 GHz. Unfortunately, the differences corresponded exactly to the uncertainties of the gas absorption models, and thus allowed no further constraint of these models. In conclusion, one can state that the accuracy of the raw brightness temperature measurements from the microwave radiometers is close to that of gaseous absorption models.

5. Retrieval Techniques

Techniques for deriving meteorological information from radiation measurements are generally based on Equation (1). Because only a finite number of imperfect radiation measurements are available, and a continuum of parameters is needed to describe profiles of temperature, water vapor, and cloud liquid, a rigorous mathematical solution does not exist, and the inverse problem is said to be ill-posed [57, 58]. Therefore, it is better to regard the measurements as constraints, and to blend them with supplementary sources of information or to drastically reduce the dimensionality of the inverse problem by projecting the profiles onto their linear functionals. Useful supplementary information can be provided by numerical meteorological forecasts, or by a priori information obtained from past data. Examples of profile linear functionals are integrated water vapor and liquid water path for moisture variables, and geopotential height for temperature profiles [45]. We briefly discuss algorithms that are commonly used in meteorological remote sensing.

Equation (1) can be approximated by a Fredholm integral equation of the first kind [9, 45]. In its discrete form it is written

$$g_e = Kf + \varepsilon , \tag{4}$$

where g_e is a vector composed of n measurements, f is an m-vector the components of which represent the profile that we want to determine, K is an $n \times m$ matrix relating the measurements to the unknown profile, and the n-vector ε explicitly denotes that the measurements have an unknown error component that will affect the solution to some degree. For mildly nonlinear problems, a perturbation form of Equation (1) is frequently used as the basis of subsequent iterations. Retrieval algorithms that require calculations of K for their implementation are called "physical." An excellent review article discussing techniques for solving Equation (4) was written by Rodgers [9].

A general algorithm for solving Equation (4) in the linear case is given by

$$\hat{f} - f_0 = \left[S_f^{-1} + K^T S_\varepsilon^{-1} K \right]^{-1} K^T S_\varepsilon^{-1} \left(g_e - K f_0 \right) . \tag{5}$$

This method is used to incorporate a priori statistics, including means and covariance matrices of f, S_f, and ε, S_ε, into the retrieval process [9, 45]. If successive approximations are used to generate Equations (4) and (5), then

$$\hat{g}_e = g_e - g\left(f_n \right) + K_n f_n , \quad n = 0,1,\ldots , \tag{6}$$

and

$$\hat{f}_{n+1} - f_0 = \left[S_f^{-1} + K_n^T S_\varepsilon^{-1} K_n \right]^{-1}$$

$$K_n^T S_\varepsilon^{-1} \left[g_e - g\left(f_n \right) + K_n \left(f_n - f_0 \right) \right] \tag{7}$$

In Equations (6) and (7), the matrices K_n are calculated for the nonlinear extension of Equation (4), using f_n as the expansion point for the required functional derivatives [9]. The matrices S_f and S_ε are defined as

$$S_f = E\{ f - f_0 \} \{ f - f_0 \}^T$$

and

$$S_\varepsilon = E\left\{\varepsilon\varepsilon^T\right\},$$

where the expectation value, E, ranges over a joint probability distribution of f and ε.

Choices of the function f_0 can include a climatological average, an initial guess based on a forecast, or an estimate derived from another remote sensor, and thus S_f is a measure of the uncertainty in the guess. In some cases the matrix could be diagonal, with $\left(\sigma_f\right)_i^2$ describing the uncertainty at the ith level, or even scalar, with $S_f = I\left(\sigma_f\right)^2$, were I is the identity matrix. Similarly, S_ε is composed of two terms: the first describes the instrumental uncertainty, and the second contains an estimate of the forward-model errors. If both S_f and S_ε are scalar, then the ratio $\gamma = (\sigma_\varepsilon)^2 \Big/ \left(\sigma_f\right)^2$ yields the regularization parameter γ of Twomey [57] and Tikonhov and Arsenin [58].

Although Equation (7) is general and many retrieval methods are its special cases, we mention a few other frequently used methods: neural-network inversion [59, 60], and Kalman filtering [61, 62, 63] and regression [64]. Kalman Filtering is also a general technique and is described in excellent books [65, 66]. Another technique of great promise is to combine radiometer data with a numerical forecast model, as has been done successfully in satellite meteorology [67, 68].

6. Radiometric Sensing of Tropospheric Meteorological Variables

Remote sensing of meteorological variables by radiometry is now a mature field, with a history of applications at least since the mid 1960s. The strengths of the techniques are accurate calibration, temporal resolutions of the order of seconds, and the ability to measure spatially integrated quantities. In this section, we review a few of the techniques that are now internationally well-established. We then present newer applications that have considerable potential for both research and operational meteorological applications.

6.1 Integrated Amounts of Water Vapor and Cloud Liquid

Both water vapor and cloud liquid are important variables in meteorology and climate. Due to thermodynamic processes of evaporation and condensation, as well as transport by winds, these quantities vary greatly in space and time. Water vapor is characterized by water-vapor density as a function of spatial coordinates and time. To characterize liquid in clouds requires knowledge of particle size, as well. Water clouds consist of a large number of droplets of varying sizes. The number of all droplets within the unit volume is the total number density [m^{-3}]. The drop-size distribution (DSD) describes the number density as a function of droplet radius, i.e., the number of drops per unit volume within a given radius interval. Due to the complex microphysical processes within clouds, drop-size distributions are highly variable in time and space. In contrast to raindrops, cloud droplets are perfect spheres. Thus, all cloud microphysical parameters can be calculated from the drop-size distribution. For example, the cloud liquid-water content (LWC) [kg m^{-3}] is given by the product of the total volume of water and the density of water. Because the volume of a sphere is proportional to the radius cubed, liquid-water content is also called the third moment of the drop-size distribution. It comprises one of the most interesting properties of clouds, and is the prognostic variable in most numerical weather-prediction and climate models for describing clouds, but few observations are available for the validation of the model results. By far the most accurate method for determining the liquid water path, the vertical integral of liquid water content, is ground-based passive microwave radiometry. However, for many applications it is also crucial to know at which altitudes the water is located. Several instruments can be used to determine the cloud-base height (e.g., cloud radars, cloud lidar ceilometers, and infrared (IR) radiometers); for cloud thickness, cloud radars are used. Finally, to determine profiles of liquid water content, the combination of passive microwave and cloud radar measurements is promising [69,70].

Dual-frequency measurements of brightness temperature at an optimum frequency near the 22.235 GHz water-vapor line and in a transmission window have been used to measure integrated water vapor and liquid water path for about 25 years [1, 45, 63]. The primary method is straightforward, and does not require the covariance matrices that are explicit in Equations (5) and (7). First, at each of the two frequencies, T_b is converted to opacity τ by use of Equation (3). The opacity, τ, is related to integrated water vapor and liquid water path, and to the dry component, τ_d, by

$$\tau = \tau_d + \kappa_V\left(IWV\right) + \kappa_L\left(LWP\right), \qquad (8)$$

where the mass absorption coefficients of water vapor, κ_V, and cloud liquid, κ_L, must be known.

In Equation (8), for example, we have

$$\kappa_V = \frac{\int_0^\infty \alpha_V\, ds}{\int_0^\infty \rho_V\, ds},$$

where α_V is the absorption coefficient due to water vapor and ρ_V is the water-vapor density. Using both a clear

and a cloud liquid-absorption model, together with an estimate of the atmospheric state (i.e., vertical profiles of pressure P; T; water-vapor density, ρ_V ; and cloud liquid density, ρ_L ;) the two mass absorption coefficients can be estimated. If the absorption models are accurate, then the accuracies of κ_V and κ_L are determined by the accuracy with which the atmospheric state is known. By solving the radiative-transfer equations at two frequencies, ν_1 and ν_2, for two unknowns, the integrated water vapor

$$IWV = \frac{\kappa_{L,\nu_2}\tau'_{\nu_1} - \kappa_{L,\nu_1}\tau'_{\nu_2}}{\kappa_{V,\nu_1}\kappa_{L,\nu_2} - \kappa_{V,\nu_2}\kappa_{L,\nu_1}}, \qquad (9)$$

and liquid water path,

$$LWP = \frac{-\kappa_{V,\nu_2}\tau'_{\nu_1} + \kappa_{V,\nu_1}\tau'_{\nu_2}}{\kappa_{V,\nu_1}\kappa_{L,\nu_2} - \kappa_{V,\nu_2}\kappa_{L,\nu_1}}, \qquad (10)$$

can be determined. The quantity τ' is $\tau - \tau_d$, where the total optical depth, τ, is determined from Equation (4). An example of integrated water vapor and liquid water path retrievals is shown in Figure 6. The general accuracy of dual-frequency radiometric measurement of integrated water vapor has been shown to be better than 1 mm rms [29]. However, because of the lack of in situ measurements of cloud liquid, an adequate experimental evaluation of liquid water path over a range of cloud conditions is not available.

Improvements on the dual-channel method can be made with multi-frequency observations. The liquid-water path can be estimated from atmospheric-emission measurements in the microwave region because in this spectral region the cloud contribution strongly increases with frequency (Figure 1). The standard dual-channel principle has been described above for the determination of integrated water vapor. For the retrieval of liquid water path, the channel close to the water-vapor absorption line corrects for the changing water-vapor concentration of the atmosphere. Such observations are – with the exception of expensive and rather limited aircraft measurements – the most accurate method for observing liquid water path with an estimated accuracy of better than 25 gm^{-2}. A rough estimation shows that about 10 gm^{-2} are caused by the measurement error, while the rest can be attributed to the under-determined retrieval problem. The additional use of the 90 GHz channel can further constrain the problem and improve accuracy to less than 15 gm^{-2} [69, 71].

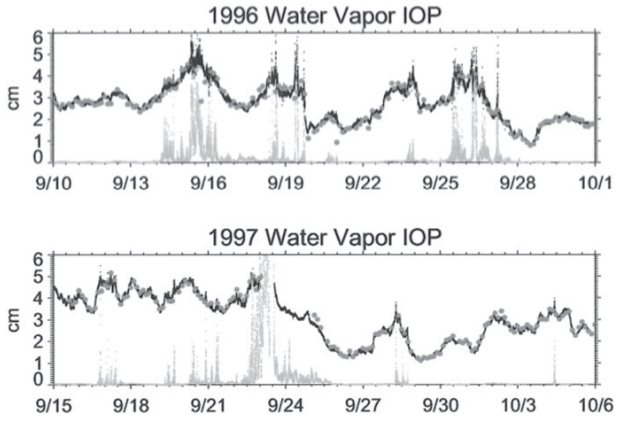

Figure 6. Precipitable water vapor and integrated cloud liquid (light solid line) derived from the NOAA/ETL microwave radiometer during the 1996 and 1997 Water Vapor Intensive Operating Periods. The circles represent PWV calculated from radiosonde profiles (after [29]).

6.2.1 Temperature Profiling

Radiometric temperature profiling can be accomplished by measuring the spectrum of radiation intensity at points along the side of the oxygen feature at 60 GHz [72]. By scanning outward from band center – where the opacity is so great that all signals originate from just above the antenna – onto the wing of the line – where the radiometer "sees" deeper (higher) into the atmosphere – altitude information is obtained. Emission at any altitude is proportional to local temperature; thus, the temperature profile can be retrieved. Either shoulder of the band center is suitable for retrieval of temperature-profile information.

A 6-channel zenith-viewing radiometer for measuring temperature was operated for several years by the NOAA Wave Propagation Laboratory (now the Environmental Technology Laboratory) [1]. The temperature-sensing channels of this radiometer were located at 52.8 GHz, 53.85 GHz, 55.45 GHz, and 58.8 GHz, and channels at 20.6 GHz and 31.65 GHz were used for measurement of water vapor and cloud liquid. The instrument was co-located with a radiosonde launch site, and its statistical accuracy was measured by comparisons with radiosondes taken twice per day. Retrievals of temperature were made every two minutes using Equation (4), with temperature covariance matrices evaluated from past radiosonde data. The rms accuracy of retrievals was generally better than 2 K rms from the surface to 500 mb. Radiometric retrievals are typically smoothed replicas of the sharp structure that is frequently exhibited by physical profiles; however, the integrals of these profiles used in deriving geopotential heights (the height of a given pressure level) were comparable in accuracy to those of radiosondes themselves. An example of geopotential height retrievals and comparisons with radiosondes is given in [45]. Radiometric temperature retrievals based on multi-channel data were also investigated in [63, 73, 74, 75].

Currently, Radiometrics Corporation has developed an advanced passive microwave radiometer based on a highly stable tunable synthesized local oscillator in the receiver. The radiometer observes atmospheric brightness temperatures in five frequency bands from 22 GHz to 30

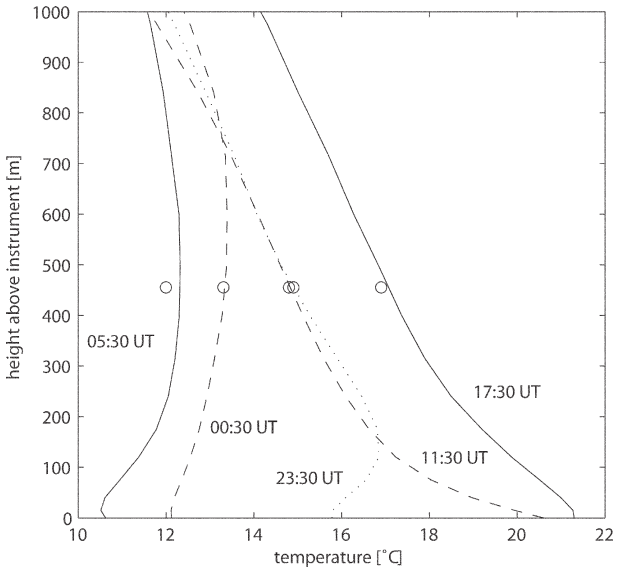

Figure 7. Temperature profiles in the lowest kilometer above ground at five different times on September 18, 2002, in Bern, measured with ASMUWARA, and a comparison with data from a meteo station (circles) located on a nearby TV tower (after [38]).

GHz, and in seven bands from 51 GHz to 59 GHz [3]. It also measures zenith infrared temperature, and surface temperature, humidity, and pressure. The radiometer has automated elevation and azimuth scanning capability, and the observation interval can be as short as several seconds. The instrument is relatively portable, with a volume of 0.12 m^3 and a weight of 32 kg. Historical radiosonde and neural network or regression methods are used for profile retrieval. Retrievals include temperature and humidity soundings up to 10 km height, and one-layer cloud liquid soundings.

Radiometric retrievals from this instrument are similar in accuracy to radiosonde soundings when used for numerical weather prediction [3]. Radiosonde assimilation errors used by the National Centers for Environmental Prediction for numerical weather analysis, and radiometric retrieval error determined from statistical comparisons with radiosondes [76], are of similar quality. Retrieval error is smaller than radiosonde sounding error for boundary-layer temperatures, and slightly higher above the boundary layer. The dominant radiosonde error is "representativeness" error. This results from the characterization of a model cell volume by a point measurement. This type of error is especially important when there are strong temporal or spatial gradients in the meteorological profiles. Radiometric retrievals are based on temporal averages, and are less susceptible to representativeness error than are radiosonde soundings. One of the potential advantages of high-temporal-resolution radiometric data (10 min to 15 min) is that the data could be directly assimilated into weather forecast models and improve short-term forecasts [76].

Temperature profiles have also been derived from the ASMUWARA [38]. The temperature profile is retrieved by optimal estimation, using Channels 5 through 8, using a climatology from radiosonde data, as described in [38, 77, 78]. Temperature profiles of September 18, 2002, are shown in Figure 7. The profiles nicely follow the temperature development measured at the meteorological station Bantiger on a nearby TV tower. At this early stage, the retrievals of temperature and of atmospheric water are independent. This works well for temperature profiles in the lowest km, where the 57 GHz channel is the dominant source of information. However, as shown in Figure 8, emission from clouds can compete with oxygen emission at the lower frequencies and, in this way, degrade the temperature retrieval. Therefore, in future applications of this instrument, the synergy of all channels is to be exploited.

6.2.2 Boundary-Layer Temperature Profiling

Angular techniques for measuring emission were developed by the ETL in the early 1970s [80], but due to mechanical simplicity, the zenith-viewing multi-spectral radiometers were chosen by ETL [1] as a component of a prototype remote-sensing system. However, in 1992, Russian scientists developed a scanning single-channel

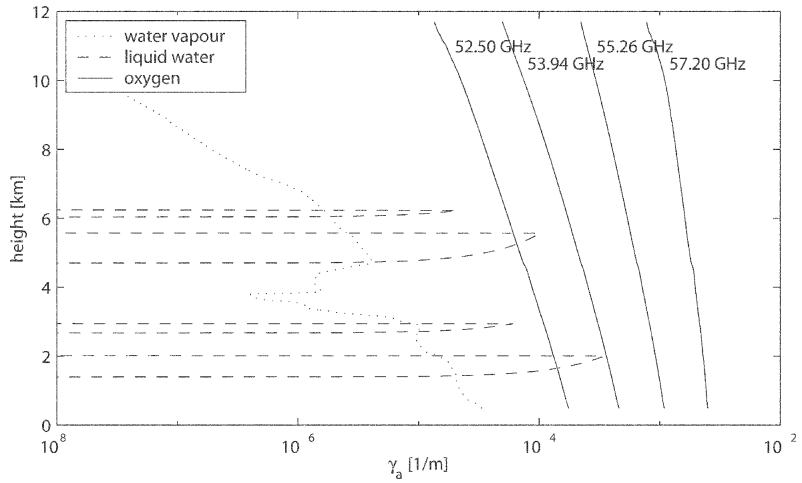

Figure 8. Vertical profiles of absorption coefficients due to oxygen of the temperature Channels 5 to 8 of ASMUWARA, and profiles of absorption coefficients at Channel 5 (52.5 GHz) due to water vapor and liquid water; simulations with MPM93 using radiosonde data from Payerne [38].

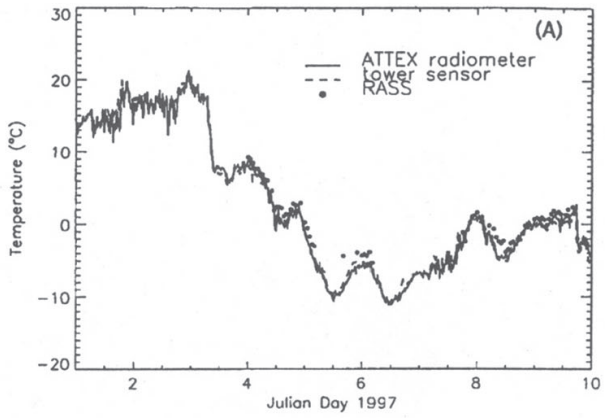

Figure 9a. A 10-day time series of temperature at 200 m as measured by the ATTEX radiometer, by the in situ measurement on the tower, and by a Radio Acoustic Sounding System (RASS) (January 1-10, 1997).

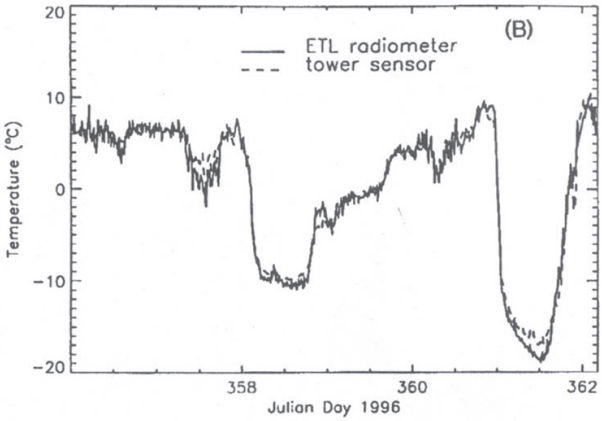

Figure 9b. A six-day time series of temperature at 200 m as measured by the ETL radiometer and by the in situ measurement on the tower (December 21-27, 1996; after [34]).

radiometer that showed promise for routine monitoring of the boundary layer [32, 73]. Development of this kind of radiometer has been continued by the Russian firm ATTEX, and numerous applications to boundary-layer studies have been published. The technique consists of measuring atmospheric emission at different angles in a wavelength band that exhibits relatively high atmospheric attenuation. The radiometer operates at 60 GHz (a wavelength of 5 mm), near the peak of the strong oxygen band; has a 6° beam width; and can yield data on a 1 sec basis. In this frequency region, the radiation in the horizontal direction can be used as a reference level, since it is essentially equal to the air temperature at the measurement height. Thus, an accurate air-temperature measurement provides a calibration of the radiometer offset. An independent measurement, such as a laboratory blackbody reference load, or calculations of T_b from radiosondes, is necessary to determine the radiometer's gain. Atmospheric air-temperature profiles can be obtained from the downwelling radiation at different elevation angles. The vertical resolution of the retrieved profiles is a function of altitude, and ranges from about 10 m near the surface to about 300 m at the 500 m altitude. Several experiments were conducted in Russia, Germany, the United Kingdom, and Japan by E. Kadygrov and his co-workers at ATTEX; a similar instrument has been operated by ETL near Boulder, Colorado, at a meteorological tower [81], at three experiments in Oklahoma, one in the tropics [28], and one at Barrow, Alaska [30]. In all cases, the rms errors were less than 0.5 K below 500 m. An example of temperature measured at 200 m above ground level (AGL) by the radiometer and by in situ measurements on a tower is shown in Figure 9. Because of the simplicity and portability of the instrument and its extremely flexible characteristics, it has been used from airborne, ship-, and ground-based platforms.

There also was a substantial amount of research into temperature profiling in particular, and microwave radiometry in general, in the former Soviet Union. A comprehensive review of this work, which contains numerous references to the original work, is contained in the book by Stepanenko et al. [89].

6.3 Profiling of Water Vapor

Information on the vertical distribution of water vapor is contained in the intensity and shape of the emission from pressure-broadened water-vapor lines. At high altitude, the emission from water vapor is from a narrow line, and at low altitudes, this line is pressure broadened. The intensity of emission is proportional to vapor density. Scanning the spectral profile and mathematically inverting the observed data can yield information on water-vapor profiles. Because of the relative weakness of the 22.235 GHz water-vapor line, frequency scanning of this line can yield only limited information on the vertical structure of profiles. In the clear troposphere, out of a possible selection of many frequencies around the 22.235 GHz line, only two or three channels are independent within radiometric noise levels of 0.5 K rms. However, because of the radiometric accuracy of better than 0.5 K that can be achieved by tipcal during clear conditions [44], it is promising that three well-calibrated measurements could have an impact on short-term moisture forecasts.

When radiometric data are accompanied by measurements from active sensors, such as cloud radars or lidars [8], added constraints can be imposed on the derived vapor profile [93]. For example, if the lower and upper boundary of a liquid cloud is known, then within the cloud layer, the relative humidity is 100%. If, in addition, information is known about the temperature profile, then the absolute humidity within the cloud layer is also known. Other synergies between radiometers and radars are also promising [82, 83].

The water-vapor line at 183.31 GHz is used for vapor profiling from aircraft and from satellites [52]. From a airborne platform, the high opacity of this line makes it ideal for lower-stratosphere and upper-troposphere water-vapor sensing. When used from a surface-based platform and for integrated water vapor amounts greater than about 5 mm, radiometric measurements in the vicinity of this line are

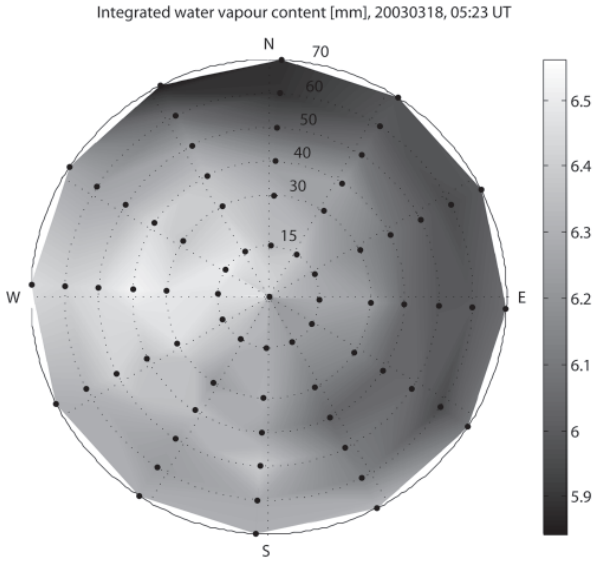

Figure 10. The hemispheric integrated water vapor distribution above Bern on March 18, 2003, as derived from ASMUWARA (after [38]).

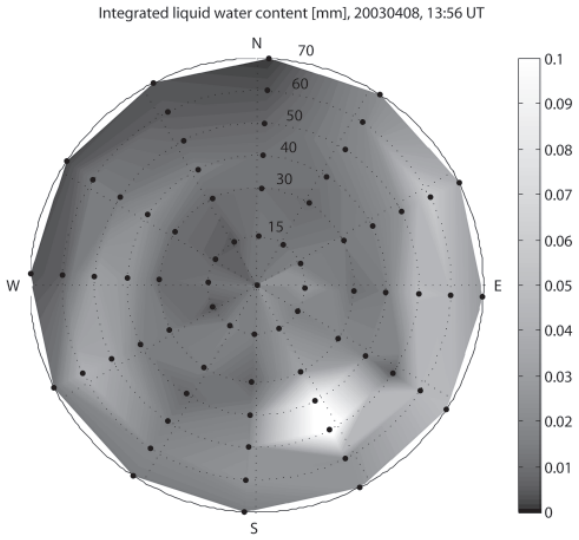

Figure 11. The hemispheric integrated liquid water distribution above Bern at 13:56 on April 8, 2003, as derived from ASMUWARA (after [38])

near saturation, and yield little information about moisture. However, during arctic winter conditions, when temperatures are frequently less than $-20°$ C and integrated water vapor is less than 2 mm, information on water-vapor structure and integrated water vapor can be obtained from multi-frequency measurements near the line [30].

6.4 Angular Scanning Observations of Cloud Liquid

As discussed in Section 4.8, the ASUMUWARA is capable of hemispheric imaging of clouds and water vapor. For channels with optically thin radiation, measured T_b can be accurately converted to opacity, τ. In turn, equivalent zenith values of integrated water vapor and liquid water path can be derived from τ. Based on local climatology and simulations based on MPM-93 [14], regression coefficients relating τ at 23.6 and 31.4 GHz to integrated water vapor and liquid water path were derived and applied to angular scanning data. An example of a hemispheric integrated water vapor image is shown in Figure 10; a spatial water-vapor variation appears with a gradient from northeast to southwest. A snapshot of the partly cloudy sky is depicted by the liquid water path data derived from channels 3 and 4 (Figure 11) and simultaneously by the thermal IR brightness temperature, T_{IR} (Figure 12). Clear sky is represented by $LWP = 0$ and T_{IR} below $-50°$ C. Liquid-water clouds with liquid water path up to 0.1 kg/m^2 and $T_{IR} \cong -25°$ C are apparent. For data evaluation, Martin et al. [38] compared integrated water vapor values in the range from 2 to 12 kg/m^2 from ASMUWARA with radiosonde data during the first winter period. The radiosonde values were slightly higher (bias 0.8 kg/m^2), whereas the standard deviation was 0.6 kg/m^2. Part of the bias was explained by the lower altitude of the Payerne station.

While the ASUMUWARA antenna beamwidth and scan patterns are optimized to provide a fast overview of the entire hemisphere, small-scale information on the cloud structure is measured by the microwave radiometer for cloud cartography (MICCY; see Section 4.6) [35]. This radiometer makes scanning measurements with high temporal (0.1 s) and angular (less than 1°) resolution. Figure 13 shows several azimuth scans observed by MICCY, made at an elevation angle of 30°.

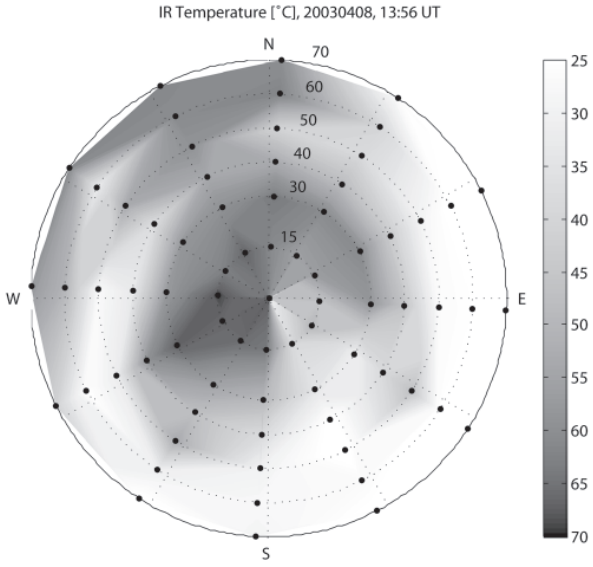

Figure 12. The hemispheric thermal IR image above Bern at 13:56 on April 8, 2003, as derived from ASMUWARA (after [38]).

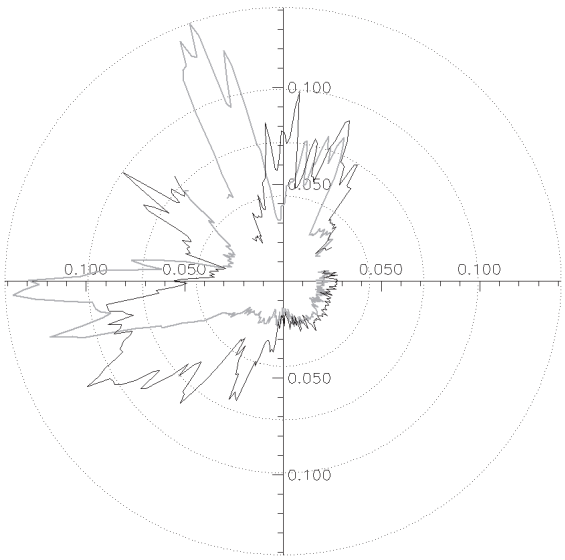

Figure 13 Series of 14 successive azimuth scans at 30 deg elevation with the multi-channel microwave radiometer MICCY having a beam width of less than 1 deg in all channels. Liquid water path was derived using a regression algorithm employing four frequency channels. After [69].

Such information can be used for studies concerning three-dimensional radiative transfer of solar radiation through clouds. Scanning measurements improve our estimate of the cloud water distribution and the cloud structure. Time series of cloud liquid water are strongly correlated on all spatial and temporal scales. Thus, for measurements in a fixed direction, it normally does not make sense to measure faster than once per second; this would only mean that you are measuring the same volume multiple times. By scanning, a new cloud volume is observed every time. Furthermore, by scanning the measurements are much better decorrelated, because the average distance between two points will be larger. Thus, a more representative, broader cloud water distribution will be found.

To extract cloud structure information from a large set of scans of liquid water path, we used the binned autocorrelation function, i.e., the correlation for all pairs of measurements within a certain range of distances (bin) was calculated and this was repeated for all bins. The correlation length (the length at which the autocorrelation function decreases below a threshold) is a strong function of the elevation angle: in one case study, the measurements made at an elevation of 43° were found to have a correlation length that is about three times as long as the correlation length at 70°. This is caused by the larger integration volume and, especially, the longer integration path of the measurements at 43°.

Scanning is important for studying the anisotropy of cloud structure. The binned autocorrelation can also be calculated for bins with a certain range of distances and angles to get a two-dimensional autocorrelation function. Two case studies showed strong anisotropies in the liquid water path field oriented in the direction of the wind. Thus, zenith measurements of the clouds that drift by on the wind would show a correlation length that is not representative of the field.

6.5 Integrated Profiling by Sensor Synergy

While the cloud water column can be derived accurately from microwave radiometer measurements alone, the information about its vertical distribution is rather limited. Therefore, microwave radiometer measurements are often combined with simultaneous cloud radar observations, which provide the radar reflectivity factor, Z, with a vertical resolution of approximately 50-100 m. Since Z is proportional to the sixth moment of the drop-size distribution and the cloud liquid-water content is proportional to the third moment, a direct conversion of Z to liquid water content results in large errors. Thus, a common approach used by Frisch et al. [70] scales the radar reflectivity profile to the liquid water path. A more sophisticated, physically based technique combines the microwave brightness temperatures, the attenuation-corrected radar reflectivity profile, the lidar-ceilometer cloud base, ground temperature and humidity, and the nearest operational radiosonde profile within an optimal estimation retrieval. The Integrated Profiling Technique (IPT) [82] can simultaneously derive profiles of temperature, humidity, and liquid water content. The retrieved IPT profiles are characterized by their physical consistency with respect to the microwave radiometer and cloud radar measurements. Additional constraints guarantee a match with the ground-level measurements, saturation within the cloud boundaries, and statistical consistency with the radiosonde temperature and humidity profiles. Error covariances of all measurements are required, such that all constraints can be met within an iterative optimal estimation procedure. The solution is interpreted as a probability density, so that a retrieval error estimate is inherently given. A further advantage of the IPT is that – in contrast to the liquid water path scaling methods – the liquid water content profiles are independent of errors of a liquid water path algorithm.

Presently, the IPT has been developed only for cases when the radar reflectivity is solely caused by liquid-water drops. This means that the occurrence of mixed-phase clouds within the vertical column above the instruments will make application of the IPT impossible. However, the presence of pure ice clouds above one or more liquid cloud layers will not influence the IPT, because ice clouds do not contribute to the microwave signal in the frequency range below 90 GHz. Furthermore, insect- and precipitation-dominated radar pixels need to be removed. Thus, to be able to apply the IPT automatically, a cloud classification was developed that distinguishes among six phases/regimes (pure ice, mixed-phase, pure liquid water, drizzle, significant precipitation, and unclassified). The classification makes

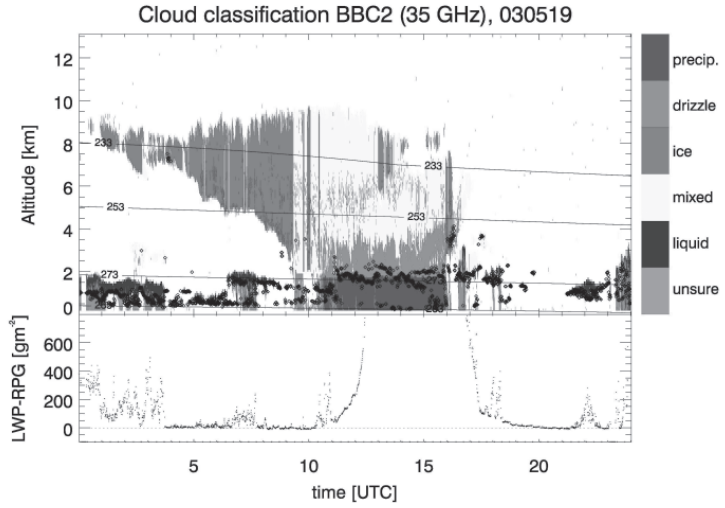

Figure 14. Cloud classification and liquid water path for May 19, 2003, at Cabauw. The temperature was derived from interpolated radiosondes. The classification was performed for each individual cloud radar range gate. The black dots indicate the cloud base height as observed by lidar ceilometer.

use of cloud radar, lidar-ceilometer, the nearest operational radiosonde temperature profiles, and microwave-radiometer-derived liquid water path. An example of the cloud classification for one day is shown in Figure 14. Obviously, the ice and mixed-phase clouds dominated the radar signal. Although the classification suggests that water clouds play a minor role, their strong influence on the solar radiation makes them of utmost importance for climate research. An IPT time series of liquid-water content, derived during the BBC2 campaign, is shown in Figure 15. Typical structures of a stratocumulus cloud can be observed with liquid water path values peaking around 400 g m^{-2}. The vertically integrated liquid water content values show quite good agreement with the liquid water path derived from a four-channel statistical retrieval.

The advantage of microwave remote sensing is that even in the presence of thick clouds, temperature and humidity can be determined with good accuracy. However, because the vertical resolution is relatively coarse (about 1-2 km [74]), sharp inversions can't be resolved completely. Figure 16 shows a time series of IPT-derived absolute humidity during the same time period shown in Figure 14. Again, quite good agreement of the integrated values can be seen between an independent statistical retrieval and the IPT. Notice the gradual increase of humidity as the cloudy period around 21.2 UTC sets in.

The IPT is a first step toward an "all-encompassing" profiling algorithm that combines measurements from all available instruments to derive the atmospheric state as accurately as possible. Since this task should ideally be accomplished in a physically consistent way, knowledge of all involved forward models is required. Future extensions will include infrared and ceilometer forward models to further constrain cloud microphysical parameters, especially in the lower part of the cloud.

7. Climate Applications

In the United States, the Department of Energy's Atmospheric Radiation Measurement (ARM) has developed a long-range program to study the effects of clouds on climate and on the development of climate models [84, 85]. In their experimental facilities to measure clouds and radiation, the ARM program has developed and operates three research sites in the Southern Great Plains (SGP), in North Central Oklahoma, USA, on the North Slope of Alaska (NSA), and in the tropical western Pacific (TWP). Because of their proven ability to measure integrated water vapor and liquid water path, ARM has deployed 10 MWRs (see Section 4.2) at their various research sites [2, 84]. The ARM facilities also routinely launch radiosondes, and

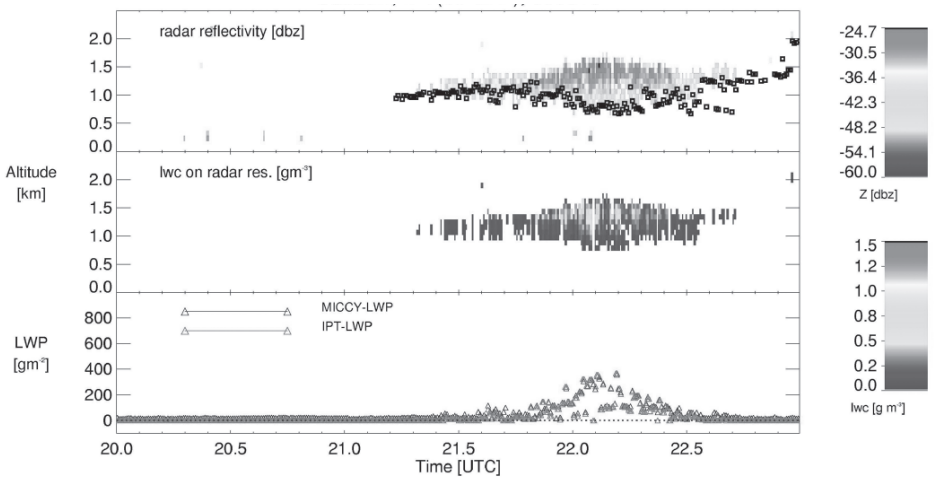

Figure 15. The radar reflectivity observed by a 35 GHz radar (top), the liquid water content retrieved using the integrated profiling technique (center), and the liquid water path (bottom), for the time period marked in Figure 14. The liquid water path was derived as the integral of the liquid water content values, and independently via a statistical algorithm from the set of brightness temperatures measured at four different frequencies.

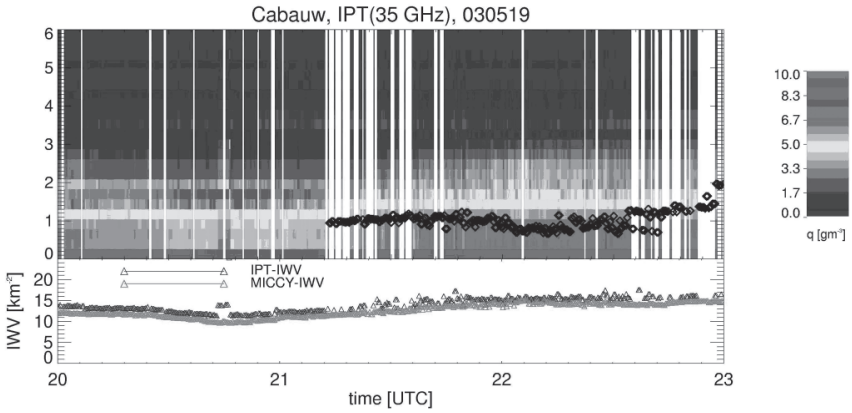

Figure 16. The time series of the specific humidity and integrated water vapor (IWV) for the same time interval as in Figure 14. The integrated water vapor was derived as the integral of the absolute humidity (q) values, and independently via a statistical algorithm from the set of brightness temperatures measured at four different frequencies.

operate infrared and optical radiation sensors, and lidar and millimeter-wave cloud radars (MMCR). In addition to providing measurement tools valuable for climate research, many of the data can be used to develop combined-sensor meteorological products.

One of the important results of MWR deployment has been the discovery and correction of dry bias humidity errors in Väisäla RS80 humidity sensors [7, 28]. The errors were first discovered in the comparison of measurements and radiosonde-based calculations of infrared radiance; consequently, three Water Vapor Intensive Operating Periods (WVIOPs) were conducted at the SGP [29] to address the problem. Several MWRs from a variety of US research institutions were deployed, and many kinds of radiosonde inter-comparisons were also done. As a result of these Water Vapor Intensive Operating Periods, currently, at the SGP site, all radiosondes are currently scaled by MWR integrated water vapor measurements. An example of the need for radiosonde corrections is shown in Figure 17, in which comparisons of calculations and MWR measurements are given. In this case, the use of an uncorrected radiosonde gave rise to a calculation error of about 10 K.

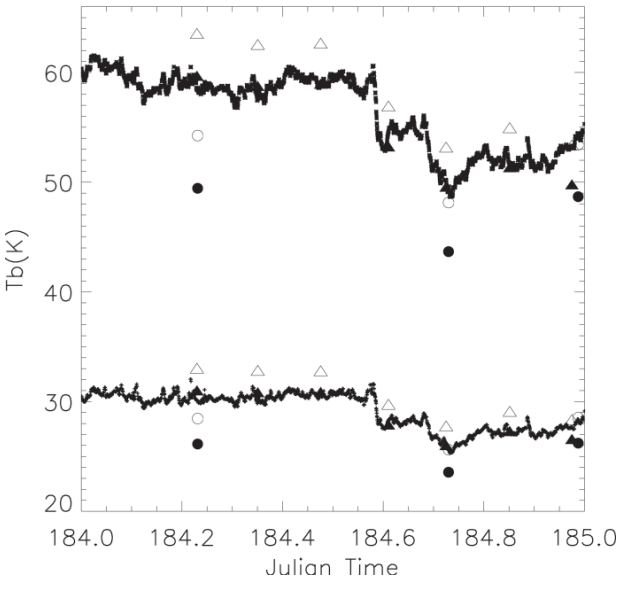

Figure 17. The 24-hr time series of T_b at 23.8 GHz (*) and 31.4 GHz (+) on July 3, 1999. The closed circles were calculated from the original ARCS-2 radiosondes (age = 315 days). The open circles were calculated from corrected ARCS-2 radiosondes. The closed triangles were calculated from the original RHB radiosondes (age = 172 days). The open triangles were calculated from corrected RHB radiosondes. The RTE model [5] was used (after [28]).

One possible limitation of MWR integrated water vapor measurements occurs during the arctic winter, when the integrated water vapor frequently is less than 2 mm, and the MWR lacks the sensitivity to provide accurate measurements. To overcome this limitation, radiometer measurements near 183 GHz have been made during cold and dry arctic conditions [30]. For example, during an entire month of cloud-free conditions at the NSA research site, the peak-to-peak variation of 23.8 GHz T_b was 3 K, while that from a millimeter-wave measurement at 183.31 ± 7 GHz was more than 80 K. An ETL/ARM experiment was conducted during March-April, 2004, to deploy a suite of radiometers ranging from 20 GHz to 380 GHz [92]. These instruments included the MWR, the Radiometric Profiler, and the GSR. Finally, this higher frequency is of great value not only for arctic regions, but also for mountain sites [79]. After instrumental improvements were completed, continuous observations at 183 GHz started again in early 2004 at the Jungfraujoch test site, at an altitude of 3600 m above sea level. About once every year, the radiometer-spectrometer instrument is also used in flight campaigns to measure the latitudinal variation of water vapor profiles in the stratosphere.

The MWR retrievals of liquid water path are also useful in developing models to calculate the transfer of solar radiation through clouds containing liquid, including mixed-phase clouds [86]. In particular, when MMCR and MWR are both available, the information on particle-size distribution can also be derived [87]. It is apparent that for years to come, the MWR will provide useful data for studying radiative transfer through clouds. For the cold arctic conditions, observations above 90 GHz can also improve cloud liquid retrievals.

8. Outlook

For the past 35 years, surface-based microwave radiometers operating below 60 GHz have provided useful data on temperature, water vapor, and clouds. Steady progress has been made in the development of robust, sensitive, and accurate radiometers. This has been accompanied by continued development of forward models for the accurate calculation of brightness temperature, although there is still some concern about cloud liquid characterization below freezing temperatures. The development of suitable inverse models has also occurred, but it now seems likely that assimilation of data with forecast models is the most promising technique for exploiting radiometer data [67, 68]. Of equal promise is the synergism of active and passive sensors, as has been achieved in cloud sensing [69, 70, 71], in moisture profiling [88, 89], and in the use of wind profiler estimates of significant moisture gradients to improve humidity profile retrieval [83].

Another promising area of research is the development of scanning radiometers that can measure horizontal gradients in water vapor and cloud liquid. For example, moisture gradients are frequently seen in tipcal measurements by MWRs [44].

The ASMUWARA has the potential to be an important tool for ground-based remote sensing of the troposphere. Advancements are expected to be made from the participation at the COST-720 inter-comparison campaign for temperature, humidity, and cloud profiling that was made in Payerne (Switzerland) from November, 2003, to January, 2004. Improvements will include the synergy of all channels in a coherent retrieval. With respect to instrumentation of ASMUWARA, an advancement will be the addition of the 151 GHz channel, which will allow higher sensitivity to clouds. Also to be exploited is the potential to measure precipitation; for this purpose, use will be made of the lower frequency channels (1 to 4) in case of rain, and the 151 GHz channel for dry snow. If the methods are successful, ASMUWARA will become a valuable tool in the ground validation of the international Global Precipitation Mission to be created by the space agencies of Europe, Japan and the USA. On the practical side, main improvements are expected from the protection of the instrument against wetting by raindrops.

Finally, the sensitivity of radiometers to both water vapor and cloud liquid increases with frequency, and arctic regions, with typical small amounts of both liquid and vapor, seem especially amenable to millimeter-wave radiometry. As satellite sensors increasingly use millimeter-wavelength radiometers, accurate forward models can be developed by using data from upward-looking sensors coupled with radiosondes. Such forward models are important in surface-, airborne-, and satellite-based remote sensing, as well as for communication.

9. Acknowledgements

We thank Ulrich Löhnert and Victor Venema for the fruitful discussions and the provision of figures. We thank Wim Hovius for his perfect management of the Cabauw observation site. Part of this work was done within the CLIWA-NET project sponsored by the EU under contract number EVK2CT-1999-00007. The algorithm development was partly funded by the German Department of Research and Education under Grant 07 AK106/0. A portion of the work presented in this paper was sponsored by the Environmental Sciences Division of the Department of Energy as a part of their Atmospheric Radiation Measurement Program. We thank Reginald Hill and Sergei Matrosov for several useful suggestions. We also thank Vinia Mattioli for her help in reformatting of several figures.

10. References

1. D. C. Hogg, M. T. Decker, F. O. Guiraud, K. B. Earnshaw, D. A. Merritt, K. P. Moran, W. B. Sweezy, R. G. Strauch, E. R. Westwater, and C. G. Little, "An Automatic Profiler of the Temperature, Wind and Humidity in the Troposphere," *Journal of Applied Meteorology*, **22**, 5, 1983, pp. 807-831.

2. J. C. Liljegren, "Automatic Self-Calibration of ARM Microwave Radiometers," in P. Pampaloni and S. Paloscia, (eds.), *Microwave Radiometry and Remote Sensing of the Earth's Surface and Atmosphere*, Utrecht, VSP Press, 2000, pp. 433-441.

3. R. Ware, R. Carpenter, J. Güldner, J. Liljegren, T. Nehrkorn, F. Solheim, and F. Vandenberghe, "A Multi-Channel Radiometric Profiler of Temperature, Humidity and Cloud Liquid," *Radio Science*, **38**, 4, 2003, pp. 8079-8032.

4. H. J. Liebe, "MPM, An Atmospheric Millimeter Wave Propagation Model," *International Journal of Infrared and Millimeter Waves*, **10**, 6, 1989, pp. 631-650.

5a. P. W. Rosenkranz, "Water Vapor Microwave Continuum Absorption: A Comparison of Measurements and Models," *Radio Science,* **33**, 4, 1998, pp. 919-928.

5b. P. W. Rosenkranz, "Correction to 'Water Vapor Microwave Continuum Absorption: A Comparison of Measurements and Models'," *Radio Science*, **34**, 4, 1999, p. 1025.

6. H. J. Liebe, G. A. Hufford, and T. Manabe, "A Model for the Complex Permittivity of Water at Frequencies below 1 THz," *International Journal of Infrared and Millimeter Waves*, **12**, 7, 1991, pp. 659-675.

7. D. Turner, B. Lesht, A. Clough, J. Liljegren, H. Revercomb and D. Tobin, "Dry Bias and Variability in Väisälä RS80-H Radiosondes: The ARM Experience," *Journal of Atmospheric and Oceanic Technology,* **20**, 1, 2003, pp. 117-132.

8. E. E. Clothiaux, T. P. Ackerman, G. G. Mace, K. P. Moran, R. T. Marchand, M. A. Miller, and B. E. Martner, "Objective Determination of Cloud Heights and Radar Reflectivities Using a Combination of Active Remote Sensors at the ARM CART Sites," *Journal of Applied Meteorology*, **39**, 5, 2000, pp. 645-665.

9. C. D. Rodgers, "Retrieval of Atmospheric Temperature and Composition from Remote Measurements of Thermal Radiation," *Reviews of Geophysics and Space Physics,* **14**, 1976, pp. 609-624.

10. Y. Han, E. R. Westwater, and R. A. Ferrare, "Applications of Kalman Filtering to Derive Water Vapor from Raman Lidar and Microwave Radiometers," *Journal of Atmospheric and Oceanic Technology*, **14**, 3, 1997, pp. 480-487.

11. M. Klein and A. J. Gasiewski, "Nadir Sensitivity of Passive Millimeter and Submillimeter Wave Channels to Clear Air Temperature and Water Vapor Variations," *Journal of Geophysical Research,* **105**, D13, 2000, pp. 17481-17511.

12. P. W. Rosenkranz, "Absorption of Microwaves by Atmospheric Gases," in Michael A. Janssen (ed.), *Atmospheric Remote Sensing by Microwave Radiometry*, New York, J. Wiley & Sons, Inc., 1993, Chapter 2, pp. 37-90.

13. H. J. Liebe and D. H. Layton, "Millimeter Wave Properties of the Atmosphere: Laboratory Studies and Propagation Modeling," National Telecommunications and Information Administration (NTIA) Report 87-24, 1987, 74 pp. (available from the National Technical Information Service, 5285 Port Royal Road, Springfield, VA, 22161 USA).

14. H. J. Liebe, G. A. Hufford, and M. G. Cotton, "Propagation Modeling of Moist Air and Suspended Water/Ice Particles at Frequencies below 1000," in *AGARD Conference Proceedings 542, Atmospheric Propagation Effects through Natural and Man-Made Obscurants for Visible through MM-Wave Radiation*, 1993, pp. 3.1 to 3.10 (available from NASA Center for Aerospace Information, Linthicum Heights, MD, USA).

15. H. C. Van de Hulst, *Light Scattering by Small Particles*, New York, Dover Publications Inc., 1981.

16. D. Deirmendjian, *Electromagnetic Scattering on Spherical Polydispersions*, New York, American Elsevier Publishing Company, Inc., 1969.

17. C. F. Bohren and D. R. Huffman, *Absorption and Scattering of Light by Small Particles*, New York, John Wiley, 1983.

18. P. Debye, *Polar Molecules*, New York, Dover, 1929.

19. E. H. Grant, J. Buchanan, and H. F. Cook, "Dielectric Behavior of Water at Microwave Frequencies," *Journal of Chemical Physics,* **26**, 1957, pp. 156-161.

20. V. I. Rosenberg, *Scattering and Extinction of Electromagnetic Radiation by Atmospheric Particles*, Leningrad, Gidrometeoizdat, 1972 (in Russian).

21. E. R. Westwater, Y. Han, M. D. Shupe, and S. Y. Matrosov, "Analysis of Integrated Cloud Liquid and Precipitable Water Vapor Retrievals from Microwave Radiometers during SHEBA," *Journal of Geophysical Research*, **106**, 23, 2001, pp. 32019-32030.

22. R. Rasmussen, R., M. Politovich, J. Marwitz, W. Sand, J. McGinley, J. Smart, R. Pielke, S. Rutledge, D. Wesley, G. Strossmeister, B. Bernstein, K. Elmore, N. Powell, E. Westwater, B. Stankov, and D. Burrows, "Winter Icing and Storms Project (WISP)," *Bulletin of the American Meteorological Society*, **73**, 7, 1992, pp. 951-974.

23. G. Hufford, "A Model for the Complex Permittivity of Ice at Frequencies below 1 THz," *International Journal of Infrared and Millimeter Waves*, **12**, 1991, pp. 677-682.

24. C. Mätzler, "Microwave Properties of Ice and Snow," in B. Schmitt et al. (eds.), *Solar System Ices, Astrophysical and Space Science Library,* **227**, Dordrecht, Kluwer Academic Publishers, 1998, pp. 241-257.

25. M. A. Janssen, "An Introduction to the Passive Remote Sensing of Atmospheres," in Michael A. Janssen (ed.), *Atmospheric Remote Sensing by Microwave Radiometry*, New York, J. Wiley & Sons, Inc,. 1993, pp. 1-36.

26. A. J. Gasiewski, "Microwave Radiative Transfer in Hydrometeors," in Michael A. Janssen (ed.), *Atmospheric Remote Sensing by Microwave Radiometry*, New York, J. Wiley & Sons, Inc., 1993, pp. 91-144.

27. S. Cruz Pol and C. S. Ruf, "Improved 20- to 32- GHz Atmospheric Absorption Model," *Radio Science*, **33**, 9, 1998, pp. 1319-1333.

28. E. R. Westwater, B. Boba Stankov, D. Cimini, Y. Han, J. A. Shaw, B. M. Lesht, and C. N. Long, "Radiosonde Humidity Soundings and Microwave Radiometers during Nauru99," *Journal of Atmospheric and Oceanic Technology*, **20**, 7, 2003, pp. 953-971.

29. H. E. Revercomb, H. E., D. D. Turner, D. C. Tobin, R. O. Knuteson, W. F. Feltz, J. Bannard, J. Bosenberg, S. Clough, D. Cook, R. Ferrare, J. Goldsmith, S. Gutman, R. Halthorne, B. Lesht, J. Liljegren, H. Linne, J. Michalsky, V. Morris, W. Porch, S. Richardson, B. Schmid, M. Splitt, T. Van Hove, E. Westwater, and D. Whiteman, "The ARM Program's Water Vapor Intensive Observation Periods: Overview, Initial Accomplishments, and Future Challenges," *Bulletin of the American Meteorological Society*, **84**, 1, 2003, pp. 217-236.

30. P. E. Racette, E. R. Westwater, Y. Han, A. J. Gasiewski, M. Klein, D. Cimini, D. C. Jones, W. Manning, E. J. Kim, J. R. Wang, V. Leuski, and P. Kiedron, "Measurement of Low Amounts of Precipitable Water Vapor Using Ground-Based Millimeterwave Radiometry," submitted to *Journal of Atmospheric and Oceanic Technology*, 2004.

31. S. Crewell, M. Drusch, E. van Meijgaard, and A. van Lammeren, "Cloud Observations and Modeling within the European BALTEX Cloud Liquid Water Network," *Boreal Environmental Research,* **7**, 2002, pp. 235-245.

32. E. N. Kadygrov and D. R. Pick, "The Potential Performance of an Angular Scanning Single Channel Microwave Radiometer and some Comparisons with In Situ Observations," *Meteorological Applications, UK*, **5**, 1998, pp. 393-404.

33. Y. G. Trokhimovski, E. R. Westwater, Y. Han, and V. Ye. Leuskiy, "The Results of Air and Sea Surface Temperature Measurements Using a 60 GHz Microwave Rotating Radiometer," *IEEE Transactions on Geoscience and Remote Sensing*, **GRS-36**, 1, 1998, pp. 3-15.

34. E. R. Westwater, Y. Han, V. G. Irisov, V. Leuskiy, E. N. Kadygrov, and S. A. Viazankin "Remote Sensing of Boundary-Layer Temperature Profiles by a Scanning 5-mm Microwave Radiometer and RASS: Comparison Experiment," *Journal of Atmospheric and Oceanic Technology*, **16**, 7, 1999, pp. 805-818.

35. S. Crewell, H. Czekala, U. Löhnert, C. Simmer, Th. Rose, R. Zimmermann, and R. Zimmermann, "Microwave Radiometer for Cloud Carthography: A 22-Channel Ground-Based Microwave Radiometer for Atmospheric Research," *Radio Science*, **36**, 2001, pp. 621-638.

36. F. T. Ulaby, R. K. Moore, and A. K. Fung, *Microwave Remote Sensing, Active and Passive. Volume 1, Microwave Remote Sensing Fundamentals and Radiometry*, Reading, Massachusetts, Addison-Wesley Publishing Company, 1981.

37. N. Skou, *Microwave Radiometer Systems: Design and Analysis*, Norwood, Massachusetts, Artech House, Inc., 1989.

38. L. Martin, A. Lüdi and C. Mätzler, "Tropospheric Monitoring with ASMUWARA," Proc. 6th International Symposium on Tropospheric Profiling (ISTP): Needs and Technologies, Leipzig, Germany, September 14-20, 2003 (also available from http://istp2003.tropos.de:8085/).

39. M. D. Jacobson and W. M. Nunnelee, "Design and Performance of a Spinning Flat Reflector for Millimeter-Wave Radiometry," *IEEE Transactions on Geoscience and Remote Sensing*, **35**, 1997, pp. 464-466.

40. M. J. Brittcliffe and R. C. Clauss, "The Effects of Water on the Noise-Temperature Contribution of Deep Space Network Microwave Feed Components," TMO Progress Report 42-145, May 15, 2001; http://tmo.jpl.nasa.gov/tmo/progress_report/42-145/145G.pdf.

41. S. Crewell, C. Simmer, A. Feijt and E. van Meijgaard, "CLIWA-NET Baltex Cloud Liquid Water Network," final report, BALTEX Report No. 26, ISSN 1681-6471.

42. J. Hach, "A Very Sensitive Airborne Radiometer Using Two Reference Temperatures," *IEEE Transactions on Microwave Theory and Techniques*, **MTT-16**, 9, 1968, pp. 629-636.

43. A. B. Tanner, A. L. Riley, "Design and Performance of a High-Stability Water Vapor Radiometer," *Radio Science*, **38**, 3, 2003, 8050, doi:10.1029/2002RS002673.

44. Y. Han and E. R. Westwater, "Analysis and Improvement of Tipping Calibration for Ground-Based Microwave Radiometers," *IEEE Transactions on Geoscience and Remote Sensing*, **GRS-38**, 2003, pp. 1260-1277.

45. E. R. Westwater, "Ground-based Microwave Remote Sensing of Meteorological Variables," in Michael A. Janssen (ed.), *Atmospheric Remote Sensing by Microwave Radiometry*, New York, J. Wiley & Sons, Inc., 1993, pp. 145-213.

46. R. Peter and N. Kämpfer, "Radiometric Determination of Water Vapor and Liquid Water and its Validation with other Techniques," *Radio Science,* **97**, D16, 1992, pp. 18173-18183.

47. C. Mätzler. "Ground-Based Observations of Atmospheric Radiation at 5, 10, 21, 35 and 94 GHz," *Radio Science*, **27**, 1992, pp. 403-415.

48. T. Ingold, R. Peter, and N. Kämpfer, "Weighted Mean Tropospheric Temperature and Transmittance Determination at Millimeter-Wave Frequencies for Ground-Based Applications," *Radio Science*, **33**, 1998, pp. 905-918.

49. R. Peter and B. Schmid, "Comparison of Columnar Water Vapor Determined from Microwave Emission and Solar Transmission Measurements," CWV4 in Proceedings Of the *Topical Symposium on Combined Optical-Microwave Earth and Atmosphere Sensing*, Albuquerque, NM, March 1993, pp. 193-198 (IEEE Cat. 93TH0519-9).

50. T. Ingold, B. Schmid, C. Mätzler, P. Demoulin, and N. Kämpfer, "Modeled and Empirical Approaches for Retrieving Columnar Water Vapor from Solar Transmittance Measurements in the 0.72, 0.82 and 0.94 μm Absorption Bands," *Journal of Geophysical Research*, **105**, D19, 2000, pp. 24327-24343.

51. C. Mätzler, L. Martin, G. Guerova, and T. Ingold, "Assessment of Integrated-Water-Vapour Data at Bern from GPS, Sun Photometry, Microwave Radiometry and Radiosonde," Proc. 2nd Workshop of COST Action 716, Exploitation of Ground-based GPS for Meteorology, GFZ Potsdam, January 28-29, 2002.

52. J. Wang, P. Racette, and L. A. Chang, "MIR Measurements of Atmospheric Water Vapor Profiles," *IEEE Transactions on Geoscience and Remote Sensing*, **GRS-35**, 1997, pp. 212-223.

53. J. Morland "TROWARA – Tropospheric Water Vapour Radiometer, Radiometer Review and New Calibration Model," IAP Research Report No. 2002-15, 2002.

54. D. Cimini, J. A. Shaw, Y. Han, E. R. Westwater, V. Irisov, V. Leuski, and J. H. Churnside, "Air Temperature Profile and Air-Sea Temperature Difference Measurements by Infrared and Microwave Scanning Radiometers," *Radio Science*, **38**, 3, 8045, 2003, doi:10.1029/2002RS002632.

55. F. Solheim, J. Godwin, E. Westwater, Y. Han, S. Keihm, K. Marsh, R. Ware, "Radiometric Profiling of Temperature, Water Vapor, and Liquid Water Using Various Inversion Methods," *Radio Science*, **33**, 1998, pp. 393-404.

56. C. Mätzler, "Messung der Wärmestrahlung der Erdoberfläche im Mikrowellengebiet," Diplomarbeit, IAP University of Bern, April 1970 (in German).

57. S. Twomey, *Introduction to the Mathematics of Inversion in Remote Sensing and Indirect Measurements*, New York, Elsevier, 1977.

58. A. N. Tikhonov and V. Y. Arsenin, *Solutions of Ill-Posed Problems*, Washington, DC, V.H. Winston and Sons, 1977.

59. J. H. Churnside, T. A. Stermitz, and J. A. Schroeder, "Temperature Profiling with Neural Network Inversion of Microwave Radiometer Data," *Journal of Atmospheric and Oceanic Technology*, **11**, 1994, pp. 105-109.

60. F. Del Frate and G. Schiavon, "A Combined Natural Orthogonal Functions/Neural Network Technique for Radiometric Estimation of Atmospheric Profiles," *Radio Science*, **33**, 1998, pp. 405-410.

61. W. M. Ledskam and D. H. Staelin, "An Extended Kalman-Bucy Filter for Atmospheric Temperature Profile Retrieval with a Passive Microwave Sounder," *Journal of Applied Meteorology*, **17**, 1978, pp. 1023-1033.

62. H. E. Moteller, L. L. Strow, and L. McMillin, and J. A. Gualtieri, "Comparison of Neural Networks and Regression-Based Methods for Temperature Retrievals," *Applied Optics*, **34**, 1995, pp. 5390-5397.

63. J. Askne and E. R. Westwater, "A Review of Ground-Based Remote Sensing of Temperature and Moisture by Passive Microwave Radiometers," *IEEE Transactions on Geoscience and Remote Sensing*, **GRS-24**, 1986, pp. 340-352.

64. N. A. Phillips, L. M. McMillin, D. Wark, and A. Gruber, "An Evaluation of Early Operational Temperature Soundings from TIROS-N," *Bulletin of the American Meteorological Society*, **60**, 1979, pp. 1188-1197.

65. A. Gelb, *Applied Optimal Estimation*, Cambridge, Massachusetts, MIT Press, 1988.

66.R. G. Brown and P. Y. C. Hwang, *Introduction to Random Signals and Applied Kalman Filtering*, New York, J. Wiley & Sons, 1997.

67.J. C. Derber and W.-S. Wu, "The Use Of TOVS Cloud-Cleared Radiances in the NCEP SSI Analysis System," *Monthly Weather Review*, **126**, 1998, pp. 2287-2302.

68. G. Ohring, K. Michell, M. Ji, S. Lord, and J. Derber, "Applications of Satellite Remote Sensing in Numerical Weather and Climate Prediction," *Advances in Space Research*, **30**, 2002, pp. 2433-2439.

69.U. Löhnert, U. S. Crewell, A. Macke, and C. Simmer, "Profiling Cloud Liquid Water by Combining Active and Passive Microwave Measurements with Cloud Model Statistics," *Journal of Atmospheric and Oceanic Technology*, **18**, 2001, pp. 1354-1366.

70.A. S. Frisch, G. Feingold, C. W. Fairall, T. Uttal, and J. B. Snider, "On Cloud Radar and Microwave Measurements of Stratus Cloud Liquid Water Profiles," *Journal of Geophysical Research*, **103**, 1998, pp. 23195-23197.

71.S. Crewell and U. Löhnert, "Accuracy of Cloud Liquid Water Path from Ground-Based Microwave Radiometry. Part II. Sensor Accuracy and Synergy," *Radio Science*, **38**, 3, 2003, doi:10.1029/2002RS002634.

72.E. R. Westwater, "Ground-Based Passive Probing Using the Microwave Spectrum of Oxygen," *Radio Science Journal of Research of the NBS* 9D, 9, 1965, pp. 1201-1211.

73. K. P. Gaikovich., E. N. Kadygrov, A. S Kosov, A. V. Troitskiy, "Thermal Sounding of the Boundary Layer of the Atmosphere at the Center of the Line of Oxygen Absorption," *Izvestia vuzov, Radiophysica*, **35**, 2, 1992, pp. 130-136.

74.J. Güldner and D. Spänkuch, "Remote Sensing of the Thermodynamic State of the Atmospheric Boundary Layer by Ground-Based Microwave Radiometry," *Journal of Atmospheric and Oceanic Technology*, **18**, 2001, pp. 925-933.

75.J. E. Liljegren, E. Clothiaux, S. Kato, and B. Lesht, "Initial Evaluation of Profiles of Temperature, Water Vapor and Cloud Liquid Water from a New Microwave Profiling Radiometer," *Proceedings of the 5th Symposium on Integrated Observing Systems*, Albuquerque, NM, American Meteorological Society, 2001

76.T. Nehrkorn and C. Grassotti, "Mesoscale Variational Assimilation of Profiling Radiometer Data," 16th Conference on Numerical Weather Prediction, Seattle, WA, American Meteorological Society, 2004.

77.A. Lüdi, L. Martin, and C. Mätzler, "The Retrieval of Temperature Profiles with the Ground-Based Radiometer System ASMUWARA," IAP Research Report No. 2003-13, September 2003.

78.L. Martin, "Microwave Transmission and Emission Measurements for Tropospheric Monitoring," Inauguraldissertation, Phil.-nat. Fakultät, Universität Bern, Juni 2003.

79.A. Siegenthaler, O. Lezeaux, D. G. Feist, and N. Kämpfer, "First Water Vapor Measurements at 183 GHz from the High Alpine Station Jungfraujoch," *IEEE Transactions on Geoscience and Remote Sensing*, **GRS-39**, 2001, pp. 2084-2086.

80.E. R. Westwater, J. B. Snider, and A. C. Carlson, "Experimental Determination of Temperature Profiles by Ground-Based Microwave Radiometry," *Journal of Applied Meteorology*, **14**, 4, 1975, pp. 524-539.

81.E. R. Westwater, Y. Han, V. G. Irisov, V. Leuskiy, E. N. Kadygrov, and S. A. Viazankin, "Remote Sensing of Boundary-Layer Temperature Profiles by a Scanning 5-Mm Microwave Radiometer and RASS: A Comparison Experiment," *Journal of Atmospheric and Oceanic Technology*, **16**,7, 1999, pp. 805-818.

82.U. Löhnert, S. Crewell, and C. Simmer, "An Integrated Approach towards Retrieving Physically Consistent Profiles of Temperature, Humidity and Cloud Liquid Water," *Journal of Applied Meteorology*, 2004 (in press).

83.B. B. Stankov, E. R. Westwater, and E. E. Gossard, "Use of Wind Profiler Estimates of Significant Moisture Gradients to Improve Humidity Profile Retrieval," *Journal of Atmospheric and Oceanic Technology*, **13**, 6, 1996, pp. 1285-1290.

84.G. M. Stokes and S. E. Schwartz, "The Atmospheric Radiation Measurement (ARM) Program: Programmatic Background and Design of the Cloud and Radiation Testbed," *Bulletin of the American Meteorological Society*, **75**, 1994, pp. 1201-1221.

85.T. P. Ackerman and G. M. Stokes, "The Atmospheric Radiation Measurement Program," *Physics Today*, **56**, 1, 2003, pp. 38-44.

86.P. Zuidema, B. Baker, Y. Han, J. Intrieri, J. Key, P. Lawson, S. Matrosov, M. Shupe, R. Stone, and T. Uttal, "An Arctic Springtime Mixed-Phase Cloudy Boundary Layer observed during SHEBA," submitted to *Journal of Atmospheric Sciences*, 2004.

87.M. D. Shupe, T. Uttal, S. Matrosov, and A. S. Frisch, "Cloud Water Contents and Hydrometeor Sizes during the FIRE Arctic Cloud Experiment," *Journal of Geophysical Research*, **106**, D14, 2001, pp. 15015-15028.

88.B. B. Stankov, B. E. Martner, and M. K. Politovich, "Moisture Profiling of the Cloudy Winter Atmosphere Using Combined Remote Sensors," *Journal of Atmospheric and Oceanic Technology*, **12**, 1995, pp. 488-510.

89.V. D. Stepanenko, G. G. Schukin, L. P. Bobylev, and S. Yu. Matrosov, *Radioteplolocatziya v Meteorologiya* (*Microwave Radiometry in Meteorology*), Leningrad, Gidrometeozdat, 1987 (in Russian).

90.J. C. Liljegren, "Improved Retrievals of Temperature and Water Vapor Profiles with a Twelve-Channel Radiometer," *2004 Proc. of the Eighth Symposium on IOAS-AOLS*, American Meteorological Society, January 11-15, 2004, Seattle, WA.

91.E. R. Westwater, P. E. Racette, and D. Cimini, "The Arctic Winter Millimeter-Wave Radiometric Experiment: Summary, Conclusions, and Recommendations," *Proc. of 11th Atmospheric Radiation Measurement (ARM) Science Team Meeting*, March 19-23, 2001 (available at http://www.arm.gov/docs/documents/technical/conf_0103/index.html).

92.E. R. Westwater, M. Klein, and V. Leuski, A. Gasiewsk, T. Uttal, D. Hazen, D. Cimini, V. Mattioli, B. L. Weber, S. Dowlatshahi,J. A. Shaw, J. Liljegren, B. M. Lesht, and B. D. Zak, "The 2004 North Slope of Alaska Arctic Winter Radiometric Experiment," *Proc. of 14th Atmospheric Radiation Measurement (ARM) Science Team Meeting*, Albuquerque, New Mexico, March 22-26, 2004 (available at http://www.arm.gov/docs/documents/technical/conf_0304/index.html).

93.Y. Han and E. R. Westwater, "Remote Sensing of Tropospheric Water Vapor and Cloud Liquid Water by Integrated Ground-Based Sensors," *Journal of Atmospheric and Oceanic Technology*, **12**, 5, 1995, pp. 1050-1059.

Progress in Radio Ray Tracing in the Ionosphere

J.A. Bennett
P.L. Dyson
R.J. Norman

Abstract

The theoretical basis of ray tracing as part of the construction of an approximate solution of Maxwell's equations is discussed. The rays can then be seen as arising as characteristic curves of a partial differential equation for the phase of the wave. If carried through in detail, this approach leads to an additional phase shift that has been discussed previously. Methods of efficiently calculating field strength, Doppler shift, and absorption of the waves are discussed, based on a variational formulation. Some history of the evolution of ionospheric radio ray tracing is given. Numerical and analytic or closed-form ray tracing are contrasted, and guidance is given on the choice of appropriate technique in a particular application. Finally, some suggestions are given for possible useful extensions of the ray-tracing approach.

1. Introduction

Many interactions between the ionosphere and radio waves at HF involve refraction and reflection due to ionospheric structure on a scale large compared with the wavelength of the radio wave. Such interactions can be studied using ray tracing or quasi-optics. This is much simpler than attempting a full solution of Maxwell's equations combined with the electromagnetic properties of the ionosphere. There are situations where scattering and diffraction in the ionosphere are important. We return to these phenomena briefly later, but a detailed discussion is beyond the scope of this review.

Ray tracing has applications in experimental studies, where the radio wave is used to probe the structure of the ionosphere; and in radio navigational systems and in radio geodesy, as well as in communication-system prediction and management. It is particularly useful when detailed knowledge about the interaction of the radio wave and the ionosphere is required, such as in over-the-horizon radar and in single-station location of distant radio transmitters.

Applications of ray tracing can fall into one of two categories: those involving calculations carried out "offline," as in system planning or analysis of experiments already carried out; and those carried out "online," as part of an operational system or interactive experiment. The latter category is usually the more demanding. For example, in an HF over-the-horizon radar (OTHR) it may be necessary to calculate thousands of rays with a refresh time of a few minutes. It is thus necessary to consider rapid techniques of ray tracing, as well as to avoid the tracing of unnecessary rays as far as possible.

This review discusses the theoretical basis and significance of ray tracing and quasi-optics, and a number of applications of ray tracing. As alluded to, the time required for ray tracing is sometimes more than just a matter of convenience, and reducing the computational time is an essential requirement. This remains true despite the continuing increase in computer speed and power. Various methods of speeding the ray-tracing process, such as the use of analytic or closed-form ray tracing, are discussed.

2. Basis of Ray tracing and Quasi-Optics

2.1 Formulation

We assume the ionosphere is slowly varying in time and space. We restrict our consideration to an effective point transmitter that is fixed in space and transmitting narrowband signals. Situations involving strong absorption are neglected. While the assumption of a slowly varying ionosphere is essential, all of the other restrictions can be relaxed by suitable extension of the theory. However, it is believed these restrictions are adequate for a discussion of the most common applications of ionospheric radio ray tracing. Striving for greater generality would distract from the purpose of this review.

J. A. Bennett is with the Department of Electrical and Computer Systems Engineering, Monash University, Vic 3800 Australia; Tel: +61 3 9905-3484; E-mail: john.bennett@eng.monash.edu.au.
P. L. Dyson and R. J. Norman are with the Department of Physics, La Trobe University, Vic 3086 Australia; Tel: +61 3 9479 1433; E-mail: r.norman@latrobe.edu.au.

Editors note: This is one of the invited *Reviews of Radio Science*, from Commission G.

The construction of approximate solutions of Maxwell's equations, based on a rapidly varying phase function (also known as the eikonal or einsatz), has come to be known as quasi-optics. Rays, with the same properties as familiar light rays, play an essential role in the construction of this approximate solution. In order to carry out the construction, rays must be traced. This may be thought of as the fundamental meaning of radio rays in the ionosphere.

Assuming a suppressed $\exp(j\omega t)$ time dependence, Maxwell's equations can be written as

$$\left\{\begin{bmatrix} 0 & -\nabla\times \\ \nabla\times & 0 \end{bmatrix} + j\omega\begin{bmatrix} \varepsilon & 0 \\ 0 & \mu \end{bmatrix}\right\}\begin{bmatrix} \mathbf{E} \\ \mathbf{H} \end{bmatrix} = -\begin{bmatrix} \mathbf{J} \\ \mathbf{J_m} \end{bmatrix}, \quad (1)$$

where $\mathbf{E}$ and $\mathbf{H}$ are the electric and magnetic field intensities; ε and μ are the dielectric permittivity tensor and magnetic permeability tensors, respectively; and $\mathbf{J}$ and $\mathbf{J_m}$ are the electric and (fictitious) magnetic current source vectors. In the ionosphere, ε is a function of frequency, ω, and of position, $\mathbf{r}$, through its dependence on plasma frequency, gyrofrequency, and the direction of the Earth's magnetic field. For the moment we neglect losses, so that the generalized permittivity tensor,

$$\Im = \begin{bmatrix} \varepsilon & 0 \\ 0 & \mu \end{bmatrix} \quad (2)$$

is Hermitian. Equation (1) can be generalized to represent more complicated situations – for example, a slowly drifting plasma – by including further off-diagonal terms in $\Im$.

Equation (1) can be thought of as a convenient shorthand way of writing Maxwell's equations. It can also be represented in terms of conventional matrices and six-element column vectors. In writing Equation (1), losses due to collisions are neglected. We return to this point later.

We seek an approximate solution of the form

$$\begin{bmatrix} \mathbf{E} \\ \mathbf{H} \end{bmatrix} = \left\{\begin{bmatrix} \mathbf{E} \\ \mathbf{H} \end{bmatrix}_0 + \cdots\right\}\exp\left(-\frac{j\omega}{c}P\right), \quad (3)$$

where c is the free-space velocity of light. The scalar quantity P is to be determined. We shall see it is essentially the phase path of a ray from the source to the point at which the wave field is to be evaluated. The construction of this approximate solution can be systematized by the introduction of a formal large expansion parameter that multiplies all frequencies, both the wave frequency and the plasma and gyro-frequencies, at each point in the ionosphere [1-3]. We omit these mathematical details. The essential point is that the phase term, $\omega P/c$, is large, so that the exponential term is rapidly varying compared with the column vector it multiplies, and compared with the scale of the ionospheric structure.

If we substitute from Equation (3) into Equation (1), we are lead to the equation

$$\left\{-\frac{j\omega}{c}\begin{bmatrix} 0 & -\nabla P\times \\ \nabla P\times & 0 \end{bmatrix} + j\omega\begin{bmatrix} \varepsilon & 0 \\ 0 & \mu \end{bmatrix}\right\}$$

$$\left\{\begin{bmatrix} \mathbf{E} \\ \mathbf{H} \end{bmatrix}_0 + \cdots\right\}\exp\left(-\frac{j\omega}{c}P\right) = \begin{bmatrix} 0 \\ 0 \end{bmatrix}. \quad (4)$$

To the lowest order, from Equation (4) we obtain

$$\mathbf{A}(\nabla P, \mathbf{r}, f)\begin{bmatrix} \mathbf{E} \\ \mathbf{H} \end{bmatrix}_0 = \begin{bmatrix} 0 \\ 0 \end{bmatrix}, \quad (5)$$

where

$$\mathbf{A}(\nabla P, \mathbf{r}, f) = \left\{\begin{bmatrix} 0 & -\nabla P\times \\ \nabla P\times & 0 \end{bmatrix} - c\begin{bmatrix} \varepsilon & 0 \\ 0 & \mu \end{bmatrix}\right\}. \quad (6)$$

The notation emphasizes that $\mathbf{A}$ depends on position and frequency through ε. For convenience, we now use f rather than radian frequency ω to describe the frequency dependence of ε. Some minor algebraic manipulation has been carried out to cast $\mathbf{A}$ in this form.

For nontrivial solutions of Equation (5) to exist, the determinant of the matrix must vanish. This can be formally written as

$$G(\nabla P, \mathbf{r}, f) = 0, \quad (7)$$

with

$$G(\nabla P, \mathbf{r}, f) = \det \mathbf{A}(\nabla P, \mathbf{r}, f). \quad (8)$$

It is also necessary that $\begin{bmatrix} \mathbf{E} \\ \mathbf{H} \end{bmatrix}_0$ must lie in the right null space of $\mathbf{A}(\nabla P, \mathbf{r}, f)$.

2.2 Ray Equations

Equation (7) is a partial differential equation for P, often know as the equation of the eikonal. It may be solved by the method of characteristics [4]. The characteristic curves are our rays. The Hamiltonian form of the ray equations can be written

$$-\frac{d\mathbf{p}}{du} = \theta\frac{\partial G}{\partial \mathbf{r}}(\mathbf{p}, \mathbf{r}, f) \quad (9)$$

$$\frac{d\mathbf{r}}{du} = \theta \frac{\partial G}{\partial \mathbf{p}}(\mathbf{p}, \mathbf{r}, f),$$

to be solved with

$$G(\mathbf{p}, \mathbf{r}, f) = 0 \cdot \tag{10}$$

In writing Equation (9), a slightly unconventional but commonly used mathematical notation has been adopted. The partial derivative $\partial G/\partial \mathbf{r}$ could be written ∇G. Similarly, $\partial G/\partial \mathbf{p}$ represents the space vector $\left(\partial G/\partial p_x, \partial G/\partial p_y, \partial G/\partial p_z\right)$.

The value of the multiplying factor θ in Equation (9) depends upon two things: the choice of the parameter u, which increases along the ray; and upon the particular form in which $G(\mathbf{p}, \mathbf{r}, f)$ is written. Note that there is no need to write $G(\mathbf{p}, \mathbf{r}, f)$ in the special form used by Hamilton [5].

Some choices of u are more convenient than others. An obvious choice is the arc length along the ray. However, sometimes – particularly in numerical ray tracing – it is more convenient to choose the elapsed group path along the ray. If θ is taken to be

$$\theta = 1 \Big/ \left(\mathbf{p} \bullet \frac{\partial G}{\partial \mathbf{p}} - f \frac{\partial G}{\partial f} \right), \tag{11}$$

then u becomes the elapsed group path, regardless of the particular form in which $G(\mathbf{p}, \mathbf{r}, f)$ is written.

Once, or as the rays are determined, P is found from

$$\frac{dP}{du} = \mathbf{p} \cdot \frac{d\mathbf{r}}{du}. \tag{12}$$

Written in terms of (wave) refractive index and arc length, s, the result is

$$P = \int_{ray} \mu \cos\alpha \, ds. \tag{13}$$

Note that there is an angle between the direction of phase propagation and the ray direction, here denoted by α. The wave refractive index is denoted μ, not to be confused with the magnetic permeability tensor occurring in Equation (1).

2.3 Refractive-Index Surface

Equation (10), for fixed $\mathbf{r}$, is the condition for the existence of plane-wave solutions of frequency f in a homogeneous medium having the same properties as the actual medium at the point $\mathbf{r}$. For fixed f, it defines a surface in $\mathbf{p}$ space. This surface is known by a number of names, including the relative-slowness surface [6] and the refractive-index surface [7], since the length of a $\mathbf{p}$ vector with its tip on the surface is the refractive index for waves propagating in the direction of the $\mathbf{p}$ vector. These freely propagating plane waves are often known as characteristic waves.

The refractive-index surface for radio waves in the ionosphere is a graphical representation of the Appleton-Lassen formula for the refractive index in a cold magneto-plasma. Since the pioneering work of Poeverlein [8-10], it has been recognized that this surface plays a vital role in the propagation of radio waves in the ionosphere. From the second part of Equation (9), it can be seen that the ray direction is normal to the refractive-index surface. There is an angle, often denoted α, between the ray direction and the direction of phase propagation.

The nature of the refractive-index surface has been extensively studied: see [7] for a detailed discussion. It is important to note that the surface consists of two sheets. These represent the two magnetoionic modes. The corresponding waves are known as characteristic waves. It is thus necessary to generalize the approximate solution of Equation (3). There will be families of rays and contributions to the wave field associated with both modes.

We now see from Equation (11) that the phase of the wave propagating in the inhomogeneous ionosphere is calculated by accumulating or integrating along the ray the phase of appropriate characteristic plane waves propagating in a series of infinitesimal slices of homogeneous plasma. Also, looking at Equation (3), it can be seen that the local polarization of the wave must be that of the characteristic wave.

The separate surfaces can touch in some circumstances for propagation in the direction of the Earth's magnetic field. This leads to coupling between modes [7], and the form of the approximation needs to be generalized. We do not pursue this here. The occurrence of the Spitze [7], to be discussed briefly in a later section, arises when the surface degenerates to segments of a straight line.

2.4 Field Strength

Because the ray direction at each point on a ray is in the direction of the ray (we omit the proof), there can be no energy flux through the walls of a tube made up of rays. Energy is conserved within ray tubes. The flux into the tube at the transmitter must equal the flux out at the receiver. The product of the cross sectional area of the ray tube and the Poynting vector must remain constant. As the ray tube spreads, the magnitude of the Poynting vector falls. This can be used to determine field strength.

2.5 Additional Phase

The variation of the electric and magnetic field intensities along the ray can be established from Equation (3).

The calculations involved in setting up the transport equations for the fields are intricate, and require the introduction of a set of normalized six-vectors describing the null space of the matrix. We omit the details here. They were set out in detail in a general context by R. M. Lewis [1]; see also [2]. The necessary calculations for the ionospheric case, generalized to allow for strong absorption, were given by [3, 11]. The solution of these transport equations gives rise to an additional phase shift. The additional phase is related to the rotation of polarization that occurs in an isotropic medium when the ray exhibits torsion [12].

Berry [13] gave Budden and Smith [14, 15] the credit for discovering this phase shift for propagation in a plane-stratified medium, and pointed out the significance of the result to the geometrical phase of quantum mechanics. Credit for the original discovery of this additional phase shift in the general case should probably go to Lewis [1]. The term was included in the solution obtained by Bennett [3] for propagation in a strongly absorbing ionosphere. Explicit formulae for the general case, also with strong absorption, were published later [11]. With strong absorption, the "additional phase" becomes complex. There is also an additional change in amplitude. The physical origin of the additional phase in the plane-stratified case has been shown to be the phase change as characteristic waves are transmitted from one slab to the next [14, 16]. These do not vanish as the slabs become infinitely thin. In the general case, it is presumed that the origin is the same, although the reviewers are unaware of a published demonstration of this point.

In HF radio propagation, the phase of a wave is usually many times 2π. The additional phase is only of practical significance when it is necessary to make detailed comparison of the phase of two rays, as in Faraday rotation or considerations of reciprocity [7]. The reviewers are unaware of any general-purpose ray-tracing program that determines the electric and magnetic fields of the wave, including the additional phase.

2.6 Initial Conditions

We have been talking about tracing rays, or, in places, families of rays. What rays should be traced ? To find the wave properties at all points we must trace all the rays leaving the source. Considering an effective point source, we require all the rays with initial $\mathbf{p}$ vectors satisfying Equation (10) when applied at the source point. If it is desired to calculate the wave properties at a particular point – say, at a target or receiver – then all the rays leaving the source and passing through that point must be traced. There may be more than one ray through a given point, for example, a high-angle ray and a low-angle ray. There may be rays associated with both magnetoionic modes.

The wave amplitudes associated with each ray are established by matching the far-field solution for the source in a homogeneous region to the ray solution. For a true point source, this involves a projection of the current-source vector onto the corresponding polarization vector: see, e.g., [11]. If the source lies below the ionosphere, this raises the difficult topic of limiting polarization [7]. When the current is distributed in space – for example, antenna current – there is a further projection in $\mathbf{p}$ space. In most circumstances, once we move away from the antenna it behaves as an effective point source, and all rays come from a single point.

3. Ray Variations

The purpose of this section is not to present a formal development of the theory of ray variations, which can be found elsewhere [17, 18]. Rather, it is to introduce some key ideas by way of example, in order to cast further light on the significance of ray tracing, and to provide some key tools that enable more efficient ray tracing. The initial discussion is in terms of derivatives, but in many applications a variational formalism is more convenient. Such a notation was introduced by Hamilton [5].

3.1 Doppler Shift

The phase of the contribution to the wave associated with a particular ray (or, more strictly, ray tube) is $-(2\pi f)P/c$. If the properties of the ionosphere are changing slowly with time, G and, consequently, P, will be functions of time. The received instantaneous frequency will be shifted by Δf, where

$$\Delta f = -(f/c)\partial P/\partial t \cdot \tag{14}$$

From Equation (12), we find

$$\frac{d}{du}\partial P/\partial t = \frac{\partial \mathbf{p}}{\partial t}\bullet\frac{d\mathbf{r}}{du} + \mathbf{p}\bullet\frac{d}{du}\frac{\partial \mathbf{r}}{\partial t}\cdot \tag{15}$$

In reversing the order of differentiation in writing Equation (15), it has been assumed that the ray does not suffer reflection from a moving conducting surface. Equation (15) can be written

$$\frac{d}{du}\partial P/\partial t = \frac{\partial \mathbf{p}}{\partial t}\bullet\frac{d\mathbf{r}}{du} + \frac{d}{du}\left(\mathbf{p}\bullet\frac{\partial \mathbf{r}}{\partial t}\right) - \frac{d\mathbf{p}}{du}\bullet\frac{\partial \mathbf{r}}{\partial t}. \tag{16}$$

Now consider Equation (10). Holding frequency, f, constant, but allowing for the time dependence, and differentiating with respect to time, we find

$$\frac{\partial G}{\partial \mathbf{p}}\bullet\frac{\partial \mathbf{p}}{\partial t} + \frac{\partial G}{\partial \mathbf{r}}\bullet\frac{\partial \mathbf{r}}{\partial t} + \frac{\partial G}{\partial t} = 0\,. \tag{17}$$

Multiplying through by θ and comparing with Equation (9), we find

$$\frac{d\mathbf{r}}{du}\bullet\frac{\partial \mathbf{p}}{\partial t} - \frac{d\mathbf{p}}{du}\bullet\frac{\partial \mathbf{r}}{\partial t} + \theta\frac{\partial G}{\partial t} = 0\,. \tag{18}$$

Substituting in Equation (16), we find

$$\frac{d}{du}\partial P/\partial t = -\theta\frac{\partial G}{\partial t} + \frac{d}{du}\left(\mathbf{p}\bullet\frac{\partial \mathbf{r}}{\partial t}\right). \qquad (19)$$

This equation can be integrated along the ray to determine the time rate of change of the phase path and, hence, the Doppler shift. If the ray endpoints are fixed, the contribution from the second term vanishes. The Doppler shift due to slow changes in the ionosphere can be written in terms of the (wave) refractive index, μ, and the arc length, s, in the familiar form [19].

$$\Delta f = -(f/c)\int_{ray}\frac{\partial\mu}{\partial t}\cos\alpha\, ds. \qquad (20)$$

The second term of Equation (19) gives the means of coping with moving transmitters, receivers, and reflectors.

This derivation has been presented at some length because it enables us to draw some general conclusions. The path of the ray is certainly a function of the time changes in the ionosphere, but provided the endpoints remain fixed, this changes do not contribute to the time derivative of the phase. To find the derivative, there is no need to perform ray tracing at successive times and perform numerical differentiation.

3.2 Group Path and Time of Flight

If the wave is now modulated with narrowband modulation, using a familiar group-delay calculation, the time of flight, τ, along the ray is given by

$$\tau = \frac{1}{c}\frac{\partial(fP)}{\partial f} = \frac{1}{c}\left(P + f\frac{\partial P}{\partial f}\right). \qquad (21)$$

That is, the modulation appears to have propagated over a distance

$$P' = P + f\frac{\partial P}{\partial f}. \qquad (22)$$

In using this notation, we are anticipating a following result. From Equation (19), assuming the ray endpoints are fixed, and replacing t with f, we find

$$\frac{dP'}{du} = \mathbf{p}\bullet\frac{d\mathbf{r}}{dt} - f\theta\frac{\partial G}{\partial f}. \qquad (23)$$

This can be integrated along the ray to find P'. Written in terms of the group refractive index, μ', and the arc length, s, the result is

$$P' = \int_{ray}\mu'\cos\alpha\, ds. \qquad (24)$$

Thus, P' is the group path as defined by Appleton (see, e.g., [7]). This result shows that the time of flight along the ray is the sum or integral of the local times of flight along each section of the ray.

Making use of Equation (9), Equation (23) can also be written

$$\frac{dP'}{du} = \theta\mathbf{p}\bullet\frac{\partial G}{\partial \mathbf{p}} - f\theta\frac{\partial G}{\partial f}. \qquad (25)$$

This is the result used in establishing Equation (11) as the condition that the ray parameter is the elapsed group path along the ray. Notice that making this choice results in

$$\frac{dP'}{du} = 1. \qquad (26)$$

We remark in passing that, from Section 3.1, it can be seen that small changes in phase path due to changes in the ionosphere involve no contribution due to changes in the ray geometry. On the other hand, changes in the group path do involve a contribution due to changes in the ray. The reason for this is that as Equation (22) shows, such changes involve a second derivative (or variation) of the phase path.

3.3 Ray Tubes

We have seen that establishing the cross-sectional area of a ray tube enables the power flux of the wave to be determined as it propagates out from the source. While it is possible to carry out ray tracing for a series of rays and to take differences to establish the cross-sectional area, this is only an approximation, since the differential quantity is required. It is also extremely inefficient in numerical ray tracing, since it requires the tracing of rays with far greater precision than would otherwise be required.

It is possible to determine the ray tube by tracing a pair of linearly independent ray variations. The variation is the linear term in the difference between the principal ray and neighboring rays. In the case of a point source, these rays differ from the principal ray in that their initial directions have been varied. This overcomes the difficulties outlined in the previous paragraph. This is an idea that has been independently discovered by a number of authors [11, 18, 2-22]; see also [7].

We set out the derivation of equations here only in general form to indicate what is involved. Details can be found in the various publications to which reference has been made. Taking variations in Equation (9),

$$-\frac{d\delta\mathbf{p}}{du} = \theta\frac{\partial\delta G}{\partial\mathbf{r}} + \delta\theta\frac{\partial G}{\partial\mathbf{r}} \qquad (27)$$

$$\frac{d\mathbf{r}}{du} = \theta\frac{\partial\delta G}{\partial\mathbf{p}} + \delta\theta\frac{\partial G}{\partial\mathbf{p}},$$

where

$$\delta G = \frac{\partial G}{\partial\mathbf{r}}\bullet\delta\mathbf{r} + \frac{\partial G}{\partial\mathbf{p}}\bullet\delta\mathbf{p}, \qquad (28)$$

subject to

$$\delta G = 0\cdot \qquad (29)$$

Were frequency or time variations – or any other variation of the ionospheric properties – to be considered, there would be an additional term in Equation (28). Notice that the fact that δG is set equal to zero does not mean that its derivatives vanish, any more than the fact that G is set equal to zero means that its derivatives vanish. The value of $\delta\theta$ depends upon what points on the rays are to be compared. The secret to successful application of the method often lies in this choice. In numerical ray tracing it is frequently convenient to take variations in surfaces of constant phase, that is, to choose

$$\mathbf{p}\bullet\delta\mathbf{r} = 0\cdot \qquad (30)$$

This requires

$$\frac{d\mathbf{p}}{du}\bullet\delta\mathbf{r} + \mathbf{p}\bullet\frac{d\delta\mathbf{r}}{du} = 0. \qquad (31)$$

Substituting from Equations (9) and (27), we have

$$-\theta\frac{\partial G}{\partial\mathbf{p}}\bullet\delta\mathbf{p} + \mathbf{p}\bullet\left(\delta\theta\frac{\partial G}{\partial\mathbf{p}} + \theta\frac{\partial\delta G}{\partial\mathbf{p}}\right) = 0. \qquad (32)$$

If G is factorized and written in a form that makes $\mathbf{p}\bullet\partial G/\partial\mathbf{p}$ equal to a constant, then

$$\mathbf{p}\bullet\frac{\partial\delta G}{\partial\mathbf{p}} + \delta\mathbf{p}\bullet\frac{\partial G}{\partial\mathbf{p}} = 0. \qquad (33)$$

Combining these results, we have

$$\delta\theta\mathbf{p}\bullet\frac{\partial G}{\partial\mathbf{p}} = \theta\left(\frac{\partial G}{\partial\mathbf{r}}\bullet\delta\mathbf{r} + \frac{\partial G}{\partial\mathbf{p}}\bullet\delta\mathbf{r}\right). \qquad (34)$$

In view of Equation (29), this choice makes $\delta\theta$ zero.

3.4 Absorption

If the effect of collisions between electrons and other particles is included, the dielectric tensor is no longer Hermitian. The theory of Section 2 can be extended to cover this case, as outlined briefly in Section 5. It is possible to examine the first- (and higher-) order effects of including collisions using ray variations [23]. In particular, scaling the collision frequency at each point in terms of a representative electron collision frequency, and obtaining the variation of the generalized phase path in terms of that collision frequency, we find

$$\frac{d\delta_\nu P}{du} = -\theta\frac{\partial G}{\partial\nu}\nu, \qquad (35)$$

where the derivative on the right-hand side and the ray path are to be evaluated in the absence of collisions. This can be integrated along the ray. Now instead of $(2\pi f/c)P$, the generalized phase path becomes $(2\pi f/c)(P+\delta_\nu P+\ldots)$. Because the quantity $\nu\partial G/\partial\nu$ is purely imaginary, we find attenuation (in nepers) that can be written

$$A = \frac{2\pi f}{c}\int_{ray}\chi\cos\alpha\, ds, \qquad (36)$$

where the generalized refractive index, n, takes the form

$$n = \mu - j\chi + O(\nu^2) + jO(\nu^3), \qquad (37)$$

where $\nu\partial n/\partial\nu = -j\chi$. The refractive index and all derivatives are to be evaluated when ν is zero. Thus, only the linear term in the dependence on collisions is used in calculating absorption. It is not correct to use the full expression for the imaginary part of the complex refractive index and integrate along the ray that results when collisions are neglected. Nor is it correct to include collisions and to base ray tracing on the real part of the resulting complex refractive index. This includes one second-order term, but neglects another equally important second-order term. Notice that, as in the cases discussed in Sections 3.1 and 3.2, the introduction of collisions does alter the ray path: it becomes complex. However, this change does not contribute to the first-order calculation of absorption.

4. Ray tracing

4.1 Some History

Many of the early methods of ionospheric ray tracing were graphical, e.g., that of Poeverlein [8-10] who discovered the phenomenon known as the Spitze [7], sharp corners that appear under some circumstances in ionospheric

radio waves, because he carried out numerical and graphical calculations, rather than purely algebraic calculations.

The widespread availability of powerful high-speed digital computers has made numerical ray tracing in the ionosphere a practical proposition. Interest in ionospheric ray tracing was stimulated by the papers of Haselgrove [24] and Haselgrove and Haselgrove [25], who went back to the work of Hamilton, first published in 1837 [5], as indeed had Poeverlein [8-10].

Since 1968, there has been a steady increase in the use of analytic or, more properly, closed-form ray tracing. Croft and Hoogasian [26] showed that for the case of a spherical ionosphere and neglecting magnetoionic effects, solutions to the ray equations can be obtained in terms of known functions by a choice of suitable functions to describe the radial structure of the ionosphere. The basic functions employed are quadratics in the inverse of the radius, and are known as quasi-parabolic functions, because the coefficients can be chosen so that the function is scarcely distinguishable from a parabola.

An account of developments in ionospheric ray tracing up to the 1960s has been given by Kelso [27, 28]. Developments up to the late 1980s were discussed by Bennett and Dyson [29]. A more general review of progress in the theory of HF waves in the second half of the 20th century has been given by Suchy [30].

4.2 Choice of Ray-Tracing Technique

The first choice that must be made in a particular application is whether to employ numerical or closed-form ray tracing. Numerical ray tracing is the more general. It allows the ionosphere to vary in three dimensions. It can, within the limitations of quasi-optics, take full account of magnetoionic effects. On the other hand, it is slow. It requires a detailed knowledge of the ionospheric structure, and particular care must be taken to avoid discontinuities in the representation of that structure. Closed-form ray tracing is much faster. However, only highly symmetrical ionospheric structures can be considered; treatment of magnetoionic effects is approximate.

The second choice is whether to adopt an existing computer program, or to write one from scratch. This is a personal choice. Factors to be considered include the following: Is a sufficiently general program, adequately documented, available ? Can the ionospheric description be entered in a manner that is convenient? Is the type of output required available ?

4.3 Numerical Ray tracing

There are several features that any numerical ray-tracing program should have if it is to provide efficient ray tracing. The method of integration should have an adaptable step size with error control, and the target error should be set realistically. It has long been recognized that choosing an elapsed group path (or time of flight) eases the step-size changes required, because when the ray geometry is changing rapidly, the group path tends to be growing slowly. The tracing of unnecessary rays should be avoided. This can involve using ray variations to calculate ray-tube spreading and homing-in to a target or receiver.

The most widely distributed general ray-tracing program is probably that developed by Jones [31, 32]. It is still in use in many places. The Jones program provides for a number of models of ionospheric electron distribution and the Earth's magnetic field. However, the program does not include automatic homing-in or field-strength calculations, but it does allow the Doppler shift to be calculated using the equivalent of Equation (19). There are other ray-tracing programs that have been adopted by different groups concerned with HF propagation in the ionosphere. They are not necessarily freely available.

There are situations in which transverse gradients are important and off-great circle paths arise, e.g., [33]. In these cases, full numerical ray tracing is required. In other cases, the propagation is essentially two dimensional, and a program capable of dealing only with two-dimensional problems may be more efficient. Coleman [34] adopted this approach, and took advantage of the redundancy in the symmetrical form of the ray equations to achieve faster, efficient ray tracing.

A general purpose ray-tracing program, incorporating variational ray-tube calculations, and neglecting magnetoionic effects, has been developed. These same varied rays were used for homing-in using a two-dimensional Newton-Raphson method [35]. Vastberg [36, 37] and Norman [38] have implemented general ray-tracing programs including ray-tube calculations based on varied rays for the full magnetoionic case. However, this does not work well when the ray endpoint is a complicated function of the initial ray direction. Strangeways [39] has used Nelder-Mead optimization to achieve homing-in.

4.4 Analytic or Closed-Form Ray Tracing

Rather than a single quasi-parabolic layer [26], Hill [40] and Milsom [41] modeled a more complicated ionosphere using several distinct quasi-parabolic and quasi-linear [42] layers.

Dyson and Bennett [43] and Baker and Lambert [44] independently demonstrated the advantages of a model consisting of smoothly joined quasi-parabolic layers or segments. Here, "smoothly joined" means that the plasma frequency and its derivative are continuous at the segment boundaries.

Chen et al. [45] showed that multiple quasi-parabolic segments could be fitted automatically to measured data,

starting at the peak of the F2 layer and working downwards. The number of segments required to achieve a specified accuracy of fit is not known a priori, and this is a disadvantage in some applications. Huang and Reinisch [46] developed a fitting technique that adjusts the segment boundaries to minimize error, and minimizes the number of segments to achieve a given error. Dick and Cander [47] determined a family of profiles characterized by standard, scaled, vertical-incidence ionospheric characteristics.

In the absence of the Earth's magnetic field, the smoothly joined multiple quasi-parabolic segment model can give expressions in terms of logarithmic functions for ground range, group path, phase path, loss of signal strength due to ray spreading, and so on, for oblique radio propagation. The results obtained are free of the spurious singularities that arise with models made up of segments that are not joined up smoothly [41]. However, there are non-physical jumps in signal strength. In addition, the calculated phase can have discontinuities of curvature with ground range. This is a problem in modeling the behavior of large antenna arrays. These problems are overcome by the use of quasi-cubic segments, that is, functions cubic in the inverse of the radius [48]. This allows the second derivatives to also be continuous at the segment boundaries. Propagation results are obtained in terms of elliptic functions.

This discussion has referred to ray tracing neglecting the Earth's magnetic field and, hence, magnetoionic effects. It is possible to take approximate account of magnetoionic effects by a frequency-scaling technique. In some cases, additional correction terms are also needed [49]. The results are surprisingly accurate except on very short paths. Nothing is learned about the change in the ray path itself associated with magnetoionic effects.

The method only applies to spherically symmetrical ionospheres. Although displacing the center of the Earth and the center of the ionosphere allows some degrees of freedom, this generalization appears to be of limited practical use. Norman and Cannon [50] have developed an approach based on segmenting the ionosphere horizontally as well as vertically. Most applications of multiple quasi-parabolic segments have been to radio waves reflected from the ionosphere, but these have also been applied to Earth-satellite paths [39].

5. Limitations and Generalizations

The theory presented in Section 2 is not valid near – or, strictly speaking, beyond – a caustic. This is clear because at a caustic, the cross section of the ray tube vanishes, predicting a non-physical infinite signal strength. It is possible to extend the theory to cope with caustics. However, in many situations, the field strength near the caustic is not required. Along the rays beyond the caustic, there is a small additional phase shift [7], which is usually not important at HF.

The theory of Section 2 dealt only with effective point sources. It is possible to deal with extended sources. The family of rays is determined by a consistency requirement at the source [4]. Thus, for example, plane-wave sources can be considered, e.g., [3]. This is important from a theoretical point of view, since in means that the WKB approximation is just a special case of three-dimensional ray tracing [7].

In the case of very wideband modulation, and also for rapidly moving sources, space-time ray tracing [1, 6, 51] is useful. Rather than variables $\mathbf{r}$ and $\mathbf{p}$, it is convenient to choose $(\mathbf{r}, \mathbf{t})$ and $(\mathbf{k}, \omega)$.

In the presence of strong absorption, the theory of Section 2 can be extended by the use of complex rays, e.g., [3, 7]. It is not often that such weak signals are of interest.

It is known that full-wave solutions are needed in the presence of strong gradients. For example, Barnes [52] has examined the limits of ray theory as applied to Faraday rotation. With the increasing interest in wideband systems, coherence bandwidth and spectral spreading have become more important. For example, spectral spreading is a serious problem in HF radars where spectral techniques are used to distinguish targets from clutter. This is probably due to weak scatter within modes. A number of approaches have been explored to embed scattering theory within a quasi-optics solution involving significant ray bending [53-58]. Strong scattering is also important in some cases, particularly within the equatorial and polar ionospheres. In these cases, we also do not necessarily have straight-line propagation. There is also a need for further systematic investigation in this area.

6. Recent Progress

Only a few papers in recent years, up to 2003, have presented new progress in ray-tracing methods. As discussed earlier, Norman and Cannon [50] developed a new two-dimensional analytic ray-tracing technique that accounts for horizontal gradients as well as vertical gradients. Norman [59] also developed a simple two-dimensional analytical ray-tracing technique to deal with horizontal gradients varying with height. Xenos and Yioultsis [60] presented a finite-difference time-domain (FDTD) computational method and applied it to an HF one-hop radio-link study. They provided results for a single propagation path, for which they found their calculated ionospheric path loss agreed very well with that determined using Davies' [61] composite empirical model, which includes various losses, such as absorption, dispersion, etc. The agreement seemed fortuitous, since the result they presented showed 175 dB of the total path loss of 148.2 dB occurring on the up-going path through the D and E regions, and virtually no loss occurring on the down-going path through these regions. The path considered was an east-west, mid-latitude link at noon, and certainly the Davies formula for the absorption losses, which Xenos and Yioultsis quoted, implies equal

contributions to signal loss on the up-going and down-going paths.

In another development, Coleman [62] applied Huygen's principle, in the form of boundary integral equations, to radiowave propagation. This approach leads to an economic form of the WKB solution that was proposed as particularly useful for the study of propagation through disturbed ionospheres.

Since 1999, there have been over 40 papers in which ray racing has been used to model and explain radio-propagation observations, indicating that ray tracing is an important and useful tool for aiding our understanding of the ionosphere and propagation via the ionosphere. Many studies have either used, or been based on, developments of the Jones ray-tracing program developed about 30 years ago [31, 32]. This demonstrates the value of an accessible computer code that basically just traces ray paths and is relatively straightforward to implement. However, in many situations the value of the results would be greater if the basic ray tracing were supplemented with calculations of some or all of the additional parameters described in earlier sections, i.e., field strength, absorption, Doppler shift, and homing-in.

Rather than review all recent papers in detail, we briefly present some examples to give an indication of the range of ray-tracing applications.

Rogers et al. [63] produced synthesized oblique ionograms by ray tracing through tomographic images of the ionosphere and ionospheric models, and compared the results with experimental oblique ionograms. They concluded that ionospheric models based on tomographic images for the F region and a climatological model of the E region provided the best description for HF-system applications.

Farges, et al. [64] used ray tracing to identify a possible source of Type I equatorial electrojet irregularities observed at 4-5 MHz and via HF radar using a broad-beam zenith radar. They traced ray paths in an undisturbed background ionosphere, determined from ionogram observations. Radar signatures of Type I and II irregularities were then determined by calculating echo intensity and Doppler shift as a function of range. They then determined that the scattering occurred on the limited number of ray paths that refracted to become horizontal near the center of the equatorial electrojet.

Yeoman et al. [65] used numerical ray tracing to evaluate the range accuracy of the simplified algorithm used in the routine determination of ground range by SuperDARN (Super Dual Auroral Radar Network) radars. They found that the standard algorithm was accurate to within 16 km for direct ionospheric scattering and 60 km for 1.5-hop backscattering. In routine operations, the SuperDARN radars use a range gate of 45 km, so that in either case, the error would be no more than one range gate.

Over the years, there have been many ray-tracing studies of the effects of traveling ionospheric disturbances (TIDs) on HF propagation. In a recent study, Stoker et al. [66] examined the variation in skip distance caused by the passage of TIDs, and proposed using the skip-distanced variation as an indicator of the TID perturbation density.

Blagoveshchensky and Borisova [67] modeled the effect of sub-storms on the signal strength and azimuthal angle of arrival of HF propagation over circuits of 2,000-11,000 km in length. Ray tracing using a global model of the ionosphere was used to identify propagation modes and to determine the angles of arrival, group and phase paths, and field strength. Not surprisingly, the observations showed a variety of effects, including, at times, quite large variability in the azimuthal angle of arrival. While the agreement between the ray-tracing results and the observations was described as excellent, only a subset of the observations was modeled. The most complete comparison was for a 6600 km path (Ottawa to St. Petersburg), for which the agreement was excellent. Overall, the results were certainly good considering the length of the circuits and the complex changes likely to occur along the paths during sub-storms. Other propagation studies of a similar nature included simulations of HF off-great-circle propagation due to the mid-latitude trough by Stocker et al. [68] and Zaalov et al. [33].

As discussed in earlier sections, analytical ray tracing has become a more useful tool primarily through the development of various schemes to describe ionospheric structure in terms of quasi-parabolic-layer segments. There is therefore value in developing techniques, such as those recently developed by Norman [69 and 70], that use the analytic ray-tracing technique developed by [43, 44] to directly invert vertical- and oblique-incidence ionograms into quasi-parabolic descriptions of the ionosphere.

7. Conclusions

Ray tracing of radio waves in the ionosphere is an essential part of constructing an approximate solution of Maxwell's equations for radio waves in the ionosphere. The approximate solution concerned is conveniently labeled the quasi-optical approximation. Many interactions of HF radio waves with the ionosphere can be understood using this approximation. The increasing power (speed and memory capacity) of computers makes ray tracing an increasingly attractive choice, compared with more simplified methods of analysis. Development of various techniques that speed the process of ray tracing have contributed to this development.

Ray tracing is being widely used to simulate a variety of radio experiments and ionospheric radio circuits in order to understand observations and to predict performance of HF systems. Such applications are likely to increase as ionospheric models become more realistic and computational speed increases. Calculating additional ray parameters using the variational approach can add

significantly to the value of ray tracing, but these techniques are not yet widely appreciated. Their use would be greatly increased by the widespread availability of a general-purpose ray-tracing program incorporating the techniques.

The most pressing reason to extend the simple quasi-optical approximation is the need to combine scattering within the ionosphere with reflection and refraction. Progress has been made on this front, but there is probably room for further developments.

8. References

1. R. M. Lewis, "Asymptotic Theory of Wave Propagation," *Arch. Ratl. Mech. Anal.*, **20**, 1965, pp. 191-250.

2. R. M. Lewis and B. Granoff, "Asymptotic Theory of Electromagnetic Wave Propagation in an Inhomogeneous Plasma," *Alta Freq.*, **38**, 1970, pp. 51-59.

3. J. A. Bennett, "Complex Rays for Radio Waves in an Absorbing Ionosphere," *Proc. IEEE*, **62**, 1974, pp. 1577-1585.

4. R. Courant and D. Hilbert, *Methods of Mathematical Physics, Vol. II*, New York, Interscience, 1962.

5. A. W. Conway, and J. L. Synge (eds.), *The Mathematical Papers of Sir William Rowan Hamilton Vol. 1, Geometrical Optics*, London, Cambridge University Press, 1931.

6. J. L. Synge, *Geometrical Mechanics and De Broglie Waves*, London, Cambridge University Press, 1954.

7. K. G. Budden, *The Propagation of Radio Waves*, Cambridge, Cambridge University Press, 1988.

8. H. Poeverlein, "Strahlweg Von Radiowellen in Der Ionosphäre," *S. B. Bayer. Akad. Wiss., Math-nat Klasse*, 1948, pp. 175-201.

9. H. Poeverlein, "Strahlweg Von Radiowellen in Der Ionosphäre. Ii Theoretische Grundlagen," *Z. Angew. Phys.*, **1**, 1949, pp. 517-525.

10. H. Poeverlein, "Strahlweg Von Radiowellen in Der Ionosphäre. Iii Bilder Theoretisch Ermittelter Strahlwege," *Z. Angew. Phys.*, **2**, 1950, pp. 152-160.

11. J. A. Bennett, "A Ray Expansion with Matrix Coefficients for Sources in Absorbing Anisotropic Media," *J. Plasma Physics*, **15**, 1976, pp. 151-163.

12. M. Kline and I. W. Kay, *Electromagnetic Theory and Geometrical Optics*, New York, Interscience, 1965.

13. M. V. Berry, "Budden and Smith's 'Additional Memory' and the Geometric Phase," *Proc. Roy. Soc. Lond.*, **A431**, 1990, pp. 531-537.

14. M. S. Smith, "Phase Memory in W.K.B. and Phase Integral Solutions of Ionospheric Propagation Problems," *Proc. R. Soc. Lond.*, **A346**, 1975, pp. 59-79.

15. K. G. Budden and M. S. Smith, "Phase Memory and Additional Memory in W.K.B. Solutions for Wave Propagation in Stratified Media," *Proc. R. Soc. Lond.*, **A350**, 1976, pp. 27-46.

16. J. A. Bennett, "A Derivation of the W.K.B. Solution for the Coupled Equations of Radio Waves in the Ionosphere," *Math. Proc. Cam. Phil. Soc.*, **80**, 1976, pp. 527-534.

17. J. A. Bennett, "On the Application of Variation Techniques to the Ray Theory of Radio Propagation," *Radio Science*, **4**, 1969, pp. 667-678.

18. J. A. Bennett, "Variations of the Ray Path and Phase Path: A Hamiltonian Formulation," *Radio Science*, **8**, 1973, pp. 737-744.

19. J. A. Bennett, "The Calculation of Doppler Shifts Due to a Changing Ionosphere," *J. Atmospheric and Terrestrial Physics*, **29**, 1967, pp. 887-891.

20. C. C. Harvey, *Low Frequency Waves above the Ionosphere*, PhD Dissertation, Cambridge, 1986.

21. R. Buckley, "On the Calculation of Intensity in Dispersive Inhomogeneous Media in the Ray Approximation," *Proc. Roy. Soc. London*, **A380**, 1982, pp. 201-209.

22. Nickisch, "Focusing in the Stationary Phase Approximation," *Radio Science*, **23**, 1988, pp. 171-182.

23. J. A. Bennett and P. L. Dyson, "On the Relation between Phase Path, Group Path and Attenuation in a Cold Absorbing Plasma," *J. Plasma Physics*, **19**, 1978, pp. 325-348.

24. J. Haselgrove, "Ray Theory and a New Method for Ray Tracing," in *The Physics of the Ionosphere*, London, Physical Society, 1955, pp. 355-364.

25. C. B. Haselgrove and J. Haselgrove, "Twisted Ray Paths in the Ionosphere," *Proc. Phys. Soc. (London)*, **75**, 1960, pp. 357-363.

26. T. A. Croft and H. Hoogasian, "Exact Ray Calculations in a Quasi-Parabolic Ionosphere," *Radio Science*, **2**, 5, 1968, pp. 69-74.

27. J. M. Kelso, *Radio Ray Propagation in the Ionosphere*, New York, McGraw-Hill, 1964.

28. J. M. Kelso, "Ray Tracing in the Ionosphere," *Radio Science*, **3**, 1968, pp. 1-12.

29. J. A. Bennett and P. L. Dyson, "Advances in Ionospheric Ray Tracing," in *Proc. Solar Terrestrial Predictions Workshop*, 1989, NOAA, Boulder, CO, USA, pp. 46-52.

30. K. Suchy, "Theory of High-Frequency (HF) Radio Waves in the Second Half of the 20th Century," *Journal of Atmospheric and Solar-Terrestrial Physics*, **62**, 2000, pp. 1683-1687.

31. R. M. Jones, "A Three Dimensional Ray-Tracing Computer Program," ESSA Tech. Rpt. IER 17-ITS 17, 1966, ESSA.

32. R. M. Jones, "A Three Dimensional Ray-Tracing Computer Program," *Radio Science*, **3**, 1968, pp. 93-94.

33. N. Y. Zaalov, E. M. Warrington, and A. J. Stocker, "The Simulation of HF Off-Great Circle Propagation Effects Due to Large Scale Electron Density Structures within the Polar Cap and Due to the Mid-Latitude Trough," in *Proc. Ninth International Conference on HF Radio Systems and Techniques, 23-26 June 2003*, 2003, IEE, pp. 250-255.

34. C. J. Coleman, "A Propagation Model for HF Radiowave Systems," in *Proceedings of MILCOM '94, 2-5 Oct. 1994*, 1994, IEEE, pp. 875-879.

35. R. J. Norman, J. A. Bennett, P. L. Dyson, and L. Nguyen, "HIRT: Homing-in Ray Tracing Program," Research Report 1994, School of Physics, La Trobe University.

36. A. Vastberg, "Signal Intensity in the Geometrical Optics Approximation for the Magnetised Ionosphere," in *Proc. HF 95 Nordic*

Shortwave Conference. Conference Proceedings, 15-17 August 1995, 1995, Telub AB, pp. 1-2.

37. A. Vastberg and B. Lundborg, "Signal Intensity in the Geometrical Optics Approximation for the Magnetized Ionosphere," *1995 URSI International Symposium on Electromagnetic Theory, 23-26 May 1995*, 1996, pp. 1579-1588.

38. R. J. Norman, *Ray Tracing Techniques in Anisotropic Media*, PhD Dissertation, LaTrobe University, 1994.

39. H. J. Strangeways and R. T. Ioannides, "Ionospheric Effects on Earth-Satellite Paths Using Mqp Modelling and Nelder-Mead Optimisation," in *Proc. IEE National Conference on Antennas and Propagation (IEE Conf. Publ. No. 461), 31 March-1 April 1999*, 1999, IEE, pp. 196-199.

40. J. R. Hill, "Exact Ray Paths in a Multisegment Quasi-Parabolic Ionosphere," *Radio Science*, **14**, 1979, pp. 855-861.

41. J. D. Milsom, "Exact Ray Path Calculations in a Modified Bradley/Dudeney Model Ionosphere," *Proc. IEE*, **132** pt. H, 1, 1985, pp. 33-38.

42. D. E. Westover, "Exact Ray-Path Solutions in a Quasi-Linear Ionosphere," *Radio Science*, **3**, 1968, pp. 75-79.

43. P. L. Dyson and J. A. Bennett, "A Model of the Vertical Distribution of the Electron Concentration in the Ionosphere and Its Application to Oblique Propagation Studies," *J. Atmospheric and Terrestrial Physics*, **50**, 1988, pp. 251-262.

44. D. C. Baker and S. Lambert, "Range Estimation for SSL HFDF Systems by Means of a Multiquasiparabolic Ionospheric Model," *IEE Proceedings*, **136**, Pt. H, 1989, pp. 120.

45. J. Chen, P. L. Dyson, and J. A. Bennett, "Automatic Fitting of Quasi-Parabolic Segments to Ionospheric Profiles with Application to Single Station Location," *J. Atmospheric and Terrestrial Physics*, **52**, 4, 1990, pp. 277-288.

46. X. Huang and B. W. Reinisch, "Multiple Quasi-Parabolic Presentation of the IRI Profile," *Advances in Space Research*, **25**, 1, 2000, pp. 129-132.

47. M. I. Dick and L. R. Cander, "Determination of HF Ray Path Parameters Using a Multi-Quasiparabolic Model Ionosphere," in *Proc. Tenth International Conference on Antennas and Propagation (Conf. Publ. No .436), 14-17 April 1997*, 1997, IEE, pp. 23-26.

48. R. J. Norman, P. L. Dyson, and J. A. Bennett, "Analytic Ray Parameters for the Quasi-Cubic Segment Model," *Radio Science*, **32**, 1997, pp. 387.

49. J. A. Bennett, J. Chen, and P. L. Dyson, "Analytic Ray Tracing for the Study of HF Magneto-Ionic Radio Propagation in the Ionosphere," *ACES Journal*, **6**, 1, 1991, pp. 192-210.

50. R. Norman and P. Cannon, "A Two-Dimensional Analytic Ray Tracing Technique Accommodating Horizontal Gradients," *Radio Science*, **32**, 2, 1997, pp. 387-396.

51. H. Poeverlein, "Sommerfeld-Runge in Law in Three and Four Dimensions," *Phys. Rev*, **128**, 1962, pp. 956-964.

52. R. I. Barnes, "Faraday Rotation in a Cold, Inhomogeneous Magnetoplasma: A Numerical Comparison of Ray and Full Wave Analyses," *Radio Science Eighth International Ionospheric Effects Symposium (IES-96), 7-9 May 1996*, 32, 4, 1997, pp. 1523-1532.

53. M. V. Tinin, N. T. Afanasyev, S. M. Mikheev, A. P. Pobedina, and O. V. Fridman, "On Some Problems of the Theory of Radio Wave Propagation in a Randomly Inhomogeneous Ionosphere," *Radio Science*, **27**, 2, 1992, pp. 245-255.

54. A. V. Kulizhsky, L. V. Pankov, Y. A. Semenei, and M. V. Tinin, "The Structure of the Field of High-Angle Rays in a Randomly Inhomogeneous Ionosphere at Frequencies Close to the Maximum Usable Frequency," *Journal of Atmospheric and Terrestrial Physics*, **56**, 11, 1994, pp. 1451-1456.

55. N. N. Zernov and B. Lundborg, "An Integral Representation of the Wave Field in Inhomogeneous Media in Terms of Diffracting Component Waves," *Radio Science*, **31**, 1, 1996, pp. 67-80.

56. C. J. Coleman, "On the Simulation of Backscatter Ionograms," *Journal of Atmospheric and Solar-Terrestrial Physics*, **59**, 16, 1997, pp. 2089-2099.

57. V. E. Gherm, N. N. Zernov, S. M. Radicella, and H. J. Strangeways, "Propagation Model for Signal Fluctuations on Transionospheric Radio Links," *Radio Science*, **35**, 5, 2000, pp. 1221-1232.

58. S. N. Kolesnik, M. V. Tinin, and N. T. Afanas'ev, "Mimic Simulations of Radio-Wave Propagation in a Randomly Irregular Ionosphere," *Izvestiya Vysshikh Uchebnykh Zavedenii, Radiofizika*, **45**, 9, 2002, pp. 731-745.

59. R. J. Norman, "Two-Dimensional Analytic HF Ray Tracing in the Ionosphere," *Radar Conference, 2003 Proceedings of the International*, 2003, pp. 375-379.

60. T. D. Xenos and T. V. Yioultsis, " FDTD Method with Oblique Incidence for Ionospheric Wave Propagation Problems – Application to an HF One-Hop Radio-Link Study," *IEEE Transactions on Magnetics*, **MAG-38**, 2002, pp. 677-680.

61. K. Davies, "Ionospheric Radio Propagation," London, Peter Peregrinus, 1990.

62. C. J. Coleman, " Huygen's principle Applied to Radio Wave Propagation," *Radio Science*, **37**, 2002, pp. 17-1-17-8.

63. N. C. Rogers, C. N. Mitchell, J. A. T. Heaton, P. S. Cannon, and L. Kersley, "Application of Radio Tomographic Imaging to HF Oblique Incidence Ray-Tracing," *Radio Science*, **36**, 2001, pp. 1591-1598.

64. T. Farges, E. Blanc, and J. P. Villain, "Interpretation of Equatorial Electrojet Irregularities Observed with a Broad Beam HF Zenithal Radar," *Radio Science*, **34**, 1999, pp. 1141-1152.

65. T. K. Yeoman, D. M. Wright, A. J. Stoker, and T. B. Jones, "An Evaluation of Range Accuracy in the Super Dual Auroral Radar Network Over-the-Horizon HF Radar Systems," *Radio Science*, **36**, 2001, pp. 801-813.

66. A. J. Stocker, N. F. Arnold, T. B. Jones, "The Synthesis of Travelling Ionospheric Disturbance (TID) signatures in HF Radar Observations using Ray Tracing," *Ann. Geophysicae*, **18**, 2000, pp. 56-64.

67. D. V. Blagovehchensky and T. D. Borisova, "Substorm Effects of Ionosphere and HF Propagation," *Radio Science*, **35**, 2000, pp. 1165-1171.

68. A. J. Stocker, E. M. Warrington, and T. B. Jones, "Comparison of Observed Deviations from the Great Circle Direction for a 4490 km HF Propagation Path along the Midlatitude Ionospheric Trough," *Radio Science*, **38**, 2003, pp. 20-1-11.

69. R. J. Norman, "An Inversion Technique for obtaining Quasi-Parabolic Layer Parameters from VI Ionograms," *Proceedings of the International Radar Conference*, *2003*, pp. 363-367.

70. R. J. Norman, "Backscatter Ionogram Inversion," *Proceedings of the International Radar Conference, 2003*, 2003, pp. 368-374.

The Use of RF Waves in Space Propulsion Systems

E.A. Bering, III
F. Chang-Diaz
J. Squire

Abstract

This paper will review the ways in which RF and microwave radiation may be used in the design of electric propulsion systems for spacecraft. RF power has been used or proposed in electric propulsion systems to ionize, to heat, and to accelerate the propellant, or to produce plasma used to inflate a magnetic field for solar-sail purposes. Direct RF propulsion using radiation pressure or ponderomotive forces is impractical, owing to efficiency considerations. Examples of various systems that have been developed or proposed will be reviewed. The variable specific impulse magneto-plasma rocket (VASIMR) uses RF for producing, heating, and accelerating plasma. Inductive RF and microwave ion thruster schemes use electromagnetic waves to ionize the plasma, which is then accelerated by use of dc grids. The details of the VASIMR, an inductive RF thruster, and a microwave ion thruster are discussed and contrasted with related RF systems.

1. Introduction

The exploration of the solar system will be one of the defining scientific tasks of the new century. One of the obvious challenges faced by this enterprise is the scale size of the system under study: 10^{10} to 10^{12} m. Over distances on this scale, the mission designer is faced with the choice of accepting multi-year or even decadal mission timelines, paying for enormous mass ratios, or finding a way to improve on the performance of today's chemical rockets. For human space flight beyond Earth's orbit, medical, psychological, and logistical considerations all dictate that drastic thruster improvement is the only choice that can be made. Even for robotic missions beyond Mars, mission timelines of years can be prohibitive obstacles to success, meaning that improvements in deep-space sustainer engines are of importance to all phases of solar-system exploration [1]. For reasons that will be discussed below, improvement in thruster performance can best be achieved by using an external energy source to accelerate or heat the propellant [2]. This paper will review the use of radio frequency (RF) and microwave electromagnetic radiation as one of the methods for feeding electrical energy into the working fluid or propellant of spacecraft propulsion systems.

1.1 The Need for Electric Propulsion

The so-called "rocket equations" are presented as examples in most elementary physics texts. The change in velocity, Δv, that can be obtained from any rocket engine is given by

$$\Delta v = u \ln \frac{M_i}{M_f}, \qquad (1)$$

where u is the exhaust velocity of the rocket motor, M_i is the initial mass of the fully fueled rocket with payload, and M_f is the final mass of the payload and empty rocket motor. The fact that the logarithm is a very weak function imposes a large mass and cost penalty on any mission that needs a Δv that is a large multiple of the exhaust velocity. The obvious solution is to find ways to increase the exhaust velocity, u, or the specific impulse, $I_{sp} = u/g$, of thrusters intended for use as deep-space sustainer engines, where g is the acceleration owing to gravity at the Earth's surface.

The fundamental obstacle to increasing the specific impulse of chemical rockets lies in thermodynamics. Chemical rockets are heat engines. The energy per molecule that is available to become kinetic energy of the exhaust is limited to the amount of Gibbs free energy per molecule available in the reaction, which is on the order of an eV or

Edgar A. Bering, III is with the University of Houston, Departments of Physics and Electrical and Computer Engineering, 617 Science and Research I, Houston, TX 77204-5005, USA; E-mail: eabering@uh.edu.
Along with Franklin Chang-Díaz and Jared Squire, he is also with the Advanced Space Propulsion Laboratory, NASA Johnson Space Center, 13000 Space Center Blvd., Houston, TX 77059, USA.

This is one of the invited *Reviews of Radio Science*, from Commission H.

less. Furthermore, most of the available energy goes into heating the exhaust gas. The nozzle then converts some of this heat energy into the kinetic energy of thrust, a process that is inexorably constrained to be inefficient by the Second Law of Thermodynamics. Thus, the best chemical rockets have I_{sp} ~ 350-460 s. All rockets, including electric propulsion systems that operate as heat engines using a physical mechanical nozzle, ultimately encounter very similar thermodynamic limits, since the real limit is the need not to melt the nozzle material. The energies required to break the chemical bonds in refractory nozzle materials are on the same order as the combustion energies. Consequently, externally heated thermal rocket designs with mechanical nozzles can only achieve I_{sp} ~ 800-1000 s. For piloted missions to Mars and any type of short-duration mission to the outer planets, I_{sp} ~ 3000-30000 s will be required [3-5]. This requirement means that one must find a method to accelerate the propellant that uses an external energy source, and either keeps the propellant away from contact with solid nozzle walls, or uses a non-thermal method of acceleration. The only non-thermal energy source available on spacecraft is the vehicle's electric power system, which means that deep-space sustainer engines are going to be electric propulsion systems of one type or another. Electric propulsion systems have the added advantage that many of the systems now under development either magnetically confine the propellant, or use non-thermal acceleration mechanisms that avoid the need for mechanical nozzles, or both.

Radio frequency or microwave electromagnetic waves have found a number of uses in electric propulsion systems. The basic motivation is to provide a method of injecting energy into the propellant gas that does not require use of electrodes that are in contact with the gas, in order to avoid life-time-limiting erosion problems with said electrodes. The purpose of this paper is to review some of the more important types of RF and microwave electric propulsion system designs.

2. Electric Propulsion Systems

2.1 Classification Schemes

There are two ways that one may classify RF electric thrusters. There is a classification scheme that applies to all types of electric thrusters, which is based on their physical method of operation [6]. One may also organize RF systems according to how the RF energy is used.

2.2 Physical Method of Operation

There are three main categories of the method of operation for electric thrusters: electrothermal, electrostatic, and electromagnetic [6]. Electrothermal thrusters are examples of what were referred to as externally heated thermal thrusters, above. Electric power is used to heat the propellant material, which then expands and exhausts through a conventional mechanical nozzle to produce thrust. Examples include resistojets and arcjets. Electrostatic thrusters produce thrust by allowing positively charged ions to enter a region containing a large dc electric field, which accelerates the ions. Examples include gridded ion engines, Hall-effect thrusters, and field-emission thrusters. Electromagnetic thrusters produce thrust by applying electromagnetic forces to the propellant. Examples include magnetohydrodynamic (MHD) thrusters, ponderomotive thrusters, and the variable specific impulse magneto-plasma rocket (VASIMR).

2.3 Role of RF Energy in Thruster Operation

One may also characterize RF electric thrusters in terms of the role that the RF energy plays in the operation of the thruster. RF or microwave energy may play one or more of four roles in thruster operation: plasma ionization, propellant heating, propellant acceleration, or direct thrust production. In this context, the term "heating" refers to any stochastic energy injection process that obeys the principle of equipartition of energy. In contrast, the term "acceleration" will be used to refer to any more deterministic process that preferentially supplies energy to a selected kinetic degree of freedom. Plasma ionization RF thrusters utilize the RF to ionize the propellant, or working fluid. Almost all RF thrusters fall in this category. Several ion thruster schemes use RF or microwave ionization sources to ionize propellant that is accelerated with an electrostatic potential. At least one thruster design, the mini-magnetosphere plasma propulsion device, uses RF-produced plasma to inflate a magnetic solar-wind sail. Plasma heating by RF or microwave is used to heat plasma in microwave electrothermal thrusters (MET).

Acceleration of plasma that has been produced in an RF or microwave source can be accomplished by use of grid-produced electrostatic fields, by ambipolar electrostatic fields that are self-consistently generated in plasmas that have elevated electron temperatures, or by ion-cyclotron resonant heating (ICRH), which is misnamed since the kinetic energy is injected preferentially into a single degree of freedom. The ICRH name and acronym will be retained, owing to the name recognition of the terminology in the fields of fusion energy and auroral physics. Examples of gridded ion thrusters with RF or microwave sources include the RF ion thruster assembly (RITA) on ESA's ARTEMIS spacecraft [7, 8], and the microwave electron-cyclotron resonance (ECR) thruster on the Japanese asteroid-sample return mission, Hayabusa (MUSES-C) [9, 10]. Relatively large ambipolar electrostatic fields are produced in the exhaust plume of magnetized RF plasma sources, because these devices typically produce plasmas with large electron pressure gradients, and $T_e > T_i$, where T_e is the electron temperature and T_i is the ion temperature. Examples of

thrusters that use ambipolar acceleration include the whistler-wave plasma thruster [11, 12] and stand-alone helicon thrusters [13-15]. VASIMR is both an example of a system that uses ion-cyclotron resonant heating to accelerate ions, and an example of a system that can be operated as an ambipolar acceleration thruster [16, 17].

Direct thrust production refers to methods that utilize either direct photon thrust, or a ponderomotive interaction with the ambient magnetospheric or solar-wind plasma. Owing to the inherent energy inefficiency of these approaches, no such thrusters are presently under development. These methods will only be practical for ultra-power-rich missions with severe mass ratio constraints.

2.4 Specific Systems

Three systems will be examined in some detail. The two space-qualified systems, RITA on ARTEMIS and the microwave electron-cyclotron resonance thruster on Hayabusa, merit detailed discussion because of their pedigree and history. The VASIMR engine will be discussed in detail for several reasons. It is the system that is best suited to scaling up to megawatt power levels. It is the only two-stage RF system under development. Finally, it is the system that the authors know best.

This paper will briefly mention all of the other major RF- or microwave-using electric thruster systems now under development. There is one electrothermal concept, the microwave electrothermal thruster (MET). There are two ambipolar devices, the whistler wave and helicon thrusters. M2P2 is the only concept in the "other" category.

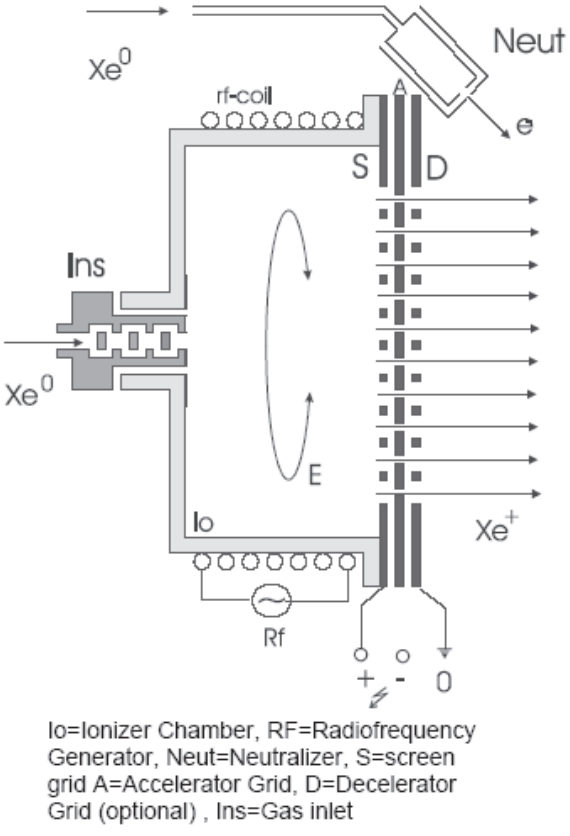

Figure 1. A cartoon schematic of the RF ion thruster (RIT), illustrating the operating principle ([20, 31]; Copyright © 2003 by EADS Space Transportation GmbH; reproduced with permission.)

2.4.1 RF-Ion Thruster (RIT)

The RF-ion thruster (RIT) has been under development for more than thirty years at the University of Giessen and at EADS Space Transportation (formerly astrium GmbH, MBB, and Dasa) [18]. The operating principle is the use of an inductive plasma discharge to ionize the propellant (presently xenon). A cylindrical solenoid coil surrounds an electrically non-conducting plasma chamber (Figure 1) [7, 19, 20]. This coil is driven by a 0.7-1 MHz RF signal. The coil produces an axial magnetic field and an azimuthal electric field in the plasma chamber. The azimuthal electric field accelerates the plasma electrons, which ionize the propellant by impact ionization. The plasma ions are then extracted from the chamber and accelerated by means of an electrostatic field, which is applied by means of a three-grid exhaust aperture.

The fundamental electrodynamic principles of operation of this device are very simple, owing to the fact that the plasma is not magnetized. There are two factors critical to the operation of the system that determine the operating frequency. Ionization efficiency maximizes when the neutral pressure in the discharge chamber is such that the electron-neutral collision frequency is equal to the input RF power. In order to penetrate the plasma, the RF input frequency must remain above the local plasma frequency. If the input flow rate of the propellant and the available RF power are sufficient to produce a plasma density such that the plasma frequency approaches the operating frequency, skin-depth effects will act to limit the penetration of the wave into the plasma and to reduce the ionization efficiency of the thruster. In effect, the device is operated in a low plasma density regime, where single-particle dynamics suffice to explain its operation.

The RIT-10 has an impressive pedigree. A qualification model has been operated for nearly 19000 hours in a laboratory qualification test [21-23]. The first space test of the RIT-10 assembly (RITA) was on the EUropean REtrievable CArrier Assembly (EURECA) [19, 24]. This experimental prototype operated at thrust levels of 5-10 mN for 240 hours before a solder joint on the input to the RF coil melted, terminating operation.

The first operational use of the RIT-10 was on the European Space Agency's Advanced Relay Technology Mission (Artemis) spacecraft. This geosynchronous

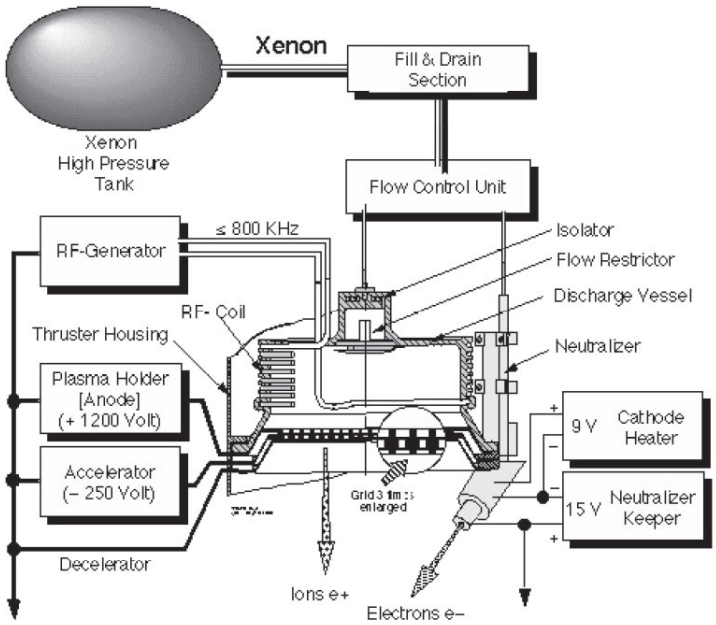

Figure 2. A block diagram of the RF ion thruster ([25, 28] copyright © 2001 astrium GmbH; reproduced with permission).

spacecraft was equipped with four ion thrusters, including two RITAs in order to perform north-south station keeping [7, 8, 24-27]. The RITA models on this mission had a mass of 15.4 kg each. They produced 15 mN of thrust at a specific impulse of 3400 s, requiring a power input $<$459 W each. It was fortunate for the mission planners that there were ion thrusters on board, because a launcher failure resulted in an initial elliptic orbit that was much lower than intended, leaving the spacecraft with insufficient chemical propulsion fuel to achieve geosynchronous orbit. The chemical apogee boost engine was used to place the spacecraft in a 31,000 km circular parking orbit. From there, the ion propulsion system was used successfully to raise the orbit and to adjust the inclination to a final position close to the nominal location for the mission. Despite the fact that the mechanical integrity of some components was compromised by excessive vibration during the launcher failure, the ion engines proved themselves up to the task. RITA1 had to be shut down after 698 hours of operation owing to a blockage in the xenon gas line. RITA2 operated successfully for 5863 hours. It appears that RITA 2 remains capable of providing station-keeping thrust for the remainder of the 10-year mission [8, 26, 27].

The major advantages of the RF-ion thruster system include the increase in expected lifetime that stems from not having a hollow cathode or other electron-bombardment device operating in contact with the plasma, and the cost reduction associated with not having to develop and qualify a high-current cathode. The major disadvantages are limitations on the upward scalability of the system. The plasma is in contact with the wall of the discharge chamber, which limits total power dissipation. The plasma-frequency or skin-depth problem mentioned above limits the plasma density, fuel flow, and maximum thrust, which means that high thrust and power can only be achieved by increasing thruster area and flying multiple thrusters. A similar constraint is imposed by the need to hold the perveance of the exhaust beam below the threshold for triggering beam plasma discharge instabilities (BPD). The use of grids to provide the electrostatic acceleration imposes a lifetime limit, as a result of grid erosion by sputtering.

In a field that is as new and as rapidly developing as electric spacecraft propulsion, operating hardware is already being re-engineered, upgraded, and improved. The RIT-10 ARTEMIS is no exception to this rule. The system is presently evolving along two separate paths. First, an effort has been made to develop an improved model of the 10-cm diameter RIT-10, known as the RIT-10 EVO (EVOlution), which provides enhanced performance within essentially the same size and weight envelope [18, 20, 25, 28, 29]. The main step taken in this effort was to increase the open-area fraction of the grids, and to improve the ion optics. The results were big increases in the range of available thrust levels or throttle ability. The RIT-10 ARTEMIS was capable of about 10% thrust variation, while the RIT-10 EVO can provide any thrust from 1 mN to 41 mN. The RIT-10 EVO can produce about 10% higher specific impulse, while operating at the same thrust level as the RIT-10 ARTEMIS. It also has reduced acceleration grid current, and reduced specific power consumption.

The other development path is intended to produce a larger thruster, capable of producing 150-200 mN of thrust. The RIT-XT has a beam diameter of 21 cm. The discharge chamber is conical, rather than cylindrical. It can produce 150 mN of thrust, with an input power of 4.5 kW and a specific impulse of ~5000 s, operating at a 2 kV beam voltage. Increased specific impulse at the same thrust level can be accomplished by increasing the beam voltage and power input [18, 20, 28-31].

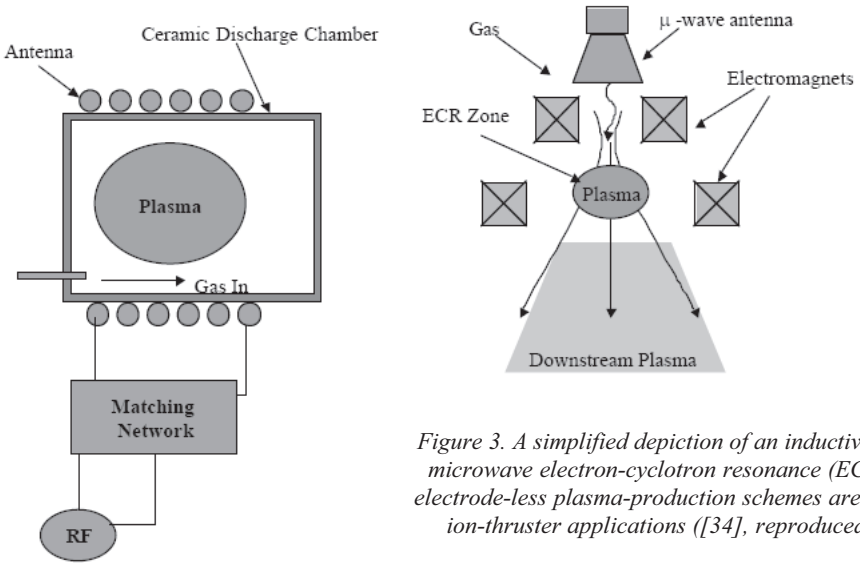

Figure 3. A simplified depiction of an inductive RF discharge and a microwave electron-cyclotron resonance (ECR) discharge. These electrode-less plasma-production schemes are readily adaptable for ion-thruster applications ([34], reproduced with permission).

2.4.2 Microwave Electron-Cyclotron Resonance (ECR) Thruster

The excitation mechanism in inductive RF discharges, such as the RF-ion thruster, is a non-resonant process. It is well known that the selection of a suitable resonance will substantially increase the ability of a propellant to absorb RF energy. The ionization mechanism of most plasma sources is ultimately electron bombardment, which means that RF ionization systems that operate at or near an electron resonance have been extensively investigated. These resonances include the electron-cyclotron resonance (ECR), and the two hybrid resonances, upper and lower. The helicon discharge, which operates near the lower hybrid resonance, will be discussed in subsequent sections. The microwave electron-cyclotron resonance thruster uses a combination of the electron-cyclotron and upper-hybrid resonance to ionize propellant and create an electrodeless cathode [9, 32-34]. A comparison of the RF induction and microwave electron-cyclotron resonance systems is shown in Figure 3 [34].

The electron-cyclotron resonance method of plasma generation has been investigated off and on since the 1960s. The early work ran into problems associated with a lack of lightweight, space-proven microwave sources, and the need for fairly intense magnetic fields, which imposed unacceptable weight penalties using the available magnet technology. By the 1980s, these problems had been solved. The needs of the communications satellite industry have led to the development of several rugged, small, and efficient microwave sources. Superconducting magnets and samarium-cobalt permanent magnets have provided two feasible alternative methods for creating the required magnetic field.

The present generation of microwave electron-cyclotron resonance thrusters traces its heritage to work done by H. Goede at the TRW Space and Technology Group during the early and middle 1980s [32]. Goede designed and tested a 30-cm device with a bucket-type ionization chamber. Two separate families of thrusters have sprung from this initial work. The Japanese Institute of Space and Astronautical Sciences (ISAS) has developed a 10-cm microwave electron-cyclotron resonance thruster

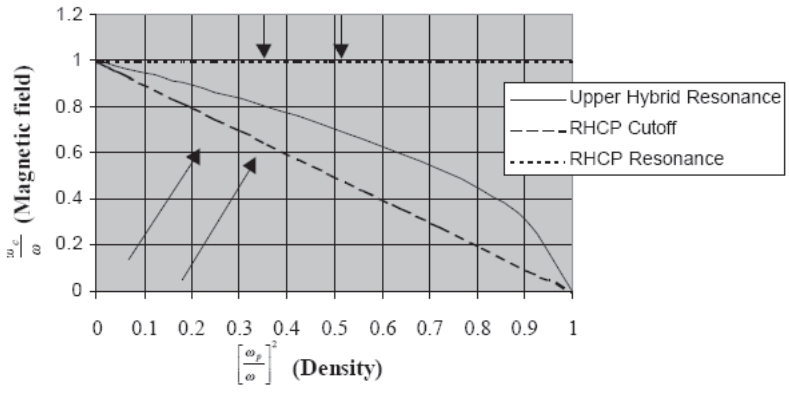

Figure 4. A CMA diagram depicting various resonances and cutoffs for a specified plasma density and magnetic field. The lower two arrows depict waves approaching the electron-cyclotron resonance from the weak-field side, while the upper two depict an approach from the high-field side ([42], reproduced with permission).

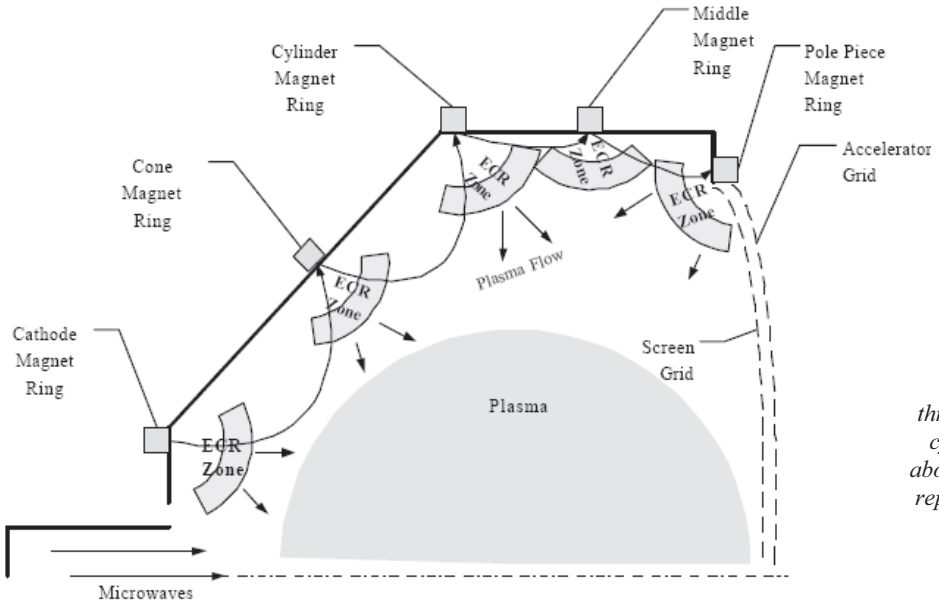

Figure 5. An electron-cyclotron resonance ion thruster. Notice the electron-cyclotron resonance zones above each magnet ring ([34], reproduced with permission).

(the mu-10) that operates at a frequency of 4.25 GHz [9, 10, 33, 35-41]. Four of these engines are presently operating successfully on the Hayabusa (formerly MUSES-C) asteroid sample return mission. A 30-cm size expanded version of the mu-10 is presently under development. A US group at NASA Glenn Research Center is developing a 25 kW microwave electron-cyclotron resonance thruster known as the High Power Electric Propulsion (HiPEP) ion engine [34, 42, NASA Press Release, 2003]. The performance parameters of these systems will be reviewed after we have discussed the physics of the resonance mechanism.

The plasma physics of the electron-cyclotron resonance thruster is subtle and interesting. Actually, the thruster is slightly misnamed, owing to the fact that the upper-hybrid resonance is also excited in many configurations. The electron-cyclotron resonance plasma source operates in regions 1, 2, 3, 6a, and sometimes 7 of the Clemmow-Mullaly-Allis (CMA) diagram, using *Stix* [43] region labeling, as shown in Figure 4. In both the mu-10 and the NASA designs, the microwave power enters the plasma chamber via an axial cylindrical waveguide, as shown in Figure 5 [42].

Circular rings of cup-type permanent magnets are used to create multiple electron-cyclotron resonance zones. This design makes use of the magnetic mirror force to exclude plasma from the microwave inlet region, which means that the waves approach the first electron-cyclotron resonance region from the high-field region. Since the microwave propagation vector, **k**, is parallel to **B** in this region, R-X mode waves have direct access to the electron-cyclotron resonance or RHCP resonance [33, 34]. In multiple-ring configurations, either planar or bucket type, the outer magnets also have associated electron-cyclotron resonance zones [9, 44, 45]. The field geometry in the vicinity of these rings is such that the microwaves approach these electron-cyclotron resonance zones either perpendicular to **B** or at an oblique angle. To reach these resonances, the R-X mode first encounters the $R = 0$ cutoff, which means that it has to tunnel through an evanescent zone to excite the upper-hybrid resonance. It is also possible for the L-O mode to enter a high-field region and to couple to the R-X mode via reflection.

These thrusters have two "modes" of operation, low and high power. In the low-power mode, bright regions of visible emission from the plasma are observed in the predicted plasma-generation zones, with very little emission detectable in the center of the device, and an enhancement of plasma density near the wall [34, 37, 44]. The perpendicular transport process whereby plasma reaches the center is presumed to result from diffusion, but it has not been studied in any detail. In the high-power mode, which has been observed in both US and Japanese studies, the visible emissions from the plasma are uniform across the thruster, showing no visible enhancements at the electron-cyclotron resonance zones [42]. There are two interpretations of this observation. It has been suggested that the uniform glow is the result of an abrupt enhancement in the rate of cross-field diffusion, with most plasma production still occurring in the electron-cyclotron resonance zones [42]. An alternative interpretation is that plasma production is occurring throughout the volume of the discharge chamber by means of the oblique, low-field upper-hybrid resonance [44]. The resolution of this controversy awaits future research.

In general, the need to keep the plasma frequency below the exciting microwave frequency limits the plasma density and, therefore, the total thrust that these devices can produce. This requirement is what dictates the need to operate at the highest practical microwave frequency and magnetic field. The fact that the electrons will gain energy continuously allows the discharge to take place at lower neutral pressures than must be used in the RF-induction thruster. In general, these are self-igniting discharges, which do not require the injection of seed electrons to ignite.

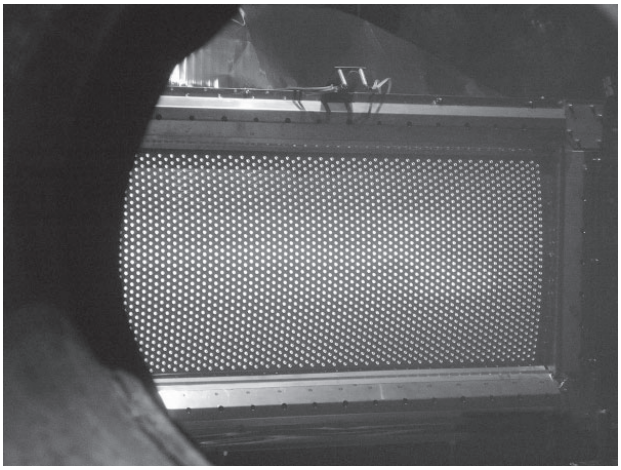

Figure 6. Initial thrust testing of the HiPEP ion engine in a vacuum chamber at NASA's Glenn Research Center (NASA press release).

The Japanese mu-10 microwave electron-cyclotron resonance thruster is one of the two fully space-qualified engines discussed in this review. The Hayabusa asteroid explorer, which was launched on May 9, 2003, is using ion propulsion for cruise phase propulsion. The ion-thruster assembly on Hayabusa consists of four mu-10 engines and associated microwave neutralizer cathodes. Each xenon mu-10 can produce 1.4-7.8 mN of thrust, with a specific impulse between 2687 and 3011 s, using 103-386 W of power each [10]. The prototype model has been endurance tested for 18000 hours [38]. As of December, 2003, the engines had operated successfully for 8147 hours, accomplishing most of the Δv required to enable the Earth-swing-by in June, 2004 [45a].

The NASA program at Glenn Research Center is aimed at high-power mission requirements. The HiPEP ion engine utilizes a microwave electron-cyclotron resonance plasma source and a unique rectangular 41 × 91 cm set of ion optics. The system is intended to be one of the candidate propulsion systems for the Jupiter Icy Moons Orbiter (JIMO) mission. A successful initial test of HiPEP was announced in November, 2003 (NASA press release). During this test, the engine operated at 12 kW, and produced an exhaust with a specific impulse of 6000-8000 s. HiPEP is designed to operate eventually at a full power level of 25 kW. Figure 6 shows a picture of the HiPEP exhaust during the initial testing.

The major advantages of the microwave electron-cyclotron resonance system include the increase in expected lifetime that stems from not having a hollow cathode or other electron-bombardment device operating in contact with the plasma, and the cost reduction associated with not having to develop and qualify a high-current cathode. Lower required amplitude of the excitation wave and lower operating neutral densities are other advantages, along with a reliable self-ignition capability. The major disadvantages are limitations on the upward scalability of the system. The excitation-region plasma can leak out through the mirror region of each magnet via pitch-angle diffusion. This process is an undesirable plasma loss, and also puts a heat load directly on the most heat-sensitive element in the discharge chamber, the Sm-Co magnets. This heat flow severely limits total power dissipation. Efficiency is limited by the difficulty of coupling the TE_{11} waveguide mode in the microwave transmission system exclusively to the R-X mode in the plasma. Any power going into the L-O mode basically represents a power loss. The plasma-frequency problem mentioned above limits the plasma density, fuel flow, and maximum thrust, which means that high thrust and power can only be achieved by increasing thruster area and by flying multiple thrusters. A similar constraint is imposed by the need to hold the perveance of the exhaust beam below the threshold for triggering beam plasma discharge instabilities. The use of grids to provide the electrostatic acceleration imposes a lifetime limit as a result of grid erosion by sputtering.

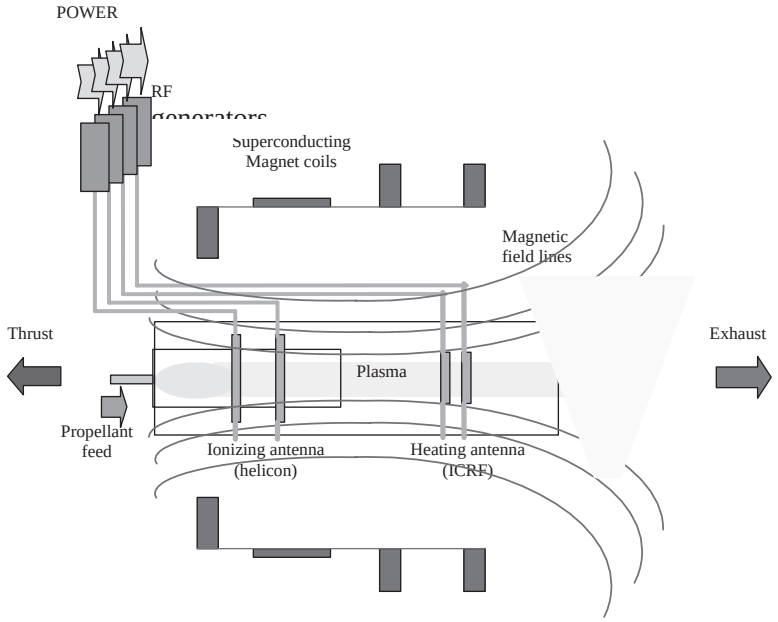

Figure 7. A simplified system schematic of the VASIMR engine ([17]).

2.4.3 Variable Specific Impulse Plasma Rocket (VASIMR)

The problem of wall losses is common to all of the systems that have been discussed so far in this paper. Systems with axial magnetic fields, such as the variable specific impulse plasma rocket (VASIMR), open up new and exciting possibilities for achieving much higher power densities and specific impulses than unmagnetized systems [16, 17, 46-48]. Utilizing ionized gases accelerated by electric and magnetic fields, these devices expand the performance envelope of rocket propulsion far beyond the limits of the chemical rocket. With a properly shaped magnetic duct, the internal energy of plasma can be extracted in the form of rocket thrust, through conservation of the first adiabatic invariant. The duct becomes a magnetic nozzle, the magnetic equivalent of a conventional nozzle. Moreover, the non-physical nature of such a nozzle also suggests an inherent adaptability, which (in analogy to the transmission in an automobile) could continuously tailor the exhaust plume to respond to the conditions of flight. An adaptable nozzle better utilizes the available rocket power, leading to better performance. Although much earlier work identified this benefit, its implementation in chemical rockets with fixed material nozzles proved impractical. In addition, magnetized systems can be designed that have electrode-less ion acceleration mechanisms. VASIMR is an example.

Research on the VASIMR engine began in the late 1970s, as a spin-off from investigations on magnetic diverters for fusion technology [49]. A simplified schematic of the engine is shown in Figure 7. Three linked magnetic stages perform specific interrelated functions. The first stage handles the main injection of propellant gas and its ionization. The second stage, also called the "RF booster," acts as an amplifier to further energize the plasma. The third stage is a magnetic nozzle, which converts the energy of the fluid into directed flow.

The VASIMR consists of three main sections: a helicon plasma source, a radio-frequency (RF) power booster, and a magnetic nozzle. Figure 7 shows these three stages integrated with the necessary supporting systems. One key aspect of this concept is its electrode-less design, which makes it suitable for high power density and long component life by reducing plasma erosion and other material complications. The magnetic field ties the three stages together and, through the magnet assemblies, transmits the exhaust reaction forces that ultimately propel the ship.

VASIMR is an RF-driven device, where the ionization of the propellant is done by a helicon-type discharge [50-52]. The plasma ions are further accelerated in the second stage by ion-cyclotron resonance heating (ICRH), a well-known technique, used extensively in magnetic confinement fusion research. Due to magnetic-field limitations on existing superconducting technology, the system presently favors the light propellants; however, the helicon, as a stand-alone plasma generator, can efficiently ionize heavier propellants, such as argon and xenon.

The physics of the VASIMR engine are being investigated primarily in the VX-10 device at the NASA Johnson Space Center (JSC.) However, supporting investigations are also being carried out at the Oak Ridge and Los Alamos National Laboratories, the University of Texas at Austin, and the NASA Marshall Space Center in Huntsville, Alabama. A trimetric view of the Johnson Space Center device and associated diagnostics is shown in Figure 8. The axial magnetic-field profile is also shown on the lower-right corner of the graph. Present operations use a cusp field at the upstream end of the helicon antenna, but future configurations will move away from this feature.

The helicon first stage is critically important, inasmuch as its performance sets the tone for that of the second stage or RF booster. The helicon discharge uses 25 MHz right-hand-polarized whistler-mode waves (regions 8b and 11 on

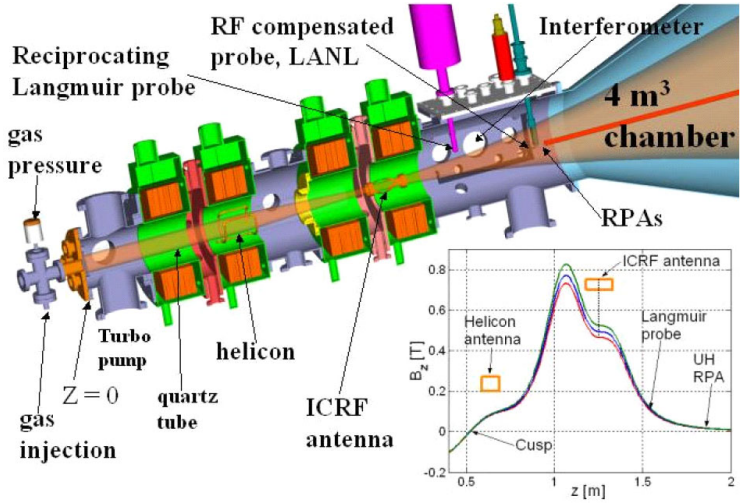

Figure 8. A trimetric view and axial field profile of the VX-10 device at JSC and associated diagnostics [17].

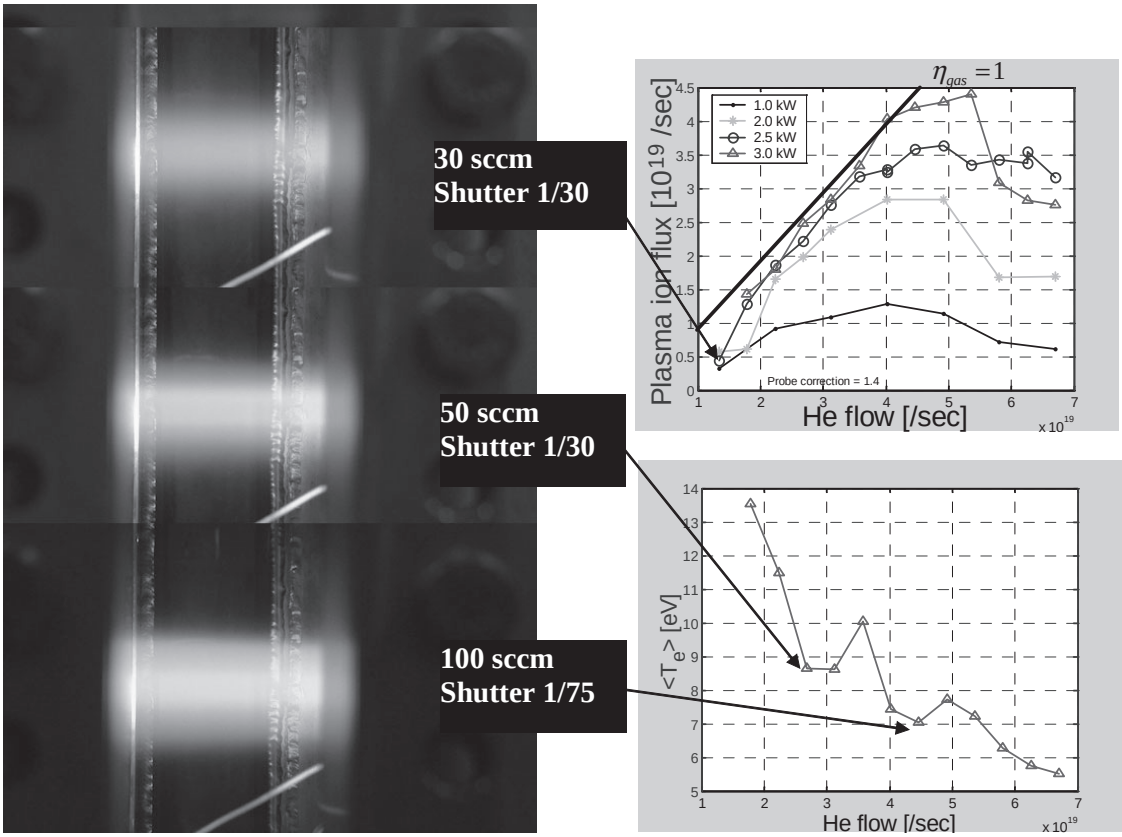

Figure 9. Plasma production and electron temperature as functions of the neutral-gas injection rate for helium. The discharge brightness at various flow rates is shown on the left. The visible color change and elevated electron temperature confirm neutral-gas depletion [17]

the CMA diagram), which approach the lower-hybrid resonance from the low-field side. The present helicon source has now been well characterized theoretically and experimentally, with hydrogen, helium, deuterium, and other propellants [53-55]. Stable plasma discharges are now routinely produced with densities in the 10^{18} to 10^{19} m^{-3} range. The present configuration features a 9-cm inner diameter helicon tube threaded through a water-cooled, double-saddle "Boswell" type antenna.

Unlike more conventional helicon discharges, used in plasma processing and other applications, the VASIMR source operates in a flowing mode, which requires careful control of the pressure field within the discharge tube. Discharges with nitrogen, argon, and xenon have also been studied, but data with these propellants are still rather sparse.

Nearly complete propellant ionization in the helicon tube has now been measured. This important result, relating to the ultimate propellant utilization efficiency of the device, is shown in Figure 9 [17, 56, 57]. In that figure, measured ion output and neutral-particle input fluxes are compared, and show a one-to-one correspondence in the range between 2×10^{19} and 4×10^{19} particles per second.

While the helicon is mainly a plasma-production stage, its operation produces non-negligible thrust. Direct measurements of the flow momentum have been carried out [58]. The standard 3 kW helicon discharge produces about 6-7 mN of force on a target placed a few centimeters away from the magnetic throat. The neutral propellant input rate (about 3×10^{-7} Kg/sec) leads to an I_{sp} estimate of about

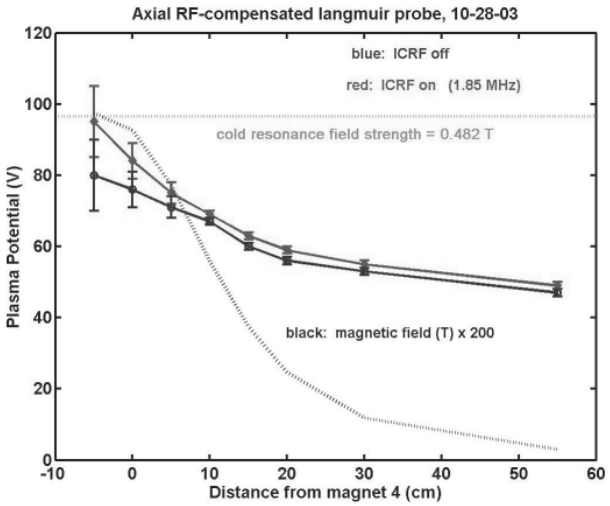

Figure 10. The profile of the plasma potential shows 30-50 V of potential drop between the ion-cyclotron resonant-frequency (ICRF) antenna and the retarding potential analyzer (RPA). The additional 30-50 V potential drop from the magnetic throat, B_{max}, is not shown [57].

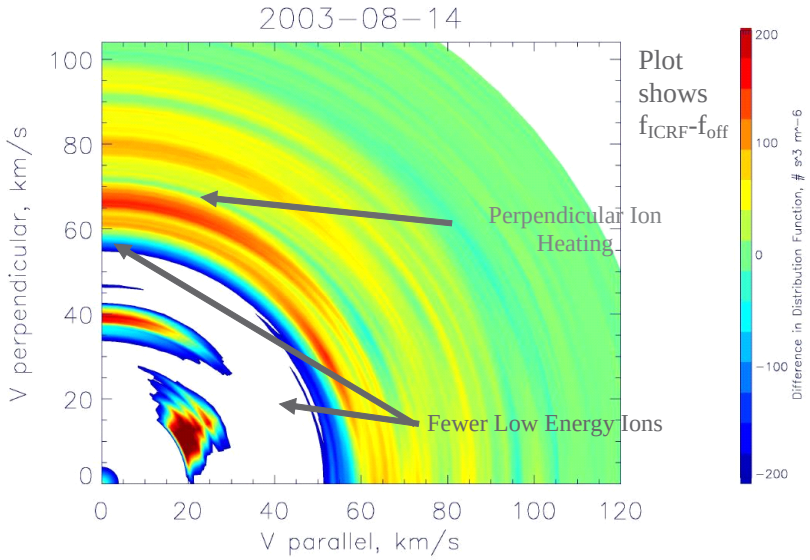

Figure 11. The difference in the velocity phase space distribution function between the ion-cyclotron resonant heating (ICRH) on and the ion-cyclotron resonant heating off conditions, plotted in spectrogram format using a linear color bar. The distribution has been mapped back to the location of the cyclotron resonance using conservation of the first adiabatic invariant. The perpendicular heating effect of the ion-cyclotron resonant heating shows up as the intense features at perpendicular velocities of 60-100 km/s [57].

2000 s. When the exhaust plasma is measured with a retarding potential analyzer (RPA) placed ~40 cm downstream from the momentum probe, the I_{sp} estimate increases to ~4000 s, with a corresponding increase in estimated thrust. We attribute this apparent acceleration to a combination of adiabatic (magnetic-mirror) acceleration and a 30-50 V ambipolar electrostatic potential drop, as shown in Figure 10. However, present pumping limitations increase the neutral background pressure downstream of the helicon throat, leading to collisions, which tend to reduce the flow momentum measured at the sensors; therefore, these measurements are presently only qualitative in nature.

Present experimental activities in the VASIMR project now focus on the physics of the RF booster, or ion-cyclotron stage. This stage is one of the unique features of the VASIMR system, in that it is the only magnetized electrode-less acceleration stage presently under development. The present configuration of the RF booster or ion-cyclotron resonant heating system uses 1.5 kW of 1.85 MHz left-hand-polarized slow-mode waves launched from the high-field, over-dense side of the resonance (region 13 of the CMA diagram). An important consideration involves the rapid absorption of ion cyclotron waves by the high-speed plasma flow. This process differs from the familiar ion-cyclotron resonance utilized in Tokamak fusion plasmas, as the particles in VASIMR pass under the antenna only once. Sufficient ion-cyclotron wave (ICW) absorption has nevertheless been predicted by recent theoretical studies [59, 60]. Recent experiments have confirmed these theoretical predictions with a number of independent measurements. What follows are brief highlights of some of these results [17, 56, 57].

The effect of the ion-cyclotron resonant heating is expected to be an increase in the component of the ion velocity perpendicular to the magnetic field. This increase will take place in the resonance region, i.e., the location where the injected RF wave frequency is equal to the ion-cyclotron frequency. Downstream of the resonance, this perpendicular heating will be converted into axial flow, owing to the requirement that the first adiabatic invariant of the particle motion be conserved as the magnetic field decreases. Since the total ion flux is not expected to increase, this axial acceleration should be accompanied by a density decrease. Furthermore, the particles should have a pitch angle distribution that does not peak at 0°. Instead, the distribution should peak at an angle that maps to a perpendicular pitch angle at resonance. Therefore, a collimated detector oriented along the magnetic field should observe a decrease in total flux and an increase in particle energy. As the acceptance angle of the detector is increased, the ion saturation current should start to show an increase when the acceptance cone includes the peak in the pitch-angle distribution.

An example of the distribution functions mapped back to the resonance that have been observed during ion-cyclotron resonant heating experiments is shown in Figure 11. During this particular experiment, the ion-cyclotron resonant-heating transmitter was operated at 1.85 MHz, at a power level of 1500 W. The data showed a pronounced enhancement or jet of ions with $v > 60$ km/s at 90° mapped pitch angle. The data also showed a depletion of ions with lower velocities. As shown in Figure 8, the magnetic-field intensity decreased rapidly with axial distance as one moved downstream away from the resonance region. At the location of the retarding potential analyzers, the field strength is down by a factor of ~40 from the value at the cyclotron resonance point. In a region like this, the effects of conservation of the first adiabatic invariant dominate ion dynamics. What conservation of the first invariant does is to force particles to lower and lower pitch angles as the field strength drops. This mechanism is the basis for the magnetic nozzle that makes the VASIMR an attractive design concept in the first place. A particle's pitch angle is given by

$$\theta = \arcsin\left(\theta_0 \sqrt{B/B_0}\right). \qquad (2)$$

A particle with a pitch angle of 90° at the resonance region will have a pitch angle of 10° at the location of the retarding potential analyzer. Thus all particles detected by the retarding potential analyzer at $\theta > 10°$ are either artifacts of the lack of collimation in the retarding potential analyzer, or particles that have been scattered or charge-exchanged. The effect of ion-cyclotron heating on the exhaust plasma is perhaps best illustrated by subtracting the "ion-cyclotron resonant heating off" distribution function from the "ion-cyclotron resonant heating on" distribution function and mapping the result back to the resonance region. The results shown in the figure are very dramatic. There was a clear depletion of low-energy ions and a significant enhancement of ions with perpendicular speeds > 60 km/s, exactly as predicted for ion-cyclotron resonant heating.

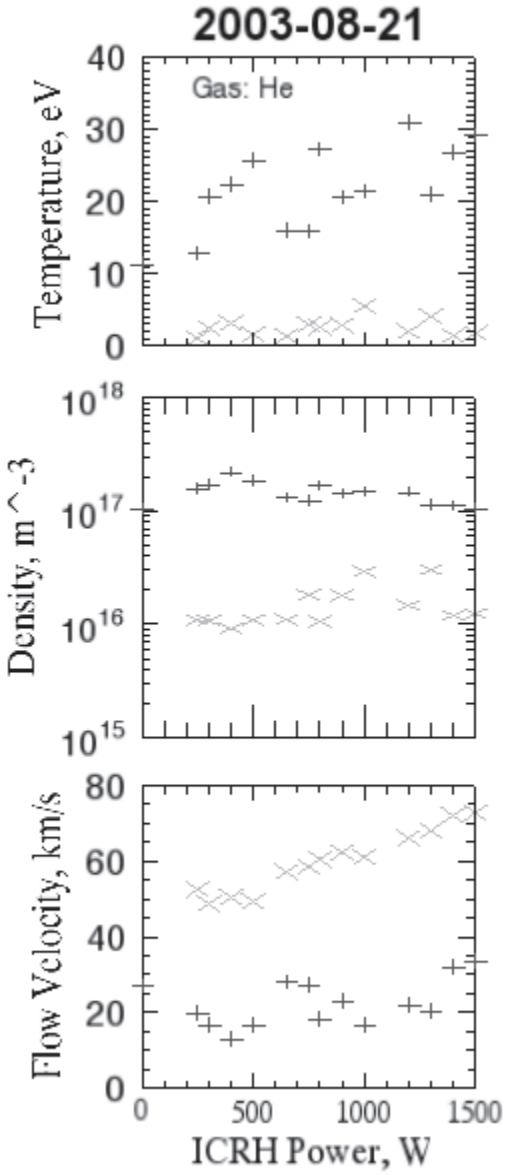

Figure 12. The fit parameters obtained by least squares fitting drifting bi-Maxwellian representations to the retarding potential analyzer data obtained during a scan of ion-cyclotron resonant heating transmitter power. From top to bottom, the panels show the ion drift velocity, the ion density, and the ion temperature in the frame of the beam. The plusses show the slow, hot component. The × marks show the fast, cold accelerated component. The round dots show the flow velocity expected for an energization rate of 70 eV/ion/kW of transmitted RF power.

The data indicates that the high remaining neutral background pressure in the present VASIMR test chamber produced a substantial amount of resonant charge exchange and scattering between the ion-cyclotron resonant heating antenna and the retarding potential analyzer location(s). The result was a pronounced "two-bump" distribution that is not well modeled by a single drifting Maxwellian. The data in Figure 11 strongly suggest using a bi-Maxwellian model, consisting of a hot, slow component and a fast component that has a low temperature in the moving frame.

The bi-Maxwellian model analysis has been used to interpret the results of a series of shots that scanned the ion-cyclotron resonant heating power input from 0 W to 1500 W. These results are presented in Figure 12. These results further strengthen the overall result of this paper, that the VASIMR VX-10 experiment is showing convincing evidence of single-pass ion-cyclotron resonant-frequency (ICRF) heating. The top panel shows that the accelerated beam had a low temperature in its reference frame, consistent with the expected output temperature of the helicon discharge. The temperature of the hot component was noisy. Generally, it was much hotter than the helicon output is expected to be, and the temperature increased with increasing ion-cyclotron resonant-heating power. The density of the accelerated component was 10-30% of the hot component, which is a measure of how much charge exchange and scattering was degrading the exhaust plume. We anticipate that the ratio of accelerated to scattered components will improve greatly with improved vacuum-pumping capacity. The flow velocity of the cold, fast component increased as the square root of input power, almost exactly in agreement with the value predicted for an energization rate of 70 eV/ion/kW of transmitted power. It is important to note that the team has barely begun the process of optimizing antenna coupling, and a substantial improvement in this performance is expected in the near future.

The ion-cyclotron resonant-heating RF booster in the VASIMR is the only known propellant-acceleration stage that is not restricted in power density by space-charge and beam-perveance effects. Furthermore, the use of an axial magnetic field allows erosion-free operation at much higher power and temperature levels than any other thruster. A 1 MW point design, suitable for use in a piloted mission to the outer planets, has been completed using technology that is presently available or feasible. The engine *alpha* parameter was just over 1 kg/kW. Thus, VASIMR has the unique advantage of being perhaps the only system discussed in

this paper that can be scaled to the requirements of a piloted mission without requiring prohibitively large thruster nozzle area.

3. Other RF Thrusters

The three systems that have been reviewed in detail here do not span the set of available RF- and microwave-using electric propulsion systems. Space does not permit detailed examination of all of the various concepts presently being explored. Some of the remaining ideas will be touched upon briefly.

3.1 Electrothermal Thrusters

Electrothermal thrusters operate by heating a gas electrically within a mechanically confined space and then releasing it through a conventional mechanical nozzle. The heating can be accomplished either by passage of a dc current through the gas, as in a resistojet or arcjet, or through microwave heating. The microwave electrothermal thruster (MET) has the advantage of not require erodable electrodes to be in contact with the heated propellant. Present microwave electrothermal thruster designs minimize discharge-chamber erosion by swirling the incoming propellant so as to confine the plasma to the center of the chamber, out of contact with the walls. The general advantage of the system is that it permits the use of inert, easily stored and common propellant materials, such as water. The systems under active development in the US are based on a design developed by Micci and coworkers at Pennsylvania State University [61-66]. Groups at Aerospace Corporation and Princeton have also contributed to the work [67-73]. These systems are intended for north-south station keeping on geosynchronous spacecraft. Most of the present generation of microwave electrothermal thrusters have I_{sp} values in the 200-400 s range, comparable to chemical systems. One Penn State system has reported an I_{sp} of 1330 s.

In an effort to develop higher I_{sp} systems, groups at Princeton and Stuttgart have begun to investigate the possibility of RF or microwave second-stage heating of electrothermal thrusters [68, 71, 72, 74]. These concepts are mostly in the numerical-modeling design phase at this time.

3.2 Ambipolar Thrusters

A number of efforts are underway to develop single-stage RF or microwave electric thrusters. Developers of these systems are trying to find a way to avoid using any gridded ion optics by using the generation of an ambipolar electric field in an axial magnetic field configuration. This approach offers two improvements over systems such as the RF ion thruster or microwave electron-cyclotron resonance thruster. The exhaust is comprised of neutral plasma instead of only ions, so no separate neutralizer cathode is required. There are no grids to erode and limit thruster lifetime. The principle of an ambipolar thruster is that a neutral exhaust requires ions and electrons to have the same exhaust velocity. The production of a hot electron gas in the ionization stage will lead to charge separation in the exhaust that is proportional to the electron pressure gradient. This violation of quasi-neutrality produces an electric field that acts to transfer energy from the electrons to the ions until the drift velocities equalize.

There are two initial ionization discharges that have been used in the development of an ambipolar thruster. The whistler-wave thruster used an approach of launching whistler waves (R mode) using a bifilar helical antenna surrounding an axial magnetic field [11, 12]. The waves propagated into a lower-field gas-injection region that contained the location of the electron-cyclotron resonance. The axial geometry contrasted with the ring cusp geometry of the microwave electron-cyclotron resonance thruster. The use of the whistler mode theoretically allowed the use of over-dense plasma. This system suffered from very high ion loss rates and low propellant utilization, owing to $\mathbf{E} \times \mathbf{B}$ drifts, and is no longer under active development.

The helicon discharge, on the other hand, is a robust, flexible heating mechanism that appears to offer an ideal source for an electrode-less ambipolar thruster. Gilland originally suggested adding a helicon discharge region to the whistler-wave thruster [13, 75, 76]. Subsequently, we reported on generation of thrust by the VASIMR light-ion helicon, operating in a stand-alone mode [48, 77]. Presently, groups at ISAS, NASA Glenn, and elsewhere have begun programs to examine the effectiveness of helicon discharges as thrusters [14, 15, 78].

3.3 Other

The only other system that uses an RF plasma discharge is the mini-magnetospheric plasma propulsion system [78-83]. This system utilizes a helicon discharge on inflate a locally produced magnetic field and create a mini-magnetosphere. The $\mathbf{j} \times \mathbf{B}$ force of the solar wind pushing on the mini-magnetosphere will then serve to provide 1-3 N of outward thrust on an interplanetary spacecraft. This system is controversial, and best suited to robotic missions to the outer planets.

4. Summary

Exploration of the solar system beyond Earth orbit is presently severely hampered by the limitations of chemical rockets. These limitations can only be removed by using electric power to provide additional energy and I_{sp} to the propellant. Given the presently available levels of electric power on spacecraft, high I_{sp} is achieved at the price of low thrust levels. These thrust levels mean that the thrusters must be able to operate reliably throughout missions of several years' duration. Electrodes and grids erode at the

elevated temperatures occurring inside electric thrusters. RF- and microwave-based systems offer a means to extend the lifetime of electric propulsion systems by avoiding the use of hollow cathodes, grids, and electrodes. Two systems have been space-qualified and lifetime rated to at least 18000 hours (~2 yr). Both of these systems have successfully operated in space for several thousand hours. RF-based systems also offer the opportunity to use neutral plasma exhaust instead of positive ions, thus obviating the need for a neutralizer cathode. Finally, one system, VASIMR, appears to offer the upward scalability to MW power levels required for human exploration of the outer planets.

5. Acknowledgements

NASA Johnson Space Center, under grant NAG 9-1524, and the Texas Higher Education Coordinating Board, under Advanced Technology Program project 003652-0464-1999, sponsored this research. The authors thank H. Bassner, K. Diamant, J. Foster, R. Killinger, H. Kuninaka, H. Leiter, M. Micci, and B. Stallard for reprints and figures.

6. References

1. K. Sankaran et al., "A Survey of Propulsion Options for Cargo and Piloted Missions to Mars," International Conference on New Trends in Astrodynamics, January 20-22, 2003.

2. F. R. Chang-Diaz, "Fast, Power-Rich Space Transportation, Key to Human Space Exploration and Survival," 53rd International Astronautical Congress/The World Space Congress, 10-19 October 2002, Houston, Texas, American Institute of Aeronautics and Astronautics.

3. F. R. Chang-Diaz et al., "Rapid Mars Transits With Exhaust-Modulated Plasma Propulsion," NASA Technical Paper 3539, 1995.

4. K. J. Hack, J. A. George, and L. A. Dudzinki, "Nuclear Electric Propulsion Mission Performance for Fast Piloted Mars Missions," AIAA/NASA/OAI Conference on Advanced SEI Technologies, September 4-6, 1991, Cleveland, OH.

5. S. N. Williams and V. Coverstone-Carroll, "Mars Missions Using Solar Electric Propulsion," *J. of Spacecraft and Rockets*, **37**, 1, 2000, pp. 71-77.

6. G. Saccoccia, J. Gonzalez del Amo, and D. Estublier, *Electric Propulsion: A Key Technology for Space Missions in the New Millennium*, 2000.

7. R. Killinger et al., "Electric propulsion system for ARTEMIS," 26th International Electric Propulsion Conference, IEPC, 1999, Kitayushu, Japan.

8. R. Killinger et al., "ARTEMIS Orbit Raising Inflight Experience with Ion Propulsion," 28th International Electric Propulsion Conference, IEPC 2003, Toulouse, France.

9. H. Kuninaka et al., "Development of Ion Thruster System for Interplanetary Missions," 23rd International Electric Propulsion Conference, IEPC 1993, Seattle, WA, USA.

10. K. Toki et al., "Flight Readiness of the Microwave Ion Engine System for MUSES-C Mission," 28th International Electric Propulsion Conference, IEPC 2003, Toulouse, France.

11. B. W. Stallard, E. B. Hooper, and J. L. Power, "Whistler-Driven, Electron-Cyclotron-Resonance-Heated Thruster: Experimental Status," *Journal of Propulsion and Power*, **12**, 1996, pp. 814-816.

12. B. W. Stallard, E. B. J. Hooper, and J. L. Power, "Plasma Confinement in the Whistler Wave Plasma Thruster," *Journal of Propulsion and Power*, **17**, 2001, pp. 433-440.

13. J. Gilland, "Application of a Helicon Discharge to Electric Propulsion," 34th Joint Propulsion Conference and Exhibit, 1998, Cleveland, OH.

14. R. Boswell and C. Charles, "The Helicon Double Layer Thruster," 28th International Electric Propulsion Conference, IEPC 2003, Toulouse, France.

15. K. Toki, "Preliminary Investigation of Helicon Plasma Source for Electric Propulsion Applications," 28th International Electric Propulsion Conference, IEPC 2003, Toulouse, France.

16. F. R. Chang-Diaz, "The VASIMR Engine," *Scientific American*, **283**, 5, 2000, pp. 72-79.

17. F. R. Chang-Diaz et al. "The VASIMR Engine: Project Status and Recent Accomplishments," 42nd Aerospace Sciences Meeting and Exhibit, 2004, Reno, NV, AIAA.

18. T. Froehlich, "RITA: High-Efficiency, Long-Life Radio-Frequency Ion Thrusters," EADS International Technology Days, 2003, Paris, France.

19. K. Groh and H. Loeb, "State of the Art of Radio-Frequency Ion Sources for Space Propulsion," *Review of Scientific Instruments*, **65**, 5, 1994, pp. 1741-1744.

20. H. Leiter et al., "Development and Performance of the Advanced Radio Frequency Ion Thruster RIT XT," 28th International Electric Propulsion Conference, IEPC 2003, Toulouse, France

21. R. F. Killinger et al., "RITA Ion Propulsion for ARTEMIS: Lifetime Test Results," 36th Joint Propulsion Conference and Exhibit, 2000, Huntsville, Alabama.

22. R. F. Killinger et al., "RITA Ion Propulsion for ARTEMIS – Results Close to the Completion of the Life Test," 37th Joint Propulsion Conference and Exhibit, Salt Lake City, Utah, 2001.

23. R. Killinger et al., "Results of the 15000 Hr Life Test of the RIT10 Ion Propulsion of ESA's ARTEMIS Satellite," 27th International Electric Propulsion Conference, IEPC 2001, Pasadena, CA, USA.

24. R. F. Killinger et al., "Electric propulsion system RITA for ARTEMIS," 35th Joint Propulsion Conference and Exhibit, 1999, Los Angeles, California.

25. H. Bassner et al., "Advantages and Applications of the RF-Ion Thruster RIT," 27th International Electric Propulsion Conference, 2001, Pasadena, CA.

26. R. F. Killinger et al., "Orbit Raising with Ion Propulsion on ESA's ARTEMIS Satellite," 38th Joint Propulsion Conference and Exhibit, 2002, Indianapolis, Indiana.

27.R. F. Killinger et al., "Final Report on the ARTEMIS Salvage Mission Using Electric Propulsion," 39th Joint Propulsion Conference and Exhibit, 2003, Huntsville, Alabama.

28.H. Bassner et al., "Development Steps of the RF-Ion Thrusters RIT," 37th Joint Propulsion Conference and Exhibit, 2001, Salt Lake City, Utah.

29.H. J. Leiter et al., "Development of the Radio Frequency Ion Thruster RIT XT," 27th International Electric Propulsion Conference, IEPC 2001, Pasadena. CA, USA.

30.H. J. Leiter et al., "Evaluation of the Performance of the Advanced 200 mN Radio Frequency Ion Thruster RIT XT," 38th Joint Propulsion Conference and Exhibit, 2002, Indianapolis, Indiana.

31.H. J. Leiter et al., "Extended Performance Evaluation of EADS ST's 200-mN Radio Frequency Ion Thruster," 39th Joint Propulsion Conference and Exhibit, 2003, Huntsville, Alabama.

32.H. Goede, "30 cm Electron Cyclotron Plasma Generator, *J. Spacecraft Rockets*, **24**, 1987, pp. 437-443.

33.H. Miyoshi et al., "Microwave Ion Thruster with Electron Cyclotron Resonance Discharge," 22nd International Electric Propulsion Conference, IEPC 1993**,** 1991, Viareggio, Italy.

34.J. E. Foster and M. J. Patterson, "Microwave ECR Ion Thruster Development Activities at NASA GRC," 38th AIAA Joint Propulsion Conference, 2002, Indianapolis, Indiana.

35.H. Kuninaka and S. Satori, "Development of Microwave Discharge Ion Thruster for Asteroid Sample Return Mission," 32nd AIAA Joint Propulsion Conference, 1996, Lake Buena Vista, FL.

36.H. Kuninaka et al., "Endurance Test of Microwave Discharges Ion Thruster Systems for Asteroid Sample Return Mission MUSES-C, 25th International Electric Propulsion Conference, IEPC 1997, Cleveland, OH, USA.

37.H. Kuninaka and S. Satori, "Development and Demonstration of a Cathodeless Electron Cyclotron Resonance Ion Thruster, *Journal of Propulsion and Power*, **14**, 1998, pp. 1022-1026.

38.H. Kuninaka et al., "Status on Endurance Test of Cathode-Less Microwave Discharge Ion Thruster," 34th AIAA Joint Propulsion Conference, 1998, Cleveland, OH.

39.H. Kuninaka et al., "Virtual Anode Phenomena Due to a Lack of Neutralization on Ion Thrusters Based on Muses-C Program," 37th AIAA Joint Propulsion Conference, 2001, Salt Lake City, UT.

40.K. Nishiyama et al., "Measurement of the Electromagnetic Emission from the MUSES-C Ion Engine System, 27th International Electric Propulsion Conference, IEPC 2001, Pasadena. CA, USA.

41.K. Toki et al., "Technological Readiness of Microwave Ion Engine System for MUSES-C Mission," 27th International Electric Propulsion Conference, IEPC 2001, Pasadena, CA, USA.

42.J. E. Foster and M. J. Patterson, "Discharge Characterization of 40 cm-Microwave ECR Ion Source and Neutralizer," 39th AIAA Joint Propulsion Conference, 2003, Huntsville, AL.

43.T. H. Stix, *Waves in Plasma*, New York, NY, American Institute of Physics, 1992.

44.I. Funaki et al., "20 mn-Class Microwave Discharge Ion Thruster," 27th International Electric Propulsion Conference, 2001, Pasadena, CA.

45.H. Toki et al., "Performance Test of Various Discharge Configurations for ECR Discharge Ion Thrusters," 27th International Electric Propulsion Conference, IEPC 2001, Pasadena. CA.

45a.H. Kuninaka, ISAS Press Release, 2003.

46.F. R. Chang-Diaz and T. F. Yang, "Design Characteristics of the Variable Isp Plasma Rocket AIDAA/AIAA/DGLR/JSASS," 22nd International Electric Propulsion Conference, October 14-17, 1991, Viareggio, Italy.

47.F. R. Chang-Diaz, "Research Status of the Variable Specific Impulse Magnetoplasma Rocket Open Systems," Transactions of Fusion Technology, July 27-31, 1998, Novosibirsk, Russia.

48.F. R. Chang-Diaz et al., "VASIMR Engine Approach to Solar System Exploration," The 39th AIAA Aerospace Sciences Meeting and Exhibit, January 8-11, 2001, Reno, NV.

49.F. R. Chang-Diaz and J. L. Fisher, "A Supersonic Gas Target for a Bundle Diverter Plasma," *Nuclear Fusion*, **22**, 8, 1982.

50.R. W. Boswell, "Very Efficient Plasma Generation by Whistler Waves Near the Lower Hybrid Frequency," *Plasma Phys. Control. Fusion*, **26**, 1984, p. 1147.

51.R. W. Boswell and F. F. Chen, "Helicons – The Early Years," *IEEE Transactions on Plasma Science*, **25**, 6, 1997, pp. 1229-1244.

52.M. D. Carter et al., "Radio Frequency Plasma Applications for Space Propulsion," International Conference on Electromagnetics in Advanced Applications (ICEAA99), 1999, Torino, Italy.

53.B. N. Breizman and A. V. Arefiev, "Ion Kinetics in a Magnetized Plasma Source, *Physics of Plasmas*, **9**, 3, 2002, pp. 1015-1024.

54.M. D. Carter et al., "Comparing Experiments with Modeling for Light Ion Helicon Plasma Sources," *Physics of Plasmas*, **9**, 12, 2002, pp. 5097-5110.

55.S. A. Cohen et al., "Ion Acceleration in Plasmas Emerging from a Helicon-Heated Magnetic-Mirror Device," *Physics of Plasmas*, **10**, 6, 2003, pp. 2593-2598.

56.F. R. Chang-Diaz et al., "Early Results of ICRH Experiments in VX-10," *Bulletin of the American Physical Society*, **DPP03**, 2003, p. RP1.138.

57.E. A. Bering, III et al., "Velocity Phase Space Studies of Ion Dynamics in the VASIMR Engine," 42nd AIAA Aerospace Sciences Meeting and Exhibit, 2004, Reno, NV, AIAA.

58.D. G. Chavers and F. R. Chang-Diaz, "Momentum Flux Measuring Instrument for Neutral and Charged Particle Flows, *Rev. Sci. Instrum.*, **73**, 10, 2002, pp. 3500-3507.

59.B. N. Breizman and A. V. Arefiev, "Single-Pass Ion Cyclotron Resonance Absorption," *Physics of Plasmas*, **8**, 3, 2001, pp. 907-915.

60. A. V. Arefiev, *Theoretical Studies of the VASIMR Plasma Propulsion Concept*, Austin, TX, The University of Texas at Austin, 2002, p. 119.

61. D. J. Sullivan and M. M. Micci, *Development of a Microwave Resonant Cavity Electrothermal Thruster Prototype*, 1993.

62. J. Mueller, J. and M. M. Micci, "Microwave Waveguide Helium Plasmas for Electrothermal Propulsion," *Journal of Propulsion and Power*, **8**, 1992.

63. P. Balaam and M. M. Micci, "Investigation of Free Floating Resonant Cavity Microwave Plasmas for Propulsion," *Journal of Propulsion and Power*, **8**, 1992.

64. P. Balaam and M. Micci, "Investigation of Stabilized Resonant Cavity Microwave Plasmas for Propulsion." *Journal of Propulsion and Power*, **11**, 1995.

65. D. J. Sullivan and M. M. Micci, "Performance Testing and Exhaust Plume Characterization of the Microwave Arcjet," 30th Joint Propulsion Conference. 1994, Indianapolis, IN.

66. F. Souliez et al., "Low-Power Microwave Arcjet Testing: Plasma and Plume Diagnostics and Performance Evaluation Micropropulsion for Small Spacecraft," in M. M. Micci and A. D. Ketsdever (eds.), AIAA, Reston, VA, 2000, pp. 199-214.

67. V. P. Chiravalle, R. B. Miles, and E.Y. Choueiri, "Numerical Simulation of Microwave-Sustained Supersonic Plasmas for Application to Space Propulsion," 39th AIAA Aerospace Sciences Meeting and Exhibit, 2001, Reno, NV.

68. V. P. Chiravalle, R. B. Miles, and E. Y. Choueiri, "Non-Equilibrium Numerical Study of a Two-Stage Microwave Electrothermal Thruster," 27th International Electric Propulsion Conference, 2001, Pasadena, CA.

69. K. D. Diamant, J. E. Brandenburg, and R. B. Cohen, "Performance Measurements of a Water-Fed Microwave Electrothermal Thruster," 37th AIAA Joint Propulsion Conference, 2001, Salt Lake City, Utah.

70. K. D. Diamant and R. B. Cohen, "High Power Microwave Electrothermal Thruster Performance on Water," 38th AIAA Joint Propulsion Conference, 2002, Indianapolis, IN.

71. V. P. Chiravalle et al., "Laser-Induced Fluorescence Measurements of a Two-Stage Microwave Electrothermal Thruster Plume," 34th AIAA Plasmadynamics and Lasers Conference, 2003, Orlando, FL.

72. V. P. Chiravalle, R. B. Miles, and V. P. Choueiri, "A Non-Equilibrium Numerical Study of a Microwave Electrothermal Thruster," 38th AIAA Joint Propulsion Conference, 2002, Indianapolis, IN.

73. K. D. Diamant, B. L. Zeigler, and R. B. Cohen, "Tunable Microwave Electrothermal Thruster Performance on Water," 39th AIAA Joint Propulsion Conference, 2003, Huntsville, AL.

74. S. Laure et al., "ATTILA-Adjustable Throttle Inductively Afterburning Arc Jet," 27th International Electric Propulsion Conference, 2001, Pasadena, CA.

75. J. Gilland, "The Potential for Compact Helicon Wave Sources for Electric Propulsion," 27th International Electric Propulsion Conference, 2001, Pasadena, CA.

76. J. Gilland, "Helicon Wave Physics Impacts on Electodeless Thruster Design," 28th International Electric Propulsion Conference, March 17-21, 2003, Toulouse, France.

77. E. A. Bering et al., "Experimental Studies of the Exhaust Plasma of the VASIMR Engine," 40th AIAA Aerospace Sciences Meeting & Exhibits, 14-17 January, 2002, Reno, NV.

78. R. M. Winglee, *Mini-Magnetospheric Plasma Propulsion (M2P2)*, Seattle, WA, University of Washington, 1999.

79. R. M. Winglee et al., "Mini-Magnetospheric Plasma Propulsion: Tapping the Energy of the Solar Wind for Spacecraft Propulsion," *Journal of Geophysical Research*, **105**, 2000, pp. 21067-21077.

80. R. M. Winglee et al., "Computer Modeling of the Laboratory Testing of Mini-Magnetospheric Plasma Propulsion (M2P2)," 27th International Electric Propulsion Conference, IEPC 2001, Pasadena, CA.

81. T. M. Ziemba et al., "Parameterization of the Laboratory Performance of the Mini-Magnetospheric Plasma Propulsion (M2P2) Prototype," 27th International Electric Propulsion Conference, IEPC 2001, 2001, Pasadena, CA.

82. R. M. Winglee et al., "Radiation Shielding Produced by Mini-Magnetospheres," Space Radiation Shielding Technology Workshop, 2002.

83. R. M. Winglee et al., "Simulation of Mini-Magnetospheric Plasma Propulsion (M2P2) Interacting with an External Plasma Wind," 39th AIAA Joint Propulsion Conference, 2003, Huntsville, AL.

Swedish SAQ Added to UNESCO World Heritage List

The Varberg Radio SAQ at Grimeton, Sweden, has been added to the UNESCO World Heritage List. It is the only remaining pre-electronic transmitter for transatlantic work, and has been kept in perfect working order. On July 4th, "2004 Alexander Day," the 80-year-old 200 kW Alexanderson alternator, with its multiple-tuned antenna, transmitted a celebration message on 17.2 kHz that was heard in Europe and on the US east coast. The return channels were by amateur radio to SA6Q and by e-mail. More information can be found on the SAQ Web site at http://www.alexander.n.se.

According to UNESCO, the Varberg Radio Station at Grimeton, in southern Sweden (built in 1922-24), is an exceptionally well preserved monument to early wireless transatlantic communication. It includes the transmitter equipment and the aerial system, consisting of six 127-m-high steel towers (Figure 1). Though no longer in regular use, the equipment has been maintained in operating condition. The 109.9-ha site comprises buildings housing the original Alexanderson transmitter, including the towers with their antennae, short-wave transmitters with their antennae, and a residential area with staff housing. The architect, Carl Åkerblad, designed the main buildings in the neoclassical style (Figure 2). The structural engineer, Henrik Kreüger, was responsible for the antenna towers, the tallest structures in Sweden at that time. The site is an outstanding example of the development of telecommunications, and is the only surviving example of a major transmitting station based on pre-electronic technology.

Ernst Fredrik Werner Alexanderson (1878-1975) was born in Sweden and emigrated to the United States in 1901. Employed by General Electric, Schenectady, New York, he remained there for the rest of his long and creative life. He began to design HF alternators based on the idea of Reginald A Fessenden, who used one for his first broadcasting experiments at Christmas, 1906, when voice, singing, and

Figure 1. Some of the six 127-m-tall steel towers that support the transmitting antennas (photo by Bengt A. Lundberg, Swedish National Heritage Board).

Figure 2. The main SAQ radio station building (photo by Bengt A. Lundberg, Swedish National Heritage Board).

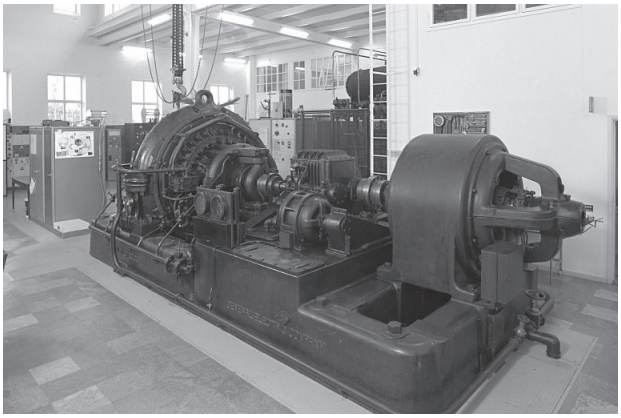

Figure 3. The 200 kW VLF alternators (photo by Bengt A. Lundberg, Swedish National Heritage Board).

music bewildered the radio officers of ships along the US east coast. Alexanderson laid the foundation for communications between Sweden and America, increasingly needed after the first World War. He was awarded decorations, medals, honorary doctorates and, at the age of 94, his 344th patent.

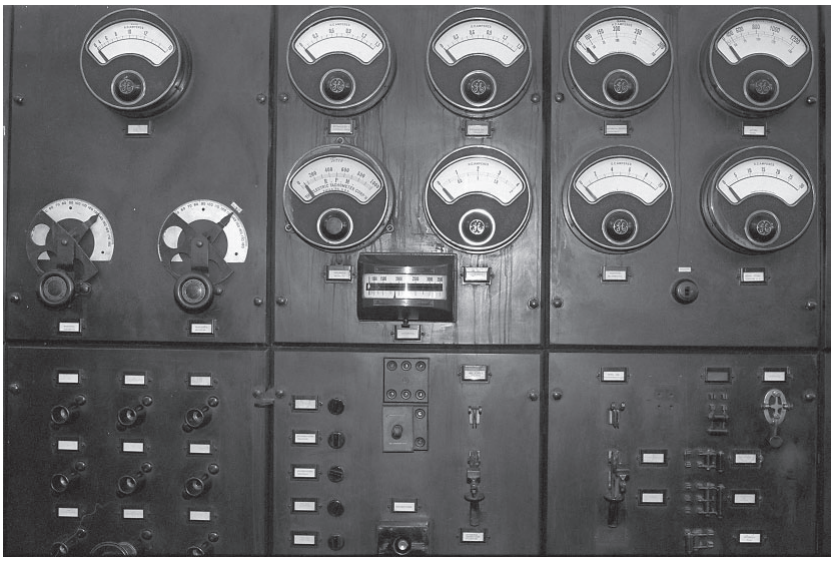

Figure 4. Part of the SAQ radio equipment (photo by Bengt A. Lundberg, Swedish National Heritage Board).

The 200 kW alternators for VLF were ready in 1918 (Figure 3). Including the very impressive multiple-tuned antenna, they were manufactured by General Electric and sold by the Radio Corporation of America around the world. Six 127-m-high towers with 46-m-long booms carried twelve 2,200-m wires that fed six vertical antenna elements from the top of each tower. The network included 18 transmitters in the continental USA, Hawaii, Wales, Poland, and Sweden (Figure 4).

The first message from SAQ was sent to Radio Central at Rocky Point, Long Island, in October, 1924. It was in commercial service slightly beyond the second World War. After that period, the alternator stood only a small chance of survival, because intercontinental communications had been taken over by HF radio. However, the Royal Swedish Navy needed SAQ for VLF traffic to submarines, and remunerated the maintenance costs. Later, the naval interest decreased, and in 1995, the Radio Services of Swedish Telecom decided to close SAQ, still in perfect working order.

As people prepared themselves to listen to the last transmission, other people started a resistance movement that succeeded in preserving the station. A year later, it was listed as a national industrial monument. Our ultimate goal of getting the unique SAQ on the UNESCO World Heritage List was reached on July 2, 2004, thanks to efforts by numerous people, predominantly radio enthusiasts, antiquarians, and others in all Sweden, in the county of Halland, and in the town of Varberg.

The world heritage declaration is a major achievement for radio people. I take the opportunity to thank all in URSI, the world's top radio science organization, for their support in this matter.

SAQ will go on the air once a year on "Alexander Day." Visitors to the station will be guided by the station crew or members of the supporting nonprofit society of Alexander. The cooling-water fountains, the clicking relays, the liquid variable resistors, and the whining alternator will recall the atmosphere of the 1920s: a tribute to Ernst Alexanderson, the complete chief engineer, inducted posthumously into the US National Inventors Hall of Fame in 1983.

Carl Henrik Walde, SM5BF
Secretary, Swedish URSI Committee
Tel: + 46 (0)70 5916061
E-mail: info@walde.se

Radio-Frequency Radiation Safety and Health

James C. Lin

Leakage of Serum Albumin in Rat Brains from Repeated Exposure to Wireless Radiation

The blood-brain barrier (BBB) is a cellular layer in the microvasculature in the brain. The blood-brain barrier partitions the circulating blood from the brain tissue proper. It regulates the passage of vital substances and nutrients into brain tissues, and the passage of carbon dioxide and metabolic waste products out of brain tissues. The selective passage prohibits harmful toxins from infiltrating the brain, and also excludes many drugs and therapeutic agents from reaching brain tissues.

Since the first report, many investigators have published studies on the effect of radio-frequency radiation on the blood-brain barrier of experimental animals, with varied results (see this column in the December, 2001, issue [1]). Studies showing – and not showing – a microwave-induced increase in rat blood-brain barrier permeability changes have used both high and low levels of radio-frequency exposure. However, a series of reports from Lund, Sweden [2-4], showing disruption of the blood-brain barrier at various times following radio-frequency exposure, has caught the attention of many in the field.

The series of reports from Lund, based on observed leakages of endogenous serum albumin in blood, suggested that repeated exposure to radio-frequency radiation from Global System for Mobile Communications (GSM) cellular telephones can alter blood-brain barrier permeability at specific absorption rates (SARs) that are well below the maximum permissible level for cellular telephones: 1.6 W/kg in North America, or 2.0 W/kg in parts of Asia and Europe. Rats were exposed singly to radio-frequency fields in a transverse electromagnetic (TEM) exposure chamber at 900 MHz. Their results have generated questions about repeated exposures of the human brain to microwaves from cellular mobile telephones. Could the normally excluded albumin and other toxic molecules leak into and accumulate around and in the brain cells?

A more recent publication from this group explored the question of whether a pathologic leakage across the blood-brain barrier might parallel damage to the neurons? They showed occurrences of "dark neurons" in the cortex, hippocampus, and basal ganglia in the rat brains [5]. The so-called "dark neurons" are abnormal neurons that appear as black and shrunken nerve cells, which were interpreted by the investigator as evidence for neuronal damage in microwave-exposed rats. In this experiment, rats were exposed for two hours to GSM cell-phone fields of various strengths. The reported SARs were 0.02 W/kg and 0.2 W/kg for the occurrence of dark neurons in the animal's brain up to 50 days following radio-frequency exposure.

The health-related questions raised by the most recent report from Lund, and the lack of independent efforts to confirm the Salford studies, prompted the European project COST 281 to convene a workshop, between the blood-brain-barrier experts and experts in bioelectromagnetics research who had published on blood-brain-barrier interactions, at Schloss Reisensburg, in Germany. This scientific meeting, entitled "The Blood-Brain Barrier (BBB): Can It be Influenced by RF-Field Interactions?" was held in November, 2003, and was organized through the cooperation of the German Research Association for Radio Applications (Forschungsgemeinschaft Funk, FGF e.V.).

A sidebar about COST and COST 281: COST stands for "European Cooperation in the Field of Scientific and Technical Research." It is a framework for international cooperation in research and development, and for coordination of national research at the European level. Note that COST is not a funding entity, but it coordinates research. Members of COST include countries from the European Union and a number of other European states.

James C. Lin is with the University of Illinois at Chicago
851 South Morgan Street (M/C 154),
Chicago, Illinois 60607-7053 USA;
Tel: +1 (312) 413-1052 (direct); +1 (312) 996-3423 (main office); Fax: +1 (312) 996-6465;
E-mail: lin@uic.edu

Within COST, there are 18 strategic European concerted research actions, which are referred to as COST Telecommunication Information Science and Technology (TIST). At the present time, the 18 domains of COST TIST encompass future technologies and services in the fields of satellite, mobile, and optical components and networking, Internet services, speech-processing technology, knowledge management, and health implications of electromagnetic fields.

COST 281 – Potential Health Implications from Mobile Communication Systems – is an action within COST-TIST [6]. The main objective of COST 281 is to obtain a better understanding of the possible health impacts of emerging technologies, especially as they are related to communication and information technologies that may result in human exposure to electromagnetic fields. At present, there are 23 signatory countries that actively participate in this action: Austria, Belgium, Bulgaria, Czech Republic, Croatia, Denmark, Finland, France, Germany, Greece, Hungary, Ireland, Italy, Latvia, Lithuania, The Netherlands, Norway, Poland, Slovenia, Spain, Sweden, Switzerland, and the United Kingdom. Some secondary objectives are to provide, on the European level, scientific evaluation of the available data for use by various decision makers involved in risk management of electromagnetic fields; to provide a basis for risk communication efforts; and to provide information on and identify possible health risks of electromagnetic-field exposures related to emerging technologies.

At the Schloss Reisensburg workshop, nearly every group that was engaged in radio-frequency-related blood-brain-barrier research in the past 10 years was invited to give presentations on their research and findings, in addition to overviews on state-of-the-art techniques by invited experts in the field. The critical reviews and discussions included all relevant reports, and the recent "dark neuron" research was presented by Dr. Salford and Prof. Persson. Indeed, an important feature of the workshop was the gathering of the principal investigators under one roof to discuss their results and to ask questions of each other, at length.

Perhaps to no one's surprise, there were considerable disagreements and speculations on the recent experimental results and interpretation. Concerns expressed included the specific strain of rats used in the experiments, the size and age of the rats, the exposure system and dosimetry, and potential confounding factors, such as restraint- and handling-induced stresses on the animals, as well as experimental protocols associated with exposure and termination of the animals and processing of tissue samples. Of course, there were issues of interpretation and relevance of the findings versus human health and safety of cell-phone use. If the results are true, is the degree of extravasation of blood albumin sufficient to be toxic to the brain, or under what conditions does the leakage reach the threshold concentration for brain damage?

A conspicuous and significant factor in the uncertainty is the paucity of experimental data. A decade following the first two reports from the Lund researchers, there were only two published attempts to confirm their well-known findings. An apparent cause was the lack of interest on the part of organizations that have funded research in the area of biological effects of wireless electromagnetic radiation. Unless impeccable, unreplicated evidence or poorly replicated experimental evidence tends to be taken as defective.

It is important to note that there were two related investigations, but the two attempts were not replication studies. Instead, they were experiments designed to either confirm or refute the findings: the investigations had employed different experimental protocols and exposure systems. As mentioned in a previous column [7], a fundamental requirement for acceptance of scientific findings is repeatability and confirmation. Without question, empirical observations can be flawed. Thus, only replicable observations of experimentally determined effects can serve as legitimate evidence for or against scientific claims.

Living organisms are famously complex. The responses of biological systems to wireless radiation can be variable. The behavior of biological systems can often be uncertain, even under similar circumstances of exposure. It is important that the same investigator replicate a given observation, which the Lund researchers apparently have done. Indeed, most working scientists are reluctant to accept or reject scientific claims on the basis of unreplicable or poorly replicated experimental findings. Because a single, self-repeated study – however well conducted – seldom provides the definitive evidence for or against a biological response, several independently repeated or confirmed studies are needed to arrive at a statistically significant association, or at a convincing answer to the health-effect question.

Significant amounts of albumin leakage can be visualized in brain slices as Evan blue dye staining, and very low level signals of extravasated albumin can be enhanced by Immunohistochemical staining. Immunohistochemical staining of serum albumin was employed in the two subsequent attempts to assess cell-phone-radiation-induced blood-brain-barrier permeability changes. In an acute study, groups of individually-restrained rats were sham or exposed, in a carousal exposure system, for four hours at average SARs ranging from 0.3 to 7.5 W/kg, using 900 MHz GSM fields [8]. The extravasation of serum albumin was assessed either at the end of exposure, or seven days later. A significant increase in serum albumin extravasation was observed only in the group exposed to the highest SAR, 7.5 W/kg, immediately after radio-frequency exposure.

In the other study, immunostaining of serum albumin was used to investigate the effect of exposure to a 1439 MHz, time-division multiple-access (TDMA) cell-phone field on

the permeability of the blood-brain barrier in rats exposed for two or four weeks [9]. Rats were positioned in an exposure system similar to the one used by Fritze et al. [8], and had their heads arrayed in a circle near the central antenna of the exposure system. A peak SAR of 2 W/kg was measured in the rat brain, and the average SAR over the whole body was 0.25 W/kg. There were no significant changes in any of the groups of rats investigated. Results from Evans blue-dye injection were also negative.

A particularly vexing problem with the Lund series of studies was that alteration of barrier permeation appeared to have been observed at many levels of radio-frequency exposures, including those that were as low as 100 times below that allowed for cell phones. While Fritze et al., using an entirely different exposure system, had failed to confirm the Salford et al. findings at SARs of 0.3 - 1.5 W/kg, they had confirmed extravasation of serum albumin at 7.5 W/kg: a level about four times greater than the maximal permissible level for cellular telephones.

It is noteworthy that an extensive replication effort has been underway by the US Air Force Laboratory in San Antonio, Texas, since shortly after the Lund studies were published. To date, results from this effort – which purportedly have used the same exposure systems as the Lund group – have yet to appear in a published form or conference presentation. It is hoped that the results from this US Air Force-sponsored in-house replication effort will speed the scientific process further along.

A potentially beneficial outcome from the workshop at Schloss Reisensburg is the brewing of an idea to replicate the reported occurrences of abnormal neurons in rat brains at several laboratories around the world. As of the closing time for this column, funding for this endeavor is still up in the air.

References

1. J. C. Lin, "Blood-Brain Barrier, Cancer, and Mobile Phones," *Radio Science Bulletin*, 299, December, 2001, pp. 19-21.

2. B. R. R. Persson, L. G. Salford, and A. Brun, "Blood-Brain Barrier Permeability in Rats Exposed to Electromagnetic Fields used in Wireless Communication," *Wireless Networks*, **3**, 1997, pp. 455-461.

3. L. G. Salford, A. Brun, J. L. Eberhardt, and B. R. R. Persson, "Permeability of the Blood-Brain Barrier Induced by 915 MHz Electromagnetic Radiation, Continuous Wave and Modulated at 8, 16, 50, and 200 Hz," *Bioeletrochemistry and Bioenergetics*, **30**, 1993, pp. 293-301.

4. L. G. Salford, A. E. Brun, K. Sturesson, J. L. Eberhardt, and B. R. R. Persson, "Permeability of the Blood-Brain Barrier Induced by 915 MHz Electromagnetic Radiation, Continuous Wave and Modulated at 8, 16, 50, and 200 Hz," *Microscopic Research and Technology*, **27**, 1994, pp. 535-542.

5. L. G. Salford, A. E. Brun, J. L. Eberhardt, L. Malmgren, and B. R. Persson, "Nerve Cell Damage in Mammalian Brain after Exposure to Microwaves from GSM Mobile Phones," *Environ Health Perspectives*, **111**, 2003, pp. 881-883.

6. COST 281, http://www.cost281.org.

7. J. C. Lin, "Cell Phone Testing and Fundamental Scientific Research," *Radio Science Bulletin*, 300, March, 2002, pp. 31-33.

8. K. Fritze, C. Sommer, B. Schmitz, G. Mies, K. A. Hossmann, M. Kiessling, and C. Wiessner, "Effect of Global System for Mobile Communication (GSM) Microwave Exposure on Blood-Brain Barrier Permeability in Rat." *Acta Neuropathologica*, **94**, 1997, pp. 465-470.

9. G. Tsurita, H. Nagawa, S. Ueno, S. Watanabe, and M. Taki, "Biological and Morphological Effects on the Brain after Exposure of Rats to a 1439 MHz TDMA Field," *Bioelectromagnetics*, **21**, 2000, pp. 364-371.

Conferences

CONFERENCE REPORT

MSMW'04

Kharkov National University, Kharkov, Ukraine, 21-26 June 2004

The Fifth International Kharkov Symposium on Physics and Engineering of Microwaves, Millimeter and Sub-Millimeter Waves (MSMW'04) took place at the Kharkov National University, Ukraine on June 21-26, 2004. It was organized by the Scientific Council of the National Academy of Sciences of Ukraine (NASU) on Radio-Physics and Microwave Electronics, in cooperation with the *A. Usikov* Institute of Radio-Physics and Electronics of NASU (IRE NASU), the Institute of Radio Astronomy of NASU (IRA NASU), the *V. Karazin* Kharkov National University (KhNU), the Kharkov National University of Radio Electronics (KhNURE), IEEE AP/MTT/ED/AES/GRS/NPS/EMB Societies East Ukraine Joint Chapter, IEEE MTT/ED/COM/CPMT/SSC Societies Central Ukraine Joint Chapter, IEEE MTT/ED/AP/CPMT/SSC Societies West Ukraine Joint Chapter and the National URSI Committee of Ukraine.

Working days of the conference were June 22 to 25. Every day the conference started with a plenary session of five 35-min invited lectures in a large auditorium. After that, four or three parallel day-long sessions of 15-min contributed papers had been working. All the papers were presented in English. June 26 was filled in with social events. The number of registered participants was 248 including 165 from Kharkov, 26 from the rest of Ukraine, 30 from Russia, 3 from Belarus, Lithuania, Japan, Mexico, and Taiwan each, 2 from Germany, and also from Canada, Czech Republic, Belgium, Finland, the Netherlands, Poland, Sweden, Turkey, and the United Kingdom. Totally around 240 papers out of 281 in the Program were presented. 28 invited papers were presented at plenary and topical sessions. Two-volume MSMW'04 Proceedings counting totally over 960 pages had been published before the symposium. Symposium program contains papers submitted Meeting world known experts in microwaves and shorter wavelength science and technology will be very useful and important to the Ukrainian participants.

The holding of the symposium became possible thanks to the support of sponsors: URSI, IEEE ED and MTT Societies. Besides of traditional founders and sponsors of MSMW, this year the list of organizers included KhNURE. Another new feature is support of the European Microwave Association (EuMA) – leading European professional association in the broad area of microwaves, radar, and electromagnetics science and engineering. EuMA has donated a special grant to be awarded to the best young scientist papers and presentations, as a number of EuMA-MSMW awards. Collaboration with EuMA has also led to adding the term "microwaves" to the title of symposium. This is also an acknowledgement of the fact that most of the associated technologies and ideas span across a wide band of wavelengths, and that MSMW programs normally accommodate papers dealing with all bands of electromagnetic spectrum. The next MSMW'07 is planned to be held in Kharkov in June, 2007.

June 21

June 21 was the day of registration. Besides, those of the Western participants who had come by that moment were able to pay a visit to IRE NASU and see the laboratories of the departments of quasioptics, computational electromagnetics, and microwave spectroscopy.

June 22

MSMW'04 started at 9:00 on June 22, 2004 by the opening ceremony at the " New Physical" auditorium of the Kharkov National University. The first to address the participants was MSMW'04 Chairman, Director of IRE NASU, Vice-Chairman of the Ukrainian National URSI Committee Prof. Vladimir M. Yakovenko. He was followed by the welcome words from the other organizations behind MSMW'04: Vice-Director of IRA NASU, Prof. Valery M. Shulga, Vice-Rector of KhNU Prof. Ilyi I. Zalubovsky and Vice-Rector of KhNURE Prof. Nikolai I. Slipchenko. Vice-Major of the city of Kharkov Prof. N. Soroka told the audience about 350-year historical and cultural heritage of Kharkov. The next to make a welcoming speech was Prof. Anatoly A. Kirilenko of IRE NASU, who spoke in the name of the IEEE AP/MTT/ED/AES/GRS/NPS/EMB Societies East Ukraine Joint Chapter. He emphasized very important contribution of the Chapter to the success of MSMW'04. Prof. Alexander I. Nosich of IRE NASU addressed the participants on behalf of the MSMW'04 Organizing Committee.

That morning the first plenary session was held, consisting of five invited talks:

- A. Raisanen, et al., Recent Results On Using Computer-generated Submm-wave Holograms for Antenna and Rcs Measurements, Helsinki, Finland
- S. Biber, et al., Design Of New Passive Thz Devices Based on Micromachining Techniques, Erlangen, Germany
- Y.K. Sirenko, Computer-aided Technique for Time-Domain Electromagnetic Simulation, Kharkov, Ukraine
- N. Klein, et al., Mems Tuneable Dielectric Resonator Structures for Microwave and Millimetre Wave Applications, Juelich, Germany
- G.A.E. Vandenbosch, Computational Electromagnetics and Antenna Design in Western Europe -Organisation and Overview of The Present Status, Leuven, Belgium

Further, after a lunch, the symposium continued working with four simultaneous sessions:

. Session V. Quasioptical Techniques and Terahertz Technology
. Session VIII. Scientific, Industrial and Biomedical Application
. Session IX. Radio Astronomy and Earth's Environment Study
. Session X. R-Functions, Atomic Functions, Wavelets and Fractals

In these sessions, the following invited papers were presented:

- (Session V) – V.K. Kiseliov, Physical Modeling of Electromagnetic Scattering in the Quasi-optical Transmission Lines, Kharkov, Ukraine
- (Session IX) – A.N. Vystavkin, Et Al., The Multiplexing of Signals in Submillimeter Direct Detector Arrays Using Projections and Frequency Division Methods, Moscow, Russia
- (Session IX) – P.M. Forkman, Et Al., Uncooled Low Noise Frontend of the Receiver System for Ground-based Monitoring Of Stratospheric Ozone and Carbon Monoxide, Sweden & Kharkov, Ukraine
- (Session X) – V.F. Kravchenko, Et Al., Application of New Weighting Functions for Design of Two-dimensional Fractal Antenna Arrays Moscow, Russia

The same evening, at 7:00 p.m., a welcome party was organized at the university restaurant. At the welcome party, Ukrainian champagne was served. This event created a perfect atmosphere to relax and shake off the troubles of long and sometimes tiring journeys that participants had to undertake to reach MSMW'04.

June 23

At the symposium morning plenary session, the following invited papers were presented:

- L.P. Ligthart, Et Al., The Shared Aperture, Sparse Array Antenna Approach to Designing Broadband Array Antennas, Delft, The Netherlands
- F. Yanovsky, Et Al., Doppler-polarimetric Method of Turbulence Intensity Retrieving in Rain Using Remote Sensing with Microwave Radar, *Kiev, Ukraine*
- G.I. Khlopov, Coherent Radar in Short Millimeter Wave Band, *Kharkov, Ukraine*
- J.W. Modelski, Et Al., Present Microwave Activities at the Warsaw University Of Technology, *Warsaw, Poland*
- D.M. Vavriv, Et Al., An Airborn Sar With Indication of Moving Target, *Kharkov, Ukraine*

This day regular sessions of contributed papers consisted of:

. Workshop. Novel Radar Technologies, from Ideas to Applications
. Session I. Electromagnetic Theory and Numerical Simulations
. Session II Waves in Semiconductors and Solid State Structures
. Session III Microwave Superconductivity

In these sessions, the following invited papers were presented:

- (Session I) – A.I. Nosich Et Al., Accurate Characterization Of A Quasioptical-Size Luneburg Lens Fed by A Printed Radiator, Kharkov, Ukraine & Boulder, USA
- (Session II) – N. M. Makarov, Et Al., Anomalous Transmission in Waveguides with Correlated Disorder, Puebla, México
- (Session III) – G.A. Melkov, Et Al., Irradiation of Hts Josephson Junctions with the Surface Wave Resonator, Kiev, Ukraine & Juelich, Germany

On this day, a bus city tour was organized, enabling participants to get acquainted with the history of Kharkov, second-largest Ukrainian city. Remarkable historical buildings and monuments, such as Assumption Cathedral, WW II Memorial, "Gosprom" complex built in the 1920's as an example of constructivism style in the architecture of the early Soviet period were visited.

June 24

On the third day, the morning plenary session looked as follows:

- I.I. Zinchenko, Scientific Goals and Prospects of Millimeter and Submillimeter Radio Astronomy, Nizhny Novgorod, Russia
- Y.M. Poplavko, Et Al., Piezo-controlled Microwave Passive Devices, Kiev, Ukraine & Pohang, Korea
- V.V. Parshin, Et Al., Cvd Diamonds for Microelectronics And Electronics of High Powers, Nizhny Novgorod, Fryazino, Russia & Kharkov, Ukraine & Karlsruhe, Germany & Madrid, Spain
- O.G. Vendik, Ferroelectric Films in Microwave Technique: Physics, Characterization, and Tunable Devices, St. Petersburg, Russia

· K. Yasumoto, Et Al., Reflection And Transmission Properties Of Multilayered Crossed Arrays Of Circular Cylinders, Fukuoka, Japan

Three parallel sessions of regular papers that day went along the following topics:

. Session IV. Vacuum Sources and Solid State Devices
. Session VI. Antennas, Waveguides and Integrated Circuits
. Session VII. Radio Spectroscopy and Electromagnetic Metrology

In this sessions the following invited papers was presented:

· (Session IV) – E.M. Ganapolskii, Et Al., Chaotic Dynamics Of Instable Nanoelectron Systems (Millimeter Wave Band Simulating), Kharkov, Ukraine
· (Session VI) – A.S. Andrenko, Et Al., Circuit Simulation And Design Of Integrated Rf Filter For Vehicle-based W-cdma Mobile Communications System, Yokosuka, Japan
· (Session VII) – S.F. Dyubko, Et Al., Laser-microwave Spectrometer FOR Investigation OF Al AND Au Atoms In Rydberg States, Kharkov, Ukraine & Lexington, USA

That evening, the symposium banquet was held at the university restaurant. This was a lovely event accompanied with live music, dancing and informal speeches. The dominant tone, however, was the joy of meeting the old friends and colleagues and making new ones.

June 25

On the last working day of the symposium, the only morning plenary session consisted of four papers:

· V.E. Lyubchenko, Fundamental Limitations and Perspectives of Application of Semiconductor Devices In Millimeter-wave System, Fryazino, Russia
· A. Velichko, Et Al., Nonlinear Microwave Properties of Hts Thin Films, Birmingham, Uk
· J. Niemeyer, Single Charge Devices for Fundamental Metrology, Braunschweig, Germany
· V.M. Pan, Microwave Properties and Applications of High-t_c Superconducting Single-crystal Films, Kiev, Ukraine

The closing ceremony of MSMW'04 took place in the "New Physical" auditorium of KhNU at 12:00. At first, several awards of the conference were announced and handed to the awardees. This year the European Microwave Association established a 1000 Euro fund to award the best Young Scientist papers orally presented at the symposium. They were divided into 6 prizes: one First Prize (300 Euro), two second prizes (200 Euro), and three third prizes (100 euro). In all, 26 papers took part in the competition. International Awards Jury consisted of 9 members: S. Biber, A.A. Kostenko, L.P. Ligthart, V.V. Meriakri, A.I. Nosich, G. Vandenbosch, O.G. Vendik, F.J. Yanovsky, and K. Yasumoto.

The First Prize was awarded to **Artem Boriskin**, Resonance Lens Antenna Analysis for MM-Wave Applications, *Kharkov, Ukraine*

Two Second Prizes were awarded to **Andrey Rusanov**, Electromagnetic Waves in a Rectangular Plasma Waveguide and their Interaction with an Electron Beam, *Kharkov, Ukraine* and **Nataliya Don,** Computation of Mode Bases for Waveguides with Complicated Cross-Sections, *Kharkov, Ukraine*

Three Third Prizes were awarded to **Vyacheslav Zemlyakov**, Mode Transformation Due to Curvature and Diameter Variations in Smooth-Wall Circular Waveguides, *Rostov, Russia,* **Anna Rudiakova,** Fifth-Harmonic Peaking Electromagnetic Stop-Band Network for Polyharmonic Power Amplifiers, *Donetsk, Ukraine and* **Ivan Karbovnyk,** Time Domain Dielectric Relaxation Spectroscopy of the Ag_2CdI_4 Superionic Conductor, *Lviv, Ukraine*

Besides, 5 Honorary Certificates were awarded for the "Next to the best papers"to: **Sergey Kurilo**, Multifrequency Microwave Imaging, *Minsk, Belarus,* **Yegor Domanov**, Effect of Radio Frequency Electromagnetic Field on the Structural State of Model Membranes, *Kharkov, Ukraine,* **Sergey Antipov**, Noise Performance of Quasioptical Ultrathin NbN Hot-Electron Bolometer Mixer at 2.5 and 3.8 THz, *Moscow, Russia*, **Andrey Lyakhovsky**, Multi-Slot Systems Based on Waveguides with Partial Dielectric Filling, *Kharkov, Ukraine*, **Andrey Perov**, Comparative Analysis of an Open-Ended Waveguide Antenna Pattern Obtained by Exact Model and by Heuristic Approaches, *Kharkov, Ukraine*

Each MSMW'04 award consisted of a colorful certificate signed by Prof. R. Sorrentino, President of the European Microwave Association and by Prof. Vladimir M. Yakovenko, MSMW'04 Chairman. Awards were handed by Prof. L.P. Ligthart of behalf of EuMA.

Besides of awards for oral papers, a special award was established by the IEEE East Ukraine Joint Chapter – for the best poster paper presented at the symposium. It consists of certificate and 50 USD money prize. This award was given to **Elena Smotrova**, Effective Index Dispersion Account in the Cold Model of Disk Resonator with Uniform Gain, *Kharkov, Ukraine*

The number of posters was large, so it was decided to mark two "Next to the best poster papers" presented at the symposium. They are by **Alexei Ivanov**, Uniform Asymptotic Theory of Diffraction by a Curvelinear Impedance Wedge, *Kharkov, Ukraine*, **Sergei Steshenko**, Radiation Patterns of "Plasma" Electron Beam Flowing over a Metal Surface with Grooves, *Kharkov, Ukraine*

The final closing address was done by Prof. Vladimir M. Yakovenko. He announced that the next Symposium, MSMW'07, will be held again in Kharkov in June, 2007, thanked the participants and organizers for creating unprecedented forum for scientific discussions and expressed a hope that the MSMW symposia series will be continued. He also expressed gratitude to international institutions such as IEEE, URSI, EuMA, which rendered valuable and timely support.

On the weekend after Symposium, the participants were proposed a social program in order to get relaxed after four days of intensive work and strengthen the links originated at the symposium.

Prof. Vladimir M. Yakovenko
Official URSI representative at MSMW'04
yakovenko@ire.kharkov.ua

2ND IAGA/ICMA WORKSHOP ON VERTICAL COUPLING IN THE ATMOSPHERE/IONOSPHERE SYSTEM

Bath, UK, 12-15 July 2004

The Second International IAGA/ICMA Workshop on "Vertical Coupling in the Atmosphere/Ionosphere System" was held at the Hilton Hotel in Bath, UK on July 12-15, 2004. The workshop was organised by Dr. Dora Pancheva and Prof. Nick Mitchell, members of the Atmospheric Dynamics and Meteor Radar Group at the Department of Electronic and Electrical Engineering, University of Bath. The meeting was attended by a total of 65 senior and young scientists from 19 countries. During the 4 days of the workshop the participants presented 60 papers, from which 9 were review solicited, 16 solicited and 35 were contributed oral presentations.

The aim of this workshop was to address the physics behind the forcing mechanisms that originate in the lower atmosphere which play an important role on the upper atmosphere and ionosphere. The meeting was designed so that research experts form both the upper neutral atmosphere and ionosphere communities come together in order to present their work and assess/debate ongoing issues relating to the theoretical, modelling and observational aspects of the dynamic processes which transfer energy and momentum from the lower atmosphere to the upper atmosphere and ionosphere.

The programme focussed on various aspects and topics of neutral dynamics as well as ionospheric electrodynamics and plasma physics. These included:

1) Gravity wave forcing in the atmosphere at equatorial, midlatitude and polar regions.
2) Tidal and planetary wave coupling in the middle atmosphere and impacts on the mesosphere and lower thermosphere.
3) Variability and tropospheric forcing of the diurnal tides in the mesosphere and lower thermosphere.
4) Planetary wave climatology and nonlinear effects in the propagation of planetary waves in the upper atmosphere.
5) Effects on the dynamical and chemical-compositional structure of the MLT region by vertically propagating atmospheric waves as well as solar effect impositions.
6) The role of thunderstorm-related electrical processes coupling the atmosphere and ionosphere.
7) Tidal and Planetary wave forcing of meteoric metal and sporadic E layers in the lower thermosphere and ionosphere.
8) Coupling of neutral dynamics and electrodynamics in the midlatitude thermosphere-ionosphere system.
9) Lower thermospheric forcing effects in the equatorial ionosphere as well and E and F region electrodynamical coupling over equatorial latitudes.

A photograph of the participants in the 2nd IAGA/ICMA workshop on Vertical Coupling in the Atmosphere-Ionosphere System, held in Bath, UK, from July 12 to 15, 2004.

10) Ionospheric topics on the forcing of the ionosphere by waves from below, mid-latitude E region plasma instabilities and irregularities, and F region links with the lower ionosphere.

This was a very well organised workshop which brought together a mix of scientists doing mostly independent research on the fields of the MLT neutral atmosphere and the ionosphere, that is, on two collocated "spheres" of the near earth environment which remain closely coupled and on a continuous interaction. The meeting provided an excellent opportunity for these research communities to interact in a supplementary manner in reviewing and debating the progress done to date in the field of the upper atmosphere-ionosphere and come up with suggestions and ideas for further research on the vertical coupling of the atmosphere-ionosphere system.

Many participants (more than 35) have agreed to submit papers for publication on a special JASTP issue that is to be dedicated to the July 2004 Bath workshop.

Financial contributions to the workshop were made by the following organisations: International Association of Geomagnetism and Aeronomy (IAGA), International Commission on the Middle Atmosphere (ICMA), the US Air force European Office for Aerospace and Development (EOARD), International Union of Geodesy and Geophysics (IUGG), and the International Union of Radio Science (URSI). In particular, URSI contributed with a grant of 500 Euros. This grant was used to support the travel expenses of the solicited speaker Dr. Jiangang Xiong of Wuhan Institute of Physics and Mathematics, Chinese Academy of Sciences, Wuhan, China.

Dr. Christos Haldoupis
Official URSI representative at the Workshop
chald@physics.uoc.gr

ISSSE'04

Linz, Austria, 10-13 August 2004

The 6th International Symposium on Signals, Systems, and Electronics, ISSSE 2004, was held in Linz, Austria on August 10-13, 2004. ISSSE is an international symposium held once every three years. This symposium is organized and sponsored by the International Union of Radio Science (URSI), Commissions C and D, and moreover, this year's event was cosponsored or technically cosponsored by the IEEE Microwave Theory and Techniques Society (MTT-S), the IEEE COM/MTT Joint Chapter Austria, the Austrian Electrotechnical Association (ÖVE), the German Association for Electrical, Electronic & Information Technologies (VDE), the government of Upper Austria, the city of Linz, the Linz Center of Mechatronics (LCM), the University of Applied Sciences of Upper Austria, and the University of Linz.

The ISSSE 2004 provided a full 3-day program, which was composed of two keynote speeches, a large number of regular sessions, poster sessions, and a tutorial on smart antennas and MIMO. The symposium proved to be an inspiring forum for discussions, exchange of ideas, and the possibility to maintain and initiate fruitful networks between scientists and developers in the fields of signal- and system theory, electronic components, and communications engineering.

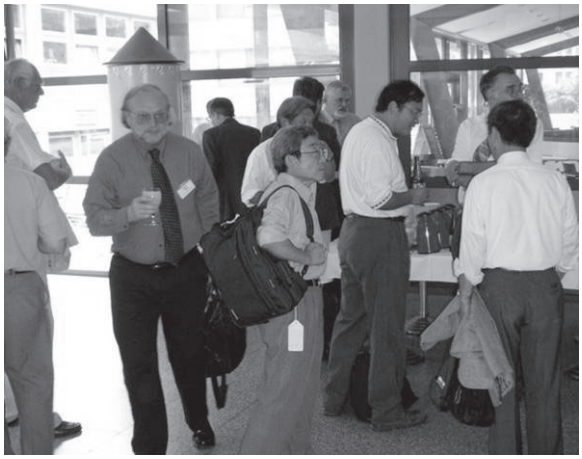

Photo : J. Zehentner (IEEE MTT-S Coordinator), B. Trew (IEEE MTT-S President), M. Akaike (Chair URSI Commission C), P. Russer (Chair URSI Commission D), Ke Wu, T. Itoh and others discussing during the coffee break

After the review of nearly 130 submissions, 89 were accepted for presentation. Authors came from more than 20 countries, thereof 63% from Europe, 29% from Asia, and 8% from North America.

Beside the technical program the social event in the monastery of St. Florian with a subsequent banquet in the monastery's rooms provided an outstanding ambience for personal conversations and cultural exchange.

During the symposium two best papers have been awarded. The winner of the ISSSE'04 URSI commission C Best Paper Award is Ronald Raulefs from the German Aerospace Center in Oberpfaffenhofen, Germany, for his paper entitled "Enhanced Detection Through Signal Space Diversity for a Coded MC-CDMA System", while Jan-Louis Sundermeyer from the Fraunhofer Institute for Integrated Circuits IIS in Erlangen, Germany, received the ISSSE'04 URSI commission D Best Paper Award for his paper "An Alexander Half-Rate Phase Detector for 80 Gb/s".

For further information concerning ISSSE 2004 please refer to http://www.icie.jku.at/issse04/. The next ISSSE will presumably be held in Montreal, Canada in 2007.

Dr. Robert Weigel
General Co-Chair ISSSE'04
r. weigel@ieee.org

THE 7TH INTERNATIONAL SCHOOL/SYMPOSIUM FOR SPACE SIMULATIONS (ISSS-7)

Kyoto, Japan, 26 - 31 March 2005

The 7th International school/symposium for space simulations (ISSS-7) will be held for promotion of science and technology related to space physics via computer simulations. The ISSS is an URSI generated school/ symposium for research fields especially related to Commissions H and G. The program of ISSS-7 is designed for schooling space plasma simulations to young scientists and graduate school students, as well as sharing recent simulation outcomes with related researchers.

The main objectives of ISSS-7 are to:

- Disseminate recent developments in simulation techniques and in high performance computing technology for space physics,
- Review the latest research achievement of simulation and modeling studies in the fields of the Solar-Terrestrial Physics (STP), space engineering and space utilization,
- Provide a forum for promoting international cooperation on theory, observation, and space simulation studies,
- Promote simulations in association with human activities in space environment and humanosphere.

Program Topics

Tutorials & Exercises

1. Introduction to space simulations
   - Scientific/technological background
2. How to implement numerical algorithms
   - Coding methods and techniques
3. How to build numerical models of physical systems
   - Initial/boundary conditions
4. How to optimize simulation codes
   - Parallelization and code tuning
5. How to realize the maximum information from the simulation results
   - Latest visualization techniques
   - Massive data handling

Symposium

Special Session:

"Sustainable Humanosphere"- Perspectives of space simulations -

Regular Sessions:

- Space Physics Simulation & Theories
- Space Data Analysis/Modeling
- Space Environment and Utilization
- Advanced Simulation Techniques

Organization

Organizing Committee

Hiroshi Matsumoto (Japan, Chair)
Maha Ashour-Abdalla (USA)
Manfred Scholer (Germany)
Tetsuya Sato (Japan)

Local Organizing Committee

Yoshiharu Omura (Japan, Chair)

Program Committee

Bertrand Lembege (France, Chair)
Hideyuki Usui (Japan, Co-chair)
David Schriver (USA, Co-chair)
Kile B. Baker (USA)
Joerg Buechner (Germany)
Steven A. Curtis (USA)
Xiaohua Deng (China)
James W. Eastwood (U.K.)
Tohru Hada (Japan)
Tatsuki Ogino (Japan)
K. Dennis Papadopoulos (USA)
Zuying Pu (China)
Toshio Terasawa (Japan)
Loukas Vlahos (Greece)
Lev M. Zelenyi (Russia)

Contact

Secretariat of ISSS-7
Research Institute for Sustainable Humanosphere,
Kyoto University,
Gokasho, Uji Kyoto 611-0011, JAPAN
FAX: +81-774-31-8463
E-mail : isss7@rish.kyoto-u.ac.jp
http://www.rish.kyoto-u.ac.jp/isss7/

Coherence and Electromagnetic Fields in Biological Systems (CEFBIOS-2005)

Prague, Czech Republic, 1 - 4 July 2005

The Froehlich's Centenary International Symposium on Coherence and Electromagnetic Fields in Biological Systems (CEFBIOS-2005) will be held in Prague, Czech Republic, 1-4 July 2005. This Symposium is organized by the Institute of Radio Engineering and Electronics (Academy of Sciences of the Czech Republic), the 1st Medical Faculty of Charles University in Prague, the Physiological Institute of the 1st Medical Faculty of Charles University and the National Institute of Public Health of Ministry of Health Care of the Czech Republic.

The Symposium is organized under the aegis of Professor Stepan Svacina, dean of the 1st Medical Faculty, Charles University, and Dr. Vlastimil Matejec, director of the Institute of Radio Engineering and Electronics, under the auspices of the International Commission K of URSI, of the National URSI Committee of the Czech Republic, and of the Czechoslovak Section of IEEE.

Topics

1) Coherence and Electromagnetism in Biological Systems
- Nonlinear mechanisms of coherence in biological systems
- Electrical polar structures in biological systems and their properties, cytoskeleton structures–microtubules and actin filaments
- Coherent vibrations in biological structures
- Energy supply and excitation of cellular and subcellular structures
- Generation of electromagnetic fields at the cellular and subcellular levels
- Measurement of electromagnetic emission from biological structures
- Endogenous electromagnetic fields and cellular signaling systems
- Electromagnetic field in the transport of reaction components in cells

2) Interaction of Biological Systems with
- External Electromagnetic Fields
- Biophysical mechanisms of interaction
- Effects of external fields on electrical polar macromolecules and polar structures in cells
- Effects of external fields on brain processes
- Reproducible non-thermal biological effects of electromagnetic fields

3) Medical Applications of Electromagnetic Fields
- Electromagnetic treatment of cancer in combination with other modalities
- Effects on brain processes and on nerve stimulation
- Cardiomyopathy and microcirculation
- Magnetotherapy in orthopaedics
- Inflamatory processes and pain relief
- Diagnostic use of electromagnetic fields
- Problems of application of external electromagnetic fields

Abstract Deadline

The deadline for receipt of abstracts at the Symposium Office is January 15, 2005. Abstracts will be reviewed by the International Scientific Committee. Authors will be notified in April of the International Scientific Committee's decision. Abstracts of accepted papers will be accessible on Internet.

Contact

Dr. Jiri Pokorny
Institute of Radio Engineering and Electronics
Symposium CEFBIOS2005
Chabersk´a 57
182 51 Prague 8 – Kobylisy, Czech Republic
Tel: +420 266773432, Fax: +420 284680222
E-mail: pokorny@ure.cas.cz
Internet: http://www.ure.cas.cz/events/cefbios2005/

2005 International Symposium on Microwave, Antenna, Propagation, and EMC Technologies for Wireless Communications (MAPE 2005)

Beijing, China, 8 - 12 August 2005

The symposium will take place in celebration of the information era milestone. The aim of the symposium is to provide a multidiscipline forum for engineers and scientists in the fields of microwave, antenna, propagation, and EMC technologies to focus on applications in the ever-growing area of wireless communications. The topics of the

symposium will cover all of the interesting theory and techniques of microwaves, antennas, propagation, and EMC necessary for wireless communications. You are cordially invited to summit papers to this important event in radio science of the world, and to meet world colleagues in 2005 in China, where there are more potential challenges and opportunities for information science and technology.

Scope

Contributions describing original research, surveys, and applications in the following areas are solicited:

1. Systems and Services
   - Mobile Satellite Communication
   - WLANs
   - Wireless Sensors and Ad Hoc Networks
   - MIMO Transmission Technologies
   - UWB and Impulse Radio
   - 4th-Generation Mobile Wireless Systems
   - Space-Time Channel Characterization and Modeling
2. Microwave Electronics
   - Passive and Active Circuits
   - Power Amplifiers, Linearization, and Active Components
   - MMICs and Microwave Circuits
   - Microwave and Millimeter-Wave ICs
   - Millimeter-Wave and Sub-Millimeter-Wave Components, Circuits, and Systems
3. Antennas
   - Microstrip and Printed Antennas
   - Active and Integrated Antennas
   - Array Antennas, Phased Arrays and Feeding Circuits
   - Mobile and Base Station Antennas
   - Adaptive and Smart Antennas
   - Multi-Band Antennas
   - Reconfigurable Antennas
   - Millimeter Wave and Sub-Millimeter Wave Antennas
   - MEMS/Nanotechnology for antennas
4. Propagation
   - Mobile and Indoor Propagation
   - Millimeter and Optical Wave Propagation
   - Earth-Space and Terrestrial Propagation
   - Radio Meteorology and Astronomy
   - Remote Sensing
   - SAR Polarimetry and Interferometry
   - Ionospheric Propagation
   - Propagation and channel characterization
   - Diversity techniques Fading countermeasures
   - Signal separation and interference rejection
5. Electromagnetic Wave Theory
   - Complex Media and Artificial Media
   - Computational Electromagnetics
   - High-Frequency Techniques
   - Time Domain Techniques
   - Inverse Problems
   - Random Media and Rough Surfaces
   - Periodic and Band-Gap Structures
   - Non-Linear Electromagnetics
6. Signal Processing, Coding, or Waveforms
   - Error control coding
   - Interference Excision/Suppression
   - Bandwidth Efficient Modulation
   - Orthogonal FDM
   - Space-Time Codes
   - Analog-to-Digital Conversion
   - Signal Processing for Communications
   - Signal Processing Tools for Ad Hoc, Multi-Hop, and Sensor Networks
7. EMC and Related Topics
   - EMC/EMI Simulations and Measurements
   - Biological Effects and Medical Applications
   - High-Power Microwave Applications
   - Advanced Materials for EM Applications
   - Subsurface Sensing
   - Satellite Systems
   - Ubiquitous Network Systems
   - Radio Technologies for Intelligent Transport Systems
   - EM Simulators, Visualization and Education

Conference Committee

The conference is co-chaired by Prof. Zong Sha, China, and Dr. W. Ross Stone, USA. The Program Committee Chair is Prof. Linchang Zhang, China. The Organizing Committee Chair is Mr. Mengqi Zhou, China.

Paper Submission

Authors are requested to submit their one-page abstracts and four-page full papers simultaneously. All submissions must be electronic in PDF format before **March 31, 2005**, to Prof. Linchang Zhang, Beijing Jiaotong University, China; E-mail:

lczhang@center.njtu.edu.cn

Contact

For more information, please visit the Web site:

http://www.cie-china.org/mape2005

or contact Mr. Mengqi Zhou, PO Box 165, Beijing 100036, China; E-mail: mqzhou@public.bta.net.cn

URSI CONFERENCE CALENDAR

An up-to-date version of this Conference Calendar, with links to the various conference web sites can be found at www.ursi.org : Calendar of supported meetings.

November 2004

URSI School on Radio Science
ICTP Trieste, Italy, 6-15 November 2004
Contact : Prof. S.M. RADICELLA, Aeronomy and Radiopropagation Laboratory, ICTP, Strada Costiera 11, PO Box 586, I-34014 TRIESTE, ITALY, Phone : +390 40 224 0331, Fax : +390 40 224 604, E-mail : sandro.radicella@ictp.trieste.it

JINA 2004 - 13 èmes Journées Internationales de Nice sur les Antennes
Nice, France, 8-10 November 2004
cf. announcement in RSB December 2003, p. 67
Contact : Secretariat JINA, France Telecom R&D, Fort de La Tête de Chien, F-06320 La Turbie, France, Fax : +33 4 92 10 65 19, E-mail : jina.2004@wanadoo.fr, Web site : http://www.jina2004.com

February 2005

EMC Zurich'05 - International Zurich Symposium & Technical Exhibition on Electromagnetic Compatibility
Zurich, Switzerland, 14-18 February 2005
Contact : EMC Zurich 2005, ETH Zentrum, Gloriastrasse 35, CH-8092 Zurich, Zwitzerland, Tel. +41 1-632 2951, Fax +41 1-632 1198, E-mail : info@emczurich.ethz.ch, http://www.emc-zurich.ch

March 2005

IWSE 2005 - International Workshop on Seismo Electromagnetics 2005
Tokyo, Japan, 15-17 March 2005
Contact : Prof. M. Hayakawa, Dept. of Electronic Engineering, The University of Electro-Communications, 1-5-1 Chofugaoka, Chofu City, 182-8585 TOKYO, JAPAN, Phone : +81 424-43 5159, Fax : +81 424-43 5783, E-mail : iwse2005@whistler.ee.uec.ac.jp , http://www.iwse.ee.uec.ac.jp

TELECOM'2005 & JFMMA
Rabat, Morocco, 23-25 March 2005
Contact : Prof. Ahmed MAMOUNI, IEMN, Cité Scientifique, Av. Poincaré, BP. 69, 59652 Villeneuve d'Ascq, France, E-mail : Ahmed.Mamouni@iemn.univ-lille1.fr

ISSS-7 - 7th International School/Symposium for Space Simulations
Kyoto, JAPAN, 26 - 31 March 2005
cf. announcement in RSB September 2004, p. 117
Contact : ISSS-7 Secretariat, Research Institute for Sustainable Humanosphere, Kyoto University, Gokasho, Uji Kyoto 611-0011, Japan, Tel. +81-774-38-3811, Fax : +81-774-31-8463, E-mail : isss7@rish.kyoto-u.ac.jp, http://www.rish.kyoto-u.ac.jp/isss7/

May 2005

IES 2005 - 11th International Ionospheric Effects Symposium
Alexandria, Virginia, USA, 3-5 May 2005
Contact : JMG Associates Ltd., IES2005 Symposium Managers, 8310 Lilac Lane, Alexandria, VA 22308, USA, Fax: +1-703-360-3954, jm_good@cox.net, Web site : http://www.ies2005.com

4th European Workshop on Conformal Antennas
Stockholm, Sweden, 23-24 May 2005
Contact : Dr. Patrik Persson, Royal Institute of Technology, Alfvén Laboratory, Division of Electromagnetic Theory, SE-100 44 Stockholm, Sweden, E-mail : patrik.persson@alfvenlab.kth.se , http://www.ewca-home.org/

June 2005

ANTEM 2005
Saint Malo, France, 15-17 June 2005
Contact : Antem 2005 - IETR Université de Rennes 1, campus Beaulieu, Bât. 11D 35042 Rennes Cedex, France, Tel. +33 2 23 23 62 17 and +33 2 23 23 69 56, Fax +33 2 23 23 69 69, http://antem2005.ietr.org/home/index.htm

EMC2005 - VIth International Symposium on Electromagnetic Compatibility and Electromagnetic Ecology
St. Petersburg, Russia, 21-24 June 2005
Contact : Dr. Pavel Asovich, Prof. Popov Str. 5, St. Petersburg 197376, Russia, Fax +7 812 234-4840, E-mail : discone@vilan.spb.ru , http://www.eltech.ru/emc2005

July 2005

CEFBIOS 2005 - Coherence and Electromagnetic Fields in Biological Systems
Prague, Czech Republic, 1-4 July 2005
cf. announcement in RSB September 2004, p. 118
Contact : Dr. Jiri Pokorny, Inst. of Radioengineering and

Electronics, Academy of Sciences of the Czech Republic, Chaberska 57, CZ-182 51 PRAGUE 8, Czech Republic, phone : +420 266 773 432, fax +420 284 680 222, pokorny@ure.cas.cz , http://www.ure.cas.cz/events/cefbios2005/

August 2005

ISAP'05 - International Symposium on Antennas and Propagation
Seoul, Korea, 3-5 August 2005
Contact : Prof. H.J. Eom, Department of Electrical Engineering and Computer Science, Korea Advanced Institute of Science and Technology (KAIST), 373-1, Guseong-dong, Yuseong-gu Daejeon, 305-701 Korea, Tel. +82 42-869 3436, Fax : +82 42-869 8036, E-mail : hjeom@ee.kaist.ac.kr, http://www/isap05.org

MAPE 2005 - International Symposium on Microwave, Antenna, Propagation, and EMC Technologies for Wireless Communications
Beijing, China, 8-12 August 2005
cf. announcement in RSB September 2004, p. 118
Contact: Mr. Mengqi Zhou, Secretary of IEEE Beijing Section, P.O. Box 165, Beijing 100036, China, Email: mqzhou@public.bta.net.cn

ISMOT 2005 - 10th International Symposium on Microwave and Optical Technology
Fukuoka, Japan, 22-25 August 2005
Contact : Prof. Kiyotoshi YASUMOTO, Dpt. Comp. Sci. & Comm. Eng., Kyushu University, 6-10-1 Hakozaki, Higashi-ku, Fukuoka 812-8581, Japan, Phone: +81-92-642-4045, Fax: +81-92-632-5204, E-mail: yasumoto@csce.kyushu-u.ac.jp , http://ismot2005.fit.ac.jp

October 2005

XXVIIIth URSI General Assembly
New Delhi, India, 23-29 October 2005
Contact : URSI Secretariat, c/o INTEC, Sint-Pietersnieuwstraat 41, B-9000 Ghent, Belgium, Tel. : +32 9 264 3320, Fax : +32 9 264 4288, E-mail : ursi@intec.rug.ac.be, http://www.ursiga2005.org

If you wish to announce your meeting in this calendar, you will find more information at www.ursi.org.
URSI cannot be held responsible for any errors contained in this list of meetings.

News from the URSI Community

NEWS FROM THE MEMBER COMMITTEES

FRANCE
Médaille du CNFRS

Le 29 mars lors des Journées scientifiques du Comité National Français de Radioélectricité Scientifique, la Médaille du CNFRS a été remise à Jean-Charles Bolomey par Bernard Picinbono. Cette médaille est "destinée à honorer les membres du CNFRS qui ont oeuvré pour le renom de la Science française et/ou participé d'une manière très significative à la vie et au renom du CNFRS." Le CNFRS souhaite ainsi souligner l'importance de la contribution de Jean-Charles Bolomey aux techniques de champs proches en électromagnétisme et à leur modélisation numérique.

Jean-Charles Bolomey, né à Paris en 1942, est membre du Comité français de l'Union Radio Scientifique Internationale (CNFRS) dont il a été délégué national pour la Commission B de 1976 à 1980. Il est également membre émérite de la Société des Electriciens et des Electroniciens (SEE) dont il a animé la section 25 de 1975 à 1982; il est aussi membre de 'l Institution of Electrical and Electronic Engineers (IEEE).

De 1982 à 1994, il a assuré la présidence des Clubs Micro-Ondes puis Rayonnement d'EDF. Par ailleurs, il a obtenu la médaille Blondel de la SEE (1976), le Prix de la Conférence européenne des Micro-ondes (1983), ainsi que le Prix Général Ferrié de l'Academie des Sciences (1984). Ses travaux sur la diffraction inverse et l'imagerie micro-onde lui ont valu de recevoir le Stichting Award de la fondation Schlumberger (1994). En 2002, il a reçu le prix de l'Antenna Measurement Technique Association (AMTA) pour sa contribution à la métrologie des antennes et plus particulièrement aux techniques rapides de champs proches.

GERMANY

50 Years of the German URSI Member Committee

In 1950, the newly founded Working Group Ionosphere decided to prepare the establishment of a German URSI Member Committee, which, as a matter of fact, became a full Member during the 1954 General Assembly in The Hague. It was then chaired by the late Honorary President of URSI, Professor Walter Dieminger.

On behalf of that occasion, a Festival Colloquium was organized during the annual September, 2004, meeting of the Member Committee in Miltenberg, Germany (the so-called Kleinheubacher Tagung). The President of URSI, Prof. Kristian Schlegel, brought the greetings of URSI, and the history of the committee was summarized by its long-term Chair, Dr. Hans J. Albrecht.

Three invited key guest speakers – Prof. Ismo Lindell, from Helsinki Technical University; Dr. Stefan Fechtel, from Infineon Technologies, in Munich; and Prof. Ursula van Rienen, from the University of Rostock – presented tutorial scientific talks. These ranged from the evolution of electromagnetics in the 19th century, through the orthogonal frequency-division multiplexing modulation technique, to electromagnetic simulation in medicine and biology.

Karl J. Langenberg
Chair of the German URSI Member Committee
E-mail: langenberg@uni-kassel.de

POLAND

XI National Symposium of Radio Science

Poznan Center of Science, Poznan, Poland, 7-8 April 2005

In a variety of life areas, increased significance of radio communications has been noticed in recent years. Radio science is an essential element of progress in new technologies, contributing to the development of information society and the rising security and everyday life standards. Evidence of this are the developing cellular phone networks, wireless data transmission networks, the concept of PCS, etc. We also witness major discoveries in radio astronomy and interesting applications of electromagnetic fields in medicine. Therefore, research in the area of radio science is finding growing use, especially in electromagnetic field and wave propagation theories, radio channel modelling, electromagnetic noise and interference cancellation, metrology, electromagnetism in medicine and biology, as well as in the field of radio communication systems design.

Topics

Topics of interest include but are not limited to the following:

- Electromagnetic Metrology
- Electromagnetic Field Theory
- Electromagnetic Fields in Biology and Medicine
- Wireless Information Networks
- Electromagnetic Noise and Interference
- Radio and TV Broadcasting
- Radar and Navigation Systems
- Radio Wave Propagation
- Signals and Systems
- Radio Astronomy
- Satellite Systems
- Mobile Communications
- Human Impact
- Nanotechnology in radio systems

Organizing Committee:

Andrzej Dobrogowski (chairman)
Members:
Hanna Bogucka
Adrian Langowski
Anna Pawlaczyk
Barbara Wagrowska

Contact

URSI 2005 Office
Poznan University of Technology
Institute of Electronics and Telecommunications
ul. Piotrowo 3A
60-965 Poznan, POLAND
tel.: 061-6652291, fax: 061-6652572
ursi@et.put.poznan.pl

TURKEY
URSI-TÜRKÝYE'2004 CONGRESS

Bilkent University, Ankara, Turkey, 8-10 September 2004

The Second National Congress of URSI-Turkey National Committee was organized at Bilkent University, Ankara, Turkey on Sept 8-10, 2004. The Co-Chairs of the organization Committee were Prof. A. Altintas and Dr. V.B. Erturk of Bilkent University. Most of the hard work of local organization has been done by Ph.D. students C.A. Tunc and B. Babaoglu. The constant interest and generous help of the Turkish National Committee Chair, Prof. Hamit Serbest is worth mentioning. The aim of the congress was to bring together Turkish speaking scientists and engineers in the URSI related areas, and to facilitate the exchange of ideas and information. Another aim was to encourage and motivate the young scientists and students in URSI topics.

Even though the congress was a national one and presentations were in Turkish, plenary sessions are held in English for the international eminent radioscientists who were invited to bring most up-to-date research topics to the attention of the audience and to expose with exciting presentations.

Besides, three of the invited plenary session speakers were the chairs of URSI Commissions. Prof. Russer of Technical University of Munich, chair of URSI Commission D, gave a talk on "Network Methods in Electromagnetic Field Computation". The approach is very useful in generating compact models of electromagnetic radiation. The second international invited speaker was Prof. O. Breinbjerg of Technical University of Denmark. Prof. O. Breinbjerg's talk was on Electric Line Source Illumination of Losssless Left-handed Cylinders- A Study of Near-Field and Far-Field Properties". This is an emerging and hot topic expected to be fruitful for many applications. Prof. Umran Inan gave an overview of VLF Remote Sensing of Lightning-Induced Effects in the Ionosphere and the Radiation Belts. His presentation was filled with many audio-visual effects. Prof. Inan, as the chair of Commission H, gave also very useful input into the workings of Turkish National Committee. Chair of Commission B Prof. M. Ando's talk (given by Prof. J. Hirokawa of Tokyo Institute of Technology) was on "Extraction of GO and Diffraction Component for Physical Optics in Terms of Line Integration of Equivalent Edge Currents by Modified Edge Representation". It is a very new and inspiring look at the old technique of PO.

For the training of young scientists, there has been three short courses offered free to all participants. These short courses were delivered by;

- Prof. Levent Sevgi, "Modeling and Simulation Strategies for Wireless Propagation: Perspectives and challenges"
- Prof. Ayhan Altintas, "High Frequency Techniques in Electromagnetics"
- Dr. Satilmis Topcu, "Propagation Prediction Techniques in Radiocommunications and Engineering Applications for Frequency Planning"

Outstanding national speakers were also invited to cover a broad range of radioscience topics and to publisize the research in Turkish universities. The national invited speakers were:

- Haldun Ozaktas, Bilkent University
- Yurdanur Tulunay, Istanbul Technical University
- Ekmel Ozbay, Bilkent University
- Irsadi Aksun, Koc University
- Mustafa Kuzuoglu, Middle East Technical University(METU)
- Ergin Atalar, Johns Hopkins and Bilkent University

There were about 150 participants with 124 presentations from 49 different institutions. The proceedings is available at the URSI Turkey web site at: http://ursi.mersin.edu.tr/ikincikongre.htm

In addition, there were two special sessions honoring Prof. M. Idemen of Isik University and Prof. A. Hizal of METU. These sessions were organized and delivered by the former students of professors.

IEEE Turkey section and AP/MTT/EMC/ED chapter supported the organization of the student paper contest. The first prize in the contest went to O. S. Ergul of Bilkent University. The second and third prize winners were S. Onat and A. E. Yilmaz, respectively, of METU.

URSI Turkey National Committte is very much thankful to the support of Tubitak, Aselsan, Havelsan, Karel and Turkcell for their sponshorship. Without their generous help, the congress would not have been that successful. Next National Congress will be held in Hacettepe University, Ankara, Turkey in 2006.

COMMISSION G

A New Commission G Working Group on Ionospheric Research to Support Radio Systems

During the XXVIIth triennial URSI General Assembly in Maastricht, it was decided by Commission G to form a new working group on ionospheric research to support radio systems (WG G.4). It is hoped that WG G.4 will provide a focus for research and collaboration that is specifically aimed at improving the performance of ionospheric radio systems. It will thus address item E of the commissions terms of reference: "Application of ionospheric information to radio systems." Performance enhancements may be due to either exploitation or mitigation of ionospheric effects. It is intended that the working group should consider a wide range of systems, which may include:

1. Communications – including LF, MF, and HF skywave radio; especially digitally modulated systems such as those embodied within the new Digital Radio Mondiale (DRM) system. Trans-ionospheric UHF satellite communications are also included.

2. Radars/surveillance – including HF over-the-horizon radar, space-based radar, and ground-based radar.

3. Navigation – including GNSS, GPS, etc., and various augmentation systems.

The research activities of the working group will include the use of the following to support the operation, testing, or development of radio systems:

1. Ray tracing.
2. Scintillation measurement, modeling and forecasting.
3. Electron-density imaging, modeling, and forecasting.
4. Sensor integration for ionospheric specification.
5. Channel modeling and simulation.

The overall roles of the working group will include:

1. Exchange of code and modeling techniques.
2. Integration of space weather resources.
3. Better understanding of the engineering utility of our research.
4. Sponsorship of meetings and sessions at the General Assembly.

In order to guide the initial work of the working group, it has been decided to focus on two topics of interest. It should be noted that it is not the intention to limit the working group to these topics, but rather that they can be used to generate initial interest in the group.

The first topic is the development of internationally recognized data sets that can be used to test ionospheric data assimilation and imaging schemes. As different ionospheric imaging techniques are developed, it will become increasingly important to undertake studies to assess their performance against independent ionospheric data. The working group test data sets should include a defined set of data to be assimilated, as well as independent data against which the fidelity of the ionospheric reconstructions can be tested. All of the data should be non-propriety, available to all, and in easy-to-manipulate formats. To open discussions on this topic, the working group Chair and vice-Chair will propose such a data set, and provide details on the working group Web site. It is hoped that it will have been possible to perform some comparative testing before the next URSI GA.

The second topic concerns the development of new HF prediction codes tailored for application to digital HF communications and broadcasting. Although this topic appears to be recognized as being of increasing importance as new digital HF standards emerge, little tangible progress has been made over the last few years. It is suggested that the working group should seek to produce a discussion document on such prediction codes that will address possible technical approaches and the availability of data sets that may contribute to better models of delay and Doppler spread.

URSI radio scientists are invited to comment on the above proposals and on the working group more generally. The working group has a Web site (http://www.ips.gov.au/IPSHosted/wg4) and a mailing list. Those URSI radio scientists wishing to be included on the working-group mailing list should either contact the Chair directly, or send an e-mail to wg4-request@ips.gov.au with no text except the word "subscribe" in the subject field or message body.

Chair: Phil Wilkinson
IPS Radio and Space Services, Level 6, 477 Pitt St.
Postal Address: IPS, PO Box 1386, Haymarket
NSW 1240, Australia.
Tel: +61 2 9213 8003; Fax: +61 2 9213 8060.
E-mail: phil@ips.gov.au.

Vice-Chair: Matthew Angling
Centre for RF Propagation and Atmospheric Research
PB108, QinetiQ, St. Andrew's Road, Malvern, Worcs,
WR14 3PS, UK
Tel: +44 (0) 1684 896460; Fax: +44 (0) 1684 895241.
E-mail: mjangling@QinetiQ.com

URSI Publications

Modern Radio Science 1999

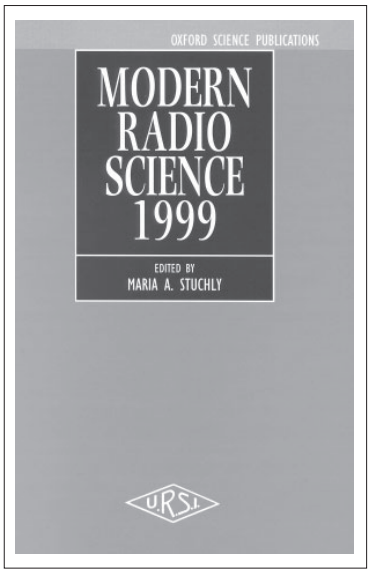

Editor: Maria Stuchly
ISBN 0-7803-6002-8
List Price : USD 49.95 Member Price : USD 45.00
IEEE Product No. PC5837

Published by Oxford University Press
in cooperation with URSI and IEEE Press
Order 24 hours a day, 7 days a week :
1-732-981 0060 (Worldwide)
1-800-678 4333 (USA & Canada)
Fax 1-732 981 9667
E-mail : customer-service@ieee.org

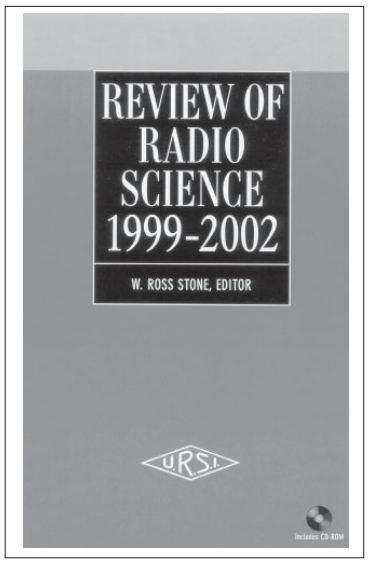

Review of Radio Science 1999-2002

Editor: W. Ross Stone
July 2002/Hardcover/977 pp
ISBN 0-471-26866-6
List Price : USD 125.00 Member Price : USD 106.25
IEEE Product No. #18493

Published by Wiley-Interscience
in cooperation with URSI and IEEE Press
Order can be sent to John Wiley & Sons, Inc.
from 8.30 a.m. to 5.30 p.m. :
1-732-469-4400 (Worldwide)
1-800-225-5945 (USA & Canada)
Fax 1-732 302-2370
E-mail : customer@wiley.com

Handbook on Radiopropagation Related to Satellite Communications in Tropical and Subtropical Countries

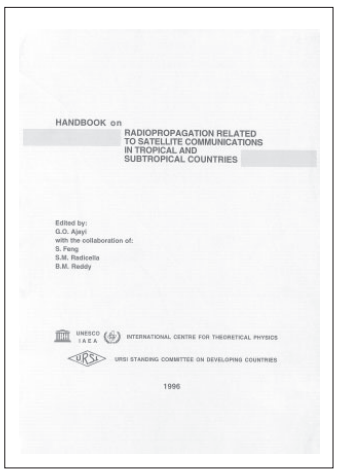

Editor: G.O. Ajayi
with the collaboration of :
S. Feng, S.M. Radicella, B.M. Reddy

Available from the URSI Secretariat
c/o Ghent University (INTEC)
Sint-Pietersnieuwstraat 41
B-9000 Gent, Belgium
tel. +32 9-264-33-20
fax +32 9-264-42-88
e-mail : ursi@intec.rug.ac.be

RADIO SCIENCE *Bimonthly!*

Radio Science contains original articles on all aspects of electromagnetic phenomena related to physical problems. Covers the propagation through and interaction of electromagnetic waves with geophysical media, biological media, plasmas, and man-made structures. Also included, but not limited to, are papers on the application of electromagnetic techniques to remote sensing of the Earth and its environment, telecommunications, signals and systems, the ionosphere, and radio astronomy.
ISSN 0048-6604.

See a recent Table of Contents on the web!
www.agu.org/ pubs/inpress.html

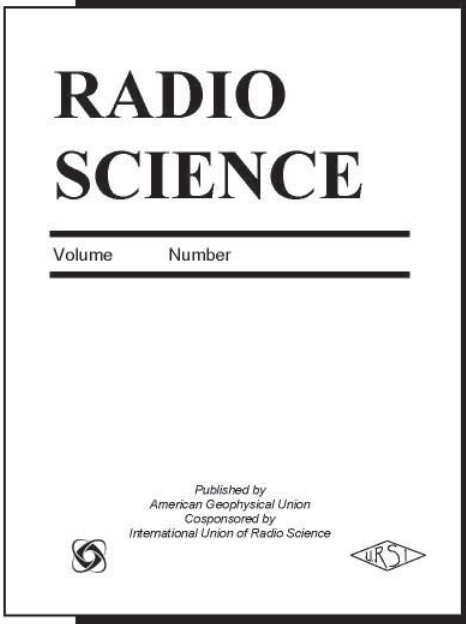

2003 Subscription Rates: On-line / Print / On-line+Print

AGU Members & U.R.S.I. correspondents:	**$33 / $55 / $65**
Student AGU Members:	**$17 / $35 / $35**

Postal surcharges outside of North America: surface postage $22, air freight $51, air mail $84.

Subscribe Today!

	European Office	U.S. Office
Online:	www.agu.org	www.agu.org
E-Mail:	agu@copernicus.org	orders@.agu.org
Voice:	+49-5556-1440	+1-202-462-6900
Fax:	+49-5556-4709	+1-202-328-0566
Mail:	AGU - Orders Max-Planck Str. 13 37191 Katlenburg-Lindau GERMANY	AGU - Orders 2000 Florida Ave., NW Washington, DC 20009 USA

Submit to *Radio Science*!

Submissions to *Radio Science* are now done through the new **GEMS** electronic submissions system at **http://radioscience-submit.agu.org/**

For details on style, contact an editor's assistant listed below or consult the last pages of a recent issue of *Radio Science*.

Tarek M. Habashy, Editor
Schlumberger Doll Research
Electromagnetic Department
Old Quarry Road
RC, CT 06877
Ph: 203-431-5563
Fax: 203-438-3819
email: thabashy@ridgefield.oilfield.slb.com

Cosponsored by U.R.S.I. International and published bimonthly by AGU.

Members of the Network of U.R.S.I. Correspondents may subscribe at the AGU member rate!

AGU

Code: URSI03

Wireless Networks

The journal of mobile communication, computation and information

Aims & Scope:
The wireless communication revolution is bringing fundamental changes to data networking, telecommunication, and is making integrated networks a reality. By freeing the user from the cord, personal communications networks, wireless LAN's, mobile radio networks and cellular systems, harbor the promise of fully distributed mobile computing and communications, any time, anywhere. Numerous wireless services are also maturing and are poised to change the way and scope of communication. WINET focuses on the networking and user aspects of this field. It provides a single common and global forum for archival value contributions documenting these fast growing areas of interest. The journal publishes refereed articles dealing with research, experience and management issues of wireless networks. Its aim is to allow the reader to benefit from experience, problems and solutions described. Regularly addressed issues include: Network architectures for Personal Communications Systems, wireless LAN's, radio , tactical and other wireless networks, design and analysis of protocols, network management and network performance, network services and service integration, nomadic computing, internetworking with cable and other wireless networks, standardization and regulatory issues, specific system descriptions, applications and user interface, and enabling technologies for wireless networks.

Wireless Networks is a joint publication of the ACM and Baltzer Science Publishers. Officially sponsored by URSI

Special Discount for URSI Radioscientists

Euro 62 / US$ 65
(including mailing and handling)

Wireless Networks ISSN 1022-0038
Contact: Mrs. Inge Heleu
Fax +32 9 264 42 88 E-mail ursi@intec.rug.ac.be
Non members/Institutions: contact Baltzer Science Publishers

For a complete overview on what has been and will be published in Telecommunication Systems please consult our homepage:

BALTZER SCIENCE PUBLISHERSHOMEPAGE
http://www.baltzer.nl/winet

BALTZER SCIENCE PUBLISHERS
P.O.Box 221, 1400 AE Bussum, The Netherlands
Tel: +31 35 6954250 Fax: +31 35 6954 258 E-mail: publish@baltzer.nl

The Journal of Atmospheric and Solar-Terrestrial Physics

SPECIAL OFFER TO URSI CORRESPONDENTS

AIMS AND SCOPE

The *Journal of Atmospheric and Terrestrial Physics* (JASTP) first appeared in print in 1951, at the very start of what is termed the "Space Age". The first papers grappled with such novel subjects as the Earth's ionosphere and photographic studies of the aurora. Since that early, seminal work, the Journal has continuously evolved and expanded its scope in concert with - and in support of - the exciting evolution of a dynamic, rapidly growing field of scientific endeavour: the Earth and Space Sciences. At its Golden Anniversary, the now re-named *Journal of Atmospheric and Solar-Terrestrial Physics* (JASTP) continues its development as the premier international journal dedicated to the physics of the Earth's atmospheric and space environment, especially the highly varied and highly variable physical phenomena that occur in this natural laboratory and the processes that couple them. The *Journal of Atmospheric and Solar-Terrestrial Physics* is an international journal concerned with the inter-disciplinary science of the Sun-Earth connection, defined very broadly. The journal referees and publishes original research papers, using rigorous standards of review, and focusing on the following: The results of experiments and their interpretations, and results of theoretical or modelling studies; Papers dealing with remote sensing carried out from the ground or space and with in situ studies made from rockets or from satellites orbiting the Earth; and, Plans for future research, often carried out within programs of international scope. The Journal also encourages papers involving: large scale collaborations, especially those with an international perspective; rapid communications; papers dealing with novel techniques or methodologies; commissioned review papers on topical subjects; and, special issues arising from chosen scientific symposia or workshops. The journal covers the physical processes operating in the troposphere, stratosphere, mesosphere, thermosphere, ionosphere, magnetosphere, the Sun, interplanetary medium, and heliosphere. Phenomena occurring in other "spheres", solar influences on climate, and supporting laboratory measurements are also considered. The journal deals especially with the coupling between the different regions. Solar flares, coronal mass ejections, and other energetic events on the Sun create interesting and important perturbations in the near-Earth space environment. The physics of this subject, now termed "space weather", is central to the Journal of Atmospheric and Solar-Terrestrial Physics and the journal welcomes papers that lead in the direction of a predictive understanding of the coupled system. Regarding the upper atmosphere, the subjects of aeronomy, geomagnetism and geoelectricity, auroral phenomena, radio wave propagation, and plasma instabilities, are examples within the broad field of solar-terrestrial physics which emphasise the energy exchange between the solar wind, the magnetospheric and ionosphericplasmas, and the neutral gas. In the lower atmosphere, topics covered range from mesoscale to global scale dynamics, to atmospheric electricity, lightning and its effects, and to anthropogenic changes. Helpful, novel schematic diagrams are encouraged. Short animations and ancillary data sets can also be accommodated. Prospective authors should review the *Instructions to Authors* at the back of each issue.

Complimentary Information about this journal:
http://www.elsevier.com/locate/JASTP?
http://earth.elsevier.com/geophysics

Audience:
Atmospheric physicists, geophysicists and astrophysicists.

Abstracted/indexed in:
CAM SCI Abstr
Curr Cont SCISEARCH Data
Curr Cont Sci Cit Ind
Curr Cont/Phys Chem & Sci
INSPEC Data
Meteoro & Geoastrophys Abstr
Res Alert

Editor-in-Chief:
T.L. Killeen, National Centre for Atmospheric Research, Boulder, Colorado, 80307 USA

Editorial Office:
P.O. Box 1930, 1000 BX Amsterdam, The Netherlands

Special Rate for URSI Radioscientists 2003:
Euro 149.00 (US$ 149.00)
Subscription Information
2002: Volume 65 (18 issues)
Subscription price: Euro 2659 (US$ 2975)
ISSN: 1364-6826

CONTENTS DIRECT:
The table of contents for this journal is now available pre-publication, via e-mail, as part of the free ContentsDirect service from Elsevier Science. Please send an e-mail message to cdhelp@elsevier.co.uk for further information about this service.

For ordering information please contact Elsevier Regional Sales Offices:

Asia & Australasia/ e-mail: asiainfo@elsevier.com
Europe, Middle East & Africa: e-mail: nlinfo-f@elsevier.com
Japan: Email: info@elsevier.co.jp
Latin America : e-mail: rsola.info@elsevier.com.br
United States & Canada : e-mail: usinfo-f@elsevier.com

Information for authors

Content

The *Radio Science Bulletin* is published four times per year by the Radio Science Press on behalf of URSI, the International Union of Radio Science. The content of the *Bulletin* falls into three categories: peer-reviewed scientific papers, correspondence items (short technical notes, letters to the editor, reports on meetings, and reviews), and general and administrative information issued by the URSI Secretariat. Scientific papers may be invited (such as papers in the *Reviews of Radio Science* series, from the Commissions of URSI) or contributed. Papers may include original contributions, but should preferably also be of a sufficiently tutorial or review nature to be of interest to a wide range of radio scientists. The *Radio Science Bulletin* is indexed and abstracted by INSPEC.

Scientific papers are subjected to peer review. The content should be original and should not duplicate information or material that has been previously published (if use is made of previously published material, this must be identified to the Editor at the time of submission). Submission of a manuscript constitutes an implicit statement by the author(s) that it has not been submitted, accepted for publication, published, or copyrighted elsewhere, unless stated differently by the author(s) at time of submission. Accepted material will not be returned unless requested by the author(s) at time of submission.

Submissions

Material submitted for publication in the scientific section of the *Bulletin* should be addressed to the Editor, whereas administrative material is handled directly with the Secretariat. Submission in electronic format according to the instructions below is preferred. There are typically no page charges for contributions following the guidelines. No free reprints are provided.

Style and Format

There are no set limits on the length of papers, but they typically range from three to 15 published pages including figures. The official languages of URSI are French and English: contributions in either language are acceptable. No specific style for the manuscript is required as the final layout of the material is done by the URSI Secretariat. Manuscripts should generally be prepared in one column for printing on one side of the paper, with as little use of automatic formatting features of word processors as possible. A complete style guide for the *Reviews of Radio Science* can be downloaded from http://www.ips.gov.au/IPSHosted/NCRS/reviews/. The style instructions in this can be followed for all other *Bulletin* contributions, as well. The name, affiliation, address, telephone and fax numbers, and e-mail address for all authors must be included with all submissions. All papers accepted for publication are subject to editing to provide uniformity of style and clarity of language. The publication schedule does not usually permit providing galleys to the author.

Figure captions should be on a separate page in proper style; see the above guide or any issue for examples. All lettering on figures must be of sufficient size to be at least 9 pt in size after reduction to column width. Each illustration should be identified on the back or at the bottom of the sheet with the figure number and name of author(s). If possible, the figures should also be provided in electronic format. TIF is preferred, although other formats are possible as well: please contact the Editor. Electronic versions of figures *must* be of sufficient resolution to permit good quality in print. As a rough guideline, when sized to column width, line art should have a minimum resolution of 300 dpi; color photographs should have a minimum resolution of 150 dpi with a color depth of 24 bits. 72 dpi images intended for the Web are generally *not* acceptable. Contact the Editor for further information.

Electronic Submission

A version of Microsoft *Word* is the preferred format for submissions. Submissions in versions of T_EX can be accepted in some circumstances: please contact the Editor before submitting. *A paper copy of all electronic submissions must be mailed to the Editor, including originals of all figures.* Please do *not* include figures in the same file as the text of a contribution. Electronic files can be send to the Editor in three ways: (1) By sending a floppy diskette or CD-R; (2) By attachment to an e-mail message to the Editor (the maximum size for attachments *after* MIME encoding is about 7 MB); (3) By e-mailing the Editor instructions for downloading the material from an ftp site.

Review Process

The review process usually requires about three months. Authors may be asked to modify the manuscript if it is not accepted in its original form. The elapsed time between receipt of a manuscript and publication is usually less than twelve months.

Copyright

Submission of a contribution to the *Radio Science Bulletin* will be interpreted as assignment and release of copyright and any and all other rights to the Radio Science Press, acting as agent and trustee for URSI. Submission for publication implicitly indicates the author(s) agreement with such assignment, and certification that publication will not violate any other copyrights or other rights associated with the submitted material.

APPLICATION FOR AN URSI RADIOSCIENTIST

I have not attended the last URSI General Assembly, and I wish to remain/become an URSI Radioscientist in the 2003-2005 triennium. Subscription to *The Radio Science Bulletin* is included in the fee.
(please type or print in BLOCK LETTERS)

Name: Prof./Dr./Mr./Mrs./Ms. _____
Family Name *First Name* *Middle Initials*

Present job title: _____

Years of professional experience: _____

Professional affiliation: _____

I request that all information, including the bulletin, be sent to my ☐ home ☐ business address, i.e.:

Company name: _____

Department: _____

Street address: _____

City and postal / zip code: _____

Province / State: _____ Country: _____

Phone: _____ ext: _____ Fax: _____

E-mail: _____

Areas of interest (please tick)

☐ A Electromagnetic Metrology
☐ B Fields and Waves
☐ C Signals and Systems
☐ D Electronics and Photonics
☐ E Electromagnetic Noise & Interference
☐ F Wave Propagation & Remote Sensing
☐ G Ionospheric Radio and Propagation
☐ H Waves in Plasmas
☐ J Radio Astronomy
☐ K Electromagnetics in Biology & Medicine

The fee is 40 Euro.
(The URSI Board of Officers will consider waiving of the fee if the case is made to them in writing)

Method of payment: VISA / MASTERCARD (we do not accept cheques)

Credit Card No ☐☐☐☐ ☐☐☐☐ ☐☐☐☐ ☐☐☐☐ Exp. date: _____

Date: _____ Signed _____

Please return this signed form to: